

SYNTHESIS AND CHARACTERIZATION OF TITANIUM BASED HARD COATINGS

A THESIS

*Submitted in partial fulfilment of the
requirements for the award of the degree*

of

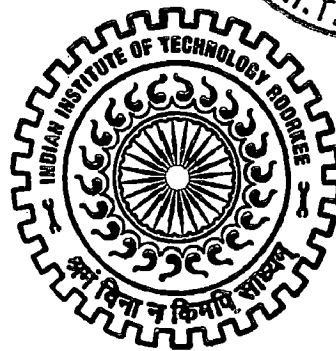
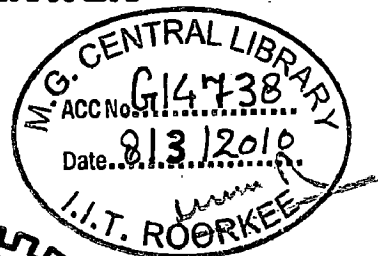
DOCTOR OF PHILOSOPHY

in

METALLURGICAL AND MATERIALS ENGINEERING

by

VIPIN CHAWLA



**DEPARTMENT OF METALLURGICAL AND MATERIALS ENGINEERING
INDIAN INSTITUTE OF TECHNOLOGY ROORKEE**

ROORKEE - 247 667 (INDIA)

DECEMBER, 2008



INDIAN INSTITUTE OF TECHNOLOGY ROORKEE ROORKEE

CANDIDATE'S DECLARATION

I hereby certify that the work which is being presented in the thesis entitled **Synthesis and Characterization of Titanium Based Hard Coatings** in partial fulfilment of the requirement for the award of the Degree of Doctor of Philosophy and submitted in the Department of Metallurgical and Materials Engineering of the Indian Institute of Technology Roorkee, Roorkee is an authentic record of my own work carried out during a period from January 2006 to December 2008 under the supervision of Dr. R. Jayaganthan, Assistant Professor, Department of Metallurgical and Materials Engineering and Dr. Ramesh Chandra, Associate Professor, Institute Instrumentation Centre, Indian Institute of Technology Roorkee, Roorkee.

The matter presented in this thesis has not been submitted by me for the award of any other degree of this or any other Institute.

Vipin Chawla

(VIPIN CHAWLA)

This is to certify that the above statement made by the candidate is correct to the best of our knowledge.

R. Chandra

(Ramesh Chandra)
Supervisor

R. Jay

(R. Jayaganthan)
Supervisor

Date: 30.12.2008

The Ph. D. Viva-Voce Examination of Mr. Vipin Chawla, Research Scholar, has been held on ...6/05/09.....

R. Jay *R. Chandra*
Signature of Supervisors
6.5.09

D. Anjilal

Signature of External Examiner

Dedicated

To

My beloved Family

ABSTRACT

Hard coatings have been successfully used for protection of materials and particularly to enhance the life of cutting tools since the 1970's and it is defined by its hardness which is the measure of resistance to plastic deformation. Hard coatings are extensively used for tribological applications and their development by various physical and chemical deposition techniques are ever growing to achieve their superior performance in the actual engineering applications such as to increase the lifetime of cutting and forming tools under dry and high speed machining conditions and the protective coatings for turbine blades and engine parts to improve their durability. Therefore, by properly selecting the coating techniques and materials, we can protect not only the substrate materials to prolong their service life, but also increase commercial value of the products.

Hard coatings of binary and ternary metal nitride materials are used in various engineering applications due to their remarkable physical and mechanical properties including high hardness, high melting point, chemical inertness, and good thermodynamic stability. The control of the microstructural characteristics in terms of grain size, crystallographic orientation, lattice defects, texture and surface morphology as well as phase composition and surface morphological evolution of transition metal nitride films are very important in realizing the aforementioned properties so as to extend the performance and life time of the coated products. The literature on the optimized process variables using sputtering techniques for the deposition of transition metal nitride films with the desirable microstructural characteristics is very limited.

Therefore, it is desirable to establish the process for producing high quality film these transition metal nitrides.

The main objectives of present work were to synthesize nanocrystalline thin film titanium based nitrides such as Titanium Nitride (TiN), Titanium Silicon Nitride (TiN), and Titanium Nitride/Silicon Nitride (TiN/SiN_x) multilayer on various substrate by DC/RF magnetron sputtering technique and to investigate the effect of sputtering process parameters on structural and mechanical properties of these materials obtaining high quality thin films. In addition, Titanium (Ti) nanocrystalline thin films were prepared and the effect of sputtering process parameters on structural properties of these films was investigated. A chapter - wise summary of the thesis is given below.

Chapter 1 gives an overview of hard coatings in which background, synthesis techniques and applications are discussed. The structural and mechanical properties of Ti based nitrides TiN, Ti-Si-N and TiN/SiN_x multilayer films and their applications are discussed in this chapter.

Chapter 2 presents the details of synthesis and characterization techniques employed for the present research work. **Section 2.1** - A brief description as to the different film growth modes, influenced by the interaction energies of substrate and film atoms is included in this section. **Section 2.2** - The process description and mechanical details of DC/RF magnetron sputtering technique used for the deposition of thin films in the present work is discussed in this section. **Section 2.3** - The methodology for characterization of deposited films by different techniques such as X-Ray Diffraction (XRD) for the phase identification and textures, grain and surface morphology of films by using techniques such as Field Emission Scanning Electron Microscopy (FESEM), Atomic Force Microscopy (AFM), and Transmission Electron Microscopy (TEM)

(TEM) are discussed. The mechanical properties of deposited films were measured by nanoindentation technique. ANSYS Finite Element Analysis software was used for simulating the thermal stress in the sputter deposited thin films in the present work.

Chapter 3 describes the synthesis and characterization of magnetron sputtered titanium films. This chapter is divided into three sections. The first section (**Section 3.1**) mainly describes the effect of substrate temperature on the microstructural morphologies of the films deposited on Silicon substrate. XRD results show that Ti films grow with a (002) preferred orientation and its intensity increases with increase in substrate temperature from room temperature to 200°C and changes to (101) at above 300°C. The grain size of Ti films increases with increase in substrate temperature due to enhanced mobility of adatoms in the film surface and showed two- and three-dimensional hexagonal structure of the grains at 200°C and > 200°C, respectively, as evident from the FE-SEM, AFM and EBSD results. **Section 3.2** discusses the deposition of Ti films on glass substrates under varying deposition parameters and XRD characterization revealed the initial (100) preferred orientation but it transformed into (002) and (101) orientation with increase in sputtering power and substrate temperature, respectively. It is due to the relaxation of compressive stress to tensile mode at higher thickness, which favors the (002) preferred orientation but the higher substrate temperature could facilitate the enhanced mobility of adatoms in the film surface leading to the formation of (101) orientation of grains. The preferred orientations of (002) and (101) were observed for the films deposited with the sputtering pressure of 5 mTorr and 20 mTorr, respectively due to the competition between strain energy and surface free energy affecting the textures of the grains. The average surface roughness of the Ti films showed an increasing trend with power, pressure and temperature from

the AFM analysis and the dense film morphology was observed in the SEM images of Ti films deposited with substrate temperature (500°C). In the last **Section 3.3**, a thermal stress in Ti films deposited on glass and silicon substrates by finite element analysis (ANSYS) was discussed. It is found that the thermal stress of Ti coating exhibits a linear relationship with deposition temperature and Young's modulus, but it exhibit an inverse relationship with the coating thickness, the results are in accordance with the analytical method. Also, the radial and shear stress distribution of the coating-substrate combination are calculated and it is observed that high tensile shear stress of Ti coating on glass substrate reduces its adhesive strength but high-compressive shear stress of Ti on Si substrate improves its adhesive strength.

Chapter 4 discusses the synthesis and characterization of magnetron sputtered titanium nitride films. This chapter is divided into three sections. The first section (**Section 4.1**) describes the effect of atmosphere and deposition time on the microstructural morphologies of the TiN films. The films deposited under an Ar+N₂ atmosphere initially exhibited a (200) preferred orientation but the film deposited under a pure N₂ atmosphere showed an initial (111) preferred orientation, which subsequently changed to a mixed (111)-(200) orientation with increase in deposition time in both atmospheres. The competition between surface energy and strain energy during film growth might contribute to the changes in preferred orientation. With an increase in deposition time and at some critical thickness, stress relaxation may reduce strain energy to a greater extent than the increase in surface energy due to the texture changes. A pyramidal shape and columnar grain morphology were observed for TiN films deposited in Ar+N₂ and pure N₂ atmosphere, respectively, as seen from the FE-SEM and AFM analysis. It is observed from the nanoindentation study that hardness (H) and

Young's modulus (E) value of TiN films decreases with increasing deposition time in both atmospheres. However, in pure N₂ atmosphere, high H and E values of TiN films are observed due to columnar morphology and less roughness, the maximum H and E values are 25.2 GPa and 395.4 GPa, respectively, when the deposition time is 60 min. **Section 4.2** discusses about the microstructural and mechanical properties of magnetron sputtered TiN films on glass substrate with increase in thickness of the film. XRD analysis showed the (200) preferred orientation up to 1.26 μm thick films due to the lowest surface free energy during film growth in comparison to strain energy but as the film thickness increases above 1.26 μm, competition between surface energy and strain energy increases and hence (220) peak develops to minimize the total energy. The deposited films were found to be very dense nanocrystalline film with less porosity as evident from their FE-SEM and AFM images. The hardness of TiN film was found to be thickness dependent and observed to be 23.2 GPa hardness value for the films having less positive micro strain. It is attributed to very fine grain size (18.5 nm) with its less active slip system. In the last **Section 4.3**, analysis of thermal stress in magnetron sputtered TiN coating on glass and silicon substrates by finite element method (ANSYS) is included. It is found that the thermal stress in TiN coating, for the planar substrate, exhibits a linear relationship with substrate temperature, substrate thickness and Young's modulus of the coating, but showed an inverse relationship with the coating thickness and all the results were in tandem with the analytical method. The thermal stress induced in the coatings for the rough substrate is higher as compared to that of the planar substrate. The radial and shear stress distribution of the coating-substrate combination were also calculated. The low and high compressive shear

stresses observed in the TiN coating on glass and Si substrate, respectively, indicate a low adhesive strength of the coating on the former than that of the latter.

Chapter 5 describes the work on synthesis and characterization of magnetron sputtered titanium silicon nitride films. This chapter is divided into two sections. The first section (**Section 5.1**) describes the effect of varying Si content on the structural and mechanical properties of Ti-Si-N films deposited on Si (100) and Stainless Steel (type 304) substrates by DC/RF magnetron sputtering. XRD analysis revealed the (111) orientation up to 12.8 at.% Si content and above 12.8 at.% Si, intensities of (200) and (220) peaks grow up but above 15.6 at.% Si, no peak could be observed as the film becomes amorphous. Microstructural analysis by FE-SEM and AFM showed that with varying Si contents, grain size and surface roughness decreases and forms a pyramidal shape, which transformed into columnar and finally to amorphous structure. The hardness and Young's modulus of the films were 34 GPa and 275 GPa, respectively, with 15.6 at.% Si contents due to the nanocrystalline TiN surrounded by a matrix of amorphous Si_3N_4 , which assist the relaxation of stresses and reduces grain boundary sliding under stress, and thus hardness increases. The reduction in hardness value of the films with further increase in Si contents is due to poor properties of amorphous phase. **Section 5.2** describes the effect of varying sputtering pressure on the structural and mechanical properties of Ti-Si-N films deposited on Si (100) substrate by DC/RF magnetron sputtering. XRD results of the films shows the formation of (111), (200) and (220) peaks but with increase in sputtering pressure, (111) orientation dominates owing to increase in grain size and the films become crystalline. The dense blurred grains transform into uniform grains with increase in porosity, grains size and surface roughness as revealed by FE-SEM and AFM analysis. The hardness and Young's

modulus of the films are 33.7 GPa and 278.6 GPa with 5 mTorr sputtering pressure but it decreases afterwards with increasing sputtering pressure due to porosity in the films.

Chapter 6 discusses the synthesis and characterization of magnetron sputtered titanium nitride/silicon nitride multilayer films. **Section 6.1** describes the effect of varying layer deposition time on the structural and mechanical properties of TiN/SiN_x multilayer films deposited on Si (100) substrate by DC/RF magnetron sputtering. XRD analysis of the films, with varying SiN_x layer deposition time from 5-30 seconds while keeping the TiN layer deposition time at 15 seconds, revealed the (111), (200) and (220) orientation and with variation of TiN layer deposition time from 5-30 seconds while keeping the SiN_x layer deposition time at 15 seconds, same orientations were observed initially but (200) orientation has increased with increase of deposition time. It is because of the stable (200) orientation with the lowest surface free energy is favored thermodynamically. The grain size of the multilayer was around 7.0 nm in varying SiN_x layer deposition time and it varied from 2.7 to 11.3 nm when TiN layer deposition time was increased. The surface roughness of the Ti-Si-N films was calculated from its AFM images and it remains constant with varying SiN_x layer deposition time but increases in the other cases, with varying TiN layer deposition time. The hardness and Young's modulus values of TiN/SiN_x multilayer films have increased up to 31.4 GPa and 365.8 GPa, respectively, with varying SiN_x layer deposition time initially but it decreased beyond the SiN_x layer deposition time of 10 seconds as it is used only to interrupt the TiN growth and facilitate its renucleation through the introduction of nanolayers of a different material. In other case, with variation of TiN layer deposition time, the H and E values of TiN/SiN_x multilayer films have increased initially, with increase in deposition time for TiN layer up to 10 seconds, followed by uniform decrease and then

finally it has increased sharply up to 33.4 GPa and 370.5 GPa, respectively for 30 seconds TiN layer deposition time. The smaller grain size of TiN nanocrystals and very thin layer of SiN_x contribute for the higher hardness of TiN/SiN_x multilayer. The increase in hardness of multilayer may be due to the one or combination of the factors such as coherency stress hardening, epitaxial stabilization of meta stable structure of crystalline SiN_x layer, Orowan-like strengthening and Hall-Petch strengthening.

Chapter 7 presents the summary and conclusion of the entire work presented in the thesis and also proposes the future directions in which these studies can be extended.

ACKNOWLEDGEMENTS

It is a pleasure to thank all people who have helped and inspired me during my doctoral study.

In the first place, I would like to express my deep and sincere gratitude to my supervisors, Dr. R. Jayaganthan and Dr. Ramesh Chandra for their supervision, advice and guidance from the very early stage of this research as well as giving me extraordinary experiences throughout the work. Above all and the most needed, they provided me unflinching encouragement and support in various ways. Their scientific intuitions have made them as a constant oasis of ideas and passions in science, which inspired and enriched my growth as a student, a researcher and to become a scientist. I am indebted to them for their valuable guidance.

I wish to express my warm and sincere thanks to Prof. S. K. Nath, Head of the Department of Metallurgical and Materials Engineering and all other faculty members of the Department for their keen interest in this work. I would like thank, especially, Dr. Vivek Pancholi for having enabled me to understand FE-SEM/EBSD and use it effectively for my research work. I am also thankful to the members of my SRC committee, Prof. S. K. Nath (Chairman), Dr. Surendra Singh (Internal member), Department of Metallurgical and Materials Engineering and Dr. Davinder Kaur (External Member), Department of Physics, IIT Roorkee for their invaluable suggestions and encouragement to carry out this work.

I am thankful to Prof. A. K. Choudhary, Head of the Institute Instrumentation Centre for extending the characterization facilities for my work.

I am highly obliged and express my sincere thanks to the official & technical staff of the Department of Metallurgical and Materials Engineering and Institute Instrumentation Centre, IIT Roorkee. Also, special thanks go to Mr. S. D. Sharma, Mr. Birendra Dutt, Mr. Anil Kumar Saini and Mr. Yashpal Singh for their kind support during my research.

I owe my most sincere gratitude to Prof. A. C. Pandey, Department of Physics, Allahabad University, Dr. Ravi C. Gundakaram, ARCI, Hyderabad and Dr. S. Dash, IGCAR, Kalpakkam who rendered me an opportunity for performing the nanoindentation measurements in their lab. I am thankful to Dr. Manavendra Kumar and Mr. Raghvendra Yadav for their help during the experimental work in Allahabad University.

All my lab buddies, Dr. Preetam Singh, Ashvani Kumar, Ashish Kumar Pandey, Deepak, Ajay Kaushal, Hetal Shah, Yogendra Kumar Gautam, Archana Mishra, R. Kathiravan, Sonal Singhal, Ritu Vishnoi, Rahul Singhal, Mukesh Kumar, Rajan Walia, Dr. Sanjeev Kumar, Shivendra Pratap Singh, Nitin and Sushant Rawal at the Nano Science Laboratory, Institute Instrumentation Centre made it a convivial place to work and I greatly enjoyed working with them during my research. I thank them all for their help, support, interest and valuable hints during the long hours in the lab and also for the entertainment in the form of cricket.

I am especially grateful to my many student colleagues, Amit Kumar, Atikur Rehman, Sushanta Kumar Panigrahi, Dr. Mahesh Anuwar, Subhash Kamal, Kuntal Maiti, Vikas Chawla and Vikas Babu for giving wise advice and help with various applications during my research.

I wish to thank my friends Navneet Kumar, Harish Kumar Sharma, Gautam Roy, Priti Kadam, Hariom Gupta and Hitender Kumar, for their kind gestures/help through my difficult times, and for all the emotional support and caring they provided.

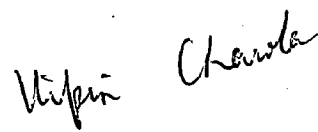
I warmly thank Prof. G. S. Agrawal, Chief Warden, Govind Bhawan for giving me an opportunity to serve as the Residential Warden of Govind Bhawan, which is very wonderful and fruitful experience as a part of administration.

The Financial support from DST and CSIR, New Delhi for this investigation is gratefully acknowledged and also the travel fund provided by DST, New Delhi for attending international conference in Singapore during my research.

Where would I be without my family? My family deserves special mention for their unflagging love and support throughout my life; this work is simply impossible without them. I am indebted to my father, Shri G. D. Chawla, for his care and love. I cannot ask for more from my mother, Smt. Saroj Chawla, as she is simply perfect. I have no suitable word that can fully describe her everlasting love to me and I remember, most of all, her delicious dishes. I feel proud of my elder brother, Dr. Amit Kumar Chawla, for his talent. He is a role model for me to follow unconsciously and my inspiration for doctoral study which is impossible without his support.

I would like to thank everybody who was important to the successful realization of thesis, as well as expressing my apology that I could not mention personally one by one.

Last but not least, thanks to God for granting me the faith and will to obtain this academic achievement that has culminated in this thesis.


(VIPIN CHAWLA)

LIST OF FIGURES

1.1	Hardness Vs grain size	3
1.2	Titanium crystal structures: (a) Hexagonal close-packed below 900°C and (b) Body centered cubic above 900°C	12
1.3	The crystal structure of Titanium Nitride	15
2.1	Schematic diagram of surface energy of substrate (γ_S), thin film material (γ_F) and interface energy of film-substrate (γ_{FS})	24
2.2	Processes generated by the impact of highly energetic particle on a target surface. The collision may terminate at the target or cause particle sputtering.	28
2.3	Electric and magnetic field lines in a magnetron gun	30
2.4	(a) Magnetron sputtering process	31
	(b) Collisions in the sputtering process near the target	31
2.5	(a) DC/RF magnetron sputtering unit set up in our Nano Science Lab	32
	(b) New & used sputtering target	32
	(c) Substrate holder/heater	32
2.6	Schematic diagram of beam path	35
2.7	X-ray diffraction (Bruker AXS, D8 Advance)	36
2.8	Schematic diagram of the Field Emission Scanning Electron Microscope (FE-SEM)	38
2.9	Field Emission Scanning Electron Microscope (FEI, Quanta 200F)	40
2.10	Schematic setup of Atomic Force Microscope (AFM)	42
2.11	Atomic Force Microscope (NT-MDT, Ntegra)	43

2.12	Graph between van der Waals force Vs distance	44
2.13	Schematic diagram of a Transmission Electron Microscope (TEM)	47
2.14	Transmission Electron Microscope (FEI, Tecnai 20)	48
2.15	(a) Bright Field (BF) imaging and (b) Dark Field (DF) imaging	49
2.16	Nanoindentation tester (CSM+)	52
2.17	(a) Loading and unloading of the indenter on the sample	54
	(b) Load is plotted against the Displacement	54
3.1	(a) XRD peaks of Ti films deposited on Si substrate as a function of substrate temperature	67
	(b) Texture coefficients of Ti films deposited on Si substrate as a function of substrate temperature	68
3.2	Cross sectional view of Ti films on Si substrate deposited at substrate temperature (a) 200°C, (b) 400°C and (c) 600°C	69
3.3	AFM images of Ti films on Si deposited at substrate temperature (a) 100°C, (b) 200°C, (c) 300°C, (d) 400°C, (e) 500°C and (f) 600°C	71
3.4	FE-SEM images of Ti films on Si deposited at substrate temperature (a) 100°C, (b) 200°C, (c) 300°C, (d) 400°C, (e) 500°C and (f) 600°C	72
3.5	Tilted FE-SEM images of Ti films on Si deposited at substrate temperature 600°C (a) HV = 3 kV and (b) HV = 20 kV	73
3.6	Orientation map of the measurement area and grain size variation as a function of area fraction of Ti films deposited on Si at substrate temperature (a-b) at 200°C, (c-d) at 400°C and (e-f) 600°C	74
3.7	XRD graphs of Ti films on glass substrates as a function of (a) sputtering power, (b) substrate temperature and (c) sputtering pressure	79

3.8	Texture coefficients of Ti films on glass substrates as a function of (a) sputtering power, (b) substrate temperature and (c) sputtering pressure	82
3.9	AFM images of Ti films on glass substrates as a function of different parameters: I) Sputtering Power (a) at 50 Watt, (b) at 100 Watt and (c) at 150 Watt II) Substrate Temperature (a) at 100°C, (d) at 300°C and (e) at 500°C III) Sputtering Pressure (f) at 5 mTorr, (a) at 10 mTorr and (g) at 20 mTorr	84
3.10	FE-SEM images of Ti films on glass substrates as a function of different parameters: I) Sputtering Power (a) at 50 Watt, (b) at 100 Watt and (c) at 150 Watt II) Substrate Temperature (a) at 100°C, (d) at 300°C and (e) at 500°C III) Sputtering Pressure (f) at 5 mTorr, (a) at 10 mTorr and (g) at 20 mTorr	87
3.11	Cross section FE-SEM image of Ti film on glass substrate	88
3.12	Schematic diagram of axisymmetric 2D solid model	95
3.13	Thermal stress variation as a function of substrate temperature on (a) Glass and (b) Si substrate	96
3.14	Thermal stress variation as a function of coating thickness on (a) Glass and (b) Si substrate	97
3.15	Thermal stress variation on Si substrate as a function of (a) substrate temperature, (b) young's modulus and (c) coating thickness	98
3.16	Comparison of thermal stress variation as a function of thickness on Glass and Si substrate (a) 1.0-3.0 mm substrate thickness (b) 0.1-0.5 mm substrate thickness	99
3.17	Thermal stress variation as a function of young's modulus on (a) Glass and	

(b) Si substrate	100
3.18 Radial stress (σ_r) distribution through the thickness of coating and substrate at different position from the edge to the center on (a) Glass and (b) Si substrate	101
3.19 Shear stress (σ_{xz}) distribution through the thickness of coating and substrate at different position from the edge to the center on (a) Glass and (b) Si substrate	102
4.1 XRD peaks and texture coefficients of TiN films deposited on Si substrate as a function of deposition time (a & c) in Ar+N ₂ atmosphere and (b & d) in N ₂ atmosphere	112
4.2 Top surface view, 60° tilt view and cross section FE-SEM images of TiN thin films deposited (a, c & e) in Ar+N ₂ atmosphere and (b, d & f) in N ₂ atmosphere	115
4.3 2D and 3D AFM images of TiN films deposited (a & c) in Ar+N ₂ atmosphere and (b & d) in N ₂ atmosphere	116
4.4 AFM <i>in-situ</i> image of the indent on the sample	117
4.5 (a) Hardness of TiN films deposited in Ar+N ₂ and N ₂ atmosphere	118
(b) Young's Modulus of same films	118
4.6 (a) XRD peaks of TiN films deposited on glass substrate	122
4.6 (b) Texture coefficients of TiN films deposited on glass substrate	123
4.7 2D & 3D AFM images of TiN films deposited on glass substrate at thickness (a-b) 0.63 μm , (c-d) 1.26 μm and (e-f) 1.89 μm	124
4.8 FE-SEM images of TiN films deposited on glass substrate at thickness	

(a) 0.63 μm , (b) 1.26 μm and (c) 1.89 μm	125
4.9 Load-Displacement curve of TiN thin films deposited on glass substrate	126
4.10 (a) Hardness of TiN thin film as a function of film thickness on glass substrate	127
(b) Young's Modulus of TiN thin film as a function of film thickness on glass substrate	127
4.11 A Schematic of axisymmetric 2D solid model of plane and rough substrates	136
4.12 Thermal stress variation as a function of substrate temperature on (a) glass and (b) silicon substrate	137
4.13 Thermal stress variation as a function of coating thickness on (a) glass and (b) silicon substrate	138
4.14 Thermal stress variation as a function of substrate thickness on (a) glass and (b) silicon substrate	139
4.15 Thermal stress variation as a function of Young's Modulus on (a) glass and (b) silicon substrate	140
4.16 Radial stress (σ_r) distribution through the thickness of coating and substrate at different position from the edge to the center on (a) glass and (b) silicon substrate	141
4.17 Shear stress (σ_{xz}) distribution through the thickness of coating and substrate at different position from the edge to the center on (a) glass and (b) silicon substrate	142
5.1 XRD peaks of Ti-Si-N films deposited with variation of Si content on (a) Si substrate and (b) Stainless Steel	152
5.2 Texture coefficients of Ti-Si-N films with variation of Si content	153

5.3	FE-SEM images of Ti-Si-N films deposited with variation of Si content (a) 3.0 at.%, (b) 9.4 at.%, (c) 15.6 at.% and (d) 21.4 at.%	156
5.4	3D AFM images of Ti-Si-N films deposited with variation of Si content (a) 3.0 at.%, (b) 9.4 at.%, (c) 15.6 at.% and (d) 21.4 at.%	157
5.5	Cross section FE-SEM images of Ti-Si-N films deposited on Si substrate at varying Si content (a) 3.0 at.%, (b) 9.4 at.%, (c) 15.6 at.% and (d) 21.4 at.%	158
5.6	Bright field image and SAD patterns by TEM of Ti-Si-N films deposited on Si substrate at varying Si content (a-b) at 6.5 at % and (c-d) at 21.4 at %	159
5.7	(a) AFM <i>in-situ</i> image of the indent on the sample	160
	(b) Hardness and Young's Modulus of Ti-Si-N films deposited with variation of Si content	160
5.8	(a) XRD peaks of Ti-Si-N films deposited on Si substrate with variation of sputtering pressure	165
	(b) Texture coefficients of the same films	165
5.9	FE-SEM topographical and cross sectional view of Ti-Si-N films deposited on Si substrate at varying sputtering pressure (a-b) at 5 mTorr, (c-d) at 20 mTorr and (e-f) at 50 mTorr	167
5.10	2D and 3D AFM images of Ti-Si-N films deposited on Si substrate at varying sputtering pressure (a-b) at 5 mTorr, (c-d) at 20 mTorr and (e-f) at 50 mTorr	169
5.11	Hardness and Young's Modulus of Ti-Si-N films deposited on Si substrate with variation of sputtering pressure	170
6.1	(a) XRD peaks of TiN/SiN _x multilayer films deposited on Si(100)	

substrate with variation of SiN _x layer deposition time	178
(b) Texture coefficients of same films	178
6.2 (a) XRD peaks of TiN/SiN _x multilayer films deposited on Si(100)	
substrate with variation of TiN layer deposition time	180
(b) Texture coefficients of same films	180
6.3 FE-SEM topographical and cross sectional view of TiN/SiN _x multilayer	
films deposited on Si(100) substrate with variation of SiN _x layer	
deposition time (a-b) 5 sec and (c-d) 30 sec	182
6.4 FE-SEM topographical and cross sectional view of TiN/SiN _x multilayer	
films deposited on Si(100) substrate with variation of TiN layer	
deposition time (a-b) 5 sec and (c-d) 30 sec	183
6.5 2D & 3D AFM images of TiN/SiN _x multilayer films deposited on Si(100)	
substrate with variation of SiN _x layer deposition time (a-b) 5 sec and	
(c-d) 30 sec	184
6.6 2D & 3D AFM images of TiN/SiN _x multilayer films deposited on Si(100)	
substrate with variation of TiN layer deposition time (a-b) 5 sec and	
(c-d) 30 sec	186
6.7 (a) TEM cross sectional view of TiN/SiN _x multilayer films showing TiN	
layer and SiN _x layer	188
(b) TEM topographical view of TiN/SiN _x multilayer film	188
(c) SAD pattern	188
6.8 Hardness and Young's Modulus of TiN/SiN _x multilayer films deposited	
on Si(100) substrate with variation of (a) SiN _x layer deposition time and	
(b) TiN layer deposition Time	189

LIST OF TABLES

1.1	Properties of Titanium at room temperature	13
1.2	Properties of Titanium Nitride at room temperature	16
3.1	Sputtering parameters for Ti films with variation of substrate temperature	66
3.2	Sputtering parameters for Ti films with variation of sputtering power, substrate temperature and sputtering pressure	78
3.3	The variation of different values of Ti thin films with varying deposition parameters	88
3.4	Properties of coating and substrates materials	93
4.1	Sputtering parameters for TiN films with variation of deposition time in different atmospheres	110
4.2	Sputtering parameters for TiN films with variation of film thickness	121
4.3	Different properties of TiN thin films with varying film thickness	129
4.4	Properties of coating and substrates materials	134
5.1	Sputtering parameters for Ti-Si-N films with varying Si content	150
5.2	Properties of Ti-Si-N films with variation of Si content	155
5.3	Sputtering parameters for Ti-Si-N films with variation of sputtering pressure	164
5.4	Properties of Ti-Si-N films with variation of sputtering pressure	168
6.1	Sputtering parameters for TiN/SiN _x multilayer films	176
6.2	Properties of TiN/SiN _x multilayer films with variation of SiN _x layer deposition time and keeping TiN layer deposition time constant	185
6.3	Properties of TiN/SiN _x multilayer films with variation of TiN layer deposition time and keeping SiN _x layer deposition time constant	187

LIST OF PUBLICATIONS

Paper published in journals

- 1) **Vipin Chawla**, R. Jayaganthan, A. K. Chawla and Ramesh Chandra,
“Morphological study of Magnetron Sputtered Ti thin films on Silicon substrate”,
Materials Chemistry and Physics, **111**, 414-418 (2008)
- 2) **Vipin Chawla**, R. Jayaganthan and Ramesh Chandra,
“FEM Analysis of Thermal Stress in Magnetron Sputtered Ti coating”,
Journal of Materials Processing Technology, **200**, 205-211 (2008)
- 3) **Vipin Chawla**, R. Jayaganthan and Ramesh Chandra,
“A Study on Microstructural Evolution in Nanocrystalline TiN thin films”,
Materials Characterization, **59**, 1015-1020 (2008)
- 4) **Vipin Chawla**, R. Jayaganthan, A. K. Chawla and Ramesh Chandra,
“Microstructural Characterizations of Magnetron Sputtered Ti films on glass
Substrate”,
Journal of Materials Processing Technology, Article in press (2008)
doi:10.1016/j.jmatprotec.2008.08.004
- 5) **Vipin Chawla**, R. Jayaganthan and Ramesh Chandra,
“FEM Analysis of Thermal Stress in Magnetron Sputtered TiN coating”,
Materials Chemistry and Physics, Article in Press (2008)
doi:10.1016/j.matchemphys.2008.09.023
- 6) **Vipin Chawla**, R. Jayaganthan and Ramesh Chandra,
“Microstructural Characteristics and Mechanical Properties of Magnetron
Sputtered Nanocrystalline TiN films on Glass substrate”,
Bulletin of Materials Science, Accepted (2008)

- 7) **Vipin Chawla**, R. Jayaganthan and Ramesh Chandra,
“A Study of Structural and Mechanical Properties of Sputter Deposited Nanocomposite Ti-Si-N thin films”,
Journal of Alloys and Compounds, Under Review (2008)
- 8) **Vipin Chawla**, R. Jayaganthan and Ramesh Chandra,
“Structural and Mechanical Properties of nanocomposite Ti-Si-N thin films”,
Surface and Coating Technology, Submitted (2008)
- 9) **Vipin Chawla**, R. Jayaganthan and Ramesh Chandra,
“Mechanical and Microstructural Properties of multilayer TiN/SiN_x thin films”,
Thin Solid Films, Submitted (2008)

Paper presented in conferences

- 1) **Vipin Chawla**, R. Jayaganthan and Ramesh Chandra,
“A Study on Characterisation of Mechanically stable Nanocrystalline TiN films on Glass Substrate”,
Nano Science and Nano Technology, NS & NT 2007, Hyderabad, India, Feb. 19th – 22th, 2007, G1-6, 114
- 2) **Vipin Chawla**, R. Jayaganthan and Ramesh Chandra,
“Nanoindentation Study of Nanocrystalline TiN thin films”,
International Conference on Metallurgical Coatings and Thin Films, ICMCTF 2007, San Diego, CA, USA, April 23th -17th, 2007, 49
- 3) **Vipin Chawla**, R. Jayaganthan and Ramesh Chandra,
“A Study on Microstructural Evolution in Nanocrystalline TiN thin films”,
International Conference on Metallurgical Coatings and Thin Films, ICMCTF 2007, San Diego, CA, USA, April 23th -17th, 2007, 12

- 4) **Vipin Chawla**, R. Jayaganthan and Ramesh Chandra,
“AFM study of nanocrystalline TiN thin films”,
International Conference on Materials for Advanced Technologies, ICMAT 2007,
Singapore, July 1th -6th, 2007
- 5) **Vipin Chawla**, R. Jayaganthan and Ramesh Chandra,
“Microstructural Characterization of Sputter Deposited Ti-Si-N thin films”,
Thin Films 2008, Singapore, July 13th -16th, 2008, 303
- 6) **Vipin Chawla**, R. Jayaganthan and Ramesh Chandra,
“Nanoindentation Study of Nanocrystalline Ti-Si-N thin films”,
Thin Films 2008, Singapore, July 13th -16th, 2008, 114
- 7) **Vipin Chawla**, R. Jayaganthan and Ramesh Chandra,
“Microstructural Characterization of Sputter Deposited TiN/SiN_x multilayer
coatings on Si substrate”,
Processing and Fabrication of Advance Materials, PFAM XVII,
New Delhi, India, Dec. 15th -17th, 2008
- 8) **Vipin Chawla**, R. Jayaganthan and Ramesh Chandra,
“Microstructural and Mechanical Properties of Sputter Deposited TiN/SiN_x
Multilayer Coatings on Si Substrate”,
International Conference on Metallurgical Coatings and Thin Films, ICMCTF
2009, San Diego, CA, USA, (Accepted)

CONTENTS

ABSTRACT	ii
ACKNOWLEDGEMENTS	x
LIST OF FIGURES	xiii
LIST OF TABLES	xx
LIST OF PUBLICATIONS	xxi

Chapter 1: Introduction

1.1	Introduction to Nanostructured coatings	2
1.2	Hard Coatings	3
1.3	Overview of Titanium based hard coatings	11
1.3.1	Titanium (Ti)	11
1.3.2	Titanium Nitride (TiN)	14
1.3.3	Titanium Silicon Nitride (Ti-Si-N)	17
1.3.4	Titanium Nitride/Silicon Nitride (TiN/SiN _x)	19

Chapter 2: Synthesis and Characterization Techniques

2.1	Thin films growth	23
2.2	Synthesis of thin films	25
2.2.1	Sputtering	26
2.2.2	Magnetron Sputtering	29
2.3	Characterization Techniques	33
2.3.1	X-Ray Diffraction (XRD)	33
2.3.2	Field Emission Scanning Electron Microscope (FE-SEM)	37

2.3.3	Atomic Force Microscope (AFM)	41
2.3.4	Transmission Electron Microscope (TEM)	46
2.3.5	Nanoindentation	51
2.3.6	ANSYS	57

Chapter 3: Synthesis and Characterization of Titanium Films

3.1	Magnetron sputtered Ti films on Silicon substrate	61
3.1.1	Introduction	61
3.1.2	Experimental Details	65
3.1.2.1	Synthesis of Ti films	65
3.1.2.2	Characterization details	66
3.1.3	Results and Discussion	67
3.1.4	Conclusion	75
3.2	Magnetron Sputtered Ti films on Glass substrate	77
3.2.1	Introduction	77
3.2.2	Synthesis of Ti films	77
3.2.3	Results and Discussion	78
3.2.4	Conclusion	88
3.3	FEM Analysis of Thermal Stress in Magnetron Sputtered Ti thin films	90
3.3.1	Introduction	90
3.3.2	Modeling	92
3.3.2.1	Analytical model for thermal stress	92
3.3.2.2	Finite Element Analysis	93
3.3.3	Results and discussion	95
3.3.4	Conclusion	103

Chapter 4: Synthesis and Characterization of Titanium Nitride Films

4.1	Structural and Mechanical Characterizations of Magnetron Sputtered nanocrystalline TiN thin films	105
4.1.1	Introduction	105
4.1.2	Experimental Details	109
	4.1.2.1 Synthesis of TiN films	109
	4.1.2.2 Characterization details	110
4.1.3	Results and Discussion	111
4.1.4	Conclusion	118
4.2	Microstructural Characteristics and Mechanical Properties of Magnetron Sputtered nanocrystalline TiN films on Glass substrate	120
4.2.1	Introduction	120
4.2.2	Experimental Details	121
	4.2.2.1 Synthesis of TiN films	121
	4.2.2.2 Characterization details	121
4.2.3	Results and Discussion	122
4.2.4	Conclusion	129
4.3	Analysis of Thermal Stress in Magnetron Sputtered TiN coating by Finite Element Method	131
4.3.1	Introduction	131
4.3.2	Modeling	133
	4.3.2.1 Analytical model for thermal stress	133
	4.3.2.2 Finite Element Analysis	134
4.3.3	Results and Discussion	136
4.3.4	Conclusion	142

Chapter 5: Synthesis and Characterization of Titanium Silicon Nitride Films

5.1	Study of Structural and Mechanical Properties of Sputter Deposited nanocomposite Ti-Si-N thin films	145
5.1.1	Introduction	145
5.1.2	Experimental Details	149
5.1.2.1	Synthesis of Ti-Si-N films	149
5.1.2.2	Characterization details	150
5.1.3	Results and Discussion	151
5.1.4	Conclusion	161
5.2	Influence of Deposition Parameters on the Structural and Mechanical Properties of nanocomposite Ti-Si-N thin films	163
5.2.1	Introduction	163
5.2.2	Experimental Details	163
5.2.2.1	Synthesis of Ti-Si-N films	163
5.2.2.2	Characterization details	164
5.2.3	Results and Discussion	164
5.2.4	Conclusion	171

Chapter 6: Synthesis and Characterization of Titanium Nitride/Silicon Nitride Multilayer Films

6.1	Microstructural and Mechanical Properties of Sputter Deposited TiN/SiN_x Multilayer thin films	173
6.1.1	Introduction	173
6.1.2	Experimental Details	175
6.1.2.1	Synthesis of TiN/SiN _x multilayer films	175
6.1.2.2	Characterization details	177
6.1.3	Results and Discussion	178

6.1.4	Conclusion	190
-------	------------	-----

Chapter 7: Conclusion

7.1	Magnetron sputtered Ti films on Silicon substrate	193
7.2	Magnetron Sputtered Ti films on Glass substrate	194
7.3	FEM Analysis of Thermal Stress in Magnetron Sputtered Ti thin films	195
7.4	Structural and Mechanical Characterizations of Magnetron Sputtered nanocrystalline TiN thin films	196
7.5	Microstructural Characteristics and Mechanical Properties of Magnetron Sputtered nanocrystalline TiN films on Glass substrate	197
7.6	Analysis of Thermal Stress in Magnetron Sputtered TiN coating by Finite Element Method	197
7.7	Study of Structural and Mechanical Properties of Sputter Deposited nanocomposite Ti-Si-N thin films	198
7.8	Influence of Deposition Parameters on the Structural and Mechanical Properties of nanocomposite Ti-Si-N thin films	199
7.9	Microstructural and Mechanical Properties of Sputter Deposited TiN/SiN _x Multilayer thin films	200

REFERENCES	203
-------------------	------------

Chapter 1

Introduction

1.1 Introduction to Nanostructured coatings

Nanostructured coatings and nanocomposite coatings represent a new generation of materials, which exhibit superior structural and functional properties as compared to that of its microcrystalline coatings. Nanocomposite films consist either of two nanocrystalline phases, or a combination of both a nanocrystalline and an amorphous phase. The nanostructured coatings due to (i) very small (10 nm) grains from which they are composed and (ii) a significant role of boundary regions surrounding individual grains behave in a different manner compared to that of conventional materials with grains greater than 100 nm and therefore exhibit superior properties such as high mechanical strength, high temperature stability, high wear and erosion resistance. The superior properties are manifested in the nanostructured coatings due to size effect and higher volume fraction of grain boundaries and interfaces between different phases. For example, ultrahigh hardness is achieved in the nanostructured coatings due to presence of nanometer scale grains, which hinders the generation and movement of dislocations, suppression of crack propagation occurs owing to the random network of grain boundaries with its large misorientation. Among various nanostructured coatings, hard coatings with nanoscale features are being developed worldwide due to its promising applications in surface engineering, especially to provide very high strength and wear resistance to the surface of materials over which they are coated. A brief overview of hard coatings is discussed in the next section.

1.2 Hard Coatings

Hard coatings have been successfully used for protection of materials and particularly to enhance the life of cutting tools since the 1970's and it is defined by its hardness which is the measure of resistance to plastic deformation and it increases with decrease in grain size by Hall-Petch relationship as

$$\sigma_y = \sigma_o + \frac{K}{\sqrt{d}} \quad (1.1)$$

where, σ_y is the yield stress of the material, σ_o is the intrinsic yield stress of the bulk material, K is the material constant and d is the grain diameter.

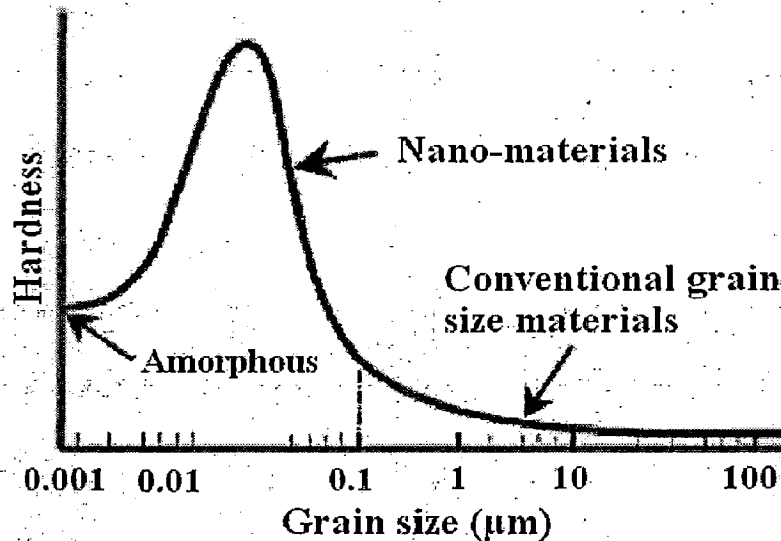


Figure 1.1: Hardness Vs grain size

It is evident from **Figure 1.1** that for conventional materials in which grain size is more than 100 nm, the hardness is very less due to the free movement of dislocation unaffected by less number of grain boundaries. However, when the grain size decreases and below 100 nm, the grain boundary volume fraction increases which obstruct the movement of the dislocations and therefore hardness increases. Again, when the grain

size reduces to less than 10 nm, hardness of the material decreases due to the grain boundary sliding and this is known as inverse Hall- Petch effect.

The hard coatings can be divided into three groups according to their hardness:

- a) The hard coatings with hardness $H < 40$ GPa;
- b) The superhard coatings with $40 \leq H \leq 80$ GPa;
- c) The ultrahard coating with $H > 80$ GPa

The hardness, wear resistance, oxidation resistance, corrosion resistance, thermal stability of the coatings is continuously being improved (Musil 2000, Shtansky *et al.* 2004). The hard coatings are extensively used for tribological applications and their development by various physical and chemical routes are competing with each other to achieve their superior performance in the actual engineering applications such as coatings for cutting tools under dry and high speed machining conditions and protective coatings for turbine blades and engine parts to improve their durability (Chandra *et al.* 2006a). By properly selecting the coating method and materials, we can protect not only the substrate materials to prolong their service life, but also increase commercial value of the products (Chou *et al.* 2001). For the development of coatings, depending on its applicability, few areas ought to given utmost importance, for example, the properties such as hardness, oxidation resistance, thermal stability, and adhesion, corrosion resistance of the coatings need to be improved significantly. The oxidation resistance of coatings has to be increased even further to a high temperature of 1000°C, because during high-speed machining, temperature of the tool tip would rise to 1000°C and therefore, coatings should be stable to sustain such a high temperature (Musil 2000).

As regards hardness, large number of materials is hard but relatively less number of materials is superhard such as cubic Boron Nitride (c-BN), amorphous diamond-like

carbon (DLC), amorphous Carbon Nitride (a-CN), and polycrystalline diamond. Moreover, these superhard materials are thermodynamically unstable, which limits their utilization in some applications. For instance, the high chemical affinity of carbon to iron limits the applicability of diamond coated cutting tools for the machining of aluminum, their alloys and wood only. The similar problems are expected when the c-BN coating is used in cutting of steels due to the chemical dissolution of boron in iron. These problems stimulated intensive research in this field, and recently new superhard materials based on superlattices and nanocomposites are developed (Musil 2000).

In recent years, binary and ternary transition metal nitride materials have played a crucial role and used in various engineering applications due to their remarkable physical and mechanical properties including high hardness, high melting point, chemical inertness, and good thermodynamic stability and have been studied in detail (Jiang *et al.* 2004). A control of the microstructural and surface morphological evolution of polycrystalline transition metal nitride films are very important in determining the performance and life time of the coated tools. This fact has spurred interest in modeling the growth of polycrystalline transition metal nitride thin films apart from the experimental studies (Thornton 1978). For example, Titanium nitride (TiN) coating improves the wear resistance and durability of machining tools because of its hardness of ~ 20 GPa (Shimazaki *et al.* 1987, Habig 1989, Wallen *et al.* 1989, Habig *et al.* 1992, Kato 1995, Sarwar *et al.* 1997). TiN based coatings are used to increase the cutting efficiency and operational life of cutting tools as well as to maintain the dimensional tolerances of components used in applications where wear is an important issue. Also, it can act as a diffusion barrier in microelectronic device fabrications, where the reliability is of utmost concern to ensure the fault free function of the devices.

However, one of the drawbacks of TiN coatings is due its limited oxidation resistance at high temperatures that can be reached during the process application. Therefore, a lot of research activities are devoted to develop new hard coating materials in order to further improve their mechanical and high-temperature properties. Ternary systems of Ti- X- N, where X = B, C, Al, Si, Cr etc. have been attractive for advanced hard coating materials because of their superior properties, in particular, higher hardness and improved oxidation resistance compared to TiN coatings (Kim *et al.* 2002a). The addition of the second phase not only prevents grain growth but also suppresses grain boundary sliding (for grain size < 10nm), and hence improve the mechanical properties (Web link 1).

An adhesion of the hard coatings with substrate is also an important property not only for microelectronics and magnetic recording industries, but also for emerging technologies such as data transmission through optical switches, which are dependent on micro electro-mechanical system (Vaz *et al.* 2002). It is possible that the films with high residual stress will spontaneously strip off. Thus, it has become essential to develop improved and new hard coatings for tools and engineering components. In pursuit of this goal, researchers are constantly focusing on the improvement of the presently applied hard coatings by utilization of strengthening mechanisms, development of new hard coatings with functional properties like self-hardening, self-lubrication, self-adaptation to the existing thermo-mechanical loads, self-repair and self-healing, establishment of design rules for tailoring the coating-substrate interface, the coating micro- and nanostructure and the coating topography, and development and optimization of analytical methods for the characterization of hard coatings and thin reaction layers. Special emphasis is also laid on in-situ methods allowing

characterization at elevated temperatures, development of new target materials for thin film applications, establishment of a complete process chain: target structure and composition - coating structure - coating properties - coating performance (Web link 2).

An increase in fatigue life and fatigue limit observed in hard coatings has been attributed mainly to three different aspects: the existence of very high compressive residual stresses in the coatings, in the range of 1–4 GPa, the elevated mechanical strength of such materials (substrate) and their excellent adhesion to the substrate onto which these coatings are deposited (Puchi-Cabrera *et al.* 2008), all of which are an important area of concern in tool coatings industries.

Nowadays, thin wear-resistant hard coatings are widely applied to increase the lifetime of cutting and forming tools and in order to enable new machining applications, these coatings are prepared by various deposition techniques and conditions so as to tailor the microstructures in terms of grain size, crystallographic orientation, lattice defects, texture and surface morphology as well as phase composition (Drexler 1981). It is worthwhile to note that superhard coatings in the form of superlattices represent a very important milestone in the development of superhard materials. The deposition techniques used for superhard coating should provide intense particle bombardment of substrate, sufficient surface mobility, high and uniform deposition rate and cleaning of substrate from impurities. Numerous techniques are now available for the preparation of conventional nitride coatings and among them, vacuum-based deposition techniques fall into two basic categories: chemical vapor deposition (CVD) and physical vapor deposition (PVD).

Chemical vapor deposition (CVD) is a process where one or more gaseous adsorption species react or decompose on a hot surface to form stable solid products:

The main steps that occur in the CVD process can be summarized as (Hitchman *et al.* 1993):

- a) Transport of reacting gaseous species to the surface
- b) Adsorption of the species on to the surface
- c) Heterogeneous surface reaction catalyzed by the surface
- d) Surface diffusion of the species to growth sites
- e) Nucleation and growth of the films
- f) Desorption of gaseous products and transport of reaction products away from the surface

Plasma-assisted chemical vapor deposition (PVCVD) technique was used to synthesize such superhard nanocomposite films at the beginning. However, in CVD techniques, molecular species in the gas phase chemically react at a film surface, leading to the formation of a condensed film as well as the emission of volatile by-products. It also makes use of aggressive chemicals as metal sources for the deposition of coatings. Due to the undesirable characteristics of chemicals emanating from CVD, physical vapor deposition (PVD) technique is considered to be more suitable for industrial-scale synthesis of these films (Li *et al.* 2005). It may be mentioned that CVD is a more complex method of forming thin films and coatings than PVD. There are other potential routes such as wire explosion technique and surface nitridation to prepare the nitrides such as AlN, CrN and TiN, respectively (Ajikumar *et al.* 2004, Sarathi *et al.* 2007).

The development of new materials, particularly in the field of refractory hard compounds, is limited by various metallurgical interrelationships. As a consequence, new materials can only be produced by means of sophisticated and therefore less

economical production methods. The deposition of solids from the vapor phase enables the production of a wide range of new materials without resorting to the problems of liquid phases (Knotek *et al.* 1987). Therefore, physical vapor deposition (PVD) is a versatile synthesis method and it is gaining more prominence in semiconductor and coating technology. PVD is capable of depositing thin film materials with structural control over atomic or nanometer scale by careful monitoring of the processing conditions. Materials with high melting points and high reactivity can be deposited easily by PVD processes. Also, homogeneous multicomponent phases as well as multilayer coatings can be easily produced with completely new material properties. In reactive mode, the stoichiometry of hard phases can be varied easily. By controlling the substrate temperature, materials can be deposited in different structures, such as amorphous, microcrystalline and the nanocrystalline structures (Knotek *et al.* 1987).

PVD involves the generation of vapor phase species either via evaporation, sputtering, laser ablation or ion beam. In evaporation, atoms are removed from the source by thermal or electron means; in sputtering, atoms are ejected from the target surface by the impact of energetic ions. In the former case, the vapor phase species that experience collisions and ionization are condensed onto a substrate following nucleation and growth phenomena. Thermal evaporation has a limitation in multi component materials since one of the metallic elements typically evaporates before the other due to the differences in vapor pressures of the evaporating species. On the contrary, sputtering is capable of depositing high melting point materials such as refractory metals and ceramics, which are difficult to fabricate using evaporation. Since the sputtered atoms carry more energy than the evaporated atoms, the sputter-grown films usually have higher density. In general, sputtering seems to be the most appropriate technique to

deposit ternary compounds because the transformation of the original materials into a gaseous state does not involve an intermediate liquid phase, but instead occurs directly as a result of an atomic momentum transfer at the target (Huang *et al.* 2005a).

Magnetron sputtering is of particular importance due to its easy handling, high reproducibility and high flexibility of large-scale as well as complex geometry shape production (Shum *et al.* 2004) and also the configuration of the magnetic field confines the electrons and gives a high degree of ionization near the target. The indirect result of this process is that the vapor flux ejection from the target is higher and, consequently, the deposition rate is increased; recent developments, such as an unbalanced magnetron, give further benefits in this respect. Another advantage in magnetron sputter deposition lies in the fact that such systems can be made to work at lower pressure than d.c. glow and r.f. discharges to obtain a high-quality, low impurity films at a reasonable deposition rate (Brizoual *et al.* 1999). Also the importance of sputtering methods is that it involves a number of parameters such as sputtering pressure, sputtering power, substrate-target distance and substrate temperature etc. whereby a number of combination of these parameters may be used to obtain high quality films with required properties.

The Ti based nitrides such as TiN, Ti-Si-N, and TiN/SiN_x multilayers have been chosen for the present investigation due to their excellent properties such as high hardness, wear and erosion resistance, non-toxicity, chemical inertness, etc. The properties of these nitrides coatings can be enhanced further by tailoring their microstructural characteristics such as grain size, textures, porosity, impurities, and residual stress by using the physical vapor deposition technique, especially, the magnetron sputtering.

1.3 Overview of Titanium based hard coatings

1.3.1 Titanium (Ti)

Titanium (Ti) is a light, strong, lustrous with a grayish color and due to its interesting properties such as high mechanical strength, excellent thermal stability, good corrosion resistance in extreme conditions and intrinsic biocompatibility i.e. reliable for the design of medical instruments or implants in the human body. Hence, titanium is a promising material used as bulk or coatings in biomedical, aerospace and other industrial applications [Boyer 1996, Shoesmith *et al.* 1997(a, b), Straumal *et al.* 2000, Textor *et al.* 2001, Choubey *et al.* 2004]. The detailed investigation on them could extend its application in various fields, such as metallization of insulator and surface modification of some materials.

Furthermore, titanium coatings are employed for microelectronics applications in very large scale integration (VLSI) technology and microelectromechanical system (MEMS) based devices (Ogawa *et al.* 1991, Fujitsuka *et al.* 1998, Yu *et al.* 1998, Ramakrishna *et al.* 2000, Mahony *et al.* 2002). They are used as bolometers in infrared sensors (Ramakrishna *et al.* 2000), electrical connectors in thermal insulating structures (Fujitsuka *et al.* 1998, Wang *et al.* 2001), superconducting edge sensors in microcalorimeters and light detectors (Lee *et al.* 1991, Gandini *et al.* 2003), and in single electron transistors (Averin *et al.* 1991, Hofmann *et al.* 2003). The unique properties and various applications of titanium coatings mostly depended on two important material factors, the chemical nature and structure. Therefore, a detailed investigation of chemical and structural characteristics of titanium coatings were given due attention in the literature so far [Iida *et al.* 1990, Ogawa *et al.* 1991, Checchetto

1997, Huth *et al.* 1997, Basame *et al.* 2000, Passeggi *et al.* 2002, Yoshinari *et al.* 2002, Batista *et al.* (2003, 2004a), Boxley *et al.* 2003, Cai *et al.* 2005, Tsuchiya *et al.* 2005, Jeyachandran *et al.* 2006]. Titanium exhibits two crystal structures, i.e. hexagonal close-packed (hcp) type α phase and body centered cubic (bcc) type β phase as shown in **Figure 1.2** (Web link 3).

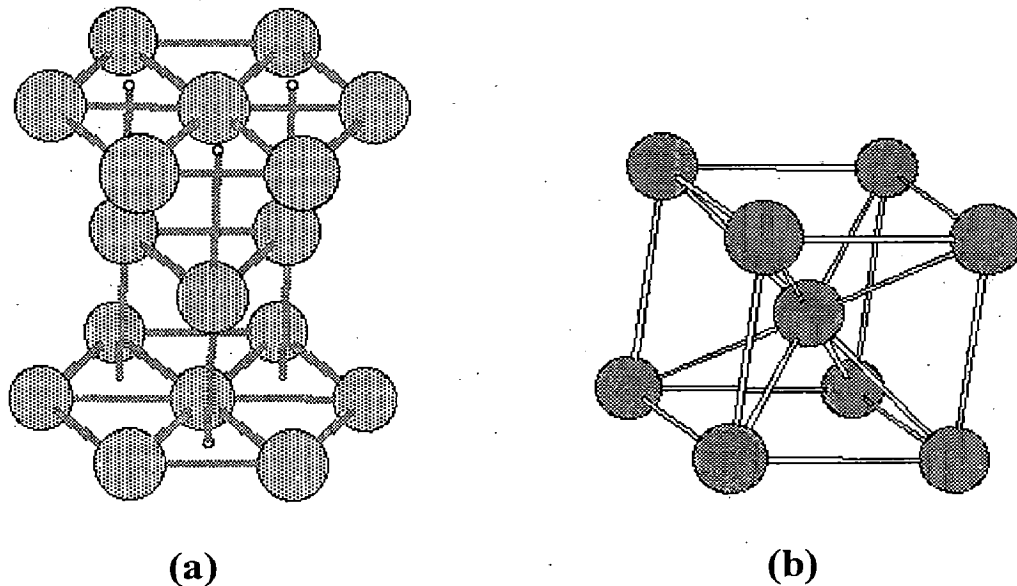


Figure 1.2: Titanium crystal structures: (a) Hexagonal close-packed below 900°C and (b) Body centered cubic above 900°C

The lattice parameters of Ti hexagonal unit cell are $a = 2.9512 \text{ \AA}$ and $c = 4.6845 \text{ \AA}$ and the c/a ratio for Ti hcp unit cell is 1.587 and the lattice parameter of Ti body centered unit cell is 3.3066 \AA (Cullity *et al.* 2001). The various properties of Titanium are summarized in **Table 1.1**.

Table 1.1: Properties of Titanium at room temperature

Atomic Number	22
Chemical series	Transition metals
Electron configuration	$1s^2 2s^2 2p^6 3s^2 3p^6 3d^2 4s^2$
Crystal structure	Hexagonal < 900°C < Body centered
Melting point (°C)	1668
Boiling point (°C)	3287
Density (gm.cm⁻³)	4.506
Ionization energies (KJ.mol⁻¹)	1 st : 658.8 2 nd : 1309.8 3 rd : 2652.5
Electical resisitivity (μΩ.m)	0.420
Thermal conductivity (W.m⁻¹.°C⁻¹)	21.9
Coefficient of Thermal expansion (°C⁻¹)	8.4 x10 ⁻⁶
Young's modulus (GPa)	120
Shear modulus (GPa)	44
Bulk modulus (GPa)	110
Poisson-ratio	0.31
Vickers hardness	970 MPa
Brinell hardness	716 MPa

The deposition of titanium thin films has been the subject of intense research for the last few decades, especially for the metallization of surfaces, for electrical contacts and in the preparation of conducting coatings (Vijaya *et al.* 1996). Physical vapor deposition processes such as electron beam evaporation and sputtering methods were extensively used to prepare Ti thin films (Batista *et al.* 2004b, Tsuchiya *et al.* 2005). Due to the high chemical reactivity of Ti, usually high vacuum is preferred for depositing Ti films. Under high vacuum conditions, the major impurity factor is the water vapor and it has

been shown that the composition and structural quality of the titanium films are strongly affected by water impurity [Poppeller *et al.* 1997(a, b)].

1.3.2 Titanium Nitride (TiN)

Titanium Nitride (sometimes known as Tinite or TiNite) is an extremely hard ceramic material, harder than carbide. TiN coatings show high hardness, high wear resistance, low friction coefficient, low chemical reactivity, low electric resistivity, excellent non-sticking surface against other materials, lubricity nature, good diffusion barrier characteristics, bioinertness and golden color. The (TiN_x) compounds are unique materials exhibiting both metallic (Ti-Ti) and covalent (Ti-N) bonding characteristics. The metallic properties are electrical conductivity and metallic reflectance; and the covalent bonding properties are high melting point, extreme hardness and brittleness, and excellent thermal and chemical stability. Due to these properties, TiN coatings are being used in a wide range of applications such as wear resistant coatings to protect cutting tools, dies, tools, sliding surfaces of bearings and gears from aggressive environments due to its good wear resistance and inertness to steels. They are also used in microelectronics devices, solar cells, decorative purposes on tableware, clocks etc. or as a non-toxic exterior for human implants (Smith *et al.* 2001, Tao *et al.* 2004, Vaz *et al.* 2004, Jeyachandran *et al.* 2007).

TiN film gives gold-like appearance and it is due to the high reflectance at the red end of the visible spectrum similar to elemental gold with low reflectance near the ultraviolet region and this gold-like color observed at the specific composition of Titanium and Nitrogen (Chandra *et al.* 2005). TiN shows intrinsic biocompatibility and hemocompatibility and therefore used as surface layers and electrical interconnects in

orthopedic prostheses, cardiac valves and other biomedical devices (Chung *et al.* 2004, Franks *et al.* 2005). It provides low friction against steels, carbides, ceramics, and platings. The unlubricated tribological tests on TiN films tend to result in coefficients of friction in the range 0.3-0.9, depending on test geometry, mating face material, etc. (Efeoglu *et al.* 1993). It is also used as a diffusion barrier for copper metallization as well as Al-based alloy due to its high thermal stability and low bulk electrical resistivity (Uhm *et al.* 2001).

The hardness of TiN is approximately $\sim 2500 \text{ kg/mm}^2$ Knoop or Vicker Hardness (~ 85 Rockwell C Hardness or 24.5 GPa) (Web link 4). The adhesion of TiN is very good as it forms a metallurgical bond to the substrate that will not flake, blister, chip or peel. In fact, the coating is actually implanted slightly into the surface layer of the substrate. It exhibits rocksalt structure (FCC bravais lattice) or NaCl-type crystal structure with a roughly 1:1 stoichiometry; however TiN_x compounds with x ranging from 0.6 to 1.2 are thermodynamically stable. The crystal structure of TiN is shown in **Figure 1.3** (Barsoum 1997), where each atom is surrounded by six nearest neighbours with octahedral geometry.

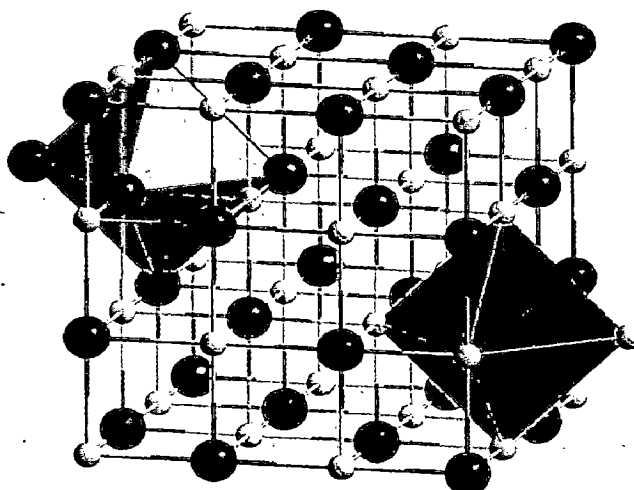


Figure 1.3: The crystal structure of Titanium Nitride

The lattice parameter of TiN is equal to 4.240 Å. It oxidizes at 600°C at normal atmosphere but more resistant in an inert atmosphere and has a melting point of 2930°C.

Different properties of TiN are summarized in **Table 1.2**.

Table 1.2: Properties of Titanium Nitride at room temperature

Crystal Structure	Face Centered Cubic
Melting point (°C)	2930
Electrical Resistivity ($\mu\Omega\text{-m}$)	0.25
Thermal Expansion Coefficient ($^{\circ}\text{C}^{-1}$)	9.4×10^{-6}
Thermal Conductivity ($\text{W}\cdot\text{m}^{-1}\cdot^{\circ}\text{C}^{-1}$)	19.32
Density ($\text{gm}\cdot\text{cm}^{-3}$)	5.22
Young's Modulus (GPa)	600
Poisson's Ratio	0.25
Heat of Formation ($\text{Cal}\cdot\text{mole}^{-1}$)	80,750 (3.5 eV/molecule)
Band Gap (eV)	3.35 - 3.45

Various methods have been employed for TiN deposition and among them sputtering techniques (dc and rf) are considered as most suitable methods and are being extensively used to obtain high quality films with required properties. Sputtering technique involves a huge amount of deposition parameters, which can influence the final film properties of TiN films such as hardness and strength. For example, the nitrogen partial pressure has intense effect on the properties of TiN films, as under low N_2 concentration, golden colored stoichiometric TiN films were obtained and at higher N_2 concentrations, nitrogen over saturation occurred in the films sometimes leading to unusual effects such as nitrogen precipitation at grain boundaries or as gas bubbles,

superstructure formation and partial crystallization were observed (Hultman *et al.* 1989, Tarniowy *et al.* 1997, Zerkout *et al.* 2003).

1.3.3 Titanium Silicon Nitride (Ti-Si-N)

The theoretical concept for the design of the superhard nanocrystalline composites is associated with the preparation of a composite material consisting of nanocrystallites embedded within a very thin amorphous matrix (Gleiter 1993, Veprek *et al.* 1995a). Such multiphase materials often display higher hardness and toughness values than for single phase materials. Ti-Si-N is a composite material developed during the early 1980s (Hirai *et al.* 1983, Park *et al.* 2006). Ti-Si-N coatings have become very attractive in recent years due to their excellent physical and chemical properties, most notably their ultra high hardness, increased wear resistance, good oxidation resistance and improved thermal stability compared to TiN (Cairney *et al.* 2005). It constitutes FCC crystal structure with a lattice parameter of about 4.29 Å (phase 1) due to the high mobility of species at the growing film in order to ensure phase segregation and the consequent formation of polycrystalline grains and the amorphous matrix, and the other system with a lattice parameter of about 4.18 Å (phase 2) where Si atoms replaced some of the Ti atoms, which might be called solid solution due to the absence of ion bombardment and low mobility of species. TEM experiments confirmed the FCC crystal structure. The phase 2 exhibit low value of the lattice parameter in comparison to phase 1 due to the replacement of some Ti atoms by the Si atoms [Vaz *et al.* (1999, 2000)].

The processing, structure, and property of Ti-Si-N nanocomposite coating were investigated in detail by Veprek *et al.* (1995a, 2005) and Prochazka *et al.* (2004). An

enhancement of hardness and refractory properties produced by the nanocomposite Ti-Si-N was elucidated with the size effect of TiN nanocrystals embedded in the Si_3N_4 amorphous matrix, which act as an effective barrier for dislocation motion as reported in their studies. Silicon content affects the physical properties of the films such as electrical resistivity, oxidation stability, and diffusivity. For example, amorphous thin films, Si_3N_4 , serve as an effective diffusion barrier than its polycrystalline films because it does not possess grain boundaries and extended defects. Si content also reduces the grain size of the TiN and especially the incorporation of amorphous SiN_x between grains or total absence of distinguishable crystalline phases, which reduce the defects, contributing to increased resistivity and barrier strength [Juo *et al.* 1981, Doyle *et al.* 1982, Nicolet (1983, 1995), Sun *et al.* 1997(a, b, c), Kacsich *et al.* {(1999a, b), (2000)}, Varesi *et al.* 2007].

The Ti-Si-N coatings with Si content of approximately 10 at.% show very high hardness values, i.e. superhardness (≥ 40 GPa). The grain boundary hardening may play a crucial role in the hardening of Ti-Si-N coatings (Kim *et al.* 2002a, Jiang *et al.* 2006). The superhardness of the coatings was due to the thin Si_3N_4 amorphous matrix interposed between the TiN crystallites, hinders the generation and movement of dislocations as well as prevents grain growth. Also, the suppression of crack propagation occurs due to the presence of high volume fraction of grain boundaries (Grain size $< 10\text{nm}$) (Kim *et al.* 2002b, Xu *et al.* 2007).

Nanocomposite Ti-Si-N coatings are prepared by variety of techniques, such as chemical vapor deposition (CVD), plasma enhanced chemical vapor deposition (PECVD) or by reactive magnetron sputtering (Jiang *et al.* 2004). In sputtering method, Si and Ti atoms ejected from Si and Ti targets, respectively, and react with N_2 and get

deposited as Ti-Si-N nanocomposite films on the substrate (Mei *et al.* 2005). The deposition conditions significantly affect the microstructure and mechanical properties of the Ti-Si-N coatings. For example, deposition temperatures and substrate bias voltages are related to the surface mobility and bombardment of ions, which leads to the changes in the microstructural characteristics of the films and thereby affect their mechanical properties such as indentation elastic modulus, hardness, wear behavior, etc (Rother *et al.* 2001, Vaz *et al.* 2001).

1.3.4 Titanium Nitride/Silicon Nitride (TiN/SiN_x)

Titanium Nitride (TiN) has been widely used as protective coatings for bearings, gears and cutting tools due to its extreme hardness, high thermal and chemical stability. Many studies have been focused to enhance further the properties of TiN such as hardness, adhesion to the substrate, and high temperature oxidation resistance by synthesizing multilayer coatings in which the TiN layers alternate with metal or ceramic layers (Mariano *et al.* 2006). An interesting combination of effects has been described in multilayer coatings: the blocking of dislocation movement at the periodical interfaces results in a hardness increase (Hall-Petch effect); crack propagation through the coating is limited due to deflection of cracks at the interfaces (Veprek *et al.* 1995a, Bull 2001). Multilayers are also useful as model systems since they allow the design and study of interfaces not readily accessible in a three-dimensional nanocomposite (Soderberg *et al.* 2006).

TiN coatings predominantly grow with a columnar grain structure. These columnar grain boundaries become the crack initiation, resulting in premature failure of TiN coatings. Therefore, its columnar structure should be eliminated and formation of fine

equiaxed microstructure throughout the coating thickness ought to be facilitated to enhance its tribological performance. A strategy to produce a fine, equiaxed grain microstructure, in TiN coatings, is by periodically interrupting its growth through the introduction of nanolayers of a different material such as amorphous SiN_x and force TiN to renucleate (Lacerda *et al.* 1999). These interlayers reduce the porosity, cutting off the paths for the corrosive solution to the substrate, increasing the protection against corrosion.

For producing multilayer coatings with high hardness, certain factors should be fulfilled as reported by, Veprek *et al.* (1995a) and Veprek (1999), such as the materials should be immiscible, preferably even at high temperatures, and one component should be amorphous, possessing high structural flexibility, i.e., its ability to accommodate coherency strain without forming dangling bonds (Veprek 1999, Soderberg *et al.* 2005). These factors are fulfilled for crystalline TiN and amorphous SiN_x , hence, amorphous SiN_x has been used for this purpose to produce TiN/ SiN_x multilayer coatings. It shows very high hardness and good wear resistance (Chen *et al.* 2002).

SiN_x has been chosen for two reasons; first, SiN_x has an amorphous structure, stable up to 1100°C . TiN is forced to renucleate each time a thin SiN_x layer (amorphous structure) is deposited. Second, a nanocomposite coating made of a mixture of nanocrystalline TiN and amorphous Si_3N_4 attains hardness value of ≥ 50 GPa and is resistant against oxidation in air up to 800°C (Veprek *et al.* 1995b). Silicon nitride (Si_3N_4 or $\text{SiN}_{1.33}$) is one of the very important ceramic materials due to its excellent chemical, mechanical and electronic properties (Katz 1980, Liu *et al.* 1990). It is polymorphic and therefore exists in several phases; the α and β phases are the most common forms and can be produced under normal pressure condition, but the γ phase

can only be synthesized under high pressures and temperatures. It is chemically inert and exhibits high dielectric constant and large electronic gap, therefore used in microelectronics devices (Powell *et al.* 1981). SiN_x has excellent thermal resistance due to its low thermal expansion coefficient and also used as diffusion barriers in semiconductors. The melting temperature of SiN_x is 1900°C and its density is 3.44 gm/cm^3 (Barsoum 1997).

Veprek *et al.* (1995a) have shown that multilayer of TiN/SiN_x attains a hardness value of $\geq 50 \text{ GPa}$ and this ultra high hardness is due to the small crystalline size (which suppresses dislocation motion and multiplication) and amorphous SiN_x boundaries (which pin dislocations). It is very important to control the Si content and TiN crystal size to obtain the high hardness and purity is also important as oxygen and other contaminants of about 1–2 at. % level act detrimentally on film properties, lowering its hardness (Veprek *et al.* 2004). Plasma enhanced chemical vapor deposition, CVD and PVD, are the most promising techniques for depositing TiN/SiN_x multilayers. A controlled ion bombardment at low energies allows one to adjust the desirable crystallite size, mechanical stress, and avoid columnar structure in the films as reported in the literature (Veprek *et al.* 1987, Sambasivan *et al.* 1994).

Chapter 2

Synthesis and Characterization Techniques

2.1 Thin films growth

Thin films are thin material layers ranging from fractions of a nanometer to several micrometers in thickness and its formation starts with nucleation followed by coalescence and subsequent thickness growth, all stages of which can be influenced by deposition parameters in all the physical vapor deposition technique (PVD). The properties of thin films of a given material depend on microstructure of the films, which depends on deposition parameters and the substrate material. Depending on the interaction energies of substrate and film atoms, any of following three growth modes can occur:

a) Layer by layer mode or Frank-Vander Merwe mode:



Frank- Van der Merwe: (layer growth; ideal epitaxy)

In this two-dimensional mode, the interaction between the substrate and the layer atoms is stronger than the interaction between neighbouring atoms. Each new layer starts to grow on top of another layer, only when the last one is completed.

b) Island growth mode or Volmer-Weber mode:



Volmer-Weber: (island growth)

In this mode, the interaction between neighbouring atoms is stronger than the overlayer-substrate interaction, the particles would rather form separate aggregates over the surface that grow in size and eventually coalesce (three-dimensional islands) during film growth.

c) Layer-plus-island growth mode or Stranski-Krastanov mode:



Stranski-Krastanov: (layer+islands)

In this mode, the film starts to grow layer by layer in a first stage followed by the formation of island agglomerates occurs.

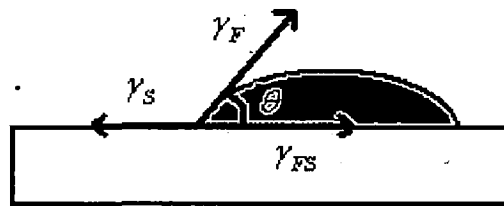


Figure 2.1: Schematic diagram of surface energy of substrate (γ_s), thin film material (γ_f) and interface energy of film-substrate (γ_{fs})

Growth modes can be systematically classified in terms of surface energies with Young's equation (**Figure 2.1**)

$$\gamma_s = \gamma_{fs} + \gamma_f \cos \theta \quad (2.1)$$

where, θ is the wetting angle of a liquid nucleus on a substrate, γ_s is the surface energy of substrate, γ_f is the surface energy of thin film material, and γ_{fs} is the interfacial energy of film-substrate. The three modes of film growth can be distinguished on the basis of **Equation 2.1**.

For layer growth, $\theta = 0$ and therefore,

$$\gamma_s = \gamma_{fs} + \gamma_f \quad (2.2)$$

For island growth, $\theta > 0$ and so,

$$\gamma_s < \gamma_{fs} + \gamma_f \quad (2.3)$$

Lastly, for layer-plus-island growth,

$$\gamma_S > \gamma_{FS} + \gamma_F \quad (2.4)$$

It occurs because the interface energy increases with film thickness; typically the layer on top of the substrate is strained to fit the substrate. The growth mode is controlled not only by interface energies but also by supersaturation. Generally, growth tends to shift from island to layer as supersaturation increases (Chopra 1969, Ohring 2002).

2.2 Synthesis of thin films

The choice of a deposition technique to deposit thin films usually depends on the specific characteristics of film required for a study or application of interest. Also, it is necessary to get highly uniform, nanocrystalline thin films with a mean grain size distribution. Physical vapor deposition (PVD) techniques such as thermal evaporation, laser ablation, and magnetron sputtering are found to be very effective for depositing thin films with the aforementioned microstructural characteristics. In PVD, the synthesis of thin films is usually carried out from the same material whose nanoparticles are to be synthesized, its purity is decided by purity of the starting materials, base vacuum and purity of the ambient gas atmosphere (Taneja *et al.* 2001, Xue *et al.* 2002, Chandra *et al.* 2006b, Du *et al.* 2006, Gohil *et al.* 2008). In contrast, in chemical vapor deposition (CVD) technique, some un-reacted chemicals and products other than the desired one are often left behind with the nanoparticles. Among various PVD techniques, sputtering process exhibits several advantages; any material can be volatilised, compounds are volatilised stoichiometrically and film deposition rates can be made uniform over large areas. Furthermore, the kinetic energy of sputtered atoms falls

largely within the energy range for displacing of surface atoms without causing subsurface damage.

2.2.1 Sputtering

Sputter deposition is one of the physical vapor deposition processes for depositing thin films by sputtering, i.e. removal of atoms from a "target"(source), which then deposits onto a substrate. In other words, it is the ejection of atoms from the surface of material (the target) by bombardment with energetic particles, the process called 'sputtering'. The ejected or sputtered atoms get condensed on a substrate and form thin films. Sputtering is largely driven by momentum exchange between the ions and atoms in the material, due to collisions. The process can be thought of as atomic billiards, with the ion (cue ball) striking a large cluster of close-packed atoms (billiard balls). Although the first collision pushes atoms deeper into the cluster, subsequent collisions between the atoms can result in some of the atoms near the surface being ejected away from the cluster.

Sputtering process begins when inert gas atoms gets ionized due to the applied negative DC potential to the target material and these positive ions of inert gas hits the target atoms, the latter gains part of the momentum and transfer it to other atoms through further collisions, leading to a cascade which results in some of the target atoms to 'sputter' out of the target with secondary electrons. The sputtered atoms, those ejected into the gas phase, are not in their equilibrium state, therefore, they tend to condense back into the solid phase upon colliding with any surface in the sputtering chamber with maximum deposition taking place on the substrate, which is in the line of sight of the target to form a thin film. It subtends the maximum area perpendicular to

the momentum of ejected target atoms and clusters. These secondary electrons collide and ionize the inert gas atoms and plasma is generated. The initial positive ions needed to trigger the generation of secondary electrons are thought to be either the stray ions always present in the atmosphere or the ions produced by field ionization of the inert gas atoms.

Other processes associated with the bombardment of a target by highly energetic ions include:

- a) Generation of secondary electrons,
- b) Ion reflection at the target surface,
- c) Ion implantation with the ion permanently buried into the target surface,
- d) Radiation damage in the structural rearrangement varying from simple vacancies and interstitial to gross lattice defects, and
- e) Emission of X-rays and photons.

These processes can be summarized as illustrated in **Figure 2.2**.

To use sputtering as a useful thin film deposition process, some criteria have to be met. First, ions of sufficient energy must be created and directed towards the surface of a target to eject atoms from the surface of the material. To achieve this, an argon gas of ionization energy 15.76 eV, for example, can be used in a chamber and by application of a sufficiently large voltage between the target and the substrate; a glow discharge is set up in a way to accelerate the positive ions towards the target to cause sputtering. Secondly, the ejected materials must be able to get to the substrate with little impedance to their movement. The pressure P determines the mean free path of the sputtered particles which according to the Paschen's relation is proportional to $1/P$.

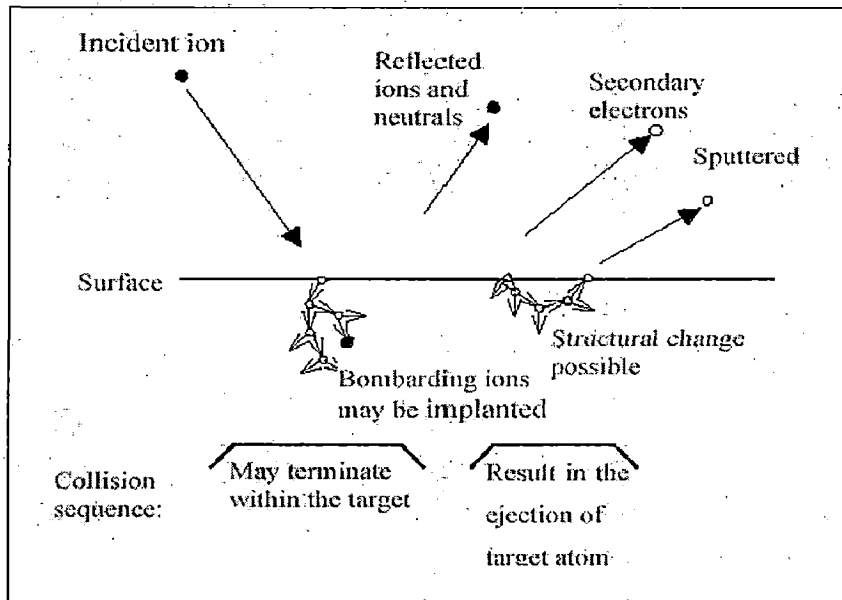


Figure 2.2: Processes generated by the impact of highly energetic particle on a target surface. The collision may terminate at the target or cause particle sputtering.

In addition to pressure, the target-substrate distance determines the scattering of the sputtered particles on their way to the substrate and also the amount of energy with which they deposit on the substrate. Generally, the average energy of sputtered atom is 10-40 eV.

Sputtering is characterized by the sputter yield S , which is the ratio of the ejected atoms to the number of incoming energetic particles, which are predominantly ions. Sputter yield depends on the energy and direction of the incident (bombarding) ions, masses of the ions and target atoms and the binding energy of atoms in the solid. By Sigmund's theory, the sputter yield is given as

For $E < 1$ KeV,

$$S = \frac{3\alpha}{4\pi^2} \frac{4M_1M_2}{(M_1 + M_2)^2} \frac{E}{E_B} \quad (2.5)$$

where, E_B is the surface binding energy of the target atom being sputtered, E is the ion bombardment energy, α is a measure of the efficiency of momentum transfer in collisions, and M_1 and M_2 are the masses of the positive ion of the gas and target material, respectively.

But for $E > 1$ KeV,

$$S = 3.56\alpha \frac{Z_1 Z_2}{Z_1^{2/3} + Z_2^{2/3}} \left(\frac{M_1}{M_1 + M_2} \right) \frac{S_n(E)}{E_B} \quad (2.6)$$

where, Z_1 and Z_2 are the atomic numbers of the incident ion and sputtered target atom respectively and $S_n(E)$ is a measure of the energy loss per unit length due to nuclear collisions, and also it is a function of the energy as well as masses and atomic numbers of the atoms involved (Ohring 2002).

2.2.2 Magnetron Sputtering

Magnetron sputtering is a thin film deposition technique based on the physical sputtering effects caused by the bombardment of a target material with accelerated ions produced in glow discharge plasma. A wide variety of thin film materials, from metals to insulators, may be produced using this technique. In sputtering, not all of the electrons escaping the target contribute to the ionized plasma glow area. The wasted electrons fly around the chamber causing radiation and other problems, for example, the heating of the target. A magnetron sputtering source addresses the electron problem by placing a set of strong permanent magnets in the gun arranged in a circular geometry giving rise to a radial magnetic field parallel to the target surface as shown in **Figure**

2.3.

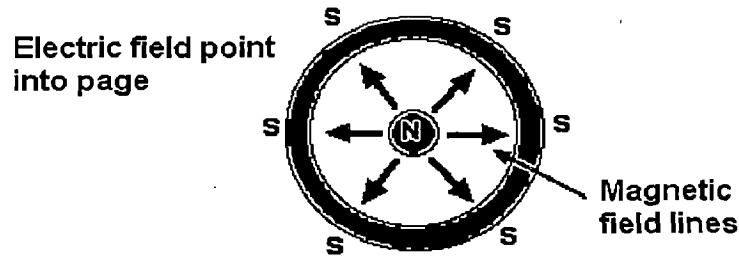


Figure 2.3: Electric and magnetic field lines in a magnetron gun

A plate of a highly permeable material (such as iron) located behind the magnets, prevents the magnetic field flux from spreading into regions other than in front of the target surface. Thus the electrons are forced to follow a closed drift path caused by the crossed electric and magnetic fields, i.e. the electrons are trapped in a channel as shown in **Figure 2.4(a)** of magnetron sputtering process (Ohring 2002). The effect of this is two fold:

- a) The probability of ionizing the inert gas atoms will increase significantly and make the plasma more intense and sustainable at low pressure
- b) An increase of the mean free path, which is inversely proportional to the pressure

Due to the confinement of secondary electrons, the larger number of sputtered atoms gets deposited as thin film on the substrate. **Figure 2.4(b)** shows the collisions involved in a magnetron sputtering process near the target.

DC magnetron sputtering is used for conducting targets such as metals or doped semiconductors but not for non-conducting targets (non metals or insulators) because of its non-conducting nature, positive ions would lead to a charging of the surface and subsequently to a shielding of the electric field. Subsequently, the ion current would die off. Therefore, RF magnetron sputtering (radio frequency of 13.56 MHz) is used for non-conducting and semiconductor targets in which an AC-voltage is applied to the

target. In one phase, ions are accelerated towards the target surface to sputter material. In the other phase, charge neutrality is achieved.

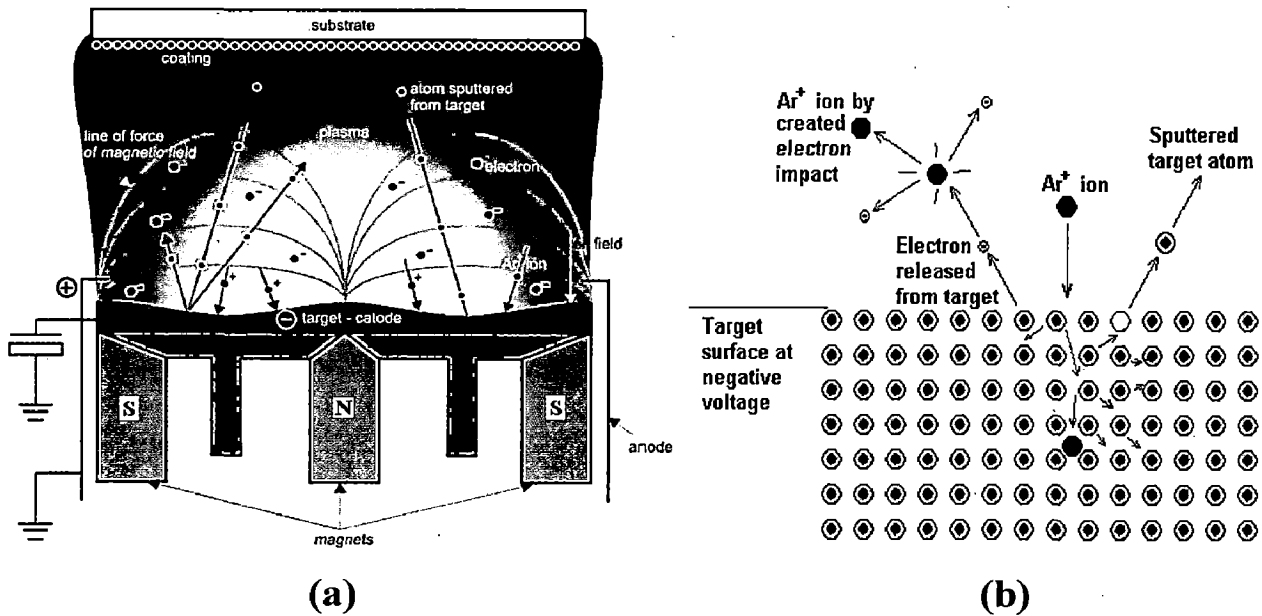


Figure 2.4: (a) Magnetron sputtering process

(b) Collisions in the sputtering process near the target

In reactive magnetron sputtering, the deposited film is formed by chemical reaction between the target material and gases like oxygen or nitrogen fed into the sputter chamber additionally to the argon, to produce oxidic or nitridic films and the reaction usually occurs either on the substrate surface or on the target itself. The composition of the films can be controlled by varying the relative pressures of the inert and reactive gases. The Titanium Nitride (TiN) films used as wear resistant coatings for tools and engineering components and decorative purposes are deposited by reactive magnetron sputtering. The magnetron sputtering set up used for the present work is shown in **Figure 2.5(a)**.

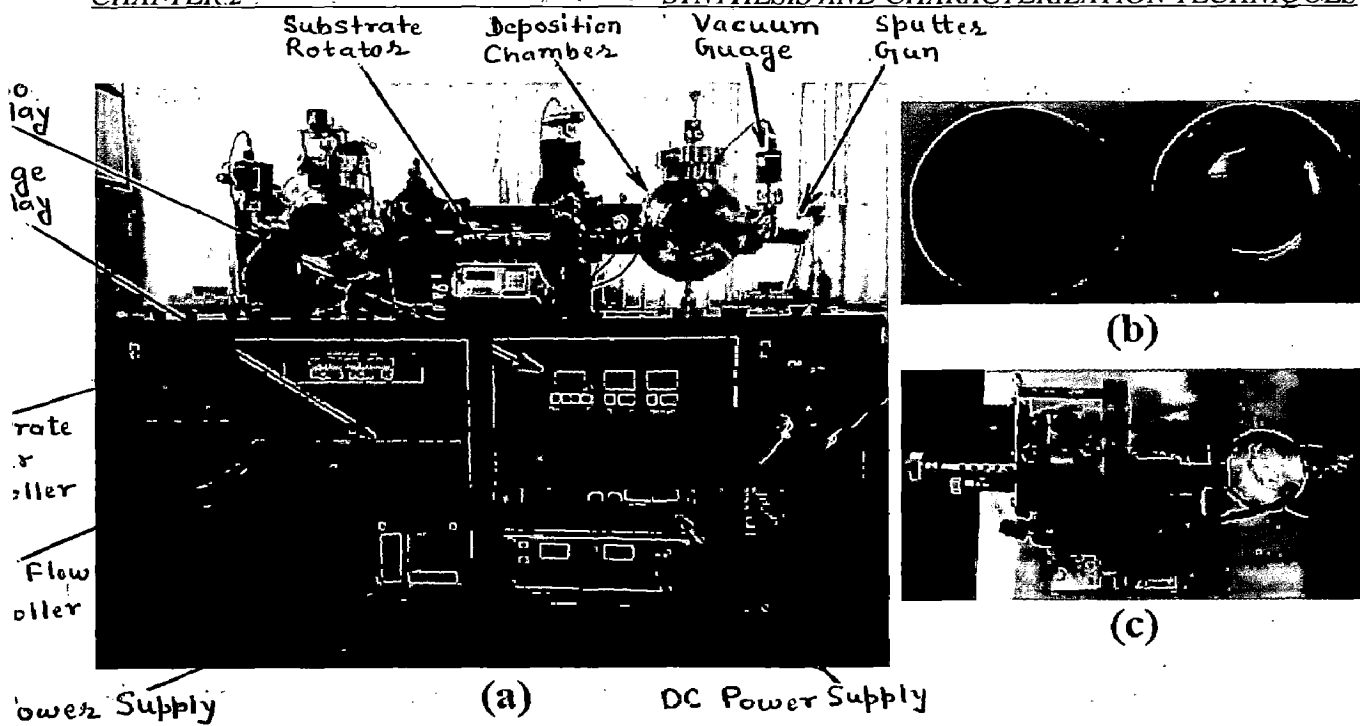


Figure 2.5: (a) DC/RF magnetron sputtering unit set up in our Nano Science Lab
 (b) New & used sputtering target
 (c) Substrate holder/heater

A circular disc of diameter 2 inch and thickness 3-5 mm of pure material used as a target is shown in **Figure 2.5(b)**, which is mounted on the magnetron gun for sputtering. The target is eroded in a circular pattern due to the use of a set of strong permanent magnets in the gun arranged in a circular geometry behind the target. The substrate is fixed on a heater [**Figure 2.5(c)**] with the help of clips as well as with the help of silver paste for the preparation of nanocrystalline thin films. The temperature of the substrate is controlled via the temperature controller of heater. After mounting the substrates, the chamber is evacuated using a turbo molecular pump, backed by rotary pump up to high vacuum ($>2 \times 10^{-6}$ Torr). After evacuation, an inert gas such as Argon (99.999% purity) is fed into the chamber via gas inlet valve. Simultaneously, the gate valve is brought into almost closed state (throttling) so as to match the gas influx and pumping-out rate. With proper throttling, the inert gas pressure and flow rate inside the

chamber can be made very stable and then the process of sputtering is the same as discussed in the **Section 2.2.1**.

The advantages of sputtering as deposition technique are as follows: The deposited films have high uniformity at large area, better reproducibility of deposited films, good adhesion of film with substrate, high flexibility of large-scale as well as complex geometry shape production, easy deposition of materials with high melting points and high reactivity. A homogeneous multicomponent phases as well as multilayer coatings can be produced with completely new material properties and the deposited films show the same concentration as that of the target material (Ohring 2002). This might be surprising since the sputter yield depends on the atomic weight of the atoms to be sputtered as discussed earlier. It may result in one component of an alloy or mixture to sputter faster than the other components, leading to a higher concentration of that component in the deposited film. Although the components are sputtered at different rates, however, since only surface atoms are sputtered, the faster sputtering of one element leaves the surface enriched with the other element, which effectively counteracts the difference in sputter rates resulting in deposited films with the same composition as the target.

2.3 Characterization Techniques

2.3.1 X-ray Diffraction (XRD)

X-ray diffraction (XRD) is a versatile, non-destructive technique that reveals detailed information about the chemical composition and crystallographic structure of a crystalline material. It is most widely used for the identification of unknown crystalline materials and also information related to the crystal structure of the films, including

lattice constants, crystallite size, phase analysis, crystal defects, stress, etc. The XRD methods are generally applied to films thicker than several angstroms on account of the strong penetrating power of the X-rays. X-rays are electromagnetic radiation of exactly the same nature as light, but of very much shorter wavelength. X-rays used in diffraction have wavelengths lying in the range of 0.5-2.5 Å where as visible light is of the order of 6000 Å. X-ray diffraction is based on constructive interference of monochromatic X-rays and a crystalline sample. When a monochromatic X-ray beam with wavelength λ is projected onto a crystalline material at an angle θ , X-rays are scattered by the electrons of the atoms without change in wavelength. As the wavelength of X-rays is close to atomic size (~ 1.5 Å), they get diffracted by atoms and ions. If, as in the case of crystals, the atoms or ions are arranged in a particular fashion, then the diffracted X-rays interfere constructively or destructively with each other depending on the path difference. W.L. Bragg formulated the condition for constructive interference as (Cullity *et al.* 2001),

$$2d \sin \theta = n\lambda \quad (2.7)$$

where, d is the spacing between two adjacent atomic planes, θ is the angle between the atomic plane and the X-rays, n is the order of diffraction maximum, and λ is the wavelength of the X-rays. The resulting diffraction pattern comprising both the positions and intensities of the diffraction effects is a fundamental physical property of the substance. Analysis of the positions of the diffraction effect leads immediately to a knowledge of the size, shape and orientation of the unit cell. The crystallite size is an important parameter, which can be determined from the width of the Bragg reflection and is given by the Scherrer's formula (Cullity *et al.* 2001);

$$t = \frac{0.9 \lambda}{B \cos \theta} \quad (2.8)$$

where, t is the crystallite size, λ is the wavelength of the target material, B is the full width at half maximum (FWHM) of the Bragg reflection in the radians on the 2θ scale and θ is the Bragg reflection angle. It is important to subtract the instrumental line width from the observed line width to get a correct estimate of broadening due to small particle size. Therefore, by the Scherrer's formula, crystallite size is inversely proportional to full width at half maximum (FWHM), hence, small crystallites give rise to broad diffraction peak while large crystallites result in sharp peaks. X-ray diffractometer consist of three basic elements: an X-ray tube, a sample holder, and an X-ray detector as shown in **Figure 2.6**. X-rays are generated in a cathode ray tube by heating a filament to produce electrons, accelerating the electrons toward a target by applying a voltage, and bombarding the target material with electrons.

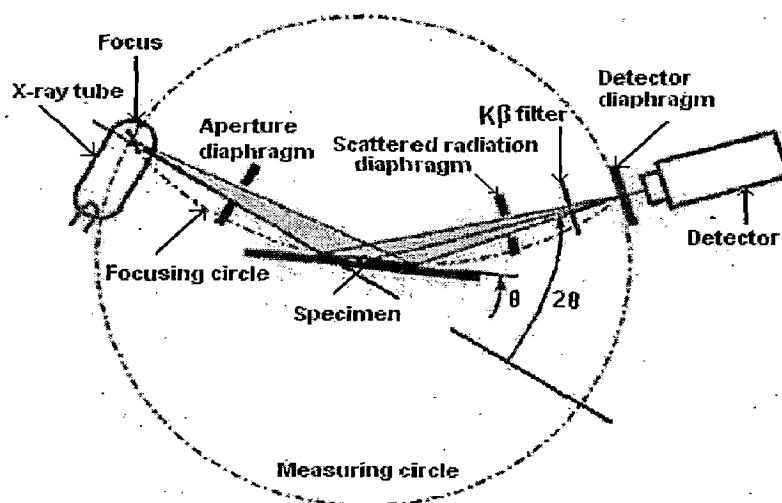


Figure 2.6: Schematic diagram of beam path

When electrons with sufficient energy dislodge the inner shell electrons of the target material, characteristic X-ray spectra are produced. Most of the kinetic energy of the

electrons striking the target is converted into heat, less than 1% being transformed into X-rays. These spectra consist of several components, the most common being K_α and K_β . The K_β line which is always present with K_α , at a slightly shorter wavelength, is filtered out using an absorbing film. K_α consists, in part, of $K_{\alpha 1}$ and $K_{\alpha 2}$. $K_{\alpha 1}$ has a slightly shorter wavelength and twice the intensity as $K_{\alpha 2}$. $K_{\alpha 1}$ and $K_{\alpha 2}$ are sufficiently close in wavelength such that a weighted average of the two is used. The specific wavelengths are characteristic of the target material (Cu, Fe, Mo, Cr). Filtering by foils of atomic number one or two less than the target material or crystal monochrometers, is required to produce monochromatic X-rays needed for diffraction.

Copper is the most common target material for X-ray diffraction, with Cu K_α radiation = 1.54 Å. These X-rays are collimated and directed onto the sample. As the target and detector are rotated, the intensity of the reflected X-rays is recorded.

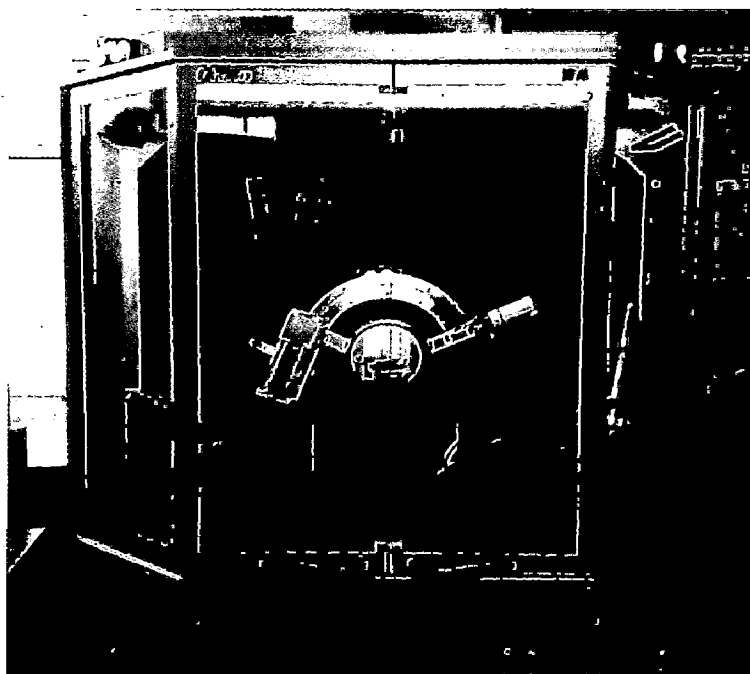


Figure 2.7: X-ray diffraction (Bruker AXS, D8 Advance)

When the geometry of the incident X-rays impinging the sample satisfies the Bragg's **Equation 2.7**, constructive interference occurs and a peak in intensity appears. A detector records and processes this X-ray signal and converts it into a count rate; a graph between 2θ versus counts is plotted. For the present work, X-ray diffraction (Bruker AXS, D8 Advance) has been used and shown in **Figure 2.7**.

2.3.2 Field Emission Scanning Electron Microscope (FE-SEM)

The scanning electron microscope (SEM) is a type of electron microscope that uses high-energy beam of electrons to scan the sample surface in a raster pattern to obtain image. The SEM produce images of high resolution, which means that closely spaced features can be examined at a high magnification and large depth of field yielding a characteristic three-dimensional appearance useful for understanding the surface structure of a sample. SEM is most widely used for revealing information about the microstructures and orientation of the samples.

In conventional SEM, electrons are thermionically emitted from a tungsten or lanthanum hexaboride (LaB_6) filament. Tungsten is used as filament because it has the highest melting point and lowest vapor pressure of all metals, thereby allowing it to be heated for electron emission. On the other hand, in Field Emission Scanning Electron Microscope (FE-SEM) electrons are emitted via field emission (FE) in which a high voltage applied between a pointed cathode and a plate anode causes current to flow. The field emission tip is generally made of a single crystal tungsten wire sharpened by electrolytic etching. FE-SEM provides 2 nm resolutions, 3 to 6 times better than conventional SEM, and minimized sample charging and damage. The field emission process itself depends on the work function of the metal, which is affected by adsorbed

gases. Due to this reason, a very high vacuum is required. **Figure 2.8** shows a schematic diagram of the field emission scanning electron microscope (Web link 5). The source of the electrons is electron gun and it produces a beam of electrons which typically has an energy ranging from a few hundred eV to 50 keV, is attracted through the anode and condensed by the condenser lens and then focused as a very fine spot on the specimen by the objective lens. A set of small coils of wire, called the scan coils, is located within the objective lens.

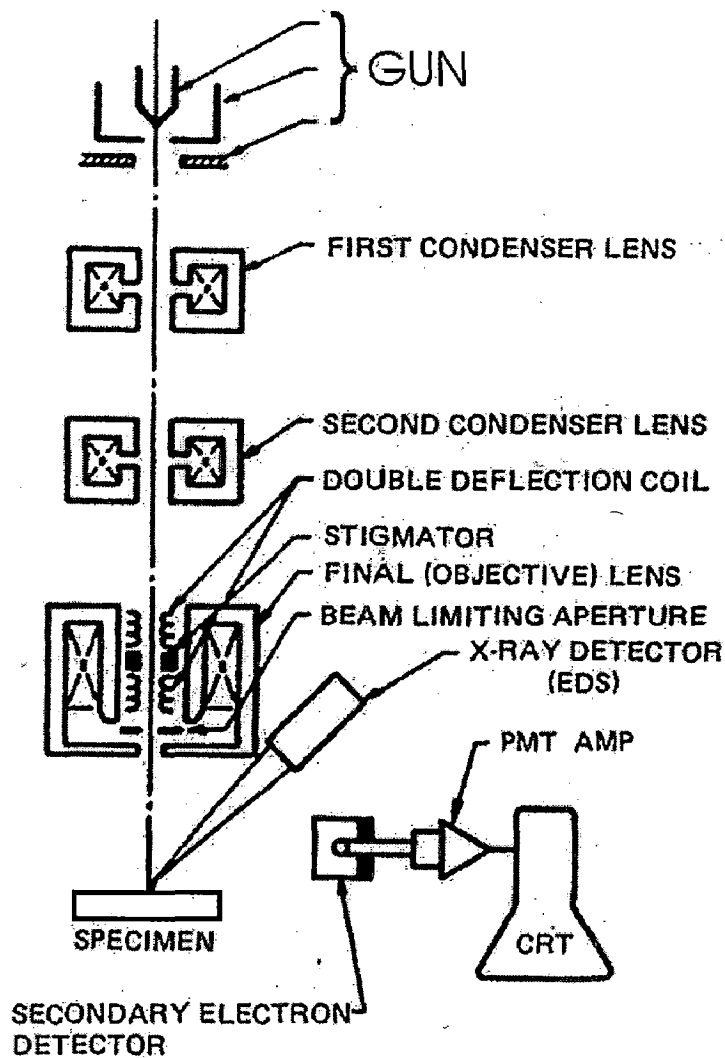


Figure 2.8: Schematic diagram of the Field Emission Scanning Electron Microscope (FE-SEM)

The coils are energized by a varying voltage produced by the scan generator and it creates a magnetic field that deflects the beam of electrons back and forth in a controlled pattern called a raster scan (point by point scanning) over a rectangular area of the sample surface. When the beam of incident electrons strikes the surface of a sample, it undergoes a series of complex interactions with the nuclei and electrons of the atoms of the sample and produce variety of signals such as

- a) Secondary electrons: for obtaining morphology and topography of samples
- b) Backscattered electrons: for illustrating contrasts in composition in multiphase samples
- c) Diffracted backscattered electrons: for obtaining crystallographic orientation of the grains
- d) Photons or characteristic X-rays: for identification of a material and quantitative or semi-quantitative analysis
- e) Visible light and
- f) Heat

A sample analyzed in SEM should be conducting. Since all metals are conductive, no special sample preparation is required for them but non-conducting or insulating samples are coated with a thin layer of conducting material, commonly carbon or gold. When a non-conducting sample is analyzed, a negative charge builds up gradually on the area where the bombardment by the beam of electrons occurs. A buildup of negative charges on the samples may produce one or more of three conditions commonly referred to as charging: a) lines on the image due to the deflection of secondary electrons by the negative charge on the sample, b) abnormal contrast in the image due to the uneven distribution of the negative charge on the sample and c) breaks or splitting

of the image due to high negative charge on the sample which deflects the beam of electrons. The choice of material for conductive coatings depends on the data to be acquired from the sample as carbon is most desirable if elemental analysis is a priority, while metal coatings such as gold are most effective for high resolution electron imaging applications (Fleger *et al.* 1993). Field Emission Scanning Electron Microscope (FEI, Quanta 200F) has been used for the present work and shown in **Figure 2.9**.

The attachments of FE-SEM such as energy dispersive spectroscopy (EDS) and electron back scatter diffraction (EBSD) are used for obtaining the chemical composition and crystallographic orientation of the grains, respectively. An EDS spectrum normally displays peaks corresponding to the energy levels for which the most X-rays had been received. Each of these peaks is unique to an atom, and therefore corresponds to a single element. Higher the peak in a spectrum indicates the element is more concentrated in the specimen.

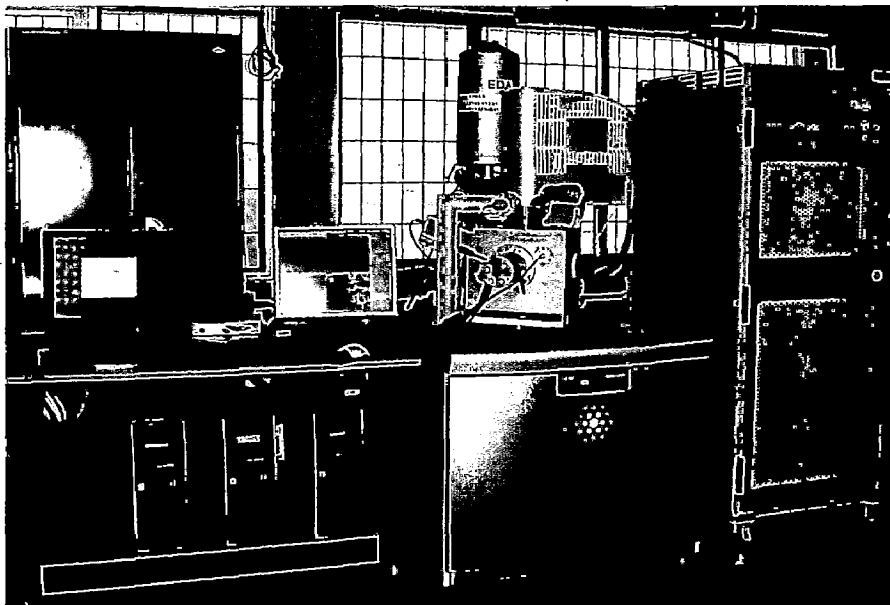


Figure 2.9: Field Emission Scanning Electron Microscope (FEI, Quanta 200F)

In EBSD, electron beam is diffracted by atomic layers of crystalline materials and these diffracted electrons are detected when they impinge on a phosphor screen and generate visible lines, called Kikuchi bands, or "EBSP's" (electron backscatter patterns). These patterns are effectively projections of the geometry of the lattice planes in the crystal, and they give direct information about the crystalline structure and crystallographic orientation of the grain from which they originate.

2.3.3 Atomic Force Microscope (AFM)

The Atomic Force Microscope (AFM) or scanning force microscope (SFM) is a very high-resolution (0.01 nm) type of scanning probe microscope. Unlike traditional microscopes, the AFM does not rely on electromagnetic radiation such as photon or electron beams to create an image but is based on the interactive forces called the van der Waals force between the sample and the tip. It does not require vacuum environment or any special sample preparation, and can be used in either an ambient or liquid environment.

A schematic setup of an atomic force microscope is shown in **Figure 2.10**. The AFM consists of a microscale cantilever with a sharp tip (probe) at its end that is used to scan the specimen surface in a raster-pattern. The cantilever is typically silicon or silicon nitride with a tip radius of curvature on the order of nanometers. A laser is focused onto the end of the cantilever and reflected into the center of a four segment photodiode. When the tip is brought into proximity of a sample surface, forces between the tip and the sample lead to a bending (vertical forces) or twisting (lateral forces) of the cantilever which changes the ratio of light falling on the four segment photodiode.

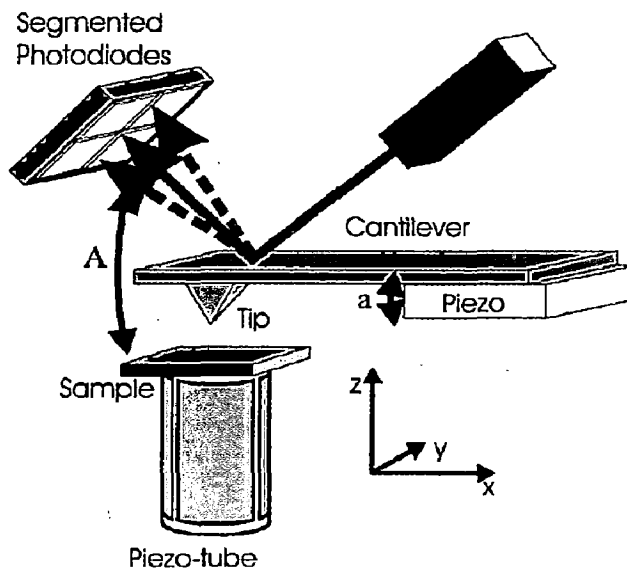


Figure 2.10: Schematic setup of Atomic Force Microscope (AFM)

The difference in the intensity falling on the four segment photodiode is used as output signal and converted into a proportional voltage by the photodiode. This voltage serves as a feedback signal enabling the tip to maintain either a constant force or a constant height above the sample. A feedback loop continuously checks the feedback signal, compares it to some user defined set point value and adjusts the height of the tip over the sample such that the difference is minimized. Stable operation is possible if the feedback signal remains constant in the tip-surface distance. The tip is then kept at a height corresponding to a constant interaction over the sample surface. Either the cantilever or the sample is mounted on a piezoelectric element, which can move the sample in the z direction for maintaining a constant force or a constant height, and the x and y directions for scanning the sample and hence obtain three-dimensional image. With good samples (clean, with no excessively large surface features), resolution in the x-y plane ranges from 0.1 to 1.0 nm and in the z direction is 0.01 nm (atomic

resolution). For the present work, Atomic Force Microscope (NT-MDT, Ntegra) has been used and shown in **Figure 2.11**.

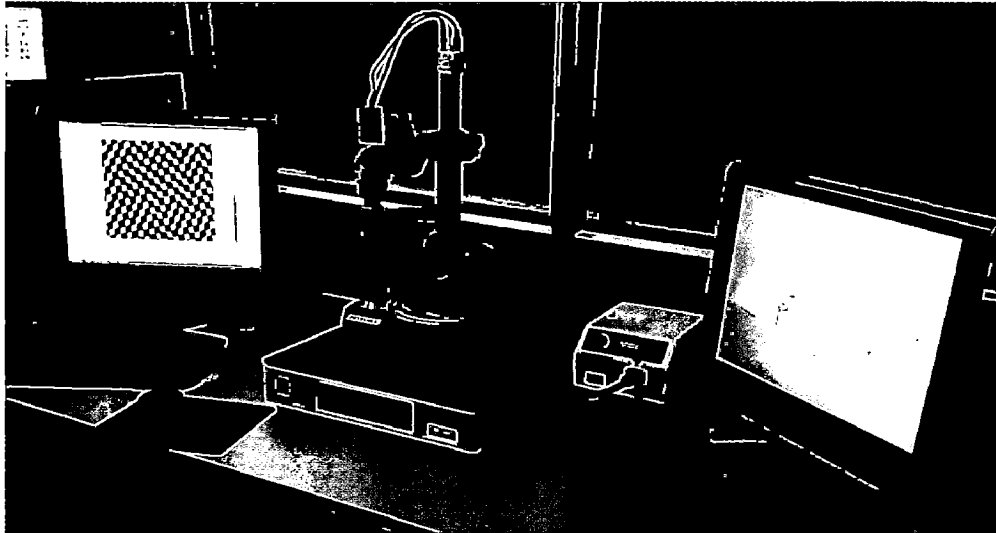


Figure 2.11: Atomic Force Microscope (NT-MDT, Ntegra)

For most applications, the AFM is operated in one of the following three modes:

- a) Contact mode
- b) Non-Contact mode
- c) Semicontact mode or Intermittent mode or Tapping mode

Different scanning modes operate in different regions: Non-contact in the attractive region, contact mode in the repulsive and intermittent or tapping mode fluctuates between the two. The relationship between van der Waals force and distance is shown in **Figure 2.12**. The tip is like a group of atoms interacting with the surface of the sample, which essentially another group of atoms. At the right side of the curve, the atoms are separated by a large distance. As the atoms are gradually brought together, they first weakly attract each other. This attraction increases until the atoms are so close together that their electron clouds begin to repel each other electrostatically. This

electrostatic repulsion progressively weakens the attractive force as the distance continues to decrease.

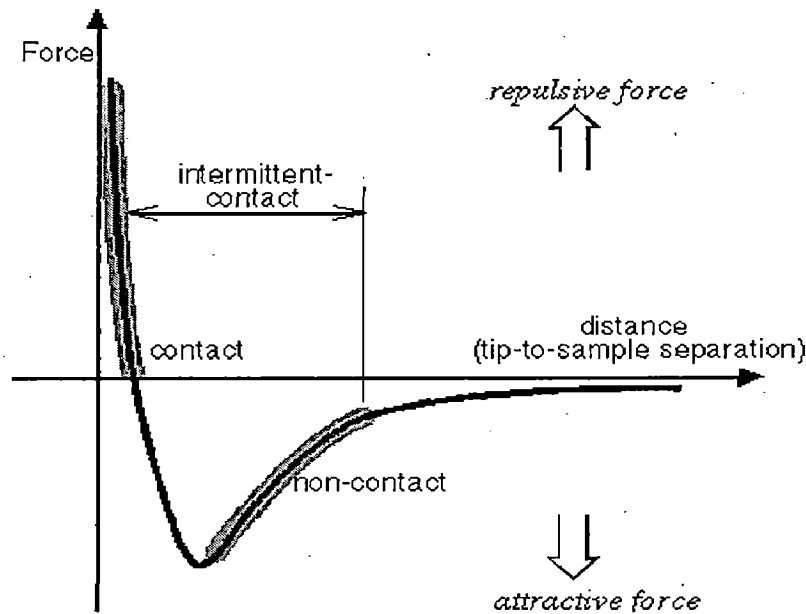


Figure 2.12: Graph between van der Waals force Vs distance

The force goes to zero when the distance reaches a couple of angstroms as shown in the **Figure 2.12**. Anything closer than this distance, the total van der Waals force becomes positive (repulsive). This distance will not change, therefore any more attempt to force the sample and tip closer will result in deformation or damage to the sample or the tip. There are two other forces that arise during the scan: a capillary force that is caused by a build-up of water, which is normally present without an inert environment, on the tip; the force caused by the cantilever itself, which is like a force caused by a compressed spring (AFM lab manual 2004).

a) Contact Mode: In this mode, the tip is held less than a few angstroms (10^{-10} m) from the sample surface and the repulsive interatomic Van der Waals forces between the tip and the sample are detected with a mean value of 10^{-9} N. This force is set by pushing the cantilever against the sample surface with a piezoelectric positioning

element. In contact mode AFM, the deflection of the cantilever is sensed and compared in a DC feedback amplifier to some desired value of deflection. If the measured deflection is different from the desired value, the feedback amplifier applies a voltage to the piezo to raise or lower the sample relative to the cantilever to restore the desired value of deflection. The voltage that the feedback amplifier applies to the piezo is a measure of the height of features on the sample surface. The typical problem with the contact mode is that the tip may scratch the surface and change its intrinsic features.

- b) Non-Contact Mode:** In the non-contact region, the cantilever is held on the order of tens to hundreds of angstroms away from the sample surface, and the attractive interatomic Van der Waals forces between the tip and sample are detected and topographic images are constructed by scanning the tip above the surface. Since the attractive forces from the sample are substantially weaker than the forces used by contact mode, the tip is given a small oscillation so that AC detection methods can be used to detect the small forces between the tip and the sample. The changes in amplitude, phase, or frequency of the oscillating cantilever in response to force gradients from the sample are measured in this non-contact mode.
- c) Semi-Contact or Tapping Mode:** In this mode, the cantilever is made to oscillate at its natural frequency by using a piezo-electric crystal. The oscillating tip is moved close to the sample surface till it begins to just tap it and is then immediately lifted off again, while the sample is continuously scanned below the tip. The change in oscillation amplitude during the tapping period is used as a feedback to maintain constant height or force between the tip and the sample. The feedback voltage

serves as a measure of the surface features. The advantages of the semi-contact mode are that as the tip is not dragged over the sample, there is no damage caused to the sample and also the tip is prevented from sticking to the sample surface due to adhesion. This method usually gives higher resolution than the previous two methods.

2.3.4 Transmission Electron Microscope (TEM)

The transmission electron microscope (TEM) operates on the same basic principles as the optical (light) microscope but uses electrons instead of light. The shorter wavelength of electrons (200 kV electrons have a wavelength of 0.025 Å) makes it possible to get a high-resolution (0.2 nm) and high-magnification thousand times better than the light microscope. Also, in an optical microscope, the lenses are made up of glass and have fixed focal lengths, whereas in TEM, the electromagnetic lenses are constructed with ferromagnets and copper coils. The focal length of electromagnetic lenses could be changed by varying the current through the coil. The TEM is used to characterize the microstructure of materials such as grain size, morphology, crystal structure and defects, crystal phases and composition, and in biological sciences, especially in the study of cells at the molecular level. The microstructure, e.g. the grain size and lattice defects are studied by use of the image mode, while the crystalline structure is studied by the diffraction mode. In addition, the chemical composition of small volumes, for example grain boundaries, can be obtained by detection of X-rays emitted from the films.

A schematic diagram of a TEM is shown in **Figure 2.13** (Web link 6). With an electron gun, a monochromatic electron beam is formed, which is accelerated by an

electric field formed by a voltage difference of, typically, 200 kV and this beam is focused to a small, thin, coherent beam by the use of condenser lenses 1 and 2.

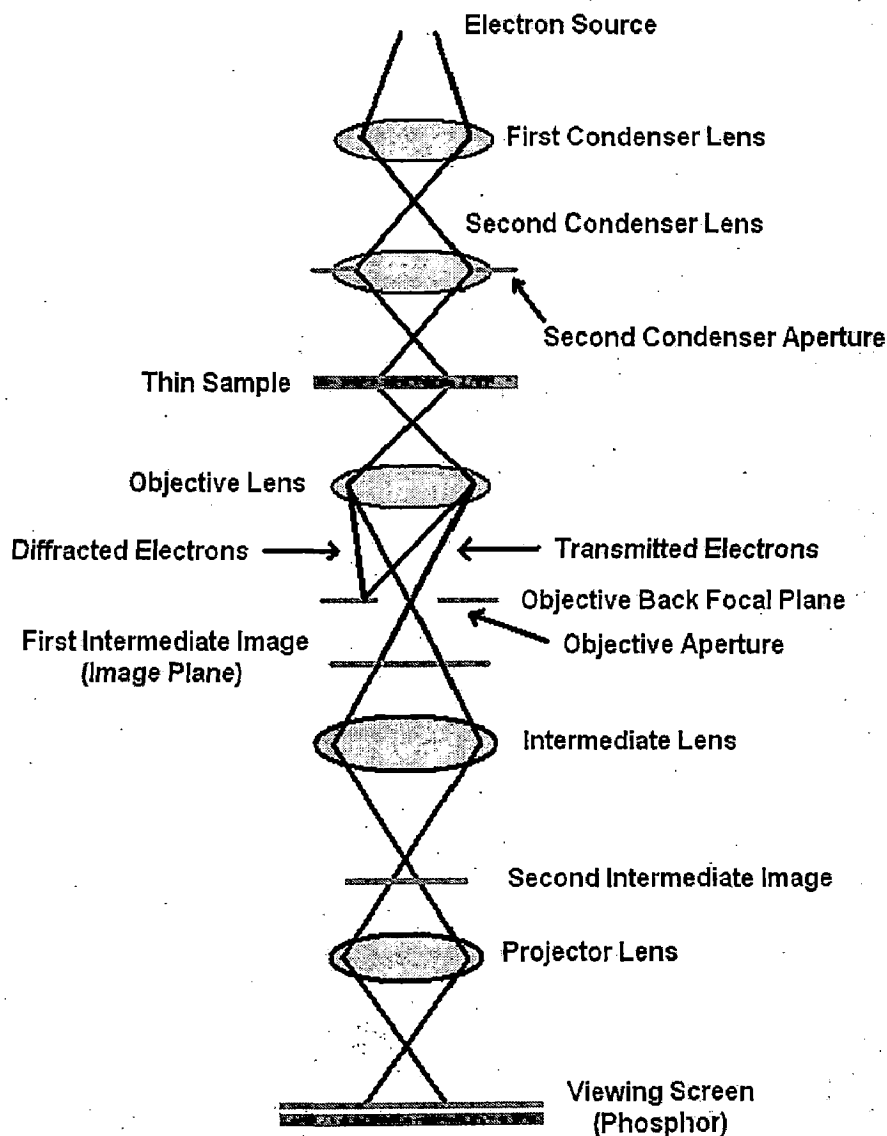


Figure 2.13: Schematic diagram of a Transmission Electron Microscope (TEM)

The first lens defines the "spot size" of the final spot that strikes the sample and the second lens changes the size of the spot on the sample from a wide dispersed spot to a pinpoint beam. The condenser lenses are fitted with apertures, which are usually small platinum disks with holes of various sizes. These apertures protect specimen from too

many stray electrons, which can contribute to excessive heat and limit the X-ray production farther down the column. The most important function of a condenser lens and its aperture is to define the angular aperture of illumination. The maximum angular aperture occurs when the beam is at crossover. In this condition, the beam is round and is at maximum intensity. When the focused electron beam strike on the sample and traversed through it, the objective lens focus it to form an intermediate image. This intermediate image is in turn magnified by a projector lens(es) to form a magnified final image. A TEM usually operates at 10^{-6} Torr in the column and 10^{-9} Torr in the electron gun chamber. Transmission Electron Microscope (FEI, Tecnai 20) has been used for the present work and shown in **Figure 2.14**.

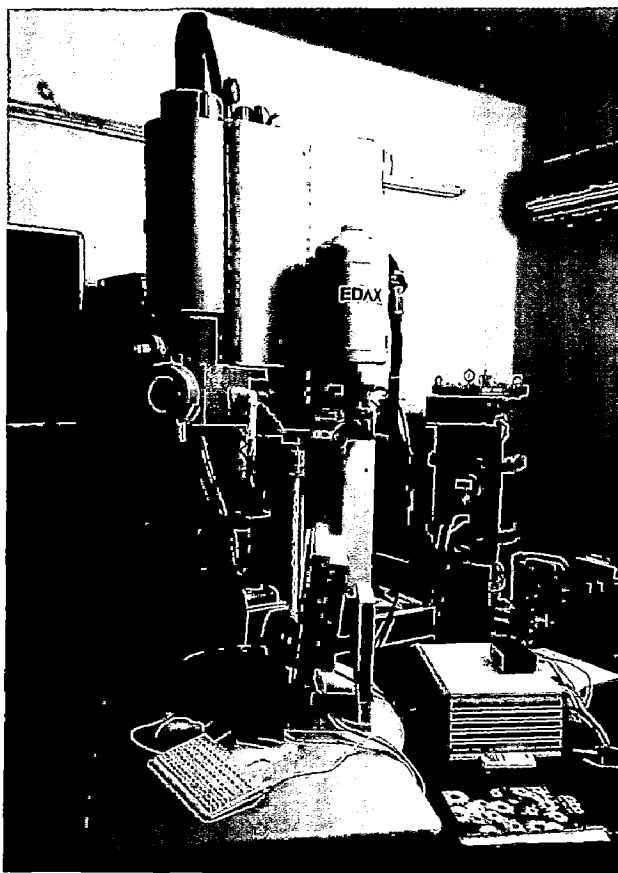


Figure 2.14: Transmission Electron Microscope (FEI, Tecnai 20)

TEM has two modes of operation:

- a) **Image mode:** In image mode, intermediate aperture is removed and only objective aperture is used. Intermediate lens is focused on the image plane of the objective lens and in image mode, two imaging systems are used:
- i) **Bright Field (BF) imaging:** When the objective aperture is positioned in the back focal plane (the flat plane at right angles to the optical axis onto which a lens will focus an image) to pass only the transmitted (undiffracted) electrons of incident electron beam and block the diffracted electrons, a bright field image is formed. In BF image, the regions that are diffracting and not diffracting appear as bright and dark, respectively. Bright field images are commonly used to examine micro-structural related features.

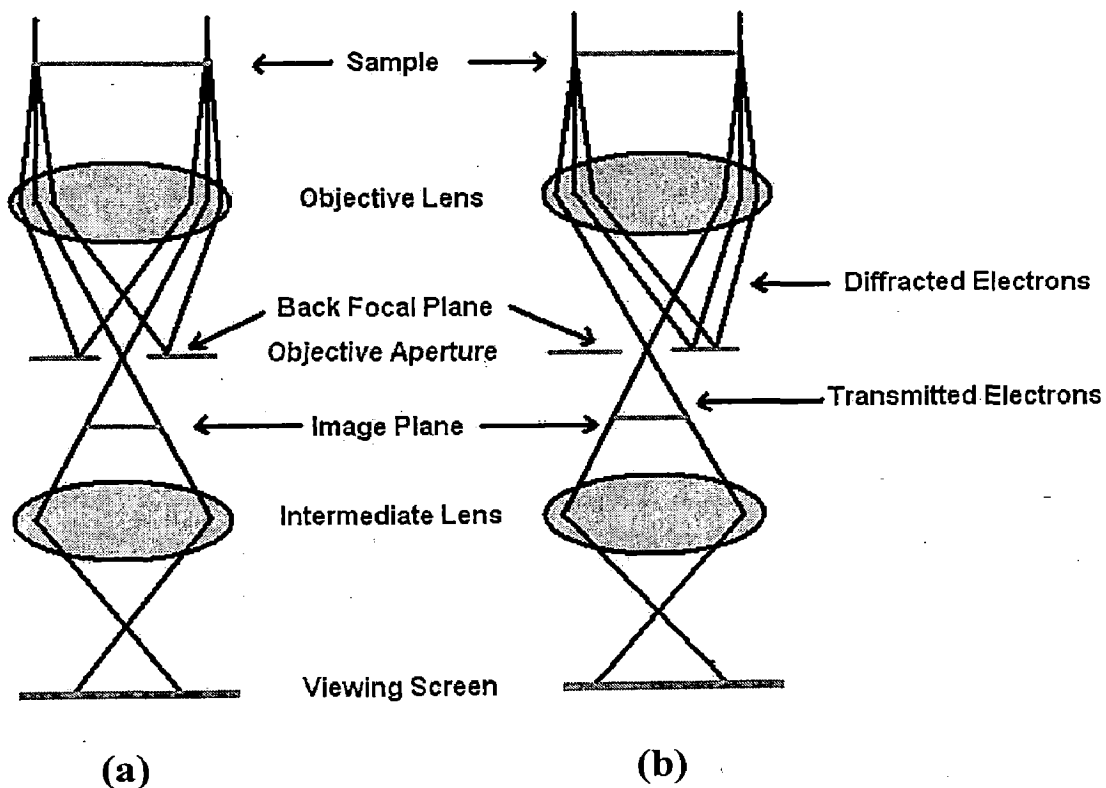


Figure 2.15: (a) Bright Field (BF) imaging and (b) Dark Field (DF) imaging

ii) **Dark Field (DF) imaging:** When the objective aperture is positioned in the back focal plane to pass only some diffracted electrons of incident electron beam, a dark field image is formed. In DF image, the regions that are diffracting appear dark and the regions that are not diffracting looks bright. Dark field images are particularly useful in examining microstructural details in a single crystalline phase. **Figure 2.15(a) and (b)** show the Bright Field (BF) imaging and Dark Field (DF) imaging, respectively.

b) **Selected Area Diffraction (SAD) mode:** In diffraction mode, objective aperture is removed and only intermediate aperture is used which passes the diffraction pattern of a selected region. The diffraction pattern that is always present in the back focal plane of the objective is brought into focus by the objective lens or in other words, intermediate lens is focused on back focal plane. Individual spots are seen when the specimen is a single crystal, while for polycrystalline material, concentric rings are observed.

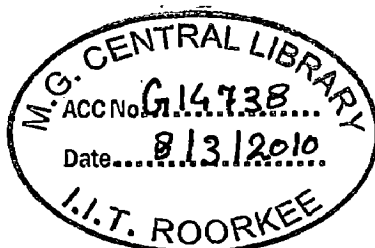
For a single crystal, the diffraction spots from planes which are equivalent by symmetry are placed symmetrically around the central (Grundy *et al.* 1976). Interplanar distance, d can be calculated from the expression

$$Rd = L\lambda \quad (2.9)$$

where, λ is the wavelength of the electron beam (0.025 Å for 200 kV), R is the distance of a particular spot from the central bright spot and L is the distance between the specimen and the diffraction plane, known as the lens constant.

There are a number of drawbacks of the TEM. Many materials require extensive sample preparation to produce a sample thin enough to be electron transparent, which makes

TEM analysis a relatively time consuming process with a low throughput of samples. The structure of the sample may also be changed during the preparation process. Also, the field of view is relatively small, raising the possibility that the region analyzed may not be characteristic of the whole sample. The sample may also be damaged by the electron beam in some cases.



2.3.5 Nanoindentation

Nanoindentation is a technique used to investigate hardness, elastic modulus and other mechanical properties of materials in which an indenter tip of known geometry is driven into a specific site of the sample by applying an increased normal load (Hay *et al.* 2000, Fischer- Cripps 2001, Han *et al.* 2005) and then the load is decreased linearly; while it continuously measures the force-displacement response. The materials with features less than 100 nm across and thin films less than 5 nm thick can be tested to understand its mechanical behavior. It is used to study the relationship between microstructure and strength and toughness of materials. In film-substrate system, a “rule of thumb” for hardness measurements is 1/10-rule that the indentation depth is smaller than 10% of the film thickness, so that there will be no substrate effect on the measured mechanical properties of the film and this statement is a first approximation. However, in cases like soft films on hard substrates or hard films on soft substrates, it tends to be either too strict or too lax. The applications of nanoindentation technique include: to study the mechanical behavior of thin films (such as hardness, elastic modulus, adhesion evaluations and wear durability), bone, and biomaterials. Hardness measurements for submicron-size features, elastic behavior of metals, ceramics, polymers, etc.

Nanoindentation technique [(CSM+), (MTS, XP) and (Hysitron)] have been used in the present work and image of CSM + nanoindenter tester is shown in **Figure 2.16**. Nanoindenter consists of two components, a measuring head for performing indentation and an optical microscope for selecting a specific location prior to the indentation and for checking the location of the imprint after indentation. If the size of the indentation is very small, Atomic Force Microscope (AFM) attached with nanoindenter is used instead of optical microscope, to image the residual imprint after indentation. The precise positioning ($0.5 \mu\text{m}$) capability of the X-Y motorized table combine with the large X-Y ranges ($20 \times 20 \mu\text{m}$ or $40 \times 40 \mu\text{m}$) of the objective ensures that the indent will always be in the centre of the field of view in both optical and AFM modes. A particular feature of this instrument is the use of a sapphire reference ring that remains in contact with the specimen surface during the indentation.

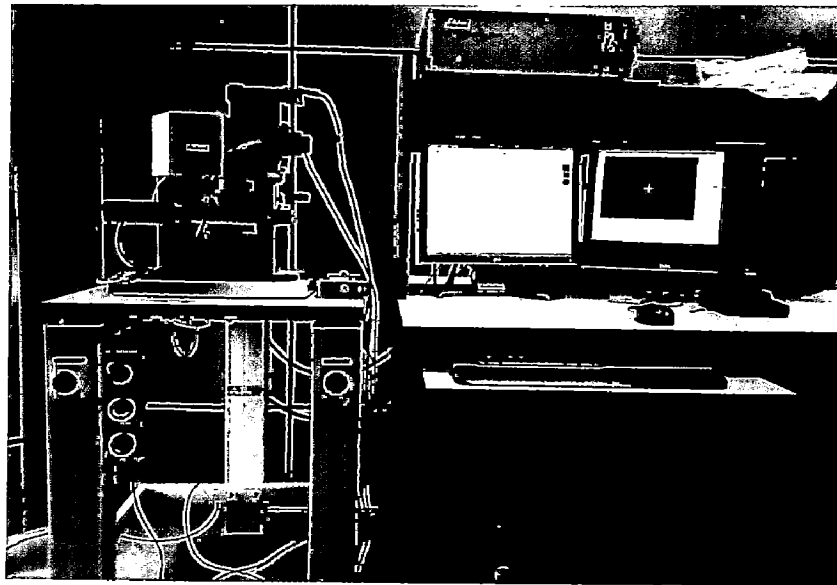


Figure 2.16: Nanoindentation tester (CSM+)

Hence, at the beginning of testing, the sample was kept under optical microscope to choose a suitable area for indentation. Afterwards, indentations were made on the

desired area of the sample whose properties are unknown by using a three-sided, pyramid-shaped Berkovich diamond indenter with nominal angle of 65.3° between the tip axis and the faces of the pyramid whose mechanical properties are known. The Nanoindenter works in two modes, load control and displacement control. In load control, the load placed on the indenter tip is increased gradually as the tip penetrates into the specimen at a selected rate and soon reaches to a selected maximum load. At this point, the load may be held constant for a period of time and then unloaded. In displacement control, the user has to set the maximum displacement of the indenter tip into the sample; the feedback loop on the load stops the measurement when the preset displacement value is reached. During loading and unloading cycle, the load is increased and decreased in a linear fashion, the area of indentation is continually measured and this area is used to obtain the load-penetration depth characteristics from which the hardness and elastic modulus values are calculated.

Figure 2.17(a) shows the loading and unloading of the indenter on the sample. For each loading and unloading cycle, the load is plotted against the displacement of the indenter as shown in **Figure 2.17(b)**. The maximum load for thin film is selected as there is no influence of the substrate material on the mechanical properties of the film.

The analysis of elastic modulus is based on the Oliver and Pharr Method (Oliver *et al.* 1992). The modulus of a material was calculated from the load-displacement curves by modeling the unloading curve with a power law relationship instead of assuming linear unloading. At any time during loading, the total displacement h is written as

$$h = h_c + h_s \quad (2.10)$$

where, h_c is the vertical distance through which contact is made (contact depth) or the

contact depth of the indenter with the sample under load and h_s is the displacement of the surface at the perimeter of the contact or sample deformation when the load is applied. The quantity h_s depends on the indenter geometry.

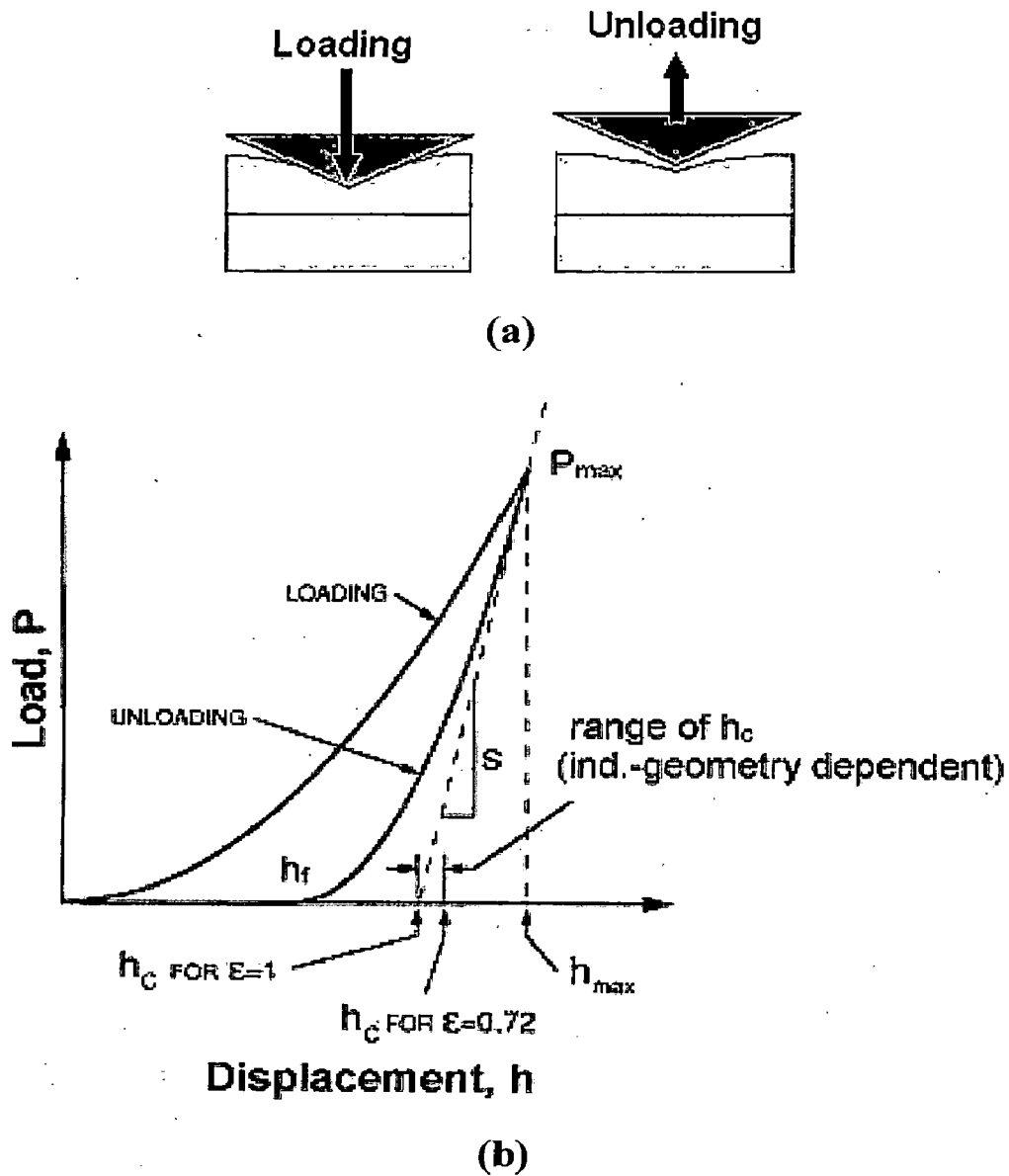


Figure 2.17: (a) Loading and unloading of the indenter on the sample
 (b) Load is plotted against the Displacement

From Sneddon's solution for a conical indenter, h_s becomes

$$h_s = \frac{(\pi - 2)}{\pi} (h - h_f) \quad (2.11)$$

where, h_f is the final depth upon unloading the indenter. The quantity $(h - h_f)$ appears rather than h by itself since Sneddon's solution applies only to the elastic component of the displacement.

Sneddon's contact solution (Sneddon 1965) predicts that the unloading data for an elastic contact for many simple indenter geometries (sphere, cone, flat punch and paraboloids of revolution) follows a power law that can be written as follows:

$$P = \alpha h^m \quad (2.12)$$

where, P is the indenter load, h is the displacement and α and m are constants.

Oliver and Pharr apply this formulation (**Equation 2.12**) to determine the contact area at maximum load as it is valid even if the contact area changes during unloading. To do this, they derived the following relationship for the contact depth from Sneddon's solutions. The contact depth h_c is expressed as

$$h_c = h_{\max} - \varepsilon \frac{P_{\max}}{S} \quad (2.13)$$

where, S is stiffness constant and equal to dP/dh , i.e derivative of a power law fit to the unloading curve and evaluated at the maximum load, P_{\max} , h_{\max} is the maximum depth, and ε refers to tip shape constant and is equal to 0.72 for a conical indenter, 0.75 for parabolic indenter and 1 for a flat indenter. The procedure for Oliver and Pharr analysis includes a fitting of power law function to the unloading segment. This yields the contact stiffness as slope of this function at maximum load. This slope in addition to the appropriate value of ε is used in order to determine the actual contact depth so that it is

finally possible to derive the elastic modulus and the hardness. To find the hardness, a measure of the indentation area is needed. A convenient way to do this is to use the projected contact area at maximum load. The area function for a perfect Berkovich tip is given as

$$Af(h_c) = 24.56h_c^2 \quad (2.14)$$

In the nanoindentation analysis, the hardness is calculated by utilizing the contact area at maximum load and the equation is given as

$$H = \frac{P_{\max}}{Af(h_c)} \quad (2.15)$$

Both values, elastic modulus as well as hardness, depend strongly on the area function $Af(h_c)$ and the accuracy with which it is determined.

The reduced elastic modulus (E_r) is calculated from

$$E_r = \frac{1}{\beta} \frac{\sqrt{\pi}}{2} \frac{S}{\sqrt{Af(h_c)}} \quad (2.16)$$

where β is a constant or correction factor related to the tip geometry and equals to 1, 1.034 and 1.012 for spherical tip, Berkovich tip and Vickers tip, respectively (Oliver *et al.* 2004).

The elastic modulus of the sample can be derived from the following equation.

$$\frac{1}{E_r} = \frac{(1-\nu^2)}{E} + \frac{(1-\nu_i^2)}{E_i} \quad (2.17)$$

where, E & ν are the elastic modulus and Poisson's ratio, respectively, for sample and E_i & ν_i are the elastic modulus and Poisson's ratio, respectively, for the indenter. For a diamond indenter tip, E_i is 1140 GPa and ν_i is 0.07 (Oliver *et al.* 2004).

2.3.6 ANSYS

ANSYS is a finite-element analysis (FEA) package used widely in industry to simulate the response of a physical system to structural loading, thermal and electromagnetic effects. ANSYS uses the finite-element method to solve the underlying governing equations and the associated problem-specific boundary conditions. It is an extremely popular, class-leading modular suite of FEA software used across a broad spectrum of industries. Its open and flexible simulation solutions provide a common platform for fast, efficient and cost-effective product development, from design concept to final-stage testing and performance validation. It is extensively used in the analysis of structural, thermal, dynamic, electromagnetic and fluid-flow in 2D and 3D models. Complementary modules include design optimization, fatigue analysis, and geometry generation capabilities.

The basic idea in the finite element analysis is to find the solution of a complicated problem by replacing it by a simpler one but as the actual problem is replaced by a simpler one, we will be able to find only an approximate solution rather than the exact solution. The existing mathematical tools will not be sufficient to find the exact solution of most of the practical problems. Thus, in the absence of any other convenient method to find even the approximate solution of a given problem, the finite element method is most preferred. Moreover, it is possible to improve or refine the approximate solution obtained in FEM analysis with more computational efforts. In the finite element method, the solution of a general continuum problem always follows an orderly step-by-step process. The step-by-step procedure of static structural problem can be stated as follows (Rao 2004):

- a) **Discretization of the structure:** The first step in the finite element method is to divide the structure or solution region into subdivisions or elements called finite elements. The number, type, size and arrangement of the elements ought to be decided. These elements are interconnected at specified joints called nodes or nodal points. The nodes usually lie on the element boundaries where adjacent elements are connected.
- b) **Selection of a proper interpolation or displacement model:** Since the displacement solution of a complex structure under any specified load conditions cannot be predicted exactly, some suitable solution within an element is assumed to approximate the unknown solution. The assumed solution must be simple from a computational point of view.
- c) **Derivation of elements stiffness matrices and load vectors:** From the assumed displacement model, the stiffness matrix $[K^{(e)}]$ and the load vector $\bar{P}^{(e)}$, of element e are constructed using either equilibrium conditions or a suitable variational principle.
- d) **Assemblage of element equations to obtain the overall equilibrium equations:** Since the structure is composed of several finite elements, the individual element stiffness matrices and load vectors need to be assembled in a suitable manner and the overall equilibrium equations have to be formulated as

$$[K] \underline{\phi} = \underline{\bar{P}} \quad (2.18)$$

where, $[K]$ is called the assembled stiffness matrix, $\underline{\phi}$ is the vector of nodal displacements and $\underline{\bar{P}}$ is the vector of nodal forces for the complete structure.

e) **Solution for the unknown nodal displacements:** The overall equilibrium equations are modified to account for the boundary conditions of the problem. After the incorporation of the boundary conditions, the equilibrium equations can be expressed as

$$[K]\vec{\phi} = \vec{P} \quad (2.19)$$

For linear problems, the vector $\vec{\phi}$ can be solved very easily. But for nonlinear problems, the solution has to be obtained in a sequence of steps, each step involving the modification of the stiffness matrix $[K]$ and/or the load vector \vec{P} .

f) **Computation of element strains and stresses:** From the known nodal displacements $\vec{\phi}$, if required, the element strains and stresses can be computed by using the necessary equations of solid or structural mechanics.

Chapter 3

Synthesis and Characterization of Titanium Films

3.1 Magnetron sputtered Ti films on Silicon substrate

In this section, the morphology and textures of Ti films deposited on Silicon substrate are discussed.

3.1.1 Introduction

Titanium (Ti) exhibits high mechanical strength, excellent thermal stability, good corrosion resistance in extreme conditions and intrinsic biocompatibility. It finds extensive use for the structural and functional applications, especially in biomedical, aerospace, and microelectronics industries [Boyer 1996, Shoesmith *et al.* 1997(a, b), Textor *et al.* 2001, Jeyachandran *et al.* 2006]. The properties of Ti thin films deposited by physical vapor deposition techniques are heavily dependent on their microstructural characteristics such as grain morphology, density, textures, and porosity. It is possible to tailor the properties of Ti films through the nanoscale features of the grains achievable by accelerating the nucleation kinetics during the sputtering process. Therefore, it is very essential to understand the influence of process parameters on the microstructural characteristics of the Ti thin films to further enhance their properties in the actual applications (Jung *et al.* 2003, Cai *et al.* 2005, Jeyachandran *et al.* 2006). Ti thin films with the enhanced strength, biocompatibility and adhesion behavior could be better substitute for Ti based nitride coatings used in the biomedical applications. The chemical and structural characteristics of Ti coatings were investigated in the earlier work (Iida 1990, Ogawa *et al.* 1991).

The Ti thin films processed by magnetron sputtering and grid attached magnetron sputtering were investigated and the formation of (100) and (002) preferred orientations of the grains in the Ti films was reported, with increase in bias voltage, in these two

temperature. The application of bias voltage has damaged the crystallinity and developed the (01 $\bar{1}$ 0) and (01 $\bar{1}$ 1) orientations although the smooth surface and dense morphology was obtained at a moderate bias voltage in their work. The DC magnetron sputtered Ti films deposited on TiNi shape memory were characterized by SEM and observed that the films exhibits uniform thickness morphology and adherent to the substrate (Sonoda *et al.* 2004).

The surface morphology of the titanium films has gradually changed from the structure consisting of fine particles to that of fine fibers with increase in substrate temperature. XRD analysis of the films showed the presence of α -titanium phase with the (002) orientation increasing up to the substrate temperature of 320°C. However, the (011) orientation gets increased while the (002) orientation diminished at a higher temperature range. The fine particles yielded the (002) peak while the fine fibers yielded the (011) peak (Sonoda *et al.* 2004). Ko *et al.* (1999) have investigated the microstructural features of Ti films formed, on p-type (001) single crystal Si wafer, by the ionized sputtering process and revealed the formation of the less strong (002) textures in the films, without the substrate bias, when compared to collimated sputtering. The residual stress and structural characteristics of Ti films on glass substrates deposited by planar magnetron sputtering were carried out by Savaloni *et al.* (2004) and they reported that the grain size increase was dependent on the substrate temperature and film thickness. The films exhibited (100) preferred orientation as observed in their work. The surface structure and composition of flat Ti thin films, deposited by e-beam evaporation technique, on glass substrate were characterized by AFM and XPS respectively (Cai *et al.* 2005). A direct linear relationship between surface roughness and evaporation rate was observed using AFM characterization. The

films with larger grains are correlated with root mean square surface roughness. Vijaya *et al.* (1996) have characterized the bias assisted magnetron sputtered Ti films on glass substrates by XRD and TEM and observed the reduction in grain size of the films with increasing bias voltage. They observed the fcc phase transformation in Ti thin films from its SAED patterns and it was attributed to the formation of oxide phase due to presence of trace amounts of water vapor or residual gases during deposition.

Jeyachandran *et al.* (2006) characterized DC magnetron sputtered Ti thin films on Si (100) substrates by using XRD, SEM, spectroscopic ellipsometry technique. The films were found to be uniform, void free and dense morphology. Its preferred orientation was (0002), from the XRD study, at the 100-150W cathode power. The Ti films deposited using pulsed magnetron sputtering were characterized in terms of optical properties, microstructure, and mechanical properties by Henderson *et al.* (2003). They reported the formation of smooth film morphology and heavily pitted surface at the frequencies of 100 kHz and 350 kHz, respectively. The effect of bias power on the growth morphology of Ti films prepared by RF magnetron sputtering was studied by Martin *et al.* (1998) and they observed the cleaning action, knocking, and resputtering of the forming film, for the weak bias, intense bias (300 W), and above 300 W, respectively. The films composed of spherical nodules of about 60 to 80 nm in diameter, which are coalescent and distinguishable under the deposition conditions without bias power.

The influence of various process parameters such as substrate temperature, pressure and power on the morphological features of Ti films needs to be thoroughly understood for its superior performance and reliability in the actual device applications. Owing to this view, the

present work has been focused to produce Ti films on Si substrate by DC Magnetron Sputtering at different substrate temperatures and characterize their microstructural features by XRD, FE-SEM/EBSD and AFM.

3.1.2 Experimental Details

3.1.2.1 Synthesis of Ti films

The Ti films were deposited by DC magnetron sputtering on Silicon (100) substrates from a 99.99% pure titanium target (2" diameter & 5mm thick). The substrate was cleaned by first rinsing in Hydrofluoric acid to remove SiO₂ layer and then ultrasonic baths of acetone and methanol and finally dried under nitrogen gas. The base pressure was better than 2×10^{-6} Torr and the sputtering were carried out in an Argon atmosphere. The ambient argon gas pressure was kept at 10 mTorr for all depositions. Before starting the actual experiment, the target was pre-sputtered for 15 minutes with a shutter located in between the target and the substrate. This shutter was used to control the deposition time. The target-substrate distance was kept at 50 mm and the deposition time was kept constant for all depositions. The sputtering parameters for Ti films with varying substrate temperature are included in **Table 3.1**.

Table 3.1: Sputtering parameters for Ti films with variation of substrate temperature

Target	Titanium
Base Pressure	2×10^{-6} Torr
Gas Used	Argon
Sputtering Pressure	10 mTorr
Deposition Time	2 hours
Sputtering Power	100 W
Substrate Used	Silicon (100)
Substrate Temperature	100-600°C

3.1.2.2 Characterization details

The Ti films were characterized by XRD (Bruker AXS, D8 Advance) with CuK_α (1.54 Å) radiation for the phase identification, grain size measurement, and texture analysis. The excitation voltage and current were set to a 40 kV and 30 mA respectively, in the diffractometer. The scan rate used was 1°/min and the scan range was from 30° to 45°. The grain size of the Ti films was estimated from the Scherrer's formula (Cullity *et al.* 2001), as given in **Equation 3.1**. The grain size t is along the surface normal direction, which is also the direction of the XRD diffraction vector is given by

$$t = \frac{0.9\lambda}{B \cos \theta} \quad (3.1)$$

where, B (crystallite) is the corrected full-width at half maximum (FWHM) of a Bragg peak, λ is the wavelength of X-ray, and θ is the Bragg angle. The grain size is measured using the preferred orientation of XRD peaks obtained for the Ti films on Si substrate. The surface topographical characterizations of the Ti films were obtained from FE-SEM

(FEI, Quanta 200F) at an acceleration voltage of 20 kV. The surface morphology of the Ti films was studied using AFM (NT-MDT, Ntegra) operated in semicontact (tapping) mode and the root-mean-square (RMS) roughness of the surface of the sample was calculated from AFM scan at five different spots for each sample. The electron backscatter diffraction (EBSD) was used to obtain the grain size distribution of Ti films.

3.1.3 Results and Discussion

XRD peaks of Ti films deposited on the Si (100) substrate in Ar atmosphere at different substrate temperatures ranging from 100-600°C are shown in **Figure 3.1(a)**. It was found that the intensity of the (002) reflection of the films increases with increase in the substrate temperature around 200°C. With further increase in temperature above 300°C, the (002) orientation subsides while (101) orientation dominates.

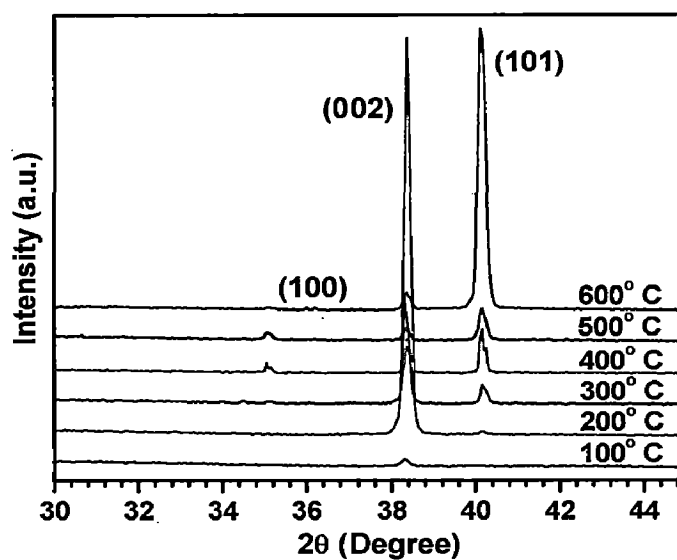


Figure 3.1(a): XRD peaks of Ti films deposited on Si substrate as a function of substrate temperature

With the increase in substrate temperature, the crystallite size also increases as expected from 40.7 nm at 100°C to 57.7 nm at 600°C, however (002) orientation transformed into (101) preferred orientation. The enhanced mobility of adatoms in the film surface with the increase in substrate temperature has favored the formation of (101) orientation of grains. The competition between strain energy and surface free energy affecting the texture of the grains are heavily dependent on the deposition parameters such as substrate temperature, power, sputtering pressure and film thickness. The thermal stress induced in the thin films deposited at higher substrate temperature might have also contributed to the modification of (002) preferred orientation, favoring the formation of (101) grains.

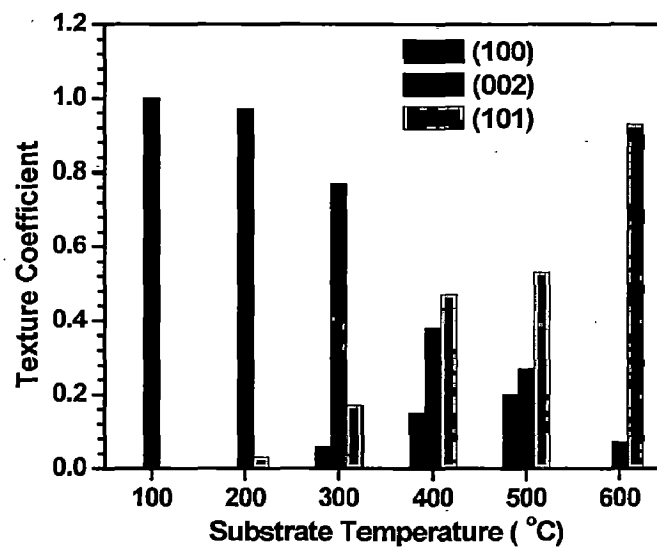


Figure 3.1(b): Texture coefficients of Ti films deposited on Si substrate as a function of substrate temperature

The texture coefficients of Ti films as a function of substrate temperature were calculated from its XRD peaks using the following formula (Huang *et al.* 2005b) and shown in **Figure 3.1(b)**.

$$\text{TextureCoefficient} = \frac{I(hkl)}{[I(100) + I(002) + I(101)]} \quad (3.2)$$

where, h, k, l are planes and represents (100) or (002) or (101) orientation.

The texture coefficients of (002) and (101) orientation are high as compared to other orientations in the Ti films deposited under Ar atmosphere. It is clear that the higher substrate temperature influences the observed changes in textures.

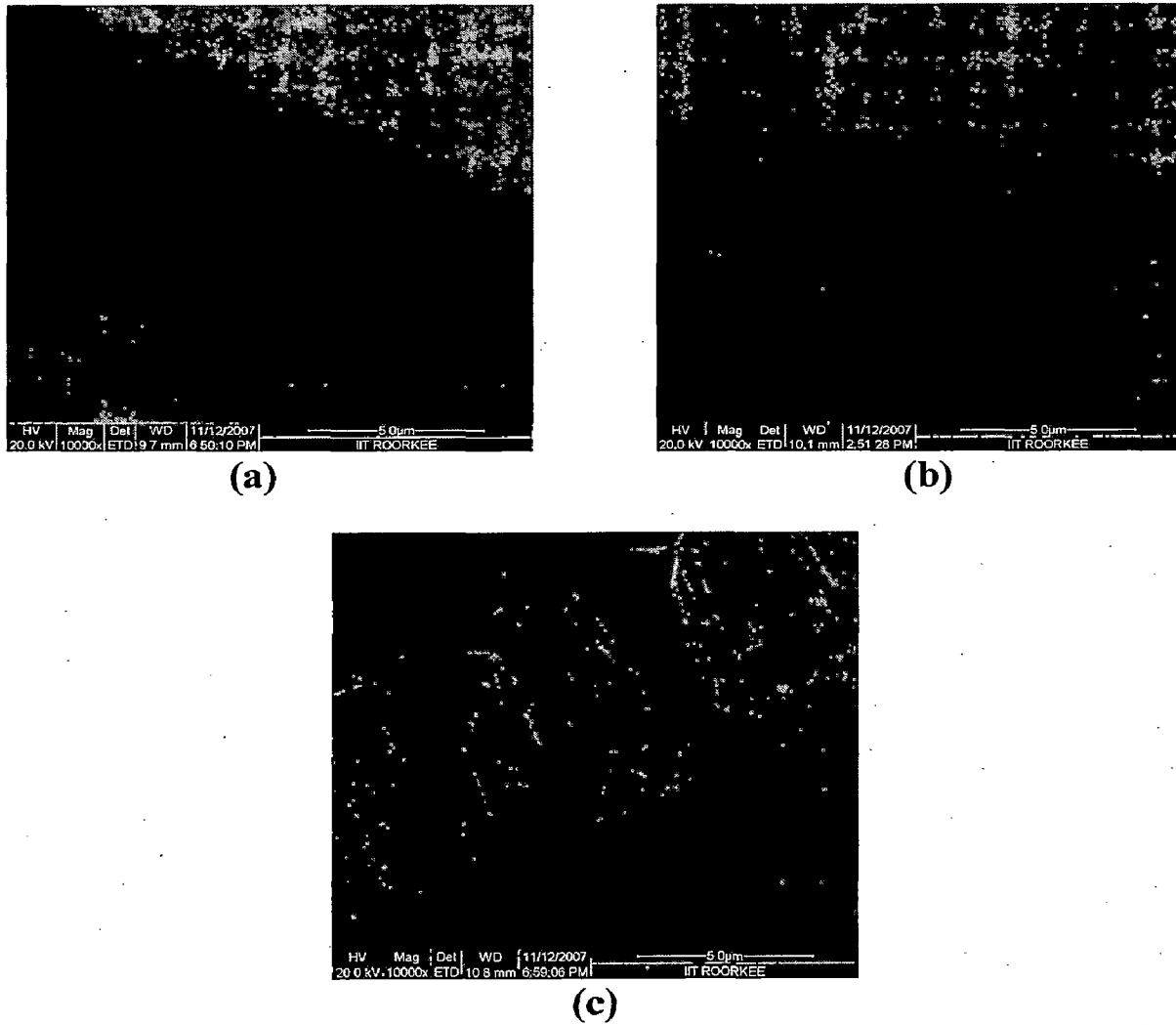
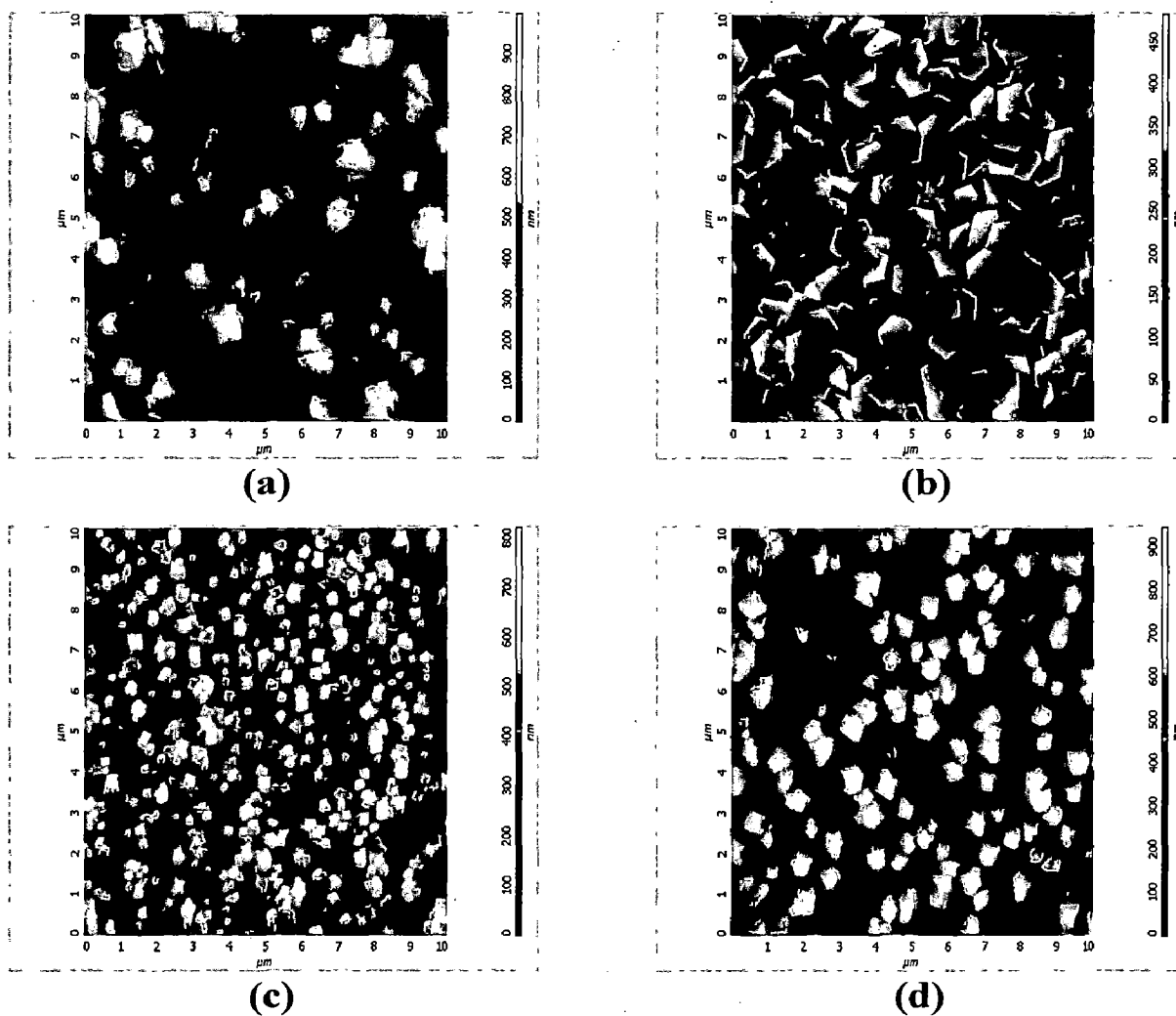


Figure 3.2: Cross sectional view of Ti films on Si substrate deposited at substrate temperature (a) 200°C, (b) 400°C and (c) 600°C

The thickness of the Ti films was measured by taking cross sectional view of Ti films by FE-SEM and it was around $6.0\ \mu\text{m}$ of all the samples. **Figure 3.2** shows the cross sectional view of Ti film deposited at 200°C , 400°C and 600°C .

Atomic force microscopy was used to study the surface topography of Ti films. **Figure 3.3** shows the AFM images of the Ti samples deposited at substrate temperature ranging from 100°C to 600°C respectively.



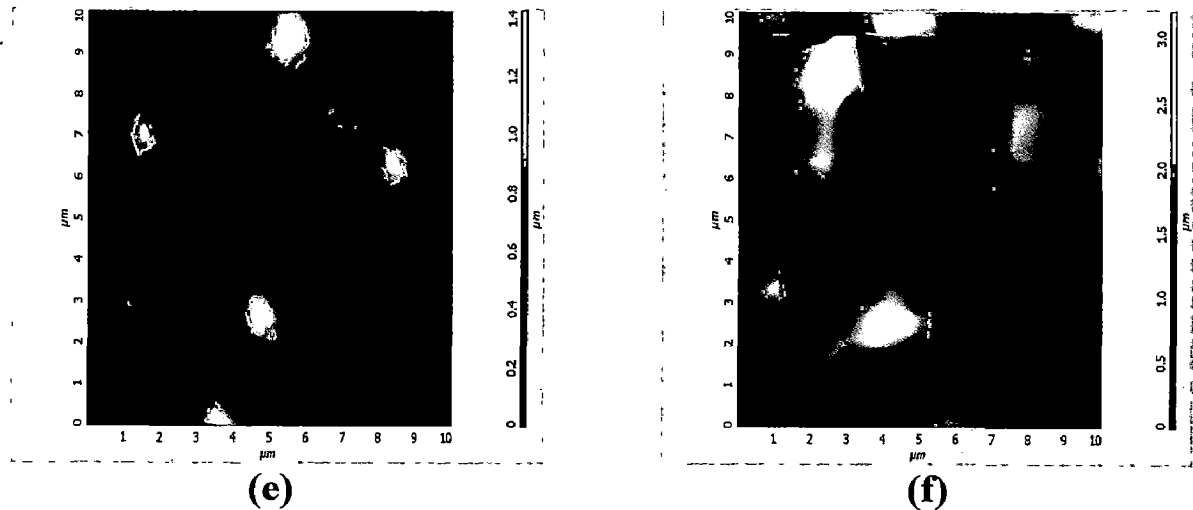


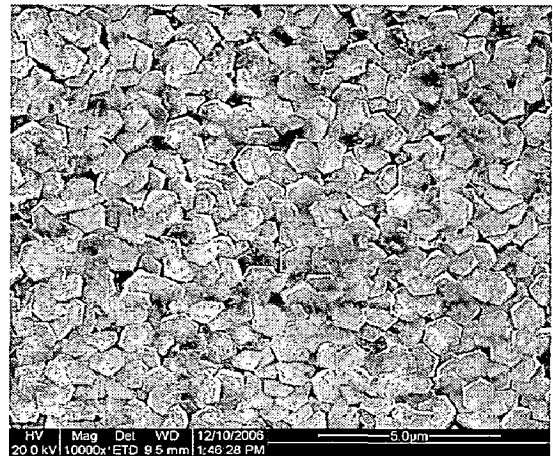
Figure 3.3: AFM images of Ti films on Si deposited at substrate temperature (a) 100°C, (b) 200°C, (c) 300°C, (d) 400°C, (e) 500°C and (f) 600°C

It can be clearly seen from the images that up to the substrate temperature of 200°C, the grains are of two-dimensional hexagonal structure and with further increase in the substrate temperature, the grain size increases and it transforms into three-dimensional hexagonal structure. The anisotropic grain growth, thermal stress and texture of the grains are responsible for evolution of three-dimensional hexagonal structures at higher substrate temperature (600°C). The anisotropic grain growth may occur in Ti thin films due to the factors such as preferred orientation of the grains, orientation dependent grain boundary mobility and grain boundary free energy, and residual stress.

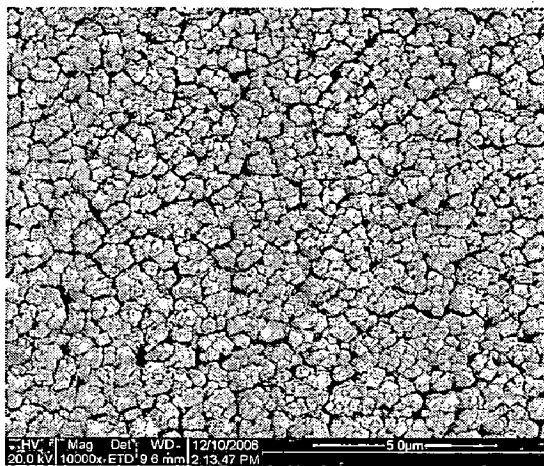
Figure 3.4 shows the FE-SEM images of the Ti films deposited at substrate temperature ranging from 100°C to 600°C, respectively. The formations of two and three-dimensional hexagonal structures of the grains in Ti thin films are evident from this FE-SEM micrograph.



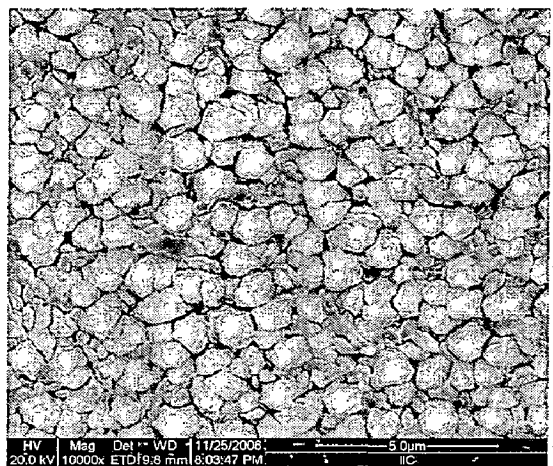
(a)



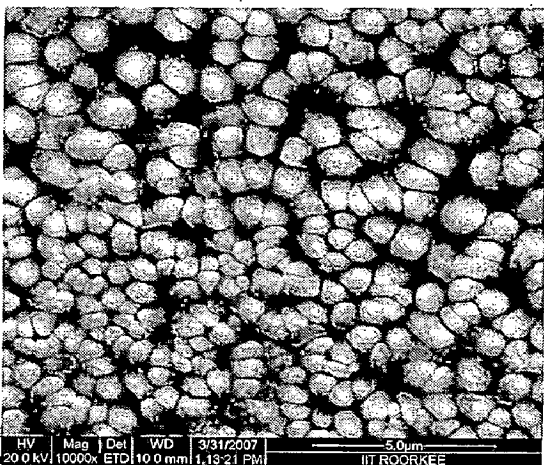
(b)



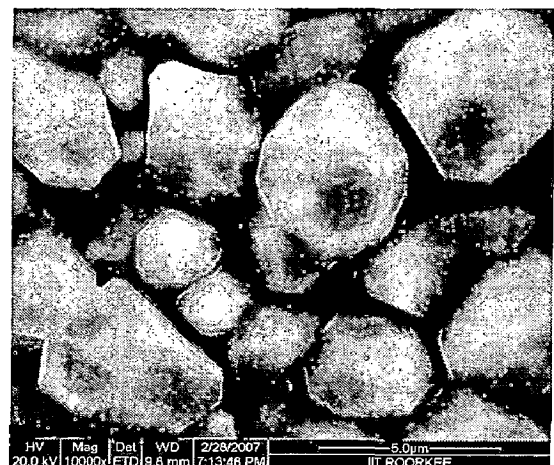
(c)



(d)



(e)



(f)

Figure 3.4: FE-SEM images of Ti films on Si deposited at substrate temperature (a) 100°C, (b) 200°C, (c) 300°C, (d) 400°C, (e) 500°C and (f) 600°C

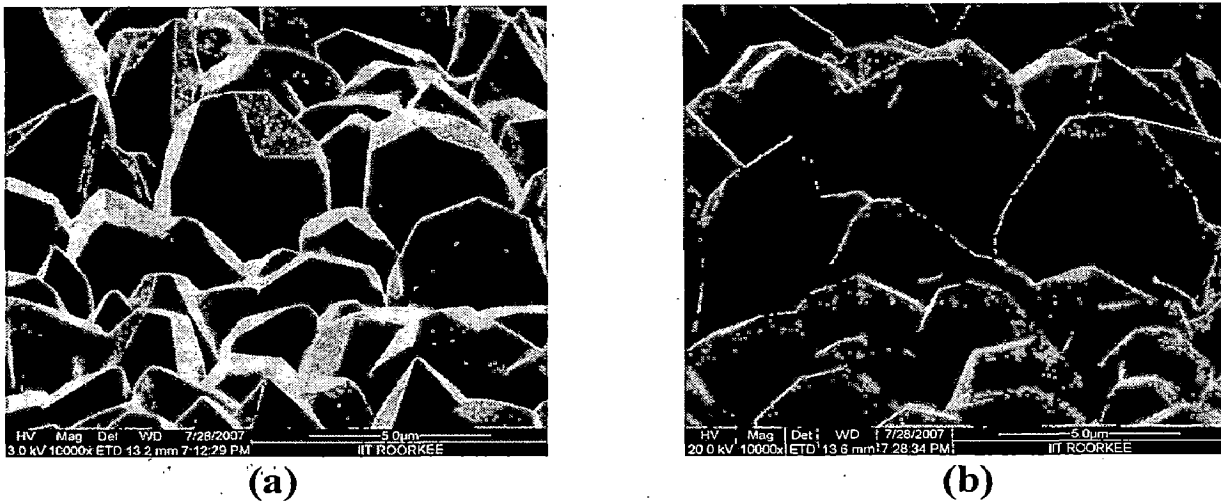
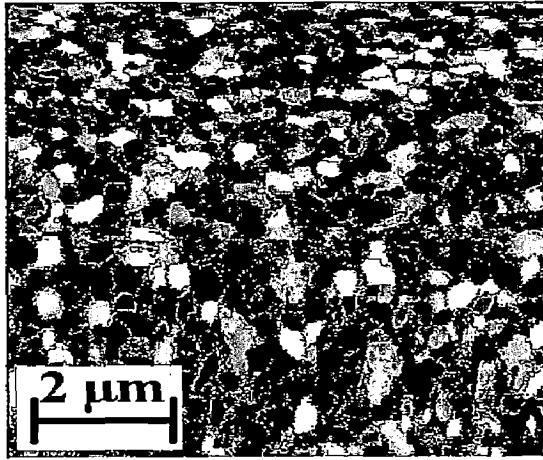
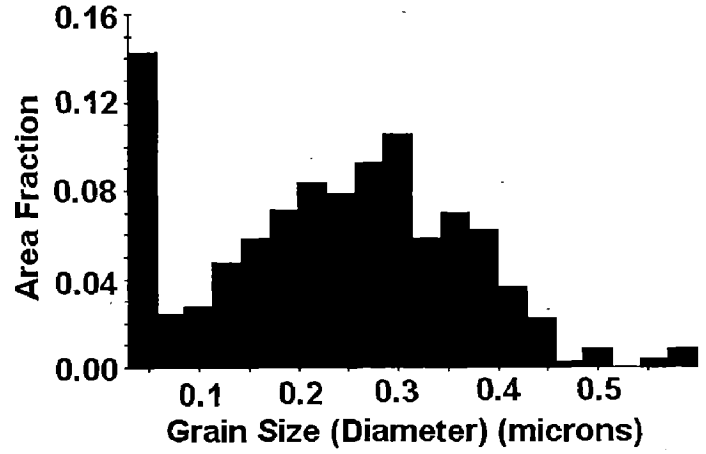


Figure 3.5: Tilted FE-SEM images of Ti films on Si deposited at substrate temperature 600°C (a) HV = 3 kV and (b) HV = 20 kV

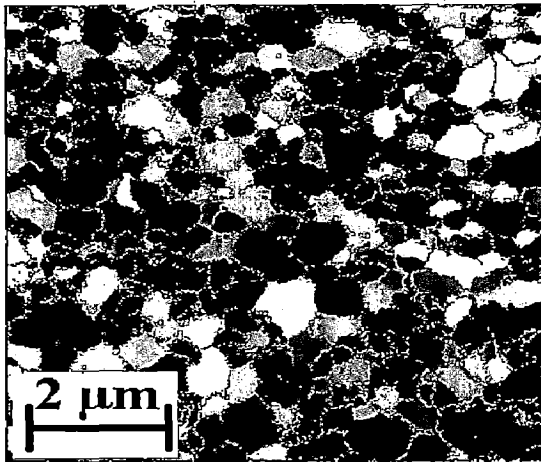
Figure 3.5 shows the 60° tilted FE-SEM images of Ti films deposited at substrate temperature 600°C and these images were taken at two different acceleration voltages i.e. 3 kV and 20 kV. At 3 kV, due to the less signal, the image gives different shades that confirms the three dimensional hexagonal structure. The shades have disappeared when the acceleration voltage increased up to 20 kV. EBSD has been used to obtain the grain size distribution of the Ti thin films deposited at substrate temperature ranging from 100°C to 600°C. To obtain best EBSD patterns, the imaging conditions in the FE-SEM were optimized through tilting the sample and adjusting the working distance so that the higher interaction volume was realized. For EBSD measurement, areas of $12 \times 12 \mu\text{m}^2$ was selected and approx. 4,50,000 measurement points were collected in a file for the analysis. The surface map of Ti in **Figure 3.6(a, c and e)** shows the orientation of the grains in the chosen area of the sample.



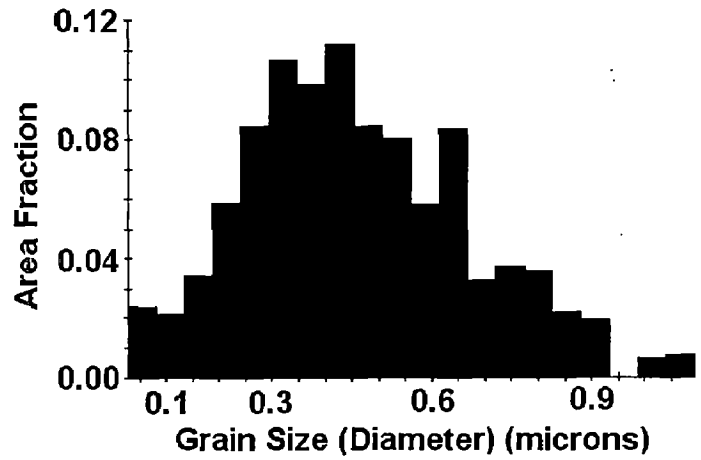
(a)



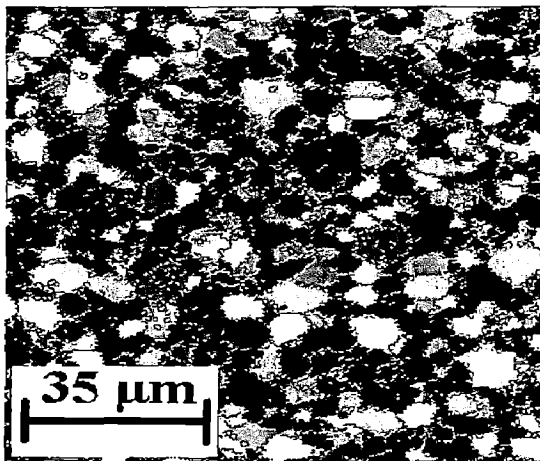
(b)



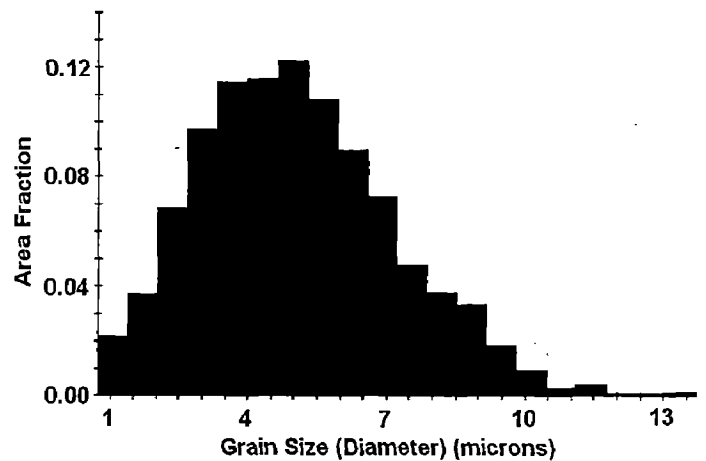
(c)



(d)



(e)



(f)

Figure 3.6: Orientation map of the measurement area and grain size variation as a function of area fraction of Ti films deposited on Si at substrate temperature (a-b) at 200°C, (c-d) at 400°C and (e-f) 600°C

The orientation of each grain is described by the three Euler angles and characterized by a distinct color. The values of the Euler angles are coded by different intensities of the fundamental colors red, green and blue. The superposition of these components results in the color associated with the orientation of the grain (Wolf *et al.* 2002). The EBSD results of Ti thin films showed the increase in grain size with increase in substrate temperature and they are in tandem with that of the analyses made by XRD and AFM. The average grain size by EBSD is 0.23 μm , 0.46 μm and 3.47 μm at 200°C, 400°C and 600°C respectively. **Figure 3.6 (b, d and f)** shows the grain size variation as a function of area fraction at substrate temperature 200°C, 400°C and 600°C respectively. The uniform grain size distribution is observed for the films grown at 200°C and 400°C. The increase in grain size is due to higher driving force associated with grain boundary free energy of the films formed at higher substrate temperature. The grain growth of Ti thin films occurs due to the enhanced mobility of adatoms in the grain boundaries at higher temperature. The grain size distribution of Ti films at higher substrate temperature (600°C) observed in the present work is not uniform due to the anisotropic grain growth of the thin films, which is influenced by texture of the grains. According to Thompson (2000), abnormal grain growth in thin films can occur when the growth of subpopulation of grains (preferred grains) is favored due to the minimization of surface and interface energy or strain energy minimization. However, the anisotropic grain growth is not pronounced in the thin films up to the substrate temperature of 200°C.

3.1.4 Conclusion

The morphological characteristics of Ti films deposited on Si (100) substrates at different substrate temperatures were investigated in the present work. The Ti film

showed a (002) preferred orientation and its intensity increases with increase in the substrate temperature around 200°C. At above 300°C, the (101) preferred orientation has increased while (002) orientation decreased. The FE-SEM analysis of the Ti films, deposited in Ar atmosphere revealed two and three-dimensional hexagonal structure of grains depending upon the substrate temperature. The increase in grain size of Ti thin films with increasing substrate temperature was confirmed by XRD, FE-SEM/EBSD and AFM. The grain size distribution is uniform for the films deposited at 200°C and 400°C but it transforms into non-uniform distribution for the films deposited at 600°C. The anisotropic grain growth observed at higher substrate temperature is due to the texture of the grains.

3.2 Magnetron Sputtered Ti films on Glass substrate

3.2.1 Introduction

It is very essential to study the systematic investigation and quantification of the influence of process parameters such as sputtering power and sputtering pressure on the texture and microstructural features of Ti thin films for enhancing its strength and adhesion in biomedical and microelectronics applications. Owing to these facts, the present work has been focused to deposit Ti films, using different process parameters, on glass substrate by DC Magnetron Sputtering and characterize their microstructural features by XRD, FE-SEM and AFM.

3.2.2 Synthesis of Ti films

The Ti films were deposited by DC magnetron sputtering onto glass substrates using a 99.99% pure titanium target (2" diameter & 5mm thick). The substrate is a microscope glass slide, which is cleaned by rinsing in ultrasonic baths of acetone and methanol and dried under nitrogen gas. The procedures adopted for deposition of Ti films on glass substrate were similar as discussed earlier in the **Section 3.1.2.1**. The sputtering parameters for Ti films with variation of sputtering power, substrate temperature and sputtering pressure are included in **Table 3.2**.

Table 3.2: Sputtering parameters for Ti films with variation of sputtering power, substrate temperature and sputtering pressure

Sputtering Parameters	SET I	SET II	SET III
Target	Titanium	Titanium	Titanium
Base Pressure	2×10^{-6} Torr	2×10^{-6} Torr	2×10^{-6} Torr
Gas Used	Argon	Argon	Argon
Sputtering Pressure	10 mTorr	10 mTorr	5-20 mTorr
Deposition Time	2 hours	2 hours	2 hours
Sputtering Power	50-150 W	50 W	50 W
Substrate Used	Glass	Glass	Glass
Substrate Temperature	100°C	100-500°C	100°C

3.2.3 Results and Discussion

The XRD graphs of Ti films deposited at varying sputtering power, substrate temperature and sputtering pressure are plotted in **Figure 3.7(a), (b) and (c)** respectively. In case of varying sputtering power, it is observed that initially the Ti film exhibit (100) preferred orientation [**Figure 3.7(a)**] but with increasing power, (002) becomes the preferred orientation. However, with increase in the substrate temperature [**Figure 3.7(b)**], the initial (100) orientation subsides and (101) orientation emerges as the preferred orientation. The XRD results of the Ti films with varying sputtering power may be interpreted on the basis of stress and strain evolution mechanism.

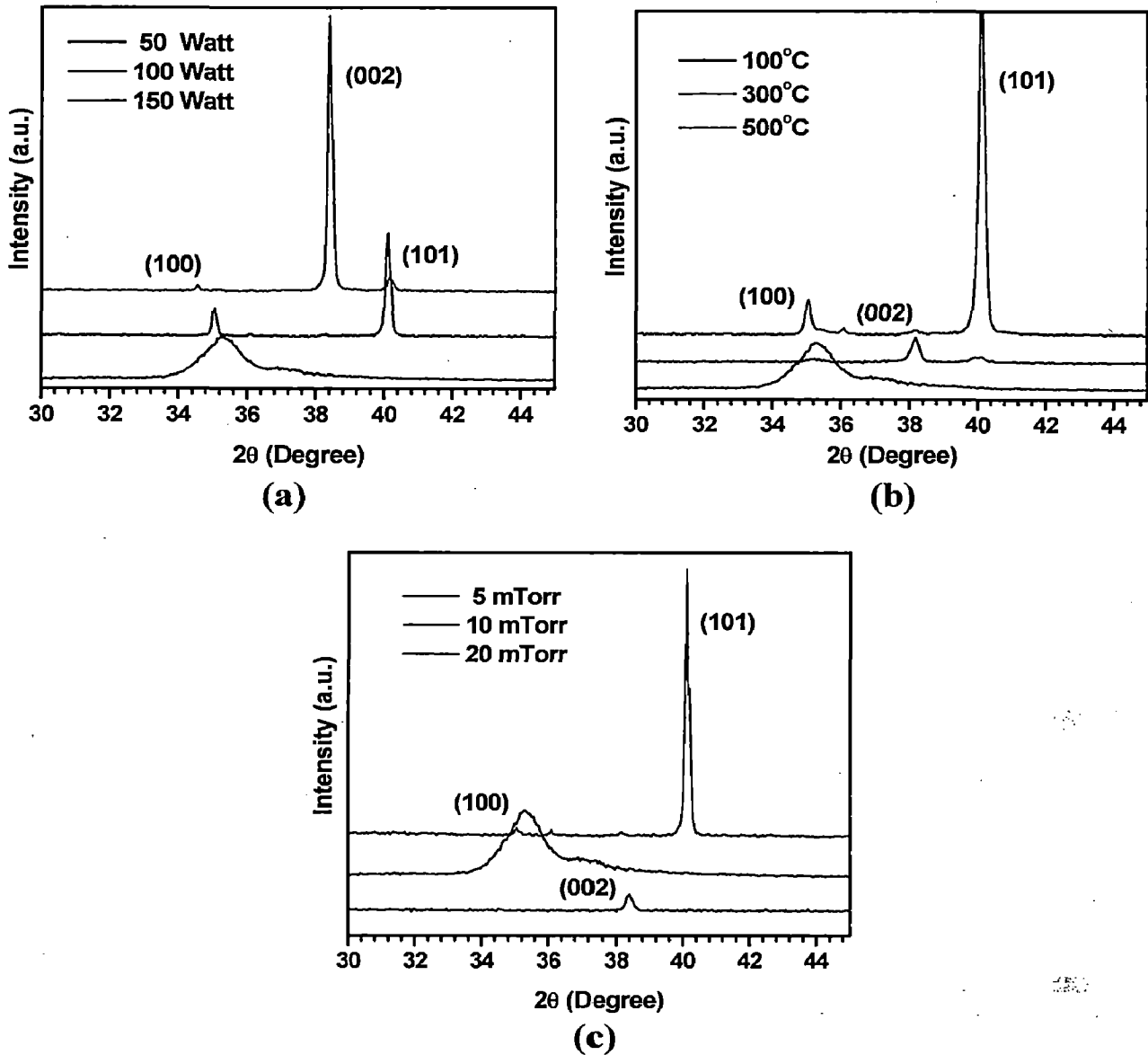


Figure 3.7: XRD graphs of Ti films on glass substrates as a function of (a) sputtering power, (b) substrate temperature and (c) sputtering pressure

The compressive stress induced in the films contributes to the development of (100) orientation and it may have relaxed to tensile mode at higher thickness favoring the (002) preferred orientation. The microstrain from (100) peak of Ti films on glass substrate was calculated by the following equation (Ong *et al.* 2002, Singh *et al.* 2008) and shown in Table 3.3.

$$\alpha = (\sigma - \sigma_o) / \sigma_o \times 100 \quad (3.3)$$

where, σ (a or c) is the lattice parameter of the strained Ti films calculated from XRD data and σ_o (a_o or c_o) is the unstrained lattice parameter of Ti ($a = 2.9512 \text{ \AA}$ and $c = 4.6845 \text{ \AA}$) (Cullity *et al.* 2001). The lattice parameters a and c of Ti films was calculated using the equation (Cullity *et al.* 2001):

$$\frac{1}{d^2} = \frac{4}{3} \frac{(h^2 + hk + k^2)}{a^2} + \frac{l^2}{c^2} \quad (3.4)$$

where, d is the interplanar distance obtained from the position of the (100) peak using the Bragg condition, a and c are the lattice parameters (being hexagonal structure $c/a = \sqrt{8/3}$) and h , k and l are planes. It has been observed that with increasing sputtering power, substrate temperature and sputtering pressure, microstrain was initially negative and then became positive with a corresponding change in crystallite size as shown in **Table 3.3**. It may be mentioned that with increase in power, the deposition rate increases, which in turn increases the thickness of the deposited film (Jeyachandran *et al.* 2007). Similarly, the peak change due to the increase in substrate temperature causes the increase of (101) orientation while the (002) orientation decreased at a higher temperature (Sonoda *et al.* 2004). The higher substrate temperature could facilitate the enhanced mobility of adatoms in the film surface and favored the formation of (101) orientation of grains. It is evident from the **Figure 3.7(c)** that the (002) peak appeared at 5 mTorr has transformed into (101) preferred orientation at 20 mTorr. The competition between strain energy and surface free energy affecting the textures of the grains are dependent on the deposition parameters such as substrate temperature, power and sputtering pressure. The thermal stress induced in the thin films at higher substrate temperature might have also contributed to the modification of (002)

preferred orientation, favoring the formation of (101) grains. The thermal stress of Ti thin films deposited on glass substrate as a function of substrate temperature has been investigated in our earlier work (Chawla *et al.* 2008a) by finite element analysis and observed that the induced thermal stress was due to the higher substrate temperature and thermal expansion mismatch between the films and glass substrate. The induced thermal stress in Ti thin film has also been reported in the literature (Naoe *et al.* 1991, Savaloni *et al.* 2004, Sonoda *et al.* 2004).

The texture coefficients of Ti films on glass substrates as a function of different parameters are calculated from its XRD peaks as shown in **Figure 3.8(a-c)** by using the formula, as given in **Section 3.1.3 (Equation 3.2)**. It is observed from **Figure 3.8(a)** that the texture coefficient of (100) orientation is high, with the sputtering power of 50 W, as compared to other orientations. However, (101) and (002) orientations exhibit higher values of texture coefficient with increasing sputtering power of 100 W and 150 W, respectively. With varying substrate temperature [**Figure 3.8(b)**], the (100) orientation showed a higher texture coefficient at 100°C as compared to other orientations. With increasing temperature, (002) and (101) orientations exhibit a higher texture coefficients at 300°C and 500°C, respectively. It is shown in **Figure 3.8(c)**, with varying sputtering pressure, that the (002) orientation showed a higher texture coefficient at 5 mTorr as compared to other orientations. With increasing pressure, (100) and (101) orientations exhibit a higher texture coefficients at 10 mTorr and 20 mTorr, respectively. The process conditions such as substrate temperature, sputtering pressure and power influence the surface energy and strain energy of grains formed in the thin films.

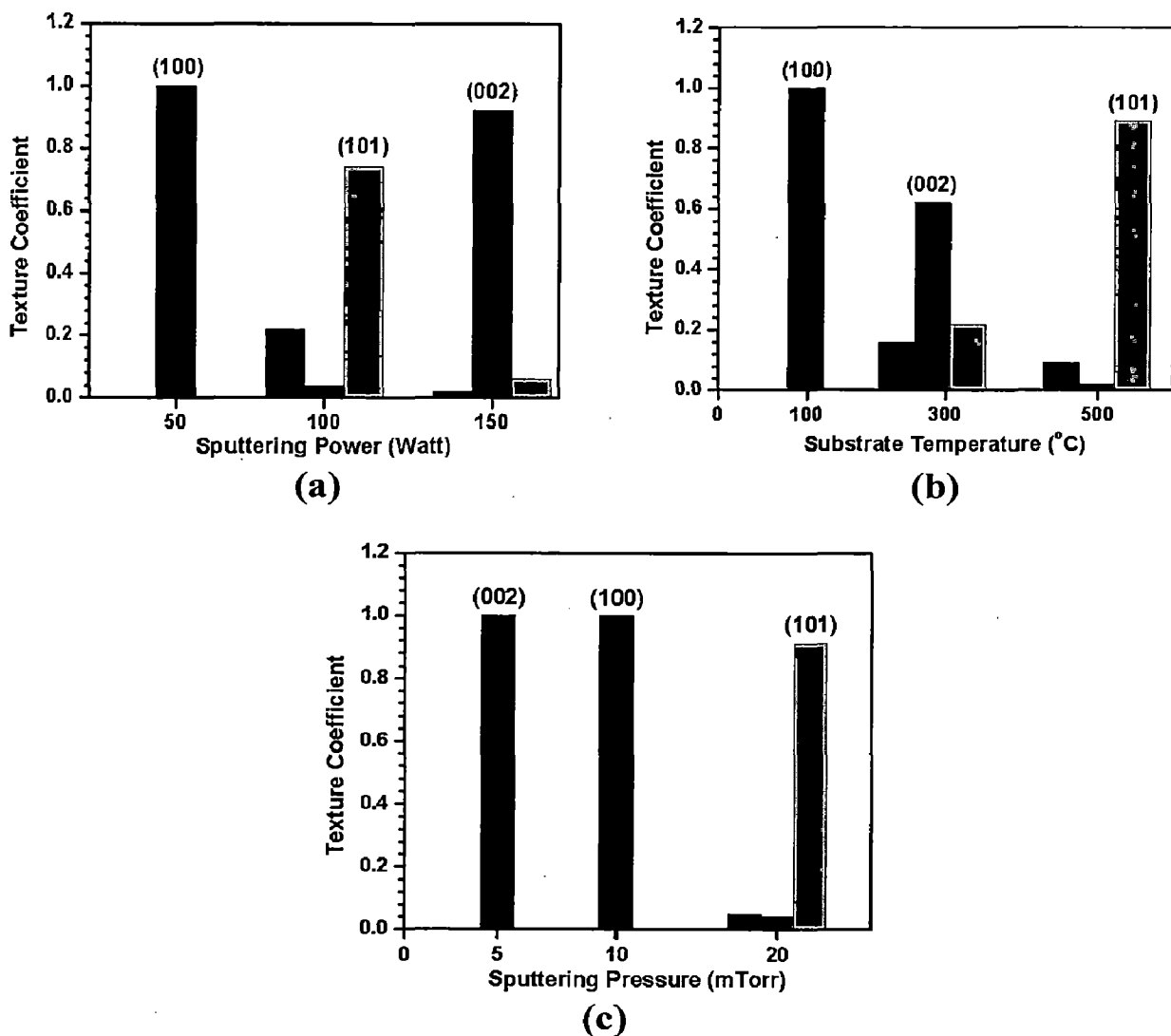
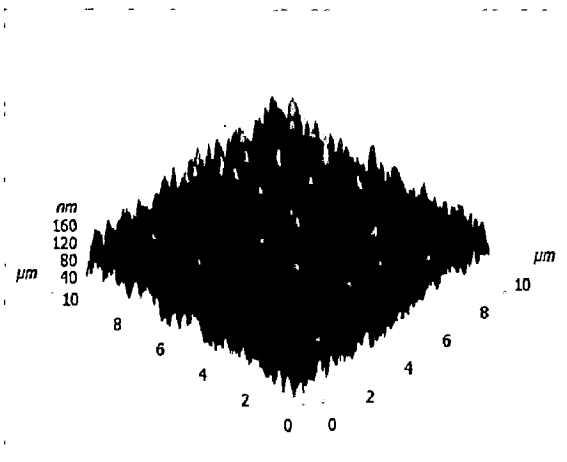


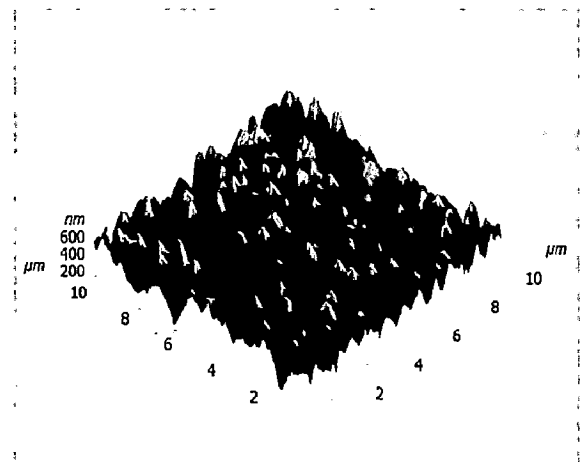
Figure 3.8: Texture coefficients of Ti films on glass substrates as a function of (a) sputtering power, (b) substrate temperature and (c) sputtering pressure

The competition between surface energy and strain energy during film growth might contribute to the changes in texture of the grains as observed in the present work. The influence of substrate temperature on the microstrains of the Ti thin films is evident from the **Table 3.3**. For sufficiently thin films, surface and interface energy minimizing textures are favored but for the thicker films with higher elastic strains, strain energy minimizing textures are formed as reported by Thompson (2000).

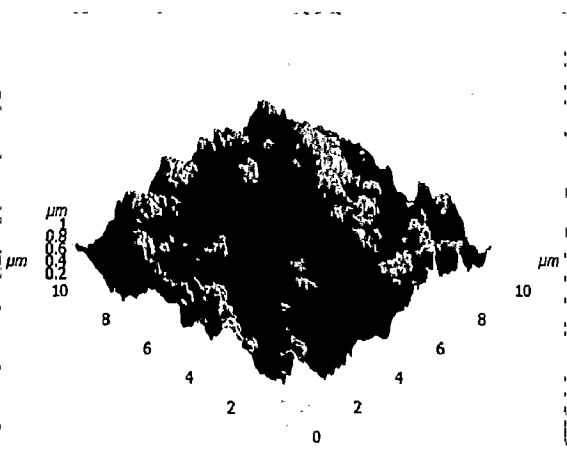
The AFM images of Ti films deposited at varying sputtering power are in **Figure 3.9(a-c)**. The images of Ti films were acquired in a $10 \times 10 \mu\text{m}^2$ area. It is observed the grain size and surface roughness of Ti films increases with increase in sputtering power. The AFM images of Ti films deposited at varying substrate temperature are shown in **Figure 3.9(d-e)**. With increase in substrate temperature, the grain size and surface roughness increases and the morphology of the grains become well crystalline. **Figure 3.9(f-g)** shows the AFM image of the Ti films deposited at sputtering pressure of 5 mTorr and 20 mTorr, respectively. The regular hexagonal crystals are observed for the films deposited at 20 mTorr.



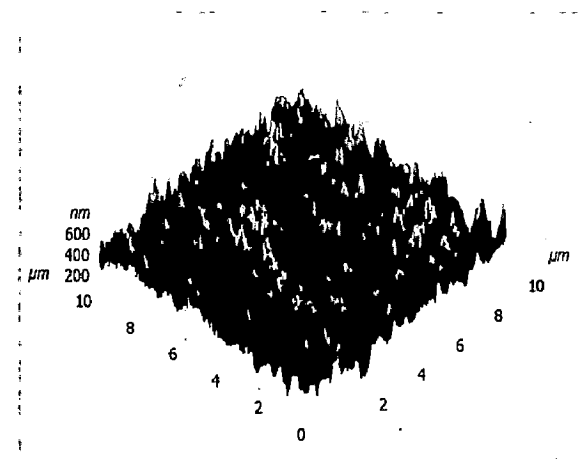
(a)



(b)



(c)



(d)

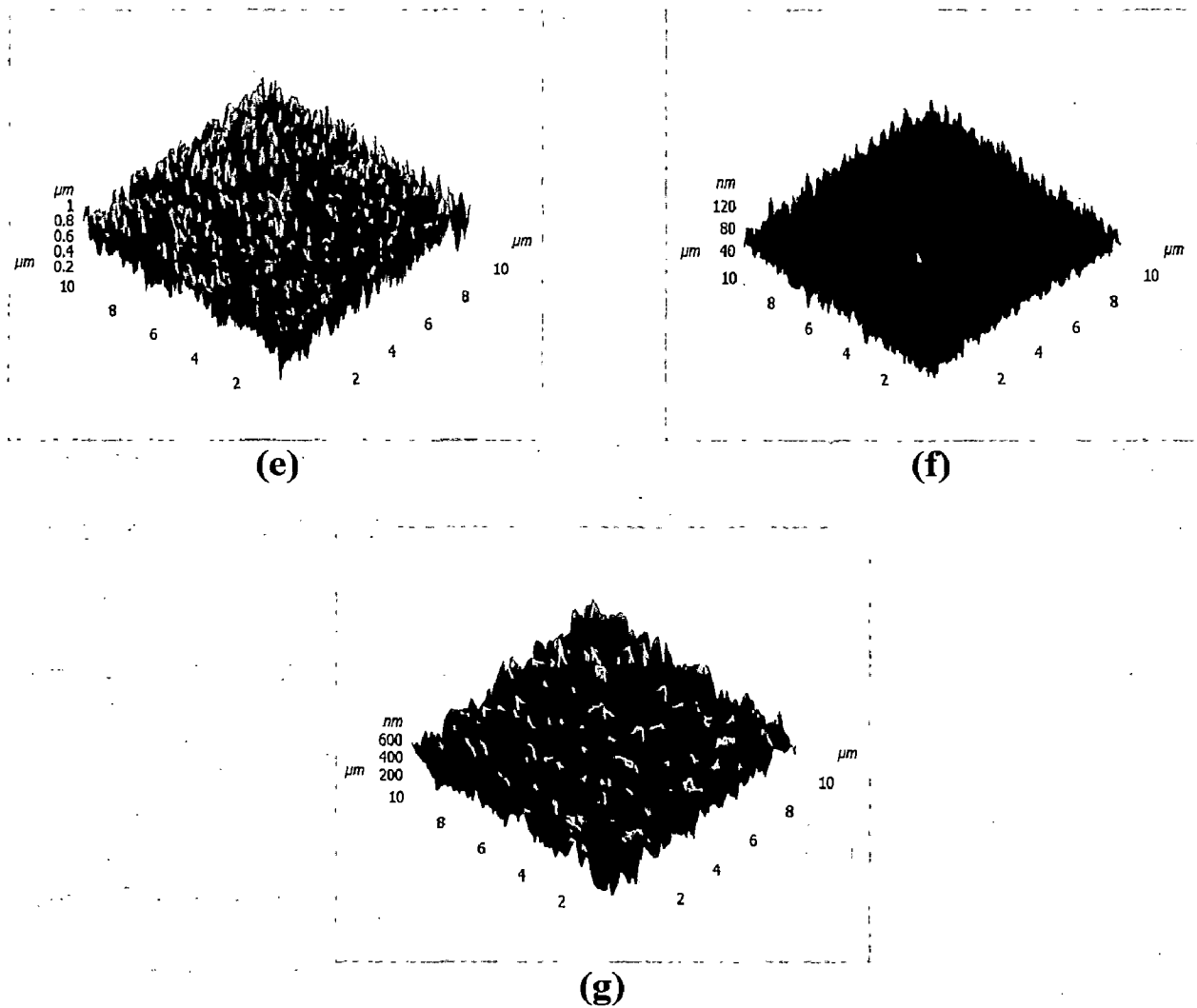


Figure 3.9: AFM images of Ti films on glass substrates as a function of different parameters:

- I) Sputtering Power **(a)** at 50 Watt, **(b)** at 100 Watt and **(c)** at 150 Watt
- II) Substrate Temperature **(a)** at 100°C , **(d)** at 300°C and **(e)** at 500°C
- III) Sputtering Pressure **(f)** at 5mTorr, **(a)** at 10 mTorr and **(g)** at 20mTorr

The surface roughness exhibits an increasing trend with the sputtering pressure. The crystallite size and surface roughness of Ti thin films deposited with varying power, substrate temperature and sputtering pressure are shown in **Table 3.3**. The increase in surface roughness of Ti thin films with higher substrate temperature is due to growth of grains with preferred orientations dictated by surface and grain boundary diffusivity,

adatom mobility, film thickness and induced thermal stress (Naeem *et al.* 1995, Savaloni *et al.* 2004). The effect of sputtering pressure can be explained by the relationship of the mean free path, λ (cm), with the sputtering pressure of the gas as given by

$$\lambda = 2.330 \times 10^{-20} \frac{T}{(P\delta_m^2)} \quad (3.5)$$

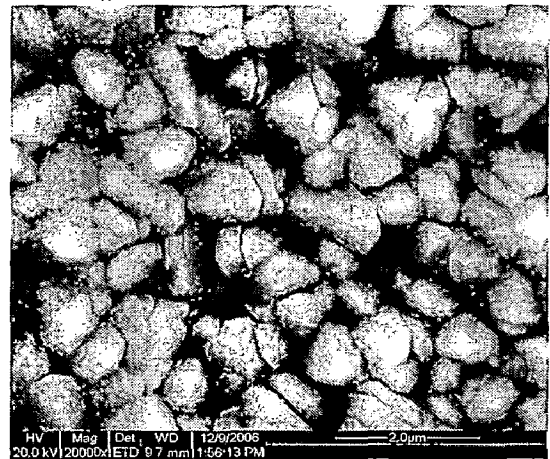
where, T (K) is the temperature, P (Torr) is the sputtering pressure and δ_m (cm) is the molecular diameter (Maissel *et al.* 1970, Chandra *et al.* 2005). According to above equation, when sputtering pressure is high, the mean free path is less so that the sputtered atoms undergo a large number of collisions, as a result, the sputtered atoms have a higher probability of agglomeration i.e. increasing in particle size before arriving at the substrate surface and hence increase in surface roughness of Ti films. With increase in sputtering power, adatom mobility and the deposition rate increases, contributing to growth of crystallite size and higher surface roughness of Ti thin films.

The FE-SEM images of Ti films deposited at varying sputtering power (50 W, 100 W and 150 W), fixed substrate temperature 100°C and sputtering pressure 10 mTorr are shown in **Figure 3.10(a-c)**. With increasing power, the density of the film has increased with lesser fraction of voids due to the higher adatom mobility. **Figure 3.10(d-e)** shows the FE-SEM images of Ti films deposited at varying substrate temperature. The sputtering power and pressure were kept constant at 50 W and 10 mTorr when the substrate temperature was varied from 100 to 500°C. It is evident that with the increase in substrate temperature, the morphology of grain changes and becomes denser due to the higher surface and bulk diffusivity of sputtered atoms. The Ti films deposited at 5

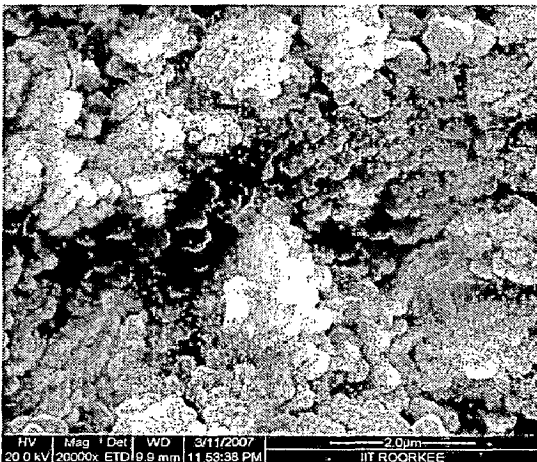
mTorr [Figure 3.10(f)] revealed fine grain morphology as compared to the columnar grains with voids observed for the films deposited at 20 mTorr [Figure 3.10(g)].



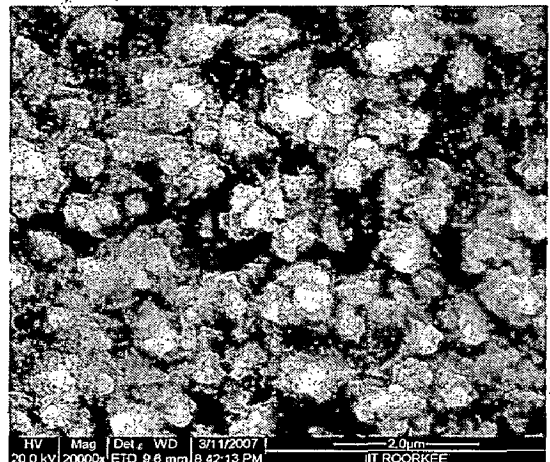
(a)



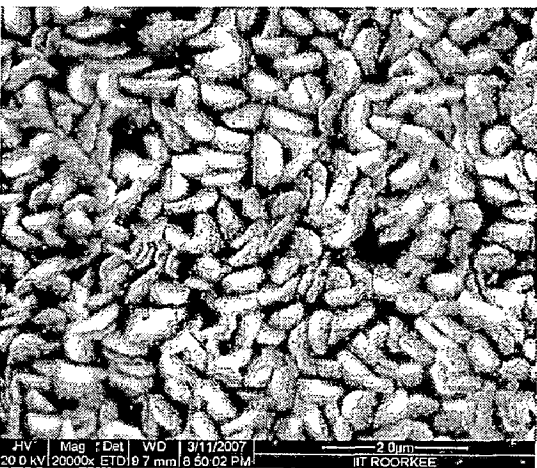
(b)



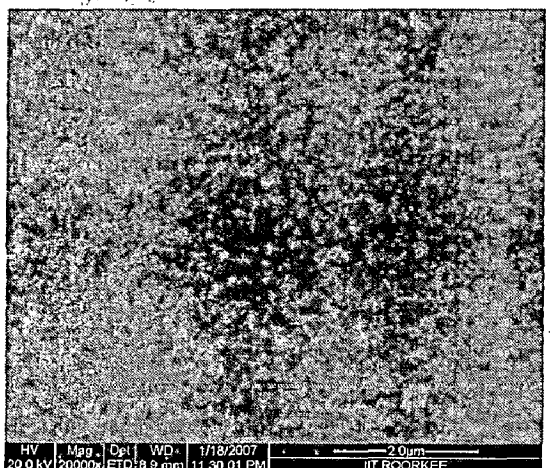
(c)



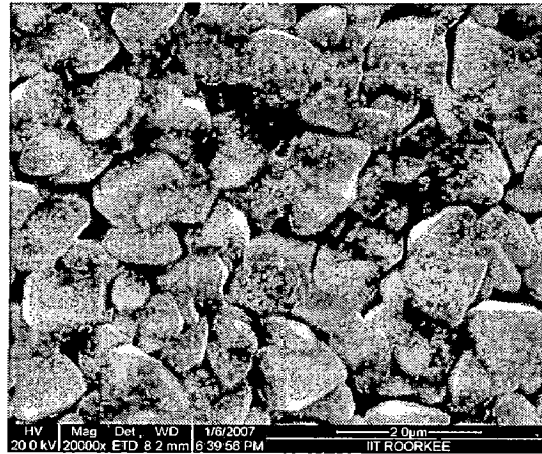
(d)



(e)



(f)



(g)

Figure 3.10: FE-SEM images of Ti films on glass substrates as a function of different parameters:

- I) Sputtering Power (a) at 50 Watt, (b) at 100 Watt and (c) at 150 Watt
- II) Substrate Temperature (a) at 100°C, (d) at 300°C and (e) at 500°C
- III) Sputtering Pressure. (f) at 5mTorr, (a) at 10 mTorr and (g) at 20mTorr

The morphology of Ti thin films deposited under varying sputtering power, substrate temperature and sputtering pressure are in accordance with the structural zone models discussed in the literature (Thornton 1977). For example, Ti films deposited with T_s/T_m ratio 0.06 showed a less dense morphology (Zone I) with the voided grain boundaries [Figure 3.10(b), (g)] but with T_s/T_m ratio of 0.3, density of the films have increased [Figure 3.10(e)]. As discussed in Savaloni *et al.* (2004) work, the increase in substrate temperature ($T_s/T_m > 0.3$) may lead to the denser film.

The thickness of the Ti films was measured by taking cross sectional view of Ti films by FE-SEM and image is shown in Figure 3.11 and the thickness data of all Ti film samples are given in Table 3.3.

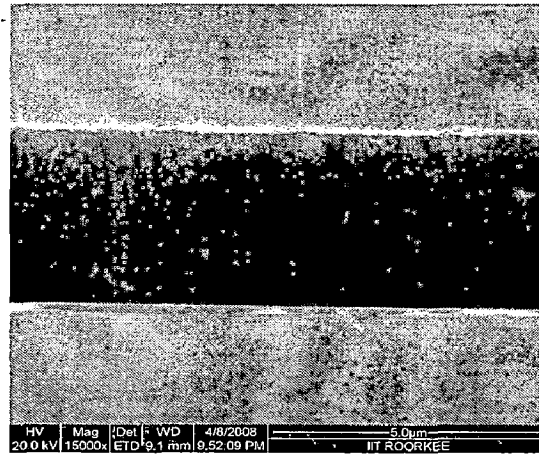


Figure 3.11: Cross section FE-SEM image of Ti film on glass substrate

Table 3.3: The variation of different values of Ti thin films with varying deposition parameters

SET	Parameters	Crystallite size (XRD) (nm)	Average Roughness (AFM) (nm)	Film Thickness (μm)	Micro Strain (100) peak
I)	50 Watt	6.4	23.7	3.12	-0.6777
	100 Watt	46.4	101.6	4.76	0.0745
	150 Watt	52.0	194.9	6.49	0.0895
II)	100°C	6.4	23.7	3.12	-0.6777
	300°C	30.8	105.1	3.27	-0.4473
	500°C	41.8	126.4	3.48	0.0779
III)	5 mTorr	5.6	13.5	2.14	--
	10 mTorr	6.4	23.7	3.12	-0.6777
	20 mTorr	39.7	95.6	4.35	0.0474

3.2.4 Conclusion

The effects of sputtering power, substrate temperature and sputtering pressure on the microstructural morphologies of the Ti films deposited on glass substrate by DC-Magnetron sputtering were investigated in the present work. XRD analysis of the

textures of the Ti films, deposited under different conditions, revealed the initial (100) preferred orientation but the (002) and (101) orientations were observed with the increasing sputtering power and substrate temperature, respectively. The development of (100) orientation was due to the compressive stress induced in the films but it transformed into (002) preferred orientation at higher thickness. The (002) and (101) preferred orientations were observed for the films deposited with the sputtering pressure of 5 mTorr and 20 mTorr, respectively. The textures of the films were affected due to the competition between strain energy and surface free energy during deposition of thin films under various process conditions such as substrate temperature, power and sputtering pressure. The thermal stress induced in the thin films at higher substrate temperature has also contributed to the formation of preferred (101) orientation. The microstrain of Ti films was initially negative and then changed to positive value with increasing sputtering power, substrate temperature, and sputtering pressure. The crystallite size has increased with increase in microstrain in the films. The average surface roughness calculated from the AFM images of the films has shown an increasing trend with varying deposition parameters. The increase in surface roughness of Ti thin films with increase in substrate temperature was due to growth of grains with preferred orientations dictated by surface and grain boundary diffusivity, adatom mobility, film thickness and induced thermal stress. The calculated grain size of Ti thin films using XRD results revealed an increasing trend with varying deposition parameters. The uniform and dense morphology of the Ti films were observed with the higher substrate temperature and sputtering pressure as observed from the FE-SEM characterization. The denser morphology of grains observed at higher substrate temperature is due to the higher surface and bulk diffusivity of sputtered atoms.

3.3 FEM Analysis of Thermal Stress in Magnetron Sputtered Ti thin films

3.3.1 Introduction

Titanium based thin hard coatings such as TiN, Ti-Si-N, and Ti-Al-N exhibit excellent mechanical and tribological properties and provides superior wear resistance over the materials on which they are coated. However, the residual stresses generated in the thin hard coatings during the deposition processes, physical and chemical vapor deposition, significantly influence their hardness, adhesion and wear resistance. The residual stress in the coating is dependent on growth stress and thermal stress, which are affected by the deposition processes. The presence of growth stress or intrinsic stress in thin coating is due to the influence of particle flux and energy striking the condensing film on the substrate during the sputtering process. The energy of bombardment and the structure of the coatings are sensitive to the deposition parameters such as substrate temperature, pressure, sputtering current, bias voltage, and substrate orientation. The intrinsic stress in sputtered thin coatings can be related to the structure zones. A low-density zone I possess voids between columns leading to coating under tensile stress. The tensile stress arises from the interaction of open columnar boundaries in the coatings. If the coating is bombarded by energetic particle such as ion or reflected neutral species during sputtering at low argon pressure and bias, compressive stresses are generated due to ion-peening mechanism. It will result in higher density zone with fewer voids (Teixeira 2001). The growth stress affects adhesion, hardness, and generation of crystalline defects in the coating. The deformation of hard-coatings occurs by stress relaxation mechanism namely; adhesive failure due to delamination at the

interface and cohesive failure caused by spallation with the coating. It is well known from the literature that the poor adhesion of the coatings on the metal surface is influenced by the complex stress states manifested at the edges of the thin coatings (Teixeira *et al.* 1999, Khor *et al.* 2000, Islamoglu *et al.* 2002).

Thermal stress in the thin coatings results from the thermophysical property mismatch between substrate and coating occurs during the sputtering process. The various factors such as coefficient of thermal expansion, Poisson's ratio, Young's modulus, thickness and thermal conductivity affects significantly the thermal stress of sputtered deposited thin coatings as reported in the literature (Boley *et al.* 1985, Gunnars *et al.* 2002, Haider *et al.* 2005). Although the growth stress is substantial in physical vapor deposition of thin coatings, thermal stress can not be ignored if the deposition temperature and CTE mismatch is high (Gunnars *et al.* 2002). Hence, analysis of residual stress in thin coatings should account for both of these stresses. It is essential to realize that the stress management is very crucial in order to ensure the reliability of coatings in the actual applications. Analytical models are generally used to describe the thermal stresses of the coatings constituting the linear-elastic or elastic-plastic behavior.

In recent times, finite element analysis (FEA) serves as potential tool to quantify the thermal stress in the thin coatings. Also, discrete element modeling (DEM) based technique is used extensively to analyse the tensile and compressive stress in the thin films and particulate system (Amin *et al.* 2006). It may be mentioned that FEA analysis (Ucar *et al.* 2001, Sarikaya *et al.* 2002, Widjaja *et al.* 2003) of thermal stress in thin film is quite prevalent in device manufacturing technology to test its reliability (Okyar *et al.* 2001) but it is very scarce in the context of failure of the coatings for the technological

applications. Ti thin coating is used in tribological, microelectromechanical systems, diffusion barrier applications due to their superior hardness, excellent thermal and chemical stability. Since the thermal stress strongly affects the mechanical properties of the coatings, it is very essential to ensure its reliability in various applications by quantifying them via experimental and modeling studies. Therefore, the present work has been focused to simulate the thermal stress generated in thin Ti coatings sputter deposited on glass and Si substrates.

3.3.2 Modeling

3.3.2.1 Analytical Model for thermal stress

Tsui *et al.* (1997) have proposed an analytical model for predicting residual stress in progressively deposited coatings for the planar geometry configuration. Their analytical model in conjunction with Stoney's equation for tension of metallic films would result in the following equation for thermal stress in thin coating as (Stoney 1909),

$$\sigma_f = \frac{E_{ef} \int_{T_r}^{T_d} (\alpha_s - \alpha_f) dT}{1 + 4(E_{ef} / E_{es})(h/H)} \quad (3.6)$$

where, $E_{ef} = E_f / (1 - \nu_f)$, $E_{es} = E_s / (1 - \nu_s)$, E_f , E_s , h , H , α_f , α_s , ν_f , ν_s , T_r and T_d are effective Young's modulus of the coating, effective Young's modulus of the substrate, Young's modulus of the coating, Young's modulus of the substrate, coating thickness, substrate thickness, coefficient of thermal expansion of the coating, coefficient of thermal expansion of the substrate, Poisson's ratio of the coating, Poisson's ratio of the substrate, room temperature and substrate temperature respectively.

3.3.2.2 Finite Element Analysis

To analyze the thermal stress generated in sputter deposited Ti coating, a cylindrical shaped glass substrate of 20 mm diameter and 3 mm thickness, and on the top surface, Ti coating of thickness 2.5 μm were considered. Similarly, for the silicon substrate, a cylindrical shape was considered but with different dimension of diameter 20 mm and thickness 0.5 mm, and coating thickness 2.5 μm . These dimensions would allow the coating-substrate to bend upon the development of thermal stress in the sputter deposition of Ti coating. For the simplicity of analysis, an isotropic and thermoelastic behavior of the coatings and substrates were assumed. The plain biaxial stress was considered along with the uniform temperature maintained over the sample at the processing temperature as well as after cooling. The orthotropic behavior of the material was also taken into account to analyze the thermal stress in the coating-substrate combination. The physical and mechanical properties of the Ti coating and substrates (Glass and Si) are given in **Table 3.4**.

Table 3.4: Properties of coating and substrates materials

S.N.	Properties	Materials		
		Titanium	Glass	Silicon
1)	Poisson's ratio	0.31	0.24	0.3
2)	Young's modulus (GPa)	120	69	167
3)	Coefficient of Thermal expansion ($\times 10^{-6} \text{ } ^\circ\text{C}^{-1}$)	8.4	9	2.33

Analyses were made to study the effect of each parameter on thermal stress by varying it, for example, substrate temperature (100 to 500 $^\circ\text{C}$), while fixing three of the other

parameters constant {Young's modulus (120 GPa), coating thickness (2.5 μm), substrate thickness (3 mm for glass and 0.5 mm for Si)}. The identical geometry of the substrates with fixed thickness was used for the analysis. The Young's modulus values of Ti vary with in the range of 100 – 120 GPa as reported in the literature (Chinmulgund *et al.* 1995, Ogawa *et al.* 1997) and in the simulation the similar variations were imposed. The axisymmetric plane parallel to XY plane was taken into account for the two dimensional FEA, as shown in **Figure 3.12** in the present work.

The simulation of thermal, shear and radial stresses generated in the Ti coating deposited on glass and Si substrates were performed by ANSYS finite element analysis (ANSYS 2003). The four-node structural and quadratic element PLANE 42 with axisymmetric option has been used to model the Ti coating on glass and Si substrates. The model was meshed with mapped meshing using the quadrilateral-shaped elements. The element size across the plane was decreased in a graded fashion near the coating-substrate interface, since this area was under very high stress concentration (Wright *et al.* 1999). The fine mesh was imparted near the edge across the thickness of the coating and substrate and it was refined until the results are consistent with only small changes. The left side of the model corresponds to the axis of the axisymmetric model and to restrict any movement, left corner of the model was pinned so that bending occurs during cooling.

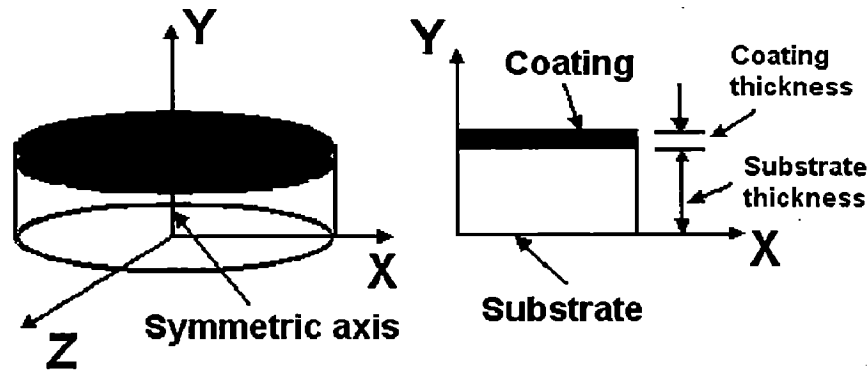


Figure 3.12: Schematic diagram of axisymmetric 2D solid model

The verification of the model was carried out by substituting the value of different properties of coating and substrate in the analytical **Equation 3.6**. The thermal stress in the FEM calculation is computed as maximum von Mises stress in the coating. The thermal load is applied over the coating-substrate combination by fixing substrate temperature as 500°C and uniform temperature as room temperature, 25°C . The sum of average value of radial and shear stress components would give the thermal stress values in the coating-substrate combination.

3.3.3 Results and Discussion

The variation of thermal stress generated in Ti coating deposited on glass and Si substrates as a function of substrate temperature is shown in **Figure 3.13(a) and (b)** respectively. It is observed that thermal stress varies linearly with substrate temperature and the values calculated by FEA analysis are in accordance with analytical model, in the present work. The thermal stress of Ti on Si substrate induces a compressive stress as shown in the **Figure 3.13(b)** against tensile stress on glass substrate. Due to the high CTE mismatch between Ti and Si substrate, the induced thermal stress in the coating is substantial.

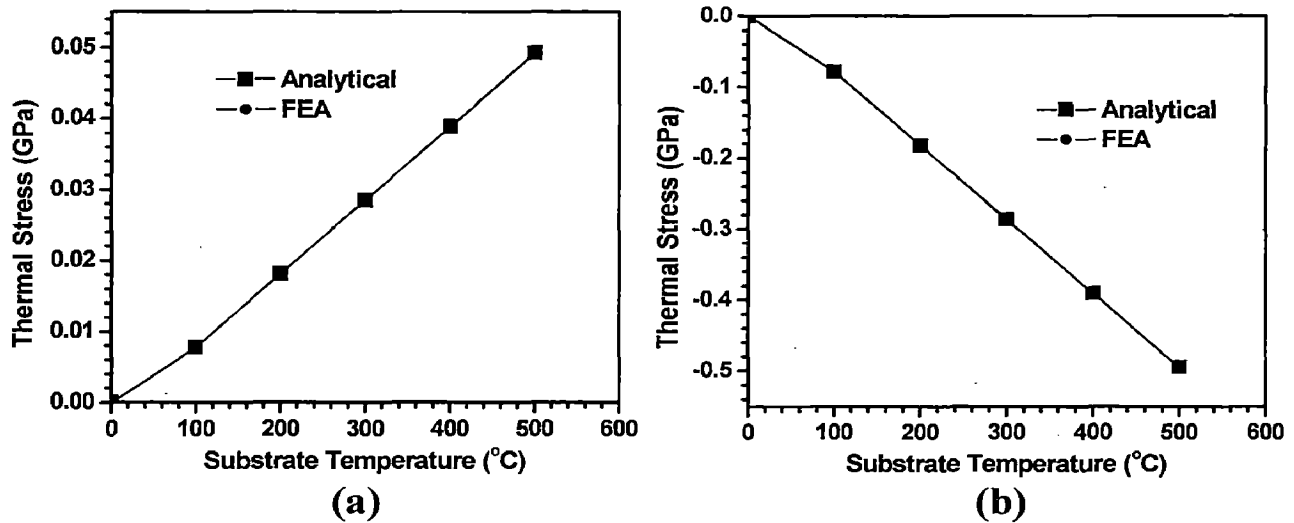


Figure 3.13: Thermal stress variation as a function of substrate temperature on (a) Glass and (b) Si substrate

The linear relationship observed between thermal stress and substrate temperature of the Ti coating on Glass and Si substrate is due to the increase in thermal gradient occurs during deposition process. The induced thermal stress in the coating is high at higher substrate temperature due to the influence of thermal gradient and CTE mismatch between coating and substrate. The thermal stress in the Ti coatings can be relieved by post-annealing treatment.

The influence of coating thickness on the thermal stress of Ti coated on Glass and Si substrates is shown in **Figure 3.14**. The decrease in thermal stress with the increase of coating thickness is evident from this **Figure 3.14(a)** and it is due to the stress relaxation caused by the bending strain induced at higher thickness of the coating. The stress is reduced in the coating and substrate in proportion to the bending strain as reported in the literature (Mencik 1995).

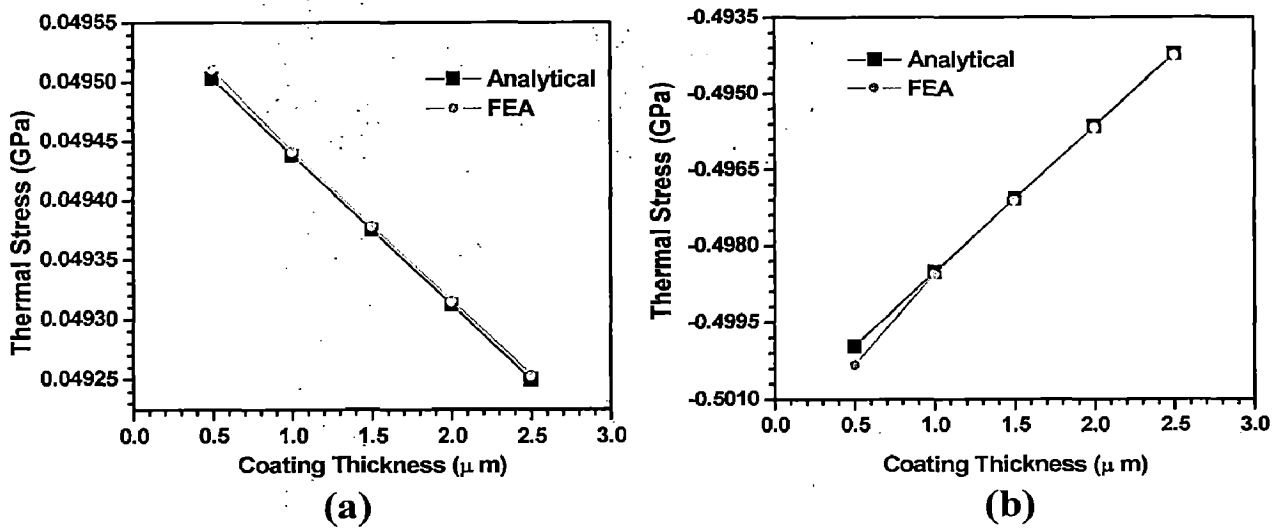


Figure 3.14: Thermal stress variation as a function of coating thickness on (a) Glass and (b) Si substrate

The bending effect is insignificant for the very thin coating with low stiffness but it is well pronounced for the coating with higher thickness values. It may be mentioned that the bending curvature in the coating-substrate manifests if the coating thickness is increased, which in turn would result in the lower stress in the coating. The thermal stress of Ti coating on Si substrate is compressive in nature and it decreases with increase in coating thickness.

When orthotropic behavior of the materials was taken into account for the FEM analysis as shown in **Figure 3.15(a-c)**, it is evident that there is a slight deviation in thermal stress values as a function of coating thickness from the values calculated for the isotropic case. However, they exhibit similar trends with respect to substrate temperature and Young's modulus.

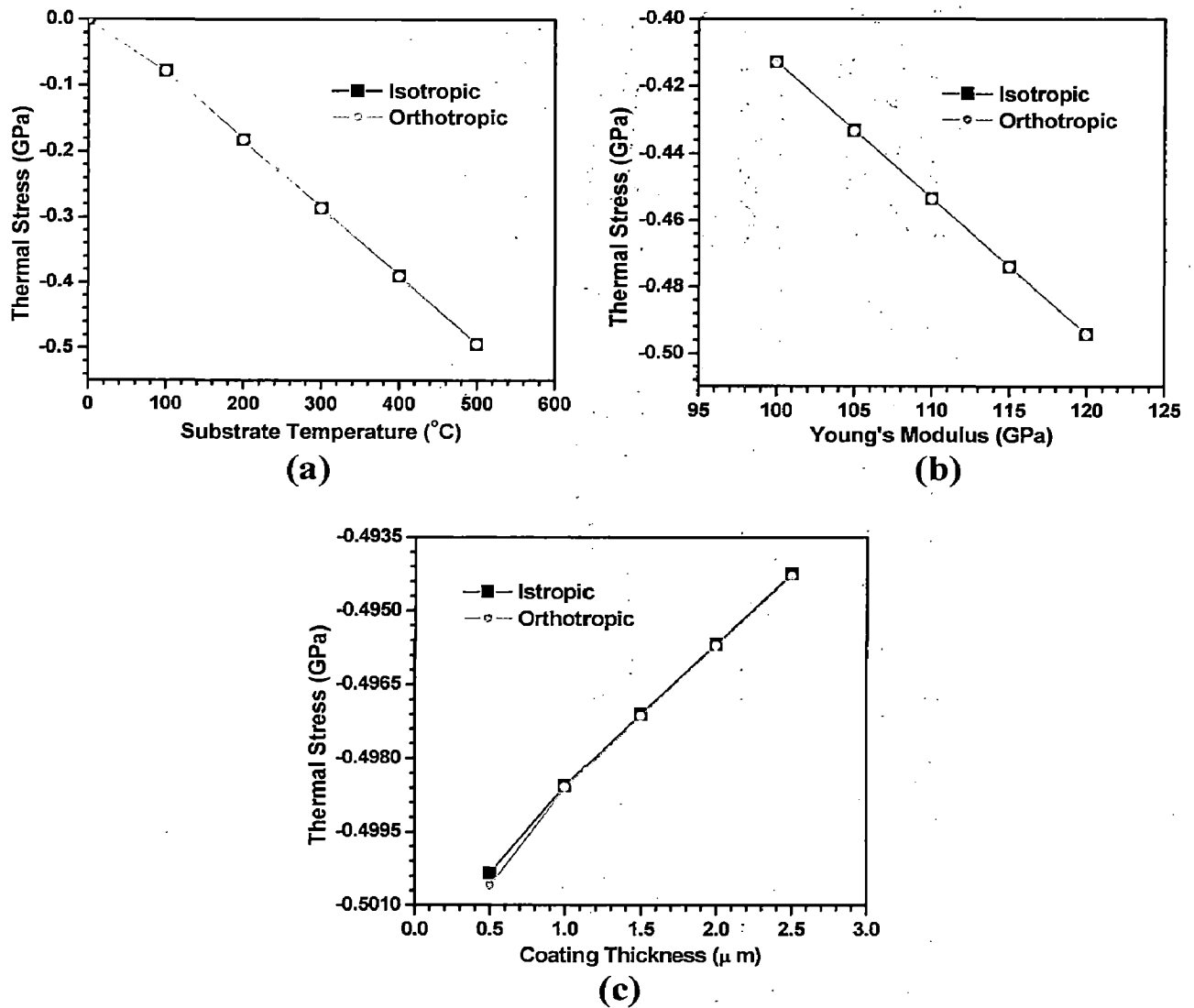
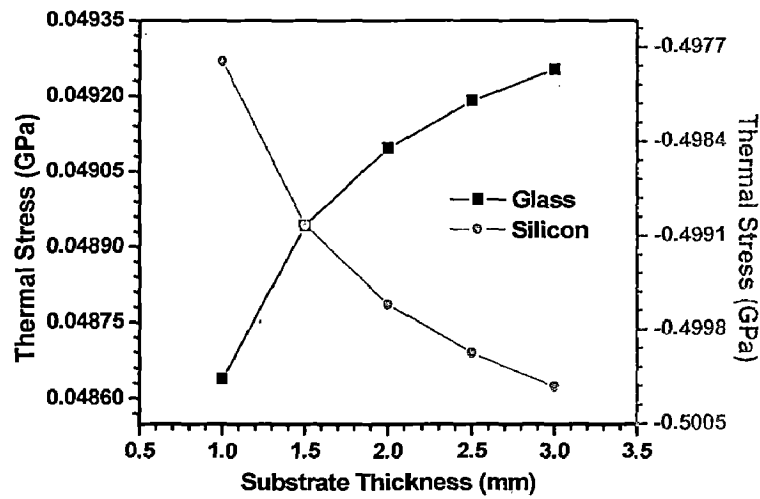
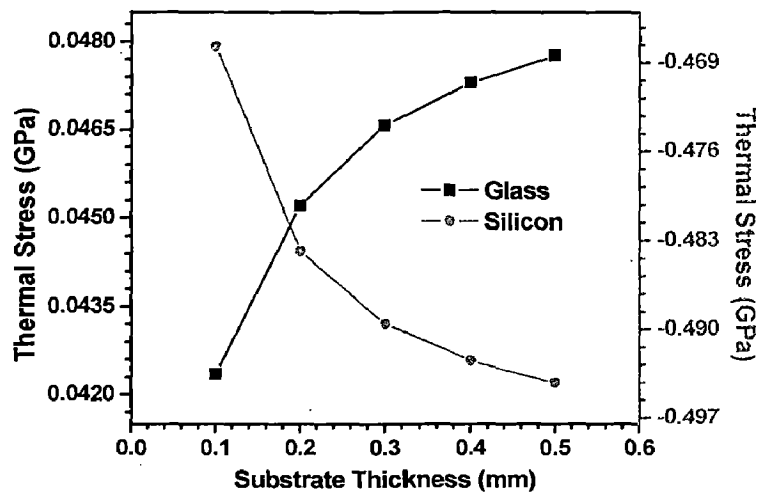


Figure 3.15: Thermal stress variation on Si substrate as a function of (a) substrate temperature, (b) young's modulus and (c) coating thickness

The identical geometry of the substrates was assumed to calculate the thermal stress of Ti coating and the results are shown in the **Figure 3.16**. It is evident that thermal stress in the coating is of tensile in nature in the case of glass substrate but compressive for the Si substrate with increasing in substrate thickness.



(a)



(b)

Figure 3.16: Comparison of thermal stress variation as a function of thickness on Glass and Si substrate (a) 1.0-3.0 mm substrate thickness (b) 0.1-0.5 mm substrate thickness

The thermal stress of Ti coating increases with glass substrate thickness and the stress relaxation at the lower thickness of the substrate is due to bending effect, which would reduce the thermal stress. The higher substrate thickness would prevent the bending effect and therefore, it can affect directly the thermal stress generated in the coatings.

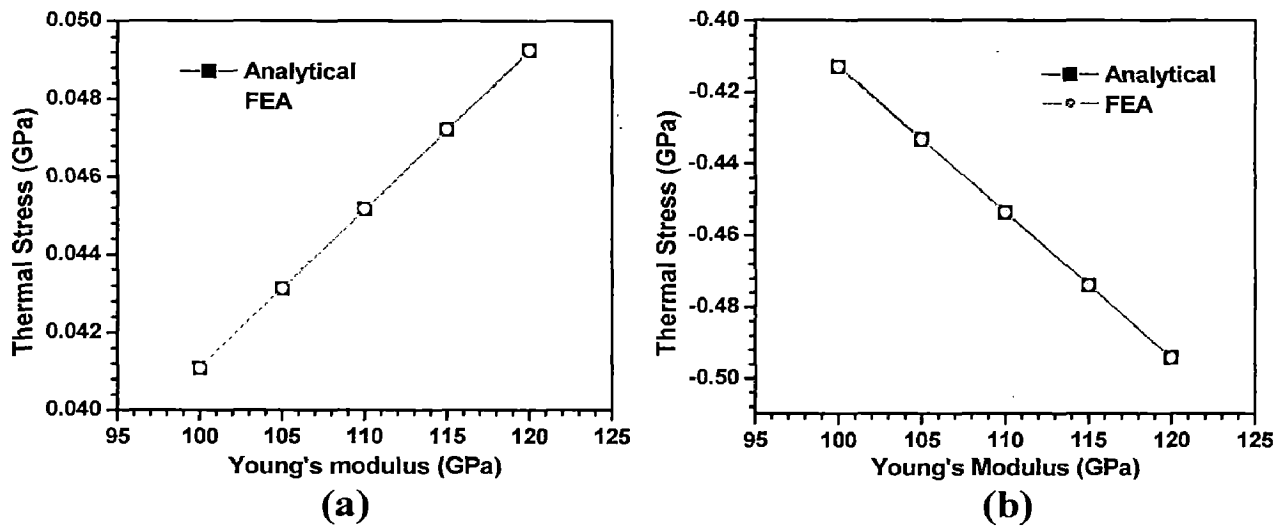


Figure 3.17: Thermal stress variation as a function of young's modulus on (a) Glass and (b) Si substrate

The variation of thermal stress in Ti coating with Young's Modulus (E), on the glass and Si substrates is plotted in **Figure 3.17(a) and (b)** respectively. The thermal stress of Ti coating increases with increase in Young's Modulus. The E value of the Ti coating depends on the sputtering process parameters such as deposition pressure, power and deposition rate. The impurities and porosity of the Ti films may affect its E value and the porosity of the coating thereby reduces the thermal stress generated.

The radial stress distribution through the thickness of the coating and substrates at different position from the edge to the center is evaluated and plotted in **Figure 3.18** for both glass and Si substrate. The stress gradient and the stress reversals from compressive to tensile occurs through the thickness of the substrate from its bottom to top surface and reaches a maximum value near the interface between coating and glass substrate. The radial stress is very high at a distance of $-5h$ from the glass substrate edge. Through the thickness of the coating, in the case of glass substrate, compressive radial stress is observed from the bottom to top surface. The minimum radial stress is

noticed at the edge of the coating but it increases with the distances, such as $-5h$, $-10h$ and $-15h$ away from the edges.

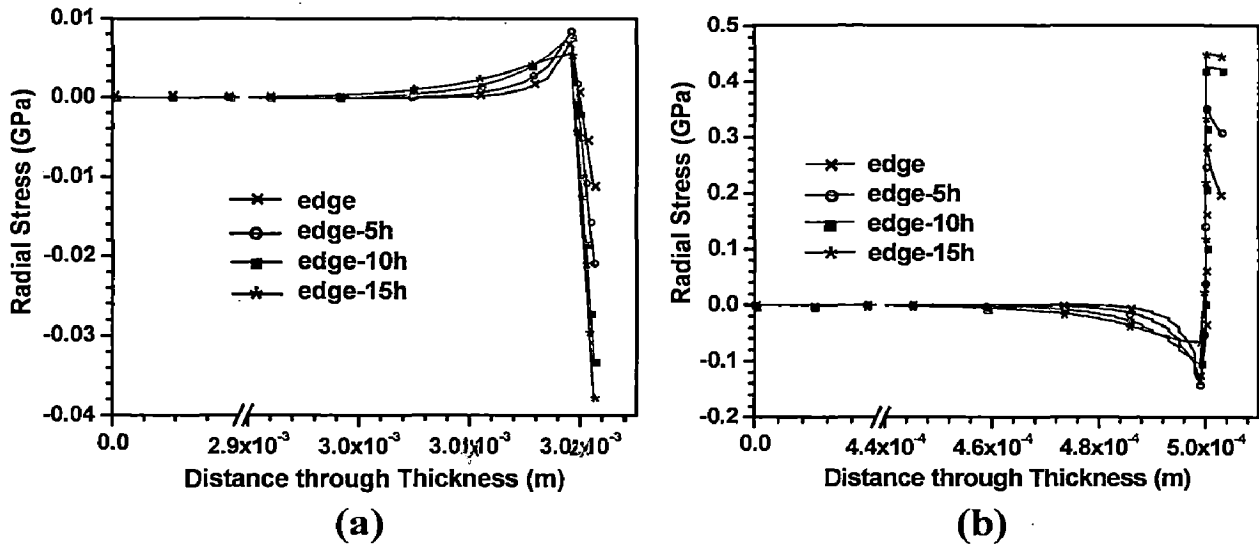


Figure 3.18: Radial stress (σ_r) distribution through the thickness of coating and substrate at different position from the edge to the center on (a) Glass and (b) Si substrate

The large compressive radial stress in the coating is due to the higher substrate-to-coating thickness ratio. It is observed that the stress reversal from tensile to compressive occurs through the thickness of Si substrate, and reaches a maximum at the interface between substrate and coating. The compressive stress is very high at a distance of $-5h$ from the edge of Si substrate. The radial stress in the coating increases upon moving at a distance of $-5h$, $-10h$ and $-15h$ from the coating edge and it is of tensile in nature in the case of Si substrate.

The shear stress distributions of Ti coating on glass and Si substrate are shown in **Figure 3.19(a) and (b)** respectively. The maximum tensile shear stress is evident at the interface in the coating edge in the case of glass substrate. The maximum compressive shear stress is observed at the interface in the coating deposited on Si substrate. The

CTE mismatch between Si and Ti is responsible for the higher compressive shear stress at the coating edge and the decreasing trend of compressive shear stress is noticed at a distance of -5h, -10h and -15h from the coating edge.

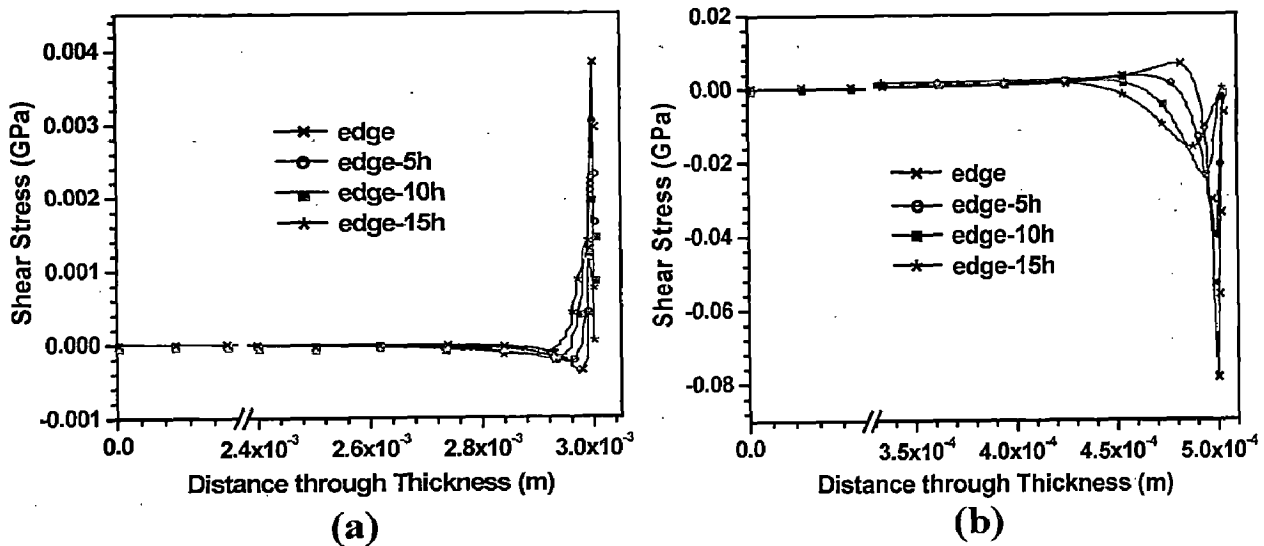


Figure 3.19: Shear stress (σ_{xz}) distribution through the thickness of coating and substrate at different position from the edge to the center on (a) Glass and (b) Si substrate

The tensile shear stress of Ti coating on glass substrate shows a decreasing trend upon moving away -5h, -10h, and -15h from the coating edge. The very small value of tensile shear stress at the top surface of the coating is due to the free surface phenomenon (Teixeira *et al.* 1999). There is no stress reversal in the coating away from its edges. At the edge of the glass substrate, the maximum tensile stress is observed at the interface and it decreases to the small value at the bottom surface of the substrate. The stress reverses from tensile at the interface to compressive at the bottom surface of the glass substrate as seen in the **Figure 3.19(a)**. The shear stress decreases at the interface when we move away from the coating edge. The shear stress is of compressive in nature in the case of Ti-coating on Si substrate as shown in **Figure 3.19(b)**. The shear

stress value can determine an adhesive strength of the coatings, as they are equivalent to each other. It may be inferred based on the reported literature (Ward *et al.* 1999) that the adhesive strength of Ti coating on glass substrate is less due to the higher tensile shear stress in the coating obtained in the present work. However, the compressive shear stress of Ti coating on Si substrate is beneficial in improving adhesive strength of the coating. The de-adhesion of the coating is due to through thickness cracks develops from the preexisting defects in the coating and generates shear stress along the interface which exceeds the bond strength between the coating and substrate (Teixeira 2001).

3.3.4 Conclusion

The thermal stress of Ti-coating sputter deposited on glass and silicon substrate has been simulated by finite element simulation package ANSYS and compared with that of analytical model. The thermal stress of coatings exhibits a linear relationship with substrate temperature and Young's modulus of the coating, but it exhibit an inverse relationship with the coating thickness due to the stress relaxation. The radial stress of the coating-substrate exhibits a maximum value at the interface near the edge and it determines the failure of the coatings. The radial stress in the Ti coating is of compressive in nature on the glass substrate but tensile on the Si substrate. The higher shear stress of the Ti coating is observed along the interface at the edge due to the higher stress concentration. The tensile and compressive shear stresses are observed for Ti coating on glass and Si substrates, respectively. The spallation of the coatings from the edge is heavily dependent on these shear stresses. The adhesive strength of the Ti coating on Si substrate is higher when compared to glass substrate due to the high compressive stress in the former.

Chapter 4

Synthesis and Characterization of Titanium Nitride Films

4.1 Structural and Mechanical Characterizations of Magnetron Sputtered nanocrystalline TiN thin films

4.1.1 Introduction

Nanocrystalline thin films exhibit enhanced mechanical and physical properties compared to that of its microcrystalline thin films. Particularly, nanocrystalline TiN thin film has been identified as a potential material for tribological and diffusion barrier applications due to their superior hardness, wear resistance, chemical stability, metallurgical stability and adhesion properties (Helmersson *et al.* 1987, Patscheider 2003, Barnett *et al.* 2004). The control of microstructural characteristics such as grain size, shape, textures, porosity, density, and packing factor are vital for ensuring the reliability of TiN thin films in structural and functional applications. Physical vapor deposition (PVD) techniques such as magnetron sputtering, filtered cathodic arc, ion plating, and plasma-based ion implantation are employed to deposit TiN thin-films. The process parameters and heat treatments used in PVD techniques affect the microstructural features of the TiN thin films. For example, in magnetron sputtering, the deposition parameters such as substrate temperature, pressure, target power, substrate bias, and energy and flux of bombarding particles utilized for growing the films are known to influence grain growth and crystallographic texture, which affect the resulting microstructure and properties of the films.

Structure zone models (Movchan *et al.* 1969, Thornton 1977, Grovenor *et al.* 1984) describe the microstructure of as deposited films. These models provide a qualitative picture of the expected microstructure of the films with respect to temperature. At low deposition temperatures, the films show an open columnar structure with extended

voids along column boundaries. The columns are composed of smaller equiaxed grains. The voids get filled with increasing film growth temperature and form a true columnar structure, in which elongated grains are observed. The boundary between these two structural zones is depicted as $T_s/T_m = 0.3$ where T_m is the melting point of the film and T_s is the substrate temperature. However, the transition between structural zones does not occur abruptly as it ignores the strong dependence of nucleation and growth kinetics affected by substrate structure and orientation, film growth rate, and the presence of impurities.

Helmersson *et al.* (1986) have investigated the microstructural evolution in TiN films (4 μm thick) reactively sputter-deposited on multiphase substrates and reported a dense columnar morphology in the films. The adatom surface diffusivities influence the growth process at all growth temperatures. The average grain size near the substrate was found to be twice as large as that of the constituent phases present in the multiphase substrate. Secondary recrystallisation and grain growth was not observed at the growth temperature investigated in their work. The grain boundaries were found to be immobile and nucleation kinetics was strongly enhanced by adatom surface diffusion. Johansson *et al.* (1985) reported that the annealing out of growth-related mechanical defects occurs in the epitaxial films only at substrate temperature above 650°C.

Patsalas *et al.* (2000) have studied the effect of substrate temperature and biasing on the mechanical properties of sputtered TiN thin films by nanoindentation technique and reported that the superior hardness and elastic behavior are exhibited by the denser films with (200) orientation. The substrate biasing and temperature had a direct influence on obtaining the denser TiN films with (200) orientation. Chandra *et al.* (2005) studied the structural, optical and electronic properties of nanocrystalline TiN

thin films deposited by DC magnetron sputtering. They observed a preferred orientation of mixed (200) and (111) for films deposited in pure N₂ and Ar+N₂ atmospheres, respectively, at low temperature. Huang *et al.* (2005b) reported the effect of nitrogen flow rate on the structure and properties of nanocrystalline TiN thin films produced by unbalanced magnetron sputtering. The (111) preferred orientation was observed initially and then changed to (200) with an increase in nitrogen flow rate.

Hainsworth *et al.* (2003) studied the effect of different substrates such as stainless steel, Ti, Brass on the mechanical properties of TiN coatings by nanoindentation technique and it was observed that the indentation response is plastically dominated. The hardness values of the films are scattered at lower load and it was due to inaccuracies manifested in evaluation of load-displacement curves. The elastic recovery and pile-up around the indentations influenced the hardness values of TiN films deposited on the different substrates. Nanocomposite TiN-TiB₂ films, investigated by XRD and HRTEM, it revealed that TiN exhibits a (111) preferred orientation which subsequently changes into a mixed (111) - (200) orientation with the addition of boron (Liu *et al.* 2004, Shen *et al.* 2006). Kim *et al.* (2005) have characterized RF magnetron sputtered nanocrystalline thin TiN films (0.7 μm) by HR-TEM and observed the formation of fine grains in the films with an increase in flow rate of N₂ gas. The columnar structure perpendicular to the Si substrate surface and 5-10 nm diameter nanocrystals were found. A reduction of grain size with increase in N₂/Ar ratio was observed during the film growth stage. For TiN films grown at relatively low substrate temperature ($T_s < 0.3 T_m$), the crystallographic texture changed with increasing film thickness; an initial random orientation, followed by a (200) preferred orientation, has been reported in 5-10 nm thick films (Troll 1971, Li *et al.* 2003, Ma *et al.* 2004). This

orientation has gradually transformed into (111), (220), or a mixed (111) and (220) texture depending upon the deposition conditions. The TiN films were characterized by using optical reflectivity measurements to predict the optimum deposition parameters for obtaining the high dense films (Glew *et al.* 2002).

The mechanical properties of TiN coatings deposited on different steel substrates were studied using nanoindentation and nanoscratch tests by Zhang *et al.* (2004) and it was shown that with the increase in indentation depth, the hardness value decrease due to the substrate effects. The deformation mechanisms of TiN coatings on steel substrates, during nanoindentation, were investigated by focused ion beam imaging and TEM [Ma *et al.* (2005, 2007)]. It was reported that the load-displacement data displayed a pop-in effect with the increase in load on the samples. The cracks were initiated at the boundaries between the columnar grains as well as the steps at the coating/substrate interface. Nanoindentation and microscopic observation revealed that the deformation of TiN coatings occurs primarily by the shear sliding along columnar grain boundaries. Ma *et al.* (2006) investigated the nanohardness of nanocrystalline TiN thin films, prepared by ion-beam assisted deposition, and found that the nanohardness is not sensitive to the packing factor or N/Ti ratio but it increases with increasing ion beam energies; The adhesion of TiN coatings on stainless substrate by high energy heavy ion irradiation has been studied by Sangeeta *et al.* (1995). They observed that the failure mode of the coatings changed from the spallation to the buckling mode, indicating the enhancement of adhesion of coatings over the substrate.

Petrov *et al.* (2003) investigated the microstructural evolution and surface morphological evolution at the atomic scale during the growth of polycrystalline TiN, prepared by sputter deposition, using HR-TEM, XRD, and SEM. At low deposition

temperatures ($T < 450^{\circ}\text{C}$), the films exhibited a columnar grain morphology with the preferential orientation of (111) textured grains. However, high temperature deposition resulted in non-competitive growth with a fully dense (200) orientation in the initial monolayer of the film and it is well known that the texture evolution mechanisms in TiN thin films are influenced by factors such as strain energy, surface free energy, surface diffusivity, adatom mobility; the influence of each varies as a function of processing parameters. The potential application of nanocrystalline TiN films for tribological and microelectronic device applications could be successfully realized only if thorough insight is gained with regard to means to achieve the formation of desired microstructures through appropriate process controls. Owing to the aforementioned facts, the present work has been focused on the characterization of the microstructural features and mechanical properties of nanocrystalline TiN films deposited by DC-Magnetron sputtering.

4.1.2 Experimental Details

4.1.2.1 Synthesis of TiN films

TiN thin films were deposited on Si (111) substrates by DC magnetron sputtering. The substrate was cleaned by first rinsing in Hydrofluoric acid to remove SiO_2 layer and then ultrasonic baths of acetone and methanol and finally dried under nitrogen gas. The sputtering target was a 99.99% pure Ti disc (2" diameter and 5 mm thick). The base pressure was lower than 2×10^{-6} Torr and the sputtering was carried out in Ar + N_2 (70:30) and pure N_2 atmospheres. Before starting the deposition, the target was presputtered for 15 minutes with a shutter located between the target and the substrate. The target-substrate distance was kept at 50 mm. The sputtering parameters for TiN

films with variation of deposition time in different atmospheres are included in **Table 4.1**.

Table 4.1: Sputtering parameters for TiN films with variation of deposition time in different atmospheres

Sputtering Parameters	Variation of Deposition time in Ar+N₂ (70:30) atmosphere	Variation of Deposition time in Nitrogen atmosphere
Target	Titanium	Titanium
Base Pressure	2×10^{-6} Torr	2×10^{-6} Torr
Gas Used	Ar+N₂ (70:30)	Nitrogen
Sputtering Pressure	10 mTorr	10 mTorr
Deposition Time	60-150 min	60-150 min
Sputtering Power	200 W	200 W
Substrate Used	Silicon (111)	Silicon (111)
Substrate Temperature	500°C	500°C

4.1.2.2 Characterization details

XRD (Bruker AXS, D8 Advance) measurements were made using CuK α (1.54 Å) radiation to characterize the TiN thin films. The scan rate used was 1°/min and the scan range was from 34 to 65°. The excitation voltage and current were set to a 40 kV and 30 mA respectively, in the diffractometer. The grain size of the TiN films was estimated from the Scherrer's formula, as given in **Section 3.1.2.2 (Equation 3.1)**.

FE-SEM (FEI, Quanta 200F) were used to characterize the microstructures of the TiN thin films at an acceleration voltage of 20 kV. The surface morphology (2D and

3D) of the TiN films was characterized by AFM (NT-MDT, Ntegra) operated in semicontact (tapping) mode and the root-mean-square (RMS) roughness of the surface of the sample was calculated from AFM scan at five different spots for each sample. The hardness and Young's modulus of the TiN films were measured by nanoindentation technique (MTS, XP) in displacement control method, in which the maximum displacement of the diamond Berkovich indenter tip into the sample is set to depth of one-tenth of coating thickness at strain rate of 0.05 /sec and the feedback loop on the load stops the measurement when the preset displacement value is reached. The maximum load thus varies for each sample based on the hardness of that sample because the displacement is kept constant. A total of ten indentations were made on each sample and the average hardness and Young's modulus of TiN films were calculated from the load-displacement curve obtained from the nanoindentation testing.

4.1.3 Results and Discussion

XRD peaks of TiN films deposited on the Si (111) substrate in Ar+N₂ and pure N₂ atmospheres at 500°C are shown in **Figure 4.1(a) and (b)**, respectively. The films deposited in the Ar+N₂ atmosphere, **Figure 4.1(a)** exhibit a (200) preferred orientation during the initial deposition time and then change to a mixture of more pronounced (111) orientation with less (200) orientation with increasing deposition time. However, the TiN thin films deposited in a pure N₂ atmosphere exhibit only (111) orientation and this is transformed into a mixed (200) - (111) orientation with increasing deposition time, **Figure 4.1(b)**.

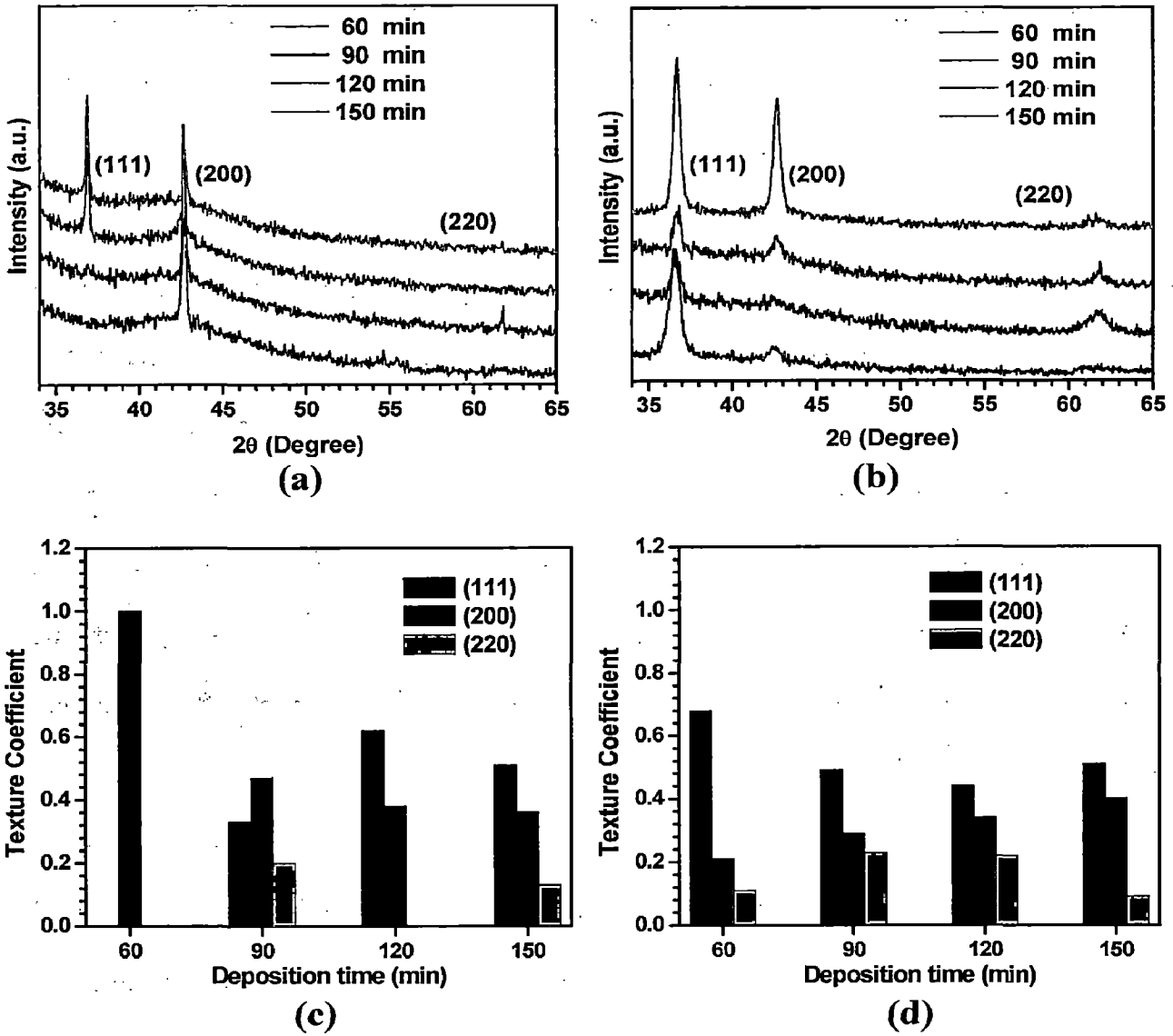


Figure 4.1: XRD peaks and texture coefficients of TiN films deposited on Si substrate as a function of deposition time (a & c) in Ar+N₂ atmosphere and (b & d) in N₂ atmosphere

The texture coefficients of the TiN films as a function of deposition time are calculated from their respective XRD peaks using the following formula (Huang *et al.* 2005b); the results are shown in **Figure 4.1(c) and (d)**.

$$\text{TextureCoefficient} = \frac{I(hkl)}{[I(111) + I(200) + I(220)]} \quad (4.1)$$

where, h, k, l are planes and represents the (111) or (200) or (220) orientations.

The texture coefficients of the (200) and (111) orientation are high compared to other orientations in the TiN films deposited under Ar+N₂ and pure N₂, respectively, during the initial deposition time. It is clear that the observed changes in textures are influenced by the high substrate temperature and time. The competition between surface energy and strain energy during film growth might contribute to these changes in preferred orientation. With an increase in deposition time and at some critical thickness, stress relaxation may reduce strain energy to a greater extent than the increase in surface energy due to the texture changes. When this occurs, an effective transition point occurs at which the texture changes. It is well known that the anisotropy of the elastic moduli will favor the growth of low strain energy-oriented grains at the expense of grains possessing higher strain energy. In addition, the substrate roughness may also affect the film texture.

From the XRD peaks, the crystallite size in the TiN films was found to be 15.3 nm and 36.7 nm after 90 minutes in N₂ and Ar+N₂ atmospheres, respectively. It is observed that the grain size increase with the deposition time is not high due to the formation of highly textured grains in the TiN films. Stability of the nanocrystalline TiN thin films is also partly due to the texture-controlled grain growth, in addition to the higher nucleation kinetics during the preparation of the films. The formation of nanograins in the TiN thin films reflects the influence of factors such as ion energy, ion flux, trace impurities, and textures as reported by Petrov *et al.* (2003) and Mayrhofer *et al.* (2006). In the present work, the bombardment by high energy sputtered atoms may damage the growing film and create a large number of defects in the films. The density of these defects becomes very high due to the high energy of the sputtered atoms and causes repeated nucleation during film growth on the substrate. These repeated nucleation

events are responsible for the formation of nanograins in the TiN thin films. Trace impurities may segregate at the grain boundaries and restrict the grain growth due to Zener drag, which is beneficial for the stability of the nanocrystalline films. During heavy ion bombardment, densification of the microstructure also occurs through the enhanced surface mobility of adatoms, which eliminates film porosity. It also increases the strain energy in the films, thereby influencing the formation of textured grains during film growth.

The microstructural morphologies of the TiN thin films as-deposited in Ar+N₂ and pure N₂ atmospheres at 500°C were characterized by FE-SEM and are shown in **Figure 4.2(a-d)**. **Figure 4.2(a) and (b)** show surface morphologies, whereas **Figure 4.2(c) and (d)** present images after 60° tilting. For the films deposited in the Ar+N₂ atmosphere, a pyramidal morphology of the grains is observed in **Figure 4.2(a)**. In the pure N₂ atmosphere, columnar grain morphology is seen in **Figure 4.2(b)**.

The tilted images clearly reveal the oriented growth morphology, particularly for the film deposited in the mixed Ar+N₂ atmosphere. It was evident from the XRD results that the initial orientation of these two films has varied; for the mixed Ar+N₂ atmosphere, the (200) orientation is dominating, whereas in pure N₂, the initial orientation is predominantly (111). Hence, the different appearance of these two films was observed. The preferred orientation (200) observed, in the present work, for the Ar+N₂ atmosphere deposited films is different from the (111) orientation reported for films deposited similarly by Chandra *et al.* (2005). This is due to the difference in substrate temperature and the substrate orientation used in these cases.

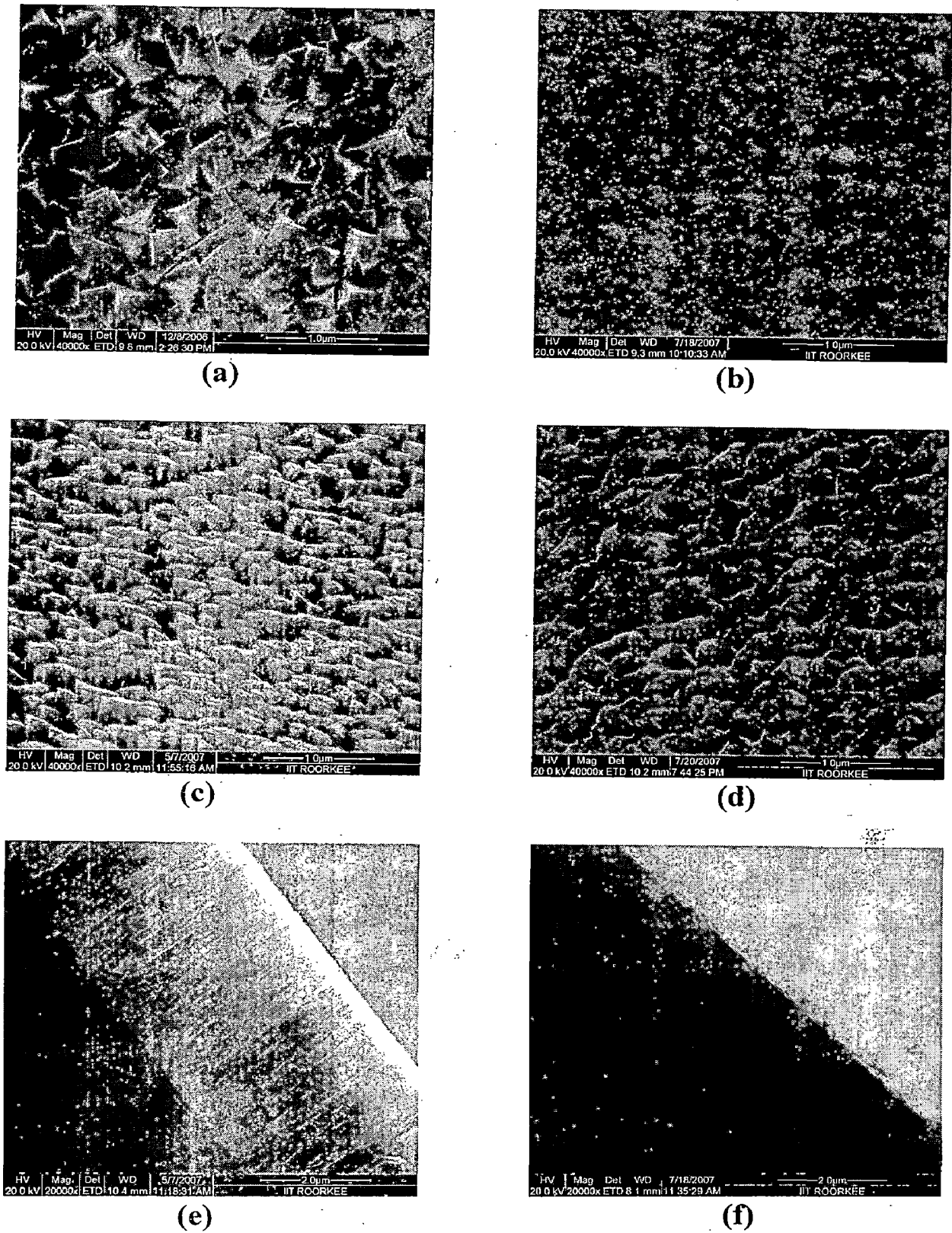


Figure 4.2: Top surface view, 60° tilt view and cross section FE-SEM images of TiN thin films deposited (a, c & e) in Ar+N₂ atmosphere and (b, d & f) in N₂ atmosphere

The pyramidal and columnar growth morphologies of the TiN films observed in this work are illustrated further in the cross-sectional FE-SEM images shown in **Figure 4.2(e) and (f)**.

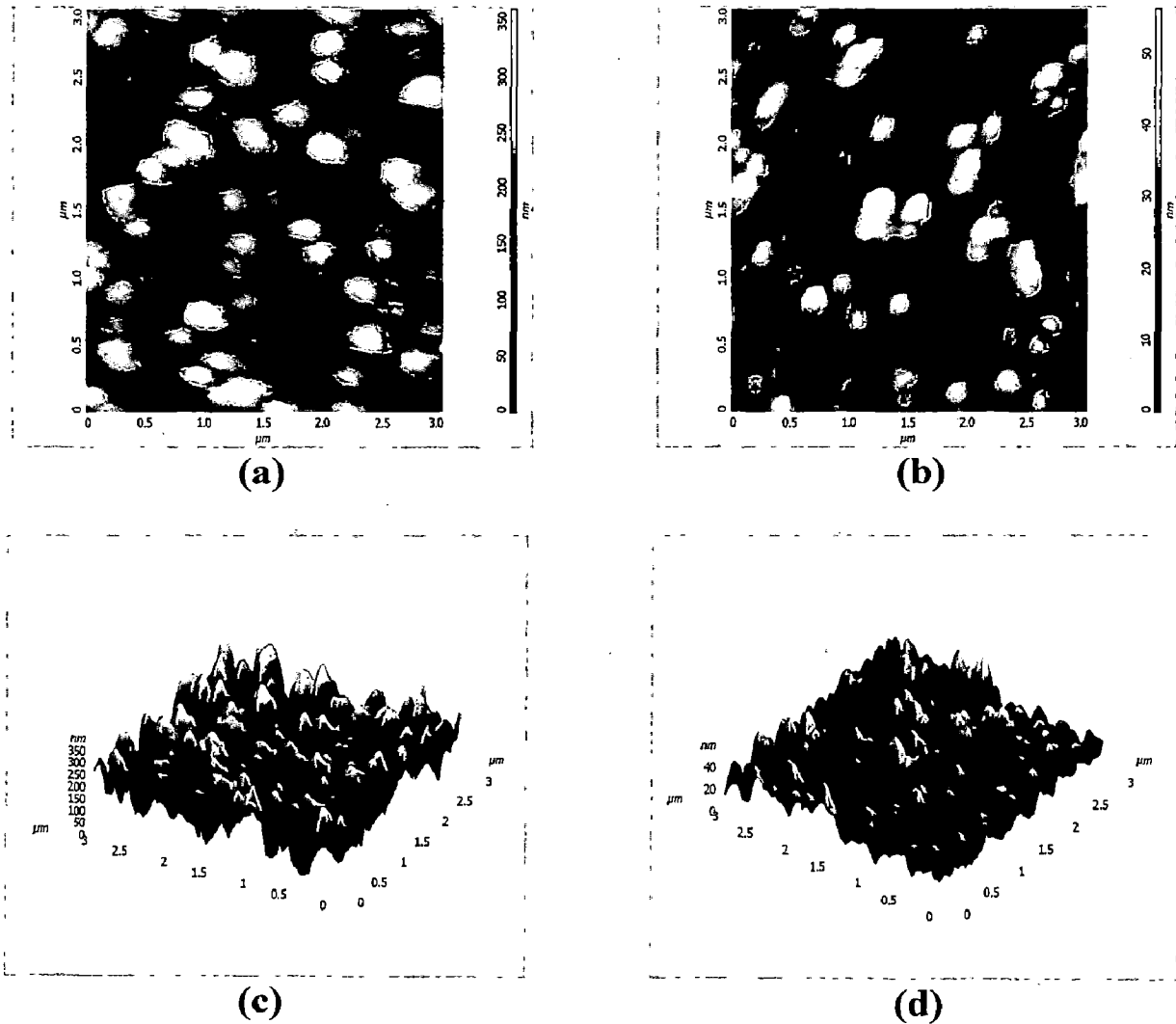


Figure 4.3: 2D and 3D AFM images of TiN films deposited **(a & c)** in Ar+N₂ atmosphere and **(b & d)** in N₂ atmosphere

Figure 4.3(a-d) shows the AFM surface morphology (2D and 3D) of the TiN films deposited in the Ar+N₂ and pure N₂ atmospheres at 500°C. The difference in morphology between the two films can be inferred by comparing the 2D images in **Figure 4.3(a) and (b)**; however, a clearer comparison of the films is afforded by

viewing the 3D images in **Figure 4.3(c) and (d)**. As the axis scale indicates, the overall roughness of the films prepared in the N_2 atmosphere [**Figure 4.3(d)**] is less than that for the films prepared in the $Ar+N_2$ atmosphere [**Figure 4.3(c)**]. **Figure 4.4** shows the AFM *in-situ* image of the indent on the sample which is obtained after the indentation.

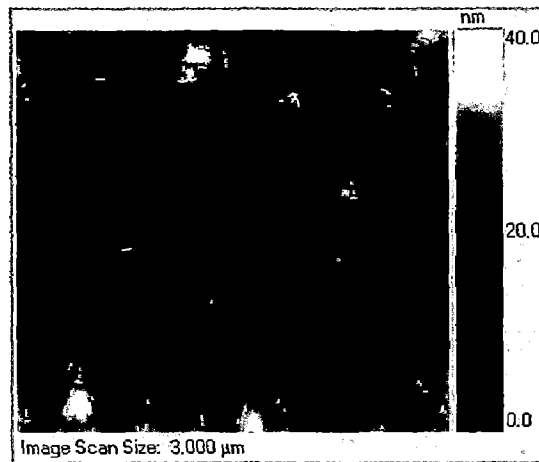


Figure 4.4: AFM *in-situ* image of the indent on the sample

Figure 4.5(a) and (b) shows the influence of sputtering atmosphere on hardness and Young's modulus of TiN films, respectively. From **Figure 4.5(a) and (b)**, it is observed that the hardness and Young's modulus values decrease with increasing deposition time in both $Ar+N_2$ and N_2 atmosphere. It may be due to the relatively less dense films when the deposition exceeds 60 minutes.

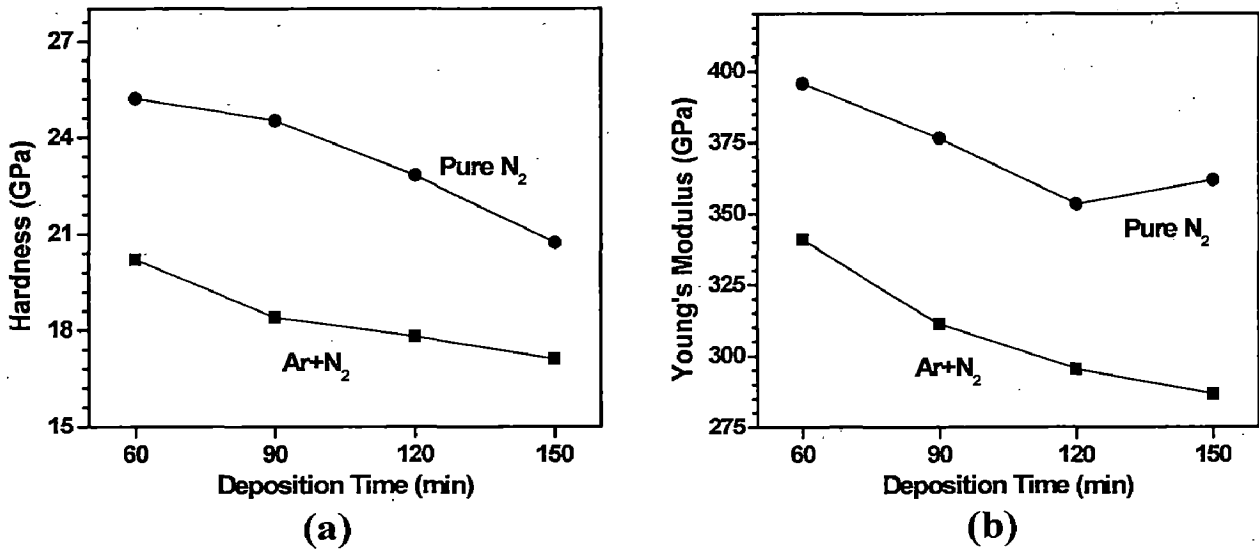


Figure 4.5: (a) Hardness of TiN films deposited in Ar+N₂ and N₂ atmosphere
(b) Young's Modulus of same films

However, in pure N₂ atmosphere, the TiN films exhibit high values due to its dense columnar morphology and less surface roughness in comparison to that of the films deposited in Ar+N₂ atmosphere. The maximum H and E values of 25.2 GPa and 395.4 GPa, respectively was observed when the deposition time is 60 min in pure N₂ atmosphere.

4.1.4 Conclusion

The microstructural morphologies and mechanical properties of nanocrystalline TiN thin films deposited on Si(111) substrates were investigated in the present work. The XRD results indicate that the TiN films prepared under an Ar+N₂ atmosphere exhibit an initial (200) preferred orientation which gradually changes into a mixed (111) - (200) orientation with longer deposition time. However, the initial preferred orientation for the TiN films prepared under a pure N₂ atmosphere is (111); this also evolves with longer deposition time to a mixed (111) - (200) orientation. These changes in texture in

the TiN thin films are due to one or combination of such factors as strain energy, surface free energy, surface diffusivity and adatom mobility; the influence of each factor depends on the processing conditions. The FE-SEM analysis of the nanocrystalline TiN thin films shows that the morphology of the films deposited in the Ar+N₂ atmosphere have a characteristic pyramidal grain shape, whereas the films deposited in a pure N₂ atmosphere exhibit a more columnar-type morphology. The AFM study revealed that the overall roughness of the films prepared in the N₂ atmosphere is less than that for the films prepared in the Ar+N₂ atmosphere. From the nanoindentation study, it is observed that the hardness and Young's modulus values of TiN films decreases with increase in deposition time in both Ar+N₂ and N₂ atmosphere. It is also observed that H and E values are higher in N₂ atmosphere as compared to Ar+N₂ atmosphere.

4.2 Microstructural Characteristics and Mechanical Properties of Magnetron Sputtered nanocrystalline TiN films on Glass substrate

4.2.1 Introduction

The effect of atmosphere and deposition time on the structural and mechanical characteristics of magnetron sputtered TiN films on silicon substrate has been reported in **Section 4.1**. Similarly, a detailed investigation is required to substantiate the influence of microstructural characteristics on the mechanical properties of TiN thin films deposited on glass substrate. It has been reported that TiN films with more than 200 nm thickness were not mechanically stable on glass substrates and peeled-off up with time on account of stress (Massiani *et al.* 1990). It is very essential to prepare mechanically stable TiN films on glass substrate and also measure its mechanical properties. In order to ensure compatibility and reliability of TiN thin films in diffusion barriers and tribological applications, the influence of processing conditions on the microstructural characteristics thin films (Soriaga *et al.* 2002) need to be thoroughly understood. Owing to these facts, the present work has been focused to measure the hardness and modulus of elasticity of DC magnetron sputtered nanocrystalline TiN thin films by nanoindentation technique. Nanoindentation technique is an effective tool to measure the elastic and plastic properties of the coatings as reported in the literature (Weppelmann *et al.* 1996, Shojaei *et al.* 1998). XRD, FE-SEM and AFM techniques were used to characterize the films deposited under different processing conditions. The mechanisms contributing to the improved strength of the films were explained using its microstructural features.

4.2.2 Experimental Details

4.2.2.1 Synthesis of TiN films

TiN thin films were deposited on glass substrates by DC magnetron reactive sputtering. The substrate is a microscope glass slide, which is cleaned by rinsing in ultrasonic baths of acetone and methanol and dried under nitrogen gas. The sputtering target was a 99.99% pure Ti disc (2" diameter and 5mm thick). The procedures adopted for deposition of TiN films on glass substrate were similar as discussed in **Section 4.1.2.1**. The sputtering parameters for TiN films with varying film thickness are included in **Table 4.2**.

Table 4.2: Sputtering parameters for TiN films with variation of film thickness

Target	Titanium
Base Pressure	2×10^{-6} Torr
Gas Used	Ar+N ₂ (70:30)
Sputtering Pressure	10 mTorr
Sputtering Power	150 W
Deposition Time	15-135 min
Film thickness	0.31-2.83 μ m
Substrate Used	Glass
Substrate Temperature	500°C

4.2.2.2 Characterization details

The characterization details are similar to that of it discussed in **Section 4.1.2.2**. The hardness and Young's modulus of the TiN thin films were measured by nanoindentation technique (CSM+). The diamond Berkovich indenter is forced into the thin films being tested under constant load conditions. The loading profile during indentation testing

followed linearly increasing with a hold time of 10 sec at the peak load. The loads used were 5 mN at different loading rates 2.5, 5.0, 10.0, 20.0 and 40.0 mN/minute in the present work. A total of four indentations for each loading rate were made on each sample and the average hardness and Young's modulus of TiN films were calculated from the load-displacement curve obtained from the nanoindentation testing.

4.2.3 Results and Discussion

The XRD peaks for the TiN films deposited, at 500°C, are shown in **Figure 4.6(a)**. It is observed that the preferred orientation of the film, with increasing thickness, is (200) up to 1.26 μm due to the lowest surface free energy during film growth in comparison to strain energy (Chawla *et al.* 2008b). When the film thickness is greater than 1.26 μm , the competition between surface energy and strain energy leads to the formation of (220) orientation which minimizes the total energy (Hoang *et al.* 1996).

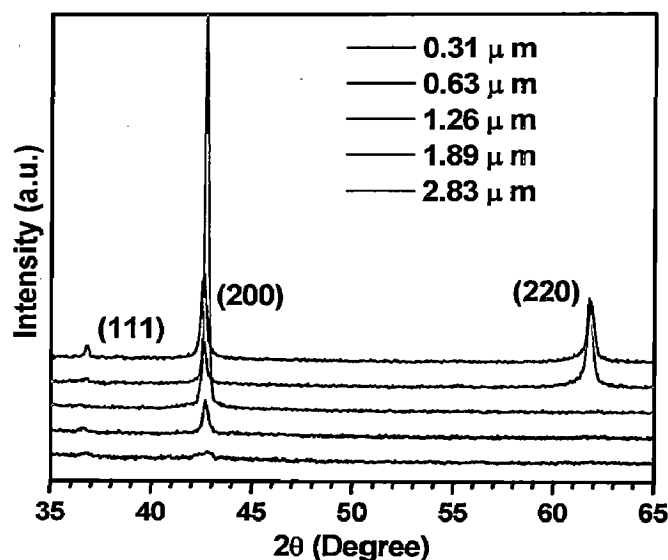


Figure 4.6(a): XRD peaks of TiN films deposited on glass substrate

With increasing deposition time and at some critical thickness, stress relaxation may reduce strain energy (John 2000, Ohring 2002) to a greater extent than the increase in surface energy due to the texture changes. It is well known that the anisotropy of the elastic moduli will favor the growth of low strain energy-oriented grains at the expense of grains possessing higher strain energy (Chawla *et al.* 2008b). **Table 4.3** shows the variation of crystallite size of TiN films as function of its thickness values. The crystallite size of the thin film with 0.31 μm thickness, calculated from the X-ray peak broadening, is 8.5 nm. It increases with increase in thickness but for the films with 1.89 μm thickness, the crystallite size is smaller as shown in **Table 4.3**.

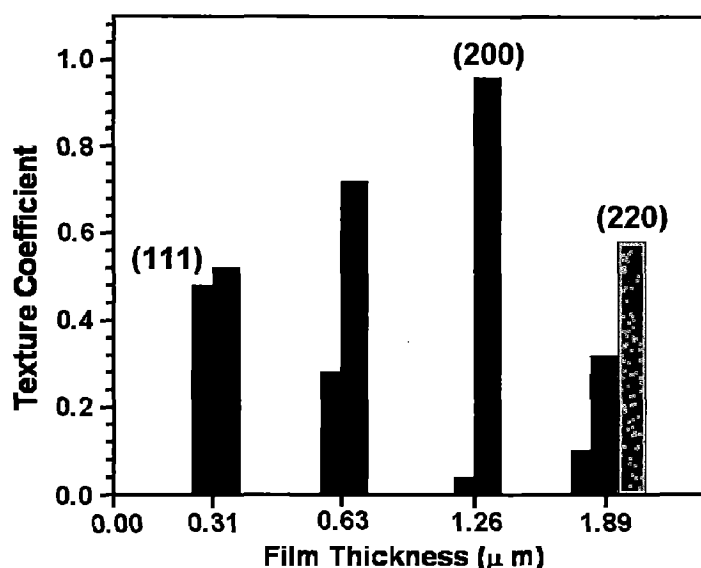
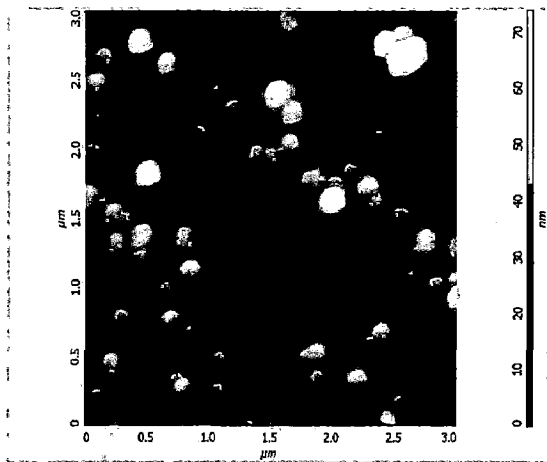
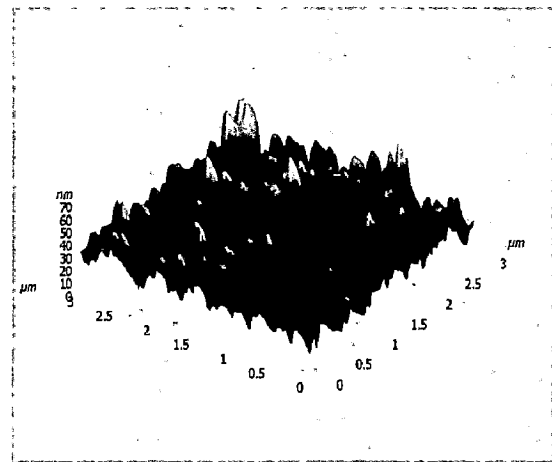


Figure 4.6(b): Texture coefficients of TiN films deposited on glass substrate

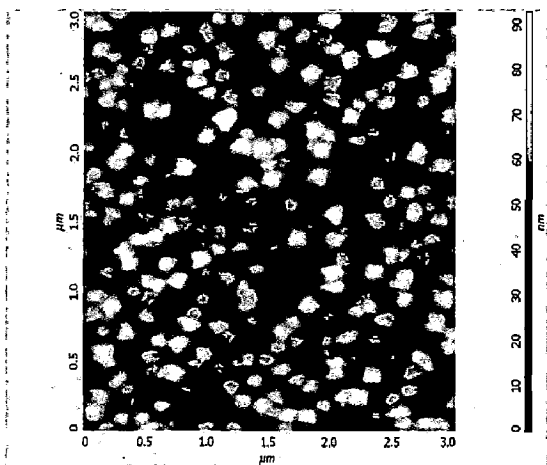
Figure 4.6(b), shows the texture coefficients of the TiN films as a function of film thickness calculated from their respective XRD peaks by using the formula, as given in **Section 4.1.3 (Equation 4.1)**. It is observed that the texture coefficient of (200) peak increases till the film reaches a thickness of 1.26 μm and afterwards (220) orientation develops.



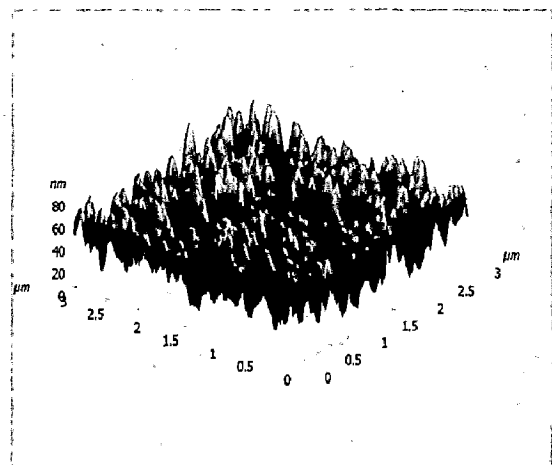
(a)



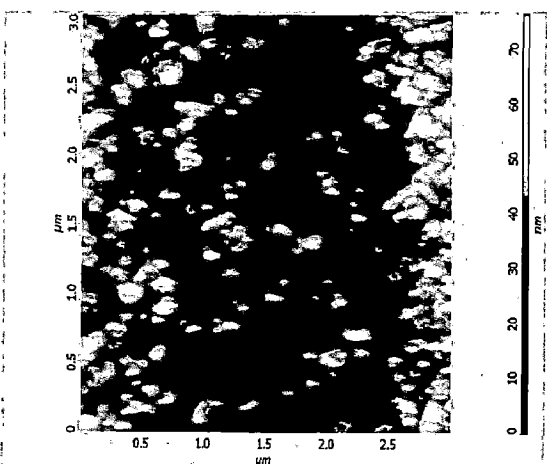
(b)



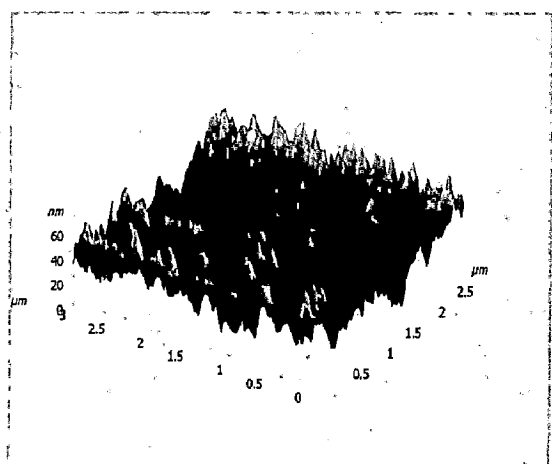
(c)



(d)



(e)



(f)

Figure 4.7: 2D & 3D AFM images of TiN films deposited on glass substrate at thickness (a-b) $0.63 \mu\text{m}$, (c-d) $1.26 \mu\text{m}$ and (e-f) $1.89 \mu\text{m}$

Figure 4.7 shows the 2D and 3D AFM images of the TiN films of 0.63 μm , 1.26 μm and 1.89 μm thicknesses. The surface roughness of the films increases with increasing thickness but for the film with thickness of 1.89 μm , a low surface roughness value is observed as shown in **Table 4.3**.

The FE-SEM image of the TiN films of 0.63 μm , 1.26 μm and 1.89 μm thicknesses are shown in **Figure 4.8**.

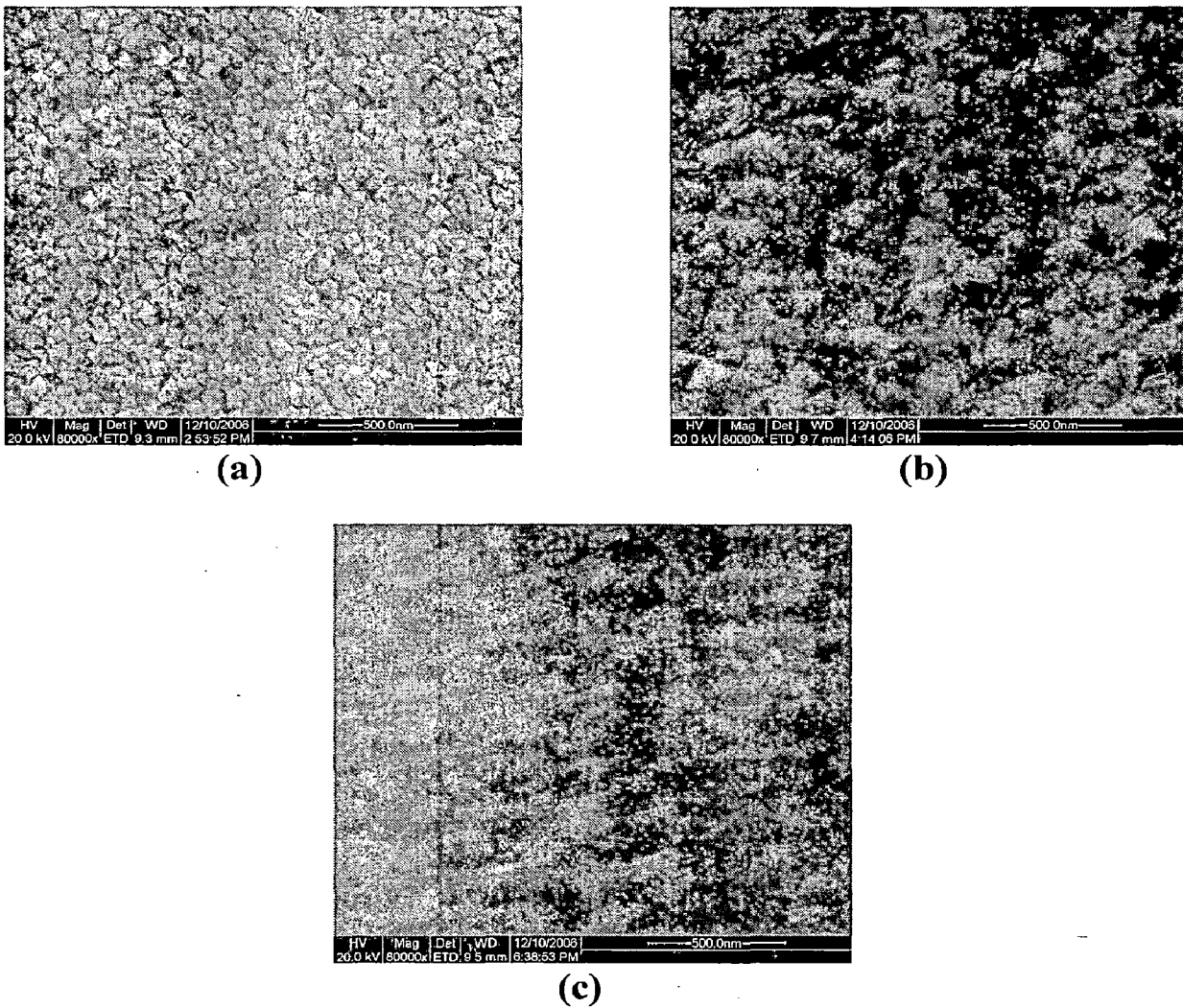


Figure 4.8: FE-SEM images of TiN films deposited on glass substrate at thickness (a) 0.63 μm , (b) 1.26 μm and (c) 1.89 μm

The preferred orientation of grains with (200) texture in TiN thin films is evident from the XRD peaks up to thickness 1.26 μm and it exhibits columnar grain shape as observed from the FE-SEM images in **Figure 4.8(a) and (b)**. However, thin films with 1.89 μm exhibit diffused grain structure when (220) peak dominates as shown in **Figure 4.8(c)**.

The load-displacement curve obtained during nanoindentation testing of the TiN thin films in different loading rates (2.5, 5.0, 10.0, 20.0 and 40.0 mN/minute) is shown in **Figure 4.9**.

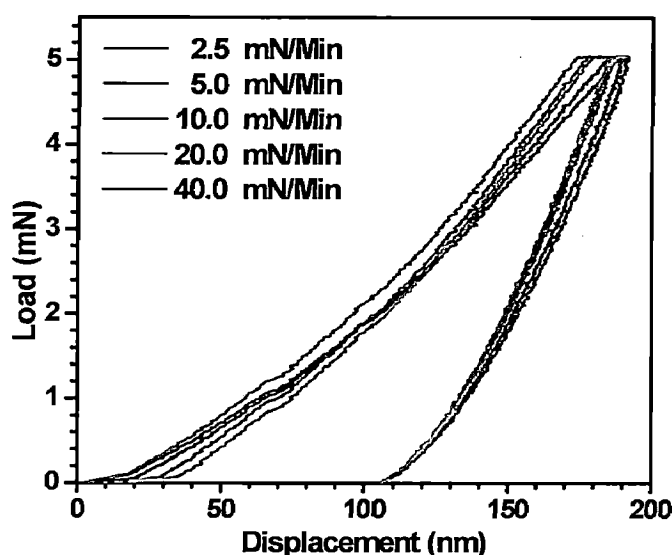


Figure 4.9: Load-Displacement curve of TiN thin films deposited on glass substrate

The maximum load used was 5 mN at different loading rates used in the present work. For each sample, fifteen measurements were performed at different loading rates and the average value was reported. **Figure 4.10(a)** shows the influence of thickness on hardness of TiN thin films. The hardness value increases with increasing film thickness from 0.3 μm to 1.89 μm but it drops for $> 2.5 \mu\text{m}$ thick films. The texture coefficient of TiN thin films increases with thickness due to the preferred orientation (220) of the

films, which in turn reflects in higher hardness value. The influence of preferred orientation (220) of the grains on the higher hardness value can be explained by relating it with the resolved shear stress on the TiN slip system.

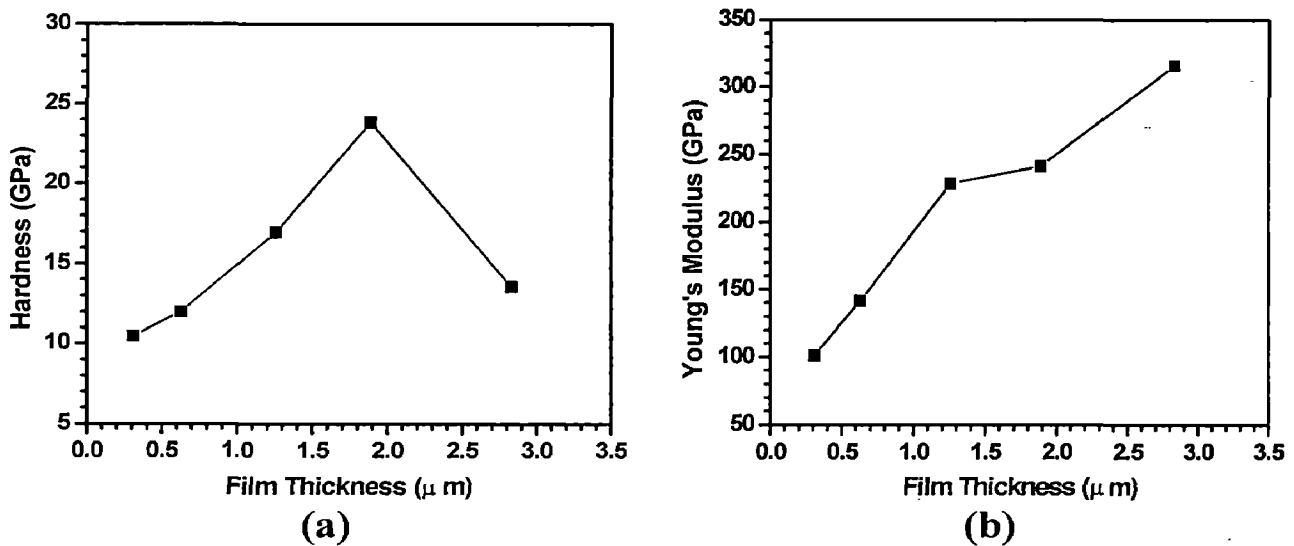


Figure 4.10: (a) Hardness of TiN thin film as a function of film thickness on glass substrate

(b) Young's Modulus of TiN thin film as a function of film thickness on glass substrate

The higher hardness of TiN films with (220) with preferred orientations may be attributed to very fine grain size (18.5 nm) with its less active slip system. The drop in hardness value of TiN thin film with thickness $> 2.5 \mu\text{m}$ may be due to higher surface roughness of the film.

The Young's modulus (E) of TiN thin films is shown in **Figure 4.10(b)**. It is evident that E increases with thickness due to increased anisotropy of the film with (220) preferred orientation. The films with higher thickness may favor the textured film as well as the higher packing factor, which could influence the E value significantly. The modulus of elasticity of TiN films is less than that of the standard values cited in the

literature due to the porosity of the sputtered films. It is due to the following reasons: i) Pores reduce the cross sectional area of the samples across which a load is applied, ii) porosity acts a stress raiser, which decreases the resistance to elastic deformation significantly. With increase in film thickness, the porosity of the films would increase depending upon the growth of columnar grains with voids, influenced by the deposition conditions such as working pressure, substrate temperature, and bias voltages. The porosity (P) of the films can be calculated by the following equation (Jin *et al.* 1995):

$$P = (d_a - d_m)/d_a \quad (4.2)$$

where, d_a is the apparent thickness of the films and d_m is the mass thickness, i.e. the theoretical thickness of the films without porosity. With increase in apparent thickness, the porosity of the film would increase as evident from the equation.

Table 4.3 show the average micro strain obtained from (111), (200) and (220) peaks of TiN film on glass substrate were calculated by the following equation (Ong *et al.* 2002, Singh *et al.* 2008):

$$\varepsilon = (a - a_o)/a_o \times 100 \quad (4.3)$$

where, a is the lattice parameter of the strained TiN films calculated from XRD data and a_o is the unstrained lattice parameter of TiN (4.23 Å). The lattice parameter, a of TiN films were calculated using the equation of cubic structure (Cullity *et al.* 2001):

$$\frac{1}{d^2} = \frac{(h^2 + k^2 + l^2)}{a^2} \quad (4.4)$$

where, d is the interplanar distance obtained from the position of the (111), (200) and (220) peaks using the Bragg condition, a is the lattice parameter and h , k and l are planes.

Table 4.3: Different properties of TiN thin films with varying film thickness

S. N.	Film Thickness (μm)	Crystallite size XRD (nm)	Average Roughness AFM (nm)	Micro Strain
1)	0.31	8.5	7.6	-0.116
2)	0.63	27.0	9.6	0.541
3)	1.26	45.1	12.4	0.002
4)	1.89	29.4	11.3	0.060
5)	2.83	47.4	19.0	0.609

It is found that initially micro strain was negative and after that all values are positive with increasing thickness. The highest hardness was found for the TiN films with thickness 1.89 μm and it showed less positive micro strain.

4.2.4 Conclusion

Nanocrystalline TiN thin films were deposited on glass substrate by DC magnetron sputtering. The effect of film thickness on H and E was investigated by nanoindentation technique. The formation of nanosized crystallites in the thin films has been confirmed from the XRD, AFM and FE-SEM characterizations. The preferred orientation of TiN film is (200) up to thickness 1.26 μm and (220) & (200) peaks dominate, respectively, with increase in thickness up to 2.83 μm . It is because of the competition between surface energy and strain energy during film growth. The hardness of TiN thin film, increases with increase in thickness up to 1.89 μm (maximum hardness of 24 GPa) but it drops for > 2.5 μm thick films. There was no drop in modulus of elasticity and it

increases with increase in film thickness. The TiN films with highest hardness exhibits a less positive micro strain.

4.3 Analysis of Thermal Stress in Magnetron Sputtered TiN coating by Finite Element Method

4.3.1 Introduction

Thin hard coatings such as TiN, Ti-Si-N, and Ti-Al-N exhibit excellent mechanical and tribological properties and provide superior wear resistance over the materials on which they are coated. The mechanical reliability of these hard coatings, deposited by various physical vapor deposition techniques (PVD), is strongly influenced by residual stress which originates from growth stresses, geometrical constraints, thermal gradients and service stress. When a coating is deposited at higher temperature and cooled down to room temperature, thermal residual stress generates due to thermal expansion mismatch between the coating and substrate. When the coating-substrate combination, is subjected to thermal gradients, the coefficient of thermal expansion mismatch (CTE) between them causes a variation of thermal stress through the thickness of the coating. Subsequently, it transforms into a shear at the interface between coating-substrate, causing the coated substrates to contract, elongate or bend (Teixeira 2001). The failure of coating may occur by cracking and spalling, which are dependent on magnitude of the residual stress and the relative strengths of coating and coating-substrate interface. The preexisting defects in the coatings, under tensile conditions, causes the formation of through thickness cracks, which generate shear stresses along the interface resulting in de-adhesion of the coatings. The spallation of the coating, under compressive stress, may occur either from the growth of a tensile, wedge crack along the interface or by buckling and cracking of the coating (Evans *et al.* 1984, Drory 1988, Thouless 1991).

The thermal residual stress of the sputter deposited thin coatings is influenced by various factors such as CTE, Poisson's ratio, Young's modulus, thickness and thermal conductivity of coating and substrates as reported in the literature (Wiklund *et al.* 1999, Haider *et al.* 2005). If the CTE mismatch and substrate temperature of thin hard coatings are very high, the induced thermal residual becomes a vital issue to ensure the reliability of the coatings for its various structural and functional applications. Wiklund *et al.* (1999) investigated the influence of residual stress on fracture and delamination of thin hard coatings such as TiN, TiC, and CrN on the different substrates with different geometries by FEM analysis. They have shown that normal stress across the interface of the coating comparable to that of residual stress is induced at a critical coating thickness, which causes the delamination of the coatings. According to their analyses, the interface stress state becomes independent of the coating thickness if the coating is thicker than about three times the amplitude of the interface roughness and it scales linearly with maximum inclination of the surface profile. The experimental study (Wiklund *et al.* 1999) has shown that the high residual stress results in fracture and delamination of ceramic coatings at the tip of an edge or rough substrate surfaces, when the thickness of the coatings was higher than that of the edge radius.

Bielawski *et al.* (2005) have measured the residual stress generated in sputter deposited TiN coatings on Si and steel substrates by using the surface curvature method. They observed that the TiN coatings sputter deposited on steel substrates at high bias and low deposition pressure are highly stressed. It was attributed to intense ion bombardment producing high compressive residual stress in the coatings. The residual stress in TiN coating on steel substrate was larger than that of the TiN coating on Si substrate due to its large difference in CTE. It was shown in their work that critical

post-annealing treatment, above the deposition temperature, is required to relieve the residual stress present in the as deposited coatings. The residual stress in DC and pulsed DC unbalanced magnetron sputtered TiN thin films on cemented carbide substrate was investigated under different deposition conditions such as bias, target power and pulsed power through XRD/Sin²Ψ method by Benegra *et al.* (2006). They observed the higher compressive residual stress in the coatings deposited with higher negative bias and the pulsed power. The microstructural characteristics and mechanical properties of the PVD deposited TiN coating are strongly influenced by the residual thermal stress in the coatings. Therefore, the present work has been focused to simulate the thermal stress generated in the sputter deposited TiN coatings on Si and glass substrate under different conditions by finite element analysis.

4.3.2 Modeling

4.3.2.1 Analytical Model for thermal stress

Tsui *et al.* (1997) have used an analytical model for calculating the residual stress in progressively deposited coatings for the planar geometry configuration. By combining their analytical model and Stoney's equation for tension of metallic films, the thermal stress in thin coating can be obtained as (Stoney 1909),

$$\sigma_f = \frac{E_{ef} \int_{T_r}^{T_d} (\alpha_s - \alpha_f) dT}{1 + 4(E_{ef} / E_{es})(h/H)} \quad (4.5)$$

where $E_{ef} = E_f / (1 - \nu_f)$, $E_{es} = E_s / (1 - \nu_s)$, E_f , E_s , h , H , α_f , α_s , ν_f , ν_s , T_r and T_d are effective Young's modulus of the coating, effective Young's modulus of the

substrate, Young's modulus of the coating, Young's modulus of the substrate, coating thickness, substrate thickness, coefficient of thermal expansion of the coating, coefficient of thermal expansion of the substrate, Poisson's ratio of the coating, Poisson's ratio of the substrate, room temperature and substrate temperature respectively.

4.3.2.2 Finite Element Analysis

The thermal stress generated in sputter deposited TiN coating was analyzed by FEM with the following dimension of the samples. A cylindrical shaped substrate of 30 mm diameter and 3.0 mm thickness, and on the top surface, TiN coating of thickness 3.0 μm were considered for both glass and silicon substrates. These dimensions allow the coating-substrate to bend upon the development of thermal stress in the sputter deposition of TiN coating. Thermoelastic behavior of the coatings and substrates were assumed during the analysis. The plain biaxial stress was considered along with the uniform temperature maintained over the sample at the processing temperature as well as after cooling. The physical and mechanical properties of the TiN coating and substrates (Glass and Silicon) are given in **Table 4.4**.

Table 4.4: Properties of coating and substrates materials

S.N.	Properties	Materials		
		TiN	Glass	Silicon
1)	Poisson's ratio	0.25	0.24	0.3
2)	Young's modulus (GPa)	600	69	167
3)	Coefficient of Thermal expansion ($\times 10^{-6} \text{ } ^\circ\text{C}^{-1}$)	9.4	9	2.33

Analyses were performed to study the effect of each parameter on thermal stress by varying it, for example, substrate temperature (100 to 600°C), while fixing three of the other parameters constant such as Young's modulus (600 GPa), coating thickness (3.0 μm), and substrate thickness (3.0 mm). The Young's modulus values of TiN vary with in the range of 350 – 600 GPa as reported in the literature (Torok *et al.* 1987, Rouzaud *et al.* 1995) and therefore in the simulation, the similar variations were imposed. The axisymmetric plane parallel to XY plane was taken into account for the two dimensional FEA, as shown in **Figure 4.11** in the present work.

The thermal, shear and radial stresses generated in the TiN coating deposited on glass and silicon substrates were simulated by ANSYS finite element analysis (ANSYS 2003). The thermal stress in TiN coated glass and Si substrate was simulated using the four-node structural and quadratic element PLANE 42 with axisymmetric condition. Mapped meshing was carried out using the quadrilateral-shaped elements. The element size across the plane was decreased in a graded fashion near the coating-substrate interface due to its very high stress concentration (Wright *et al.* 1999). The fine mesh was imparted near the edge across the thickness of the coating and substrate and it was refined until the results are consistent with only small changes. The left side of the model corresponds to the axis of the axisymmetric model and to restrict any movement, left corner of the model was pinned so that bending occurs during cooling. The similar axisymmetric configuration was used for the coating on rough substrate as shown in **Figure 4.11**.

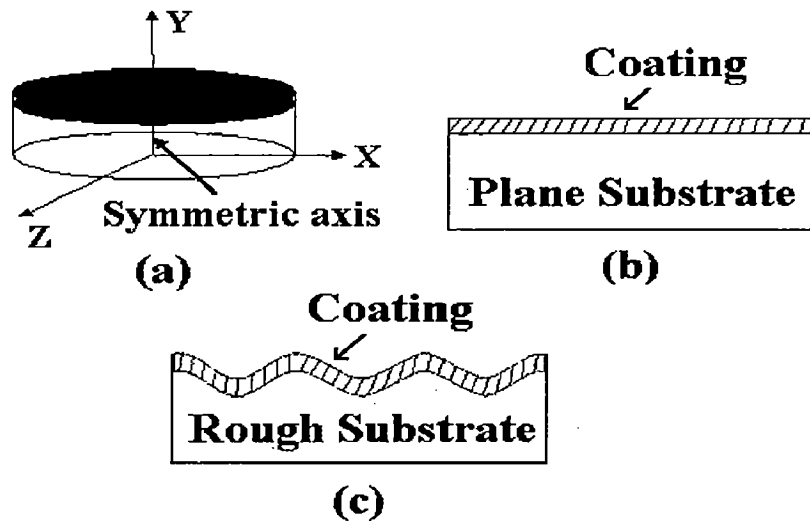


Figure 4.11: A Schematic of axisymmetric 2D solid model of plane and rough substrates

The substrate temperature of 600°C and uniform temperature of 25°C were fixed as reference temperature and uniform temperature, respectively for applying the thermal load over the substrate-coating system. The verification of the model was carried out by substituting the value of different properties of coating and substrate in the analytical **Equation 4.5**. The thermal stress in the FEM calculation is computed as maximum von Mises stress in the coating. The thermal load is applied over the coating-substrate combination and the induced thermal stress in the coating-substrate combination is computed as the sum of average value of radial and shear stress components.

4.3.3 Results and Discussion

For the isotropic behavior of the materials, the following results were obtained by the FEM analysis. The variation of thermal stress generated in TiN coating deposited on glass and Si substrates as a function of substrate temperature is shown in **Figure 4.12(a)** and **(b)** respectively.

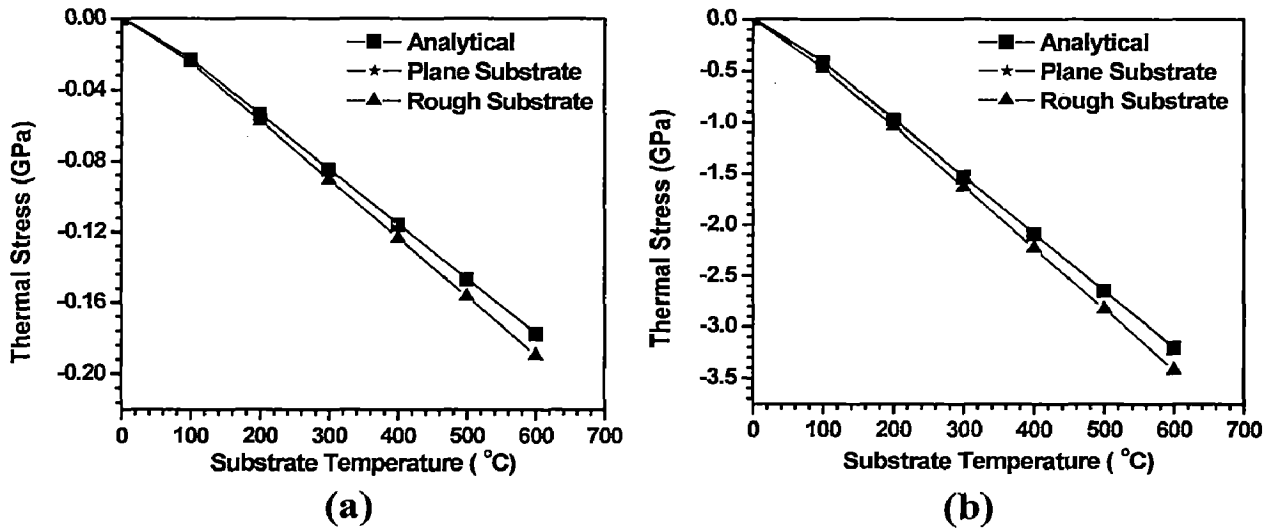


Figure 4.12: Thermal stress variation as a function of substrate temperature on (a) glass and (b) silicon substrate

It is evident that the thermal stress varies linearly with substrate temperature for the plane substrate and the values calculated by FEA analysis are in accordance with analytical model.

The thermal stress of TiN on silicon substrate induces a high compressive stress as shown in the **Figure 4.12(b)** against low compressive stress on glass substrate [**Figure 4.12(a)**]. Due to the high CTE mismatch between TiN and silicon substrate, the induced thermal stress in the coating is substantial. The linear relationship observed between thermal stress and substrate temperature of the TiN coating on glass and silicon substrate is due to the occurrence of increased thermal gradient during deposition process. The thermal stress in the TiN coatings can be relieved by post-annealing treatment. The influence of plane and rough surface topography of substrates (Glass and Si) on the thermal stress induced in the coating is compared in **Figure 4.12(a) and (b)**. It is evident that the compressive stress induced in the coating due to the thermal stress is higher with rough substrate when compared to planar substrate. The rough substrate

affects the adhesion of the coating-substrate interface and its thermal expansion behavior, thereby influencing the induced thermal stress in the deposited coatings at high temperature. It is well known that the rough substrate influence the differential nucleation and growth of deposited atoms on the substrate surface and subsequently lead to the intrinsic stress during the growth of the thin films.

The influence of coating thickness on the thermal stress of TiN coated on glass and silicon substrates is shown in **Figure 4.13**. The decrease in thermal stress with the increase of coating thickness is evident from this **Figure 4.13(a)** and it is due to the stress relaxation caused by the bending strain induced at higher thickness of the coating. The stress is reduced in the coating and substrate in proportion to the bending strain as reported in the literature (Mencik *et al.* 1995).

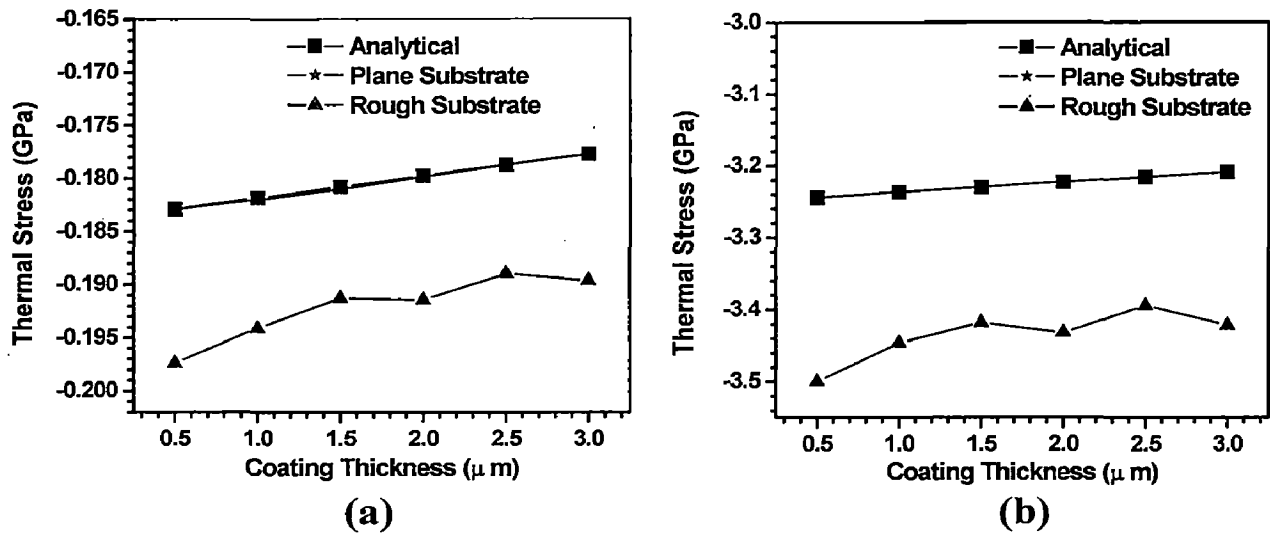


Figure 4.13: Thermal stress variation as a function of coating thickness on (a) glass and (b) silicon substrate

The bending effect is insignificant for the very thin coating with low stiffness but it is well pronounced for the coating with higher thickness values. The bending curvature in the coating-substrate may occur if the coating thickness is increased, which result in the

lower stress in the coating. The thermal stress of TiN coating on both glass and silicon substrates is compressive in nature and it decreases with increase in coating thickness. The influence of planar and rough surface topography of substrates (Glass and Si) on the thermal stress induced in the coating as a function of coating thickness is shown in **Figure 4.13(a) and (b)**. The rough substrate contributes to very high compressive stress in the coating as observed in this figure. The substrate roughness may influence the thickness of the deposited coatings, which in turn affect the induced thermal stress in the coatings.

The thermal stress of TiN coating increases with substrate thickness as shown in **Figure 4.14**. It is evident that thermal stress with increasing substrate thickness is compressive in nature in both cases (glass and silicon substrates), with a higher value for the silicon substrate.

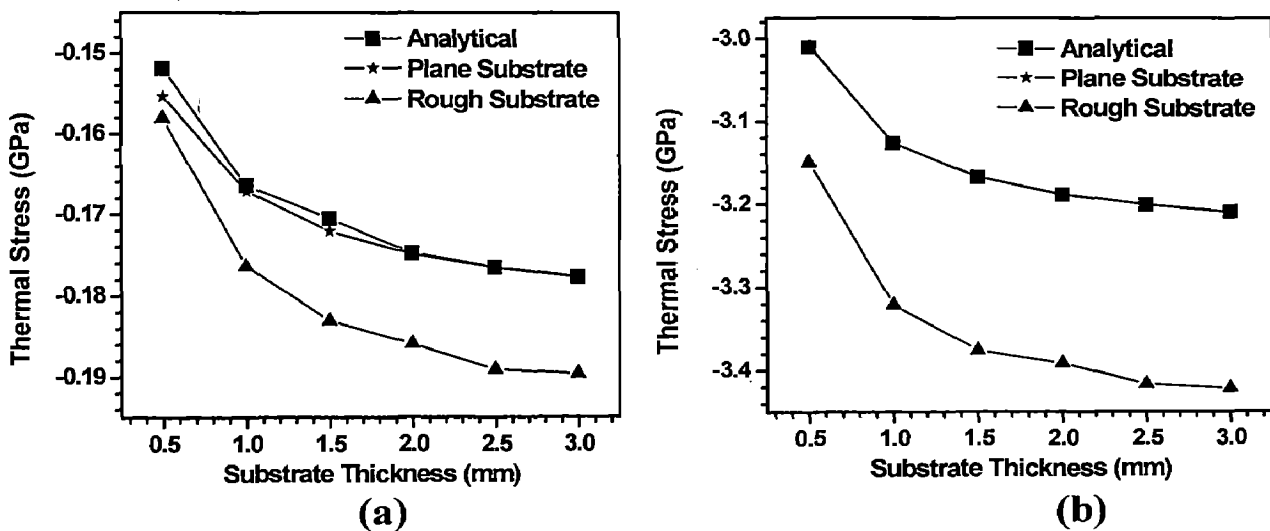


Figure 4.14: Thermal stress variation as a function of substrate thickness on (a) glass and (b) silicon substrate

The higher substrate thickness prevents the bending effect and therefore it can affect directly the thermal stress generated in the coating. The rough surface topography of

substrates (Glass and Si) increases the thermal stress, which becomes highly compressive in the coating with increasing thickness of substrate as compared to the planar surface of the substrates shown in **Figure 4.14(a) and (b)**.

The variation of thermal stress in TiN coating with Young's Modulus (E), on the glass and silicon substrates is plotted in **Figure 4.15(a) and (b)** respectively. The thermal stress of TiN coating increases with increase in Young's Modulus. The E value of the TiN coating depends on the sputtering process parameters such as deposition pressure, power and deposition rate.

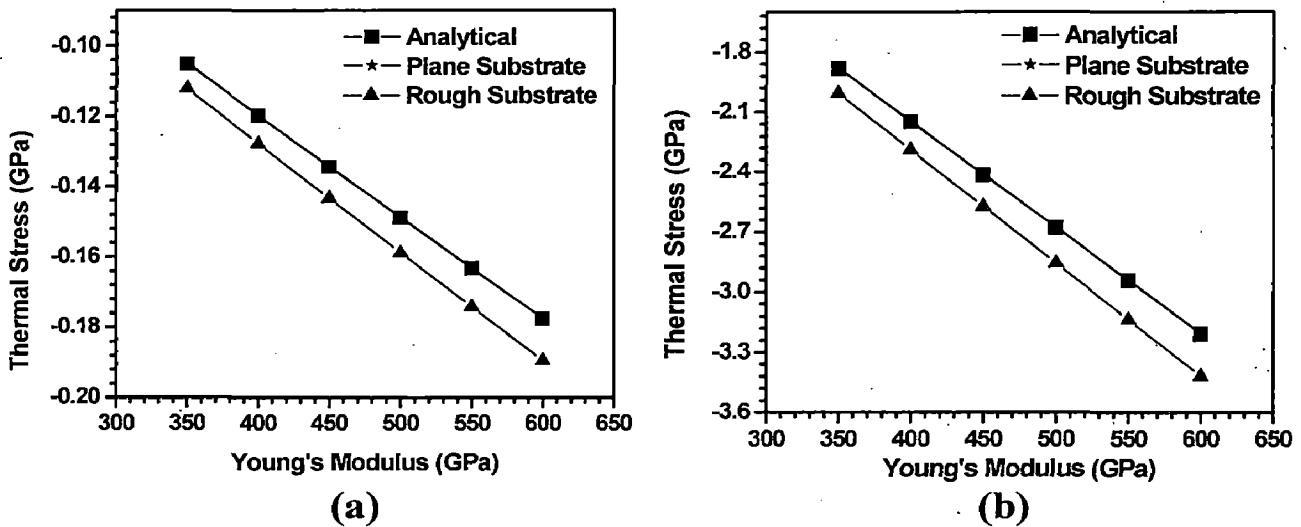


Figure 4.15: Thermal stress variation as a function of Young's Modulus on (a) glass and (b) silicon substrate

The impurities and porosity of the TiN films may affect its E value and the porosity of the coating thereby reduces the thermal stress generated. The higher thermal stress in the coating is observed for the rough substrates (Glass and Si) than that of the planar substrates, and exhibited a linear relationship with increase in Young's modulus.

The radial stress distribution through the thickness of the coating and substrates at different position from the edge to the center is evaluated and plotted in **Figure 4.16** for

both glass and silicon substrate. The stress gradient and its transition from tensile to compressive occurs through the thickness of the substrates and reaches a maximum value near the interface between coating and substrates. The radial stress is very high at a distance of $-5h$ from the substrate edge. Through the thickness of the coating, in case of both substrates, tensile radial stress is observed from the bottom to top surface.

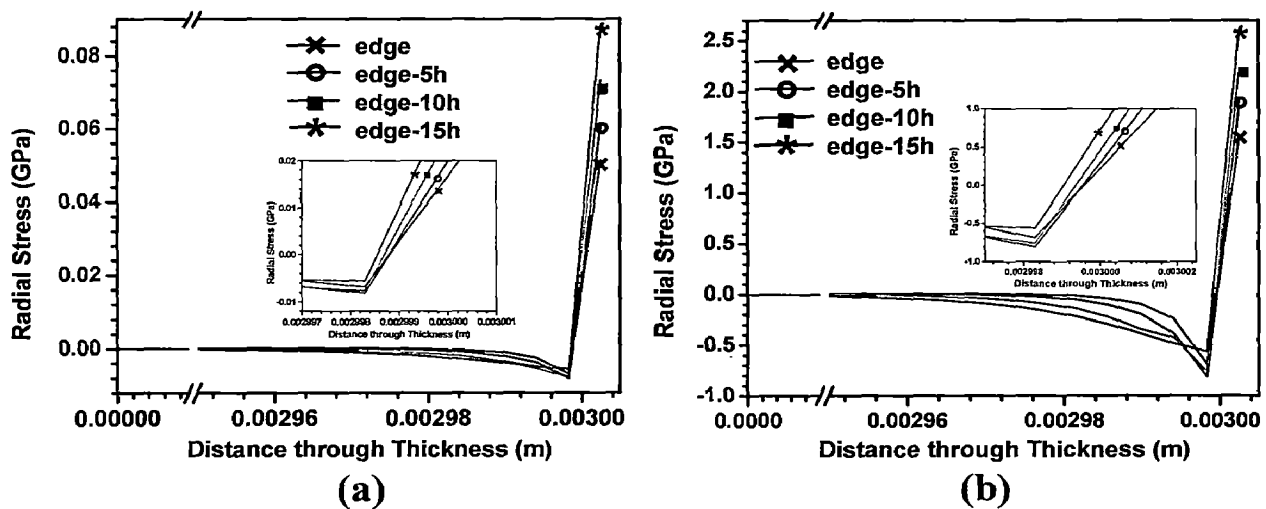


Figure 4.16: Radial stress (σ_r) distribution through the thickness of coating and substrate at different position from the edge to the center on (a) glass and (b) silicon substrate

The minimum radial stress is noticed at the edge of the coating but it increases with the distances, such as $-5h$, $-10h$ and $-15h$ away from the edges. In between the two substrates, coating on silicon substrate exhibit high tensile radial stress as compared to coating on glass substrate. The large tensile radial stress in the coating is due to the higher substrate-to-coating thickness ratio.

The shear stress distributions of TiN coating on glass and silicon substrates are shown in **Figure 4.17(a) and (b)** respectively. The maximum compressive shear stress is evident at the interface in the coating edge in the case of both glass and silicon

substrates. The CTE mismatch between substrates (Glass and Si) and TiN is responsible for the compressive shear stress at the coating edge and it exhibited a decreasing trend at a distance of -5h, -10h and -15h away from the edge in both substrates.

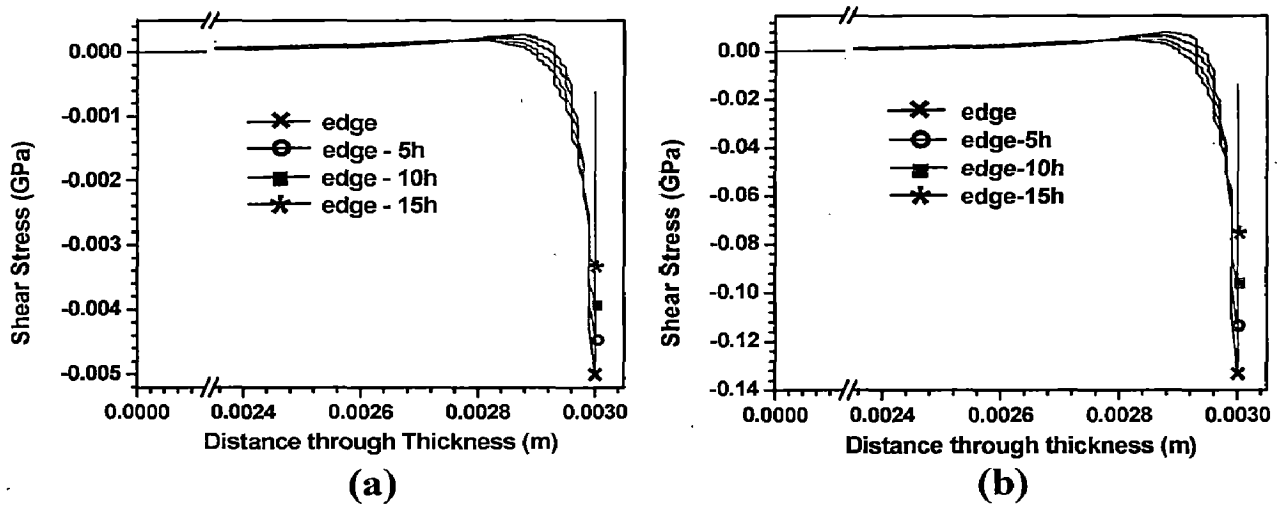


Figure 4.17: Shear stress (σ_{xz}) distribution through the thickness of coating and substrate at different position from the edge to the center on (a) glass and (b) silicon substrate

There is no stress reversal in the TiN coating away from its edges. The adhesive strength of TiN coating on glass substrate may be less due to the less compressive shear stress observed in the present work. However, the high compressive shear stress of TiN coating on Si substrate is beneficial in improving adhesive strength of the coating.

4.3.4 Conclusion

The thermal stress of TiN coating sputter deposited on glass and silicon substrate has been simulated by finite element analysis (ANSYS) and compared with that of analytical model. The thermal stress of coatings exhibits a linear relationship with substrate temperature, substrate thickness and Young's modulus of the coating. However, it exhibits an inverse relationship with the coating thickness due to the stress

ation. The thermal stress induced in the coatings for the rough substrate is higher compared to that of the planar substrate. The radial stress of the TiN coating is tensile nature on both substrates but it is high on the silicon substrate. The higher shear stress of the TiN coating is observed along the interface at the edge due to the higher stress concentration. The compressive shear stresses are observed for TiN coating on glass and silicon substrates. The spallation of the coatings from the edge is heavily dependent on these shear stresses. The adhesive strength of the TiN coating on silicon substrate is higher when compared to glass substrate due to the high compressive stress developed in the former.

Chapter 5

Synthesis and Characterization of Titanium Silicon Nitride Films

5.1 Study of Structural and Mechanical Properties of Sputter Deposited nanocomposite Ti-Si-N thin films

5.1.1 Introduction

Ti-Si-N nanocomposite coatings have been shown immense interest in recent years due to its very high hardness, high wear resistance, and improved thermal stability as compared to TiN [Shizhi *et al.* 1992, Desirens *et al.* (1998, 1999), Veprek *et al.* (1998, 2000), Vaz *et al.* 2000, Patscheider *et al.* 2001, Martin *et al.* 2003]. It was developed during the early 1980s (Hirai *et al.* 1983, Park *et al.* 2006) and the processing, structure, and property of nanocomposite coating were investigated in detail by Veprek *et al.* (1995a, 2005) and Prochazka *et al.* (2004). According to Veprek *et al.* (2005), for the development of superhard and thermally stable nanocomposites, the formation of stable nanostructures by self-organisation is essential through the thermodynamically driven spinodal phase segregation. A high nitrogen activity (partial pressure $\geq 1 \times 10^{-3}$ mbar) and deposition temperature of 500-600°C are required to realize the formation of thermally stable nanocomposites. The maximum hardness of nanocomposites is achieved when one monolayer of Si₃N₄ covers the surface of polar, hard transition metal nitride nanocrystals such as TiN, W₂N, etc. They reported that the factors such as formation of atomically sharp interfaces, impurities (oxygen contents) < 0.2 at %, and formation of tiny nanocrystals achieved through the deposition conditions favorable for thermodynamically driven phase segregation is essential for fabricating superhard nanocomposite coatings. Prochazka *et al.* (2004) has synthesized nanocomposite TiN/Si₃N₄ with stable nanostructures by reactive magnetron sputtering and observed its high hardness value of ≥ 45 GPa. They reported that its high hardness value is due to

the higher nitrogen pressure ≥ 0.002 mbar and high deposition temperature 550-630°C used in the sputtering, which are favorable for the formation of stable nanostructures facilitated by phase segregation. An enhancement of hardness and refractory properties manifested in the nanocomposite Ti-Si-N was elucidated with the size effect of TiN nanocrystals embedded in the Si₃N₄ amorphous matrix, which act as an effective barrier for dislocation motion as reported in the literature (Veprek *et al.* 2005). Silicon content affects the physical properties of the films such as electrical resistivity, oxidation stability, and diffusivity. For example, the formation of amorphous Si₃N₄ thin films depends on Si content, which serves as an effective diffusion barrier than its polycrystalline films due to the absence of grain boundaries and extended defects. The Si content also reduces grain size of the TiN in nanocomposite Ti-Si-N thin films through the incorporation of amorphous SiN_x between grains. The absence of distinguishable crystalline phases in the nanocomposite films with fewer defects contribute to increased resistivity and barrier strength [Juo *et al.* 1981, Doyle *et al.* 1982, Nicolet *et al.* 1983, Nicolet 1995, Sun *et al.* 1997(a, b, c), Kacsich *et al.* {(1999a, b), (2000)}, Varesi *et al.* 2007].

Kim *et al.* (2002b) have investigated Ti-Si-N hard coatings deposited on SKD11 steel substrates, in which TiN was deposited by the arc ion plating (AIP) method while Si was incorporated into the films by sputtering technique. A maximum hardness of 45 GPa at Si content of 7.7 at.% was observed in the coatings. The size of TiN crystallites has reduced with increasing Si content and it was distributed with multiple orientations in the amorphous silicon nitride phase. Surface roughness of the Ti-Si-N coating also has decreased with increase of Si content. Mei *et al.* (2005) have deposited Ti-Si-N nanocomposite films on high speed steel substrates by reactive magnetron sputtering.

The microstructure and mechanical properties of films are affected by the varying percentage of Si contents. TiN nanocrystals with grain size of about 20 nm were formed in the Ti-Si-N films, with the Si contents ranging from 4.0 at.% to 9.0 at.%, and they were surrounded by Si_3N_4 interphase (1 nm thick) as observed in their work. The hardness (H) and elastic modulus (E) of films have increased with increasing Si contents and its maximum H and E values were 34.2 GPa and 398 GPa, respectively. With the further increase of Si content, the mechanical properties of films have reduced gradually and finally it reached lower than that of the TiN films. Jiang *et al.* (2004) have deposited Ti-Si-N on Si (100) substrates at room temperature by reactive unbalanced DC-magnetron sputtering and characterized by XPS. It was shown that in Ti-Si-N films, the Si bonding was in the form of Si_3N_4 with low Si contents (≤ 14 at.%), while it was in the form of both Si and Si_3N_4 at high Si contents (≥ 18 at.%). Also, the grain size and surface roughness have decreased due to higher nucleation rate with increase in Si content.

Kim *et al.* (2002a) have investigated the DC reactive magnetron sputtered Ti-Si-N on SKD 11 steel substrate using HRTEM and XPS. They reported that the films consist of nano-sized TiN crystallites surrounded by an amorphous Si_3N_4 and crystallites of initially aligned microstructure are finer, randomly oriented, and fully penetrated by amorphous phase with increase in Si content; the films showed a nearly amorphous phase with higher Si content. The free Si was observed in the films, due to the deficit of the nitrogen source, when Si content was increased. The hardness value of approximately 38 GPa was obtained from the Ti-Si-N films with the Si content of 11 at.%, which showed a microstructure of fine TiN crystallites dispersed uniformly in an amorphous matrix. The hardness reduction with increase of Si content beyond a critical

point was attributed to the thickening effect of amorphous Si_3N_4 rather than to the effect of free Si. Cairney *et al.* (2005) have deposited Ti-Si-N coatings on Si(100) wafers by concurrent cathodic arc evaporation and magnetron sputtering. These Ti-Si-N coatings of varying Si contents were examined by cross-sectional transmission electron microscopy and observed that the samples with low contents (0.8 and 1.5 at.% Si) exhibits a columnar grain structure, which is deformed by intergranular cracking and shear sliding at the grain boundaries, while samples with higher Si contents (9.5 and 12.5 at.% Si) consisted of TiN nanocrystals of 5 nm in size connected by an amorphous Si_3N_4 matrix. Xu *et al.* (2007) have studied the reactive magnetron sputtered Ti-Si-N films on 321 steel substrates and substantiated the influence of Si into TiN, especially on microstructure and adhesion of the coating/substrate system. They have reported that the films consist of fine TiN crystals surrounded by an amorphous Si_3N_4 matrix and with increasing Si contents, the orientation of TiN crystals shifts from (111) to (200), the crystallite size significantly diminishes from 15 nm in a pure TiN thin films to 4.2 nm in the Ti-Si-N thin films containing 22.6 at.% Si. The addition of a certain amount of Si increases the hardness and Young's modulus of the coatings, reaching maximum values to 42 GPa and 320 GPa, respectively. The scratch tests indicated that the adhesive strength also improves with Si addition. Rebouta *et al.* (2000) have deposited Ti-Si-N films on polished tool steel and high speed steel substrates (AISI M2) by reactive magnetron sputtering. The films revealed higher hardness values than those obtained for TiN. The hardness increases with small Si additions reaching the maximum values for Si content between 4 and 10 at.%. The denser sample (4.7 g/cm^3) with a Si content of approximately 2 at.% showed maximum E value of 462 GPa.

Nanocomposite Ti-Si-N thin films deposited on Si (100) and stainless steel (type 304) substrate require a detailed investigation as a function of varying deposition parameters to substantiate the influence of microstructures on its mechanical properties. In order to ensure compatibility and reliability of the sputter deposited Ti-Si-N thin films in diffusion barriers and tribological applications, the present work has been focused to investigate the DC/RF magnetron sputtered nanocomposite Ti-Si-N thin films with varying Si content. The films were characterized by XRD, FE-SEM, AFM and TEM to reveal the influence of processing parameters on microstructural characteristics and the atomic percentage of Si in the Ti-Si-N thin films were measured using Energy Dispersive Spectroscopy (EDS) attached with FE-SEM. The hardness and Young's modulus of the films were measured by nanoindentation technique.

5.1.2 Experimental Details

5.1.2.1 Synthesis of Ti-Si-N films

The Ti-Si-N films were deposited on Si (100) and Stainless Steel (type 304) substrates by DC/RF magnetron sputtering. The Si substrate was cleaned by first rinsing in Hydrofluoric acid to remove SiO₂ layer and then ultrasonic baths of acetone and methanol and finally dried under nitrogen gas. The Stainless Steel (type 304) substrate was first polished by using 1/0, 2/0, 3/0 and 4/0 grid SiC emery papers and then cloth polished upto mirror finish. The substrates were cleaned by ultrasonic baths to remove the SiC and dust particles. The sputtering targets were 99.99% pure Ti & Si disc (2" diameter & 5 mm thick) fixed at an angle of 45° to each other and with the use of rotator, the substrate was rotated between Ti & Si targets continuously to perform a co-sputtering. DC sputtering and RF sputtering for Ti and Si targets were used,

respectively, during deposition. The base pressure was better than 2×10^{-6} Torr and the sputtering was carried out in an Ar + N₂ atmosphere with the ratio 80:20. Reactive sputtering was used to deposit Ti-Si-N films in the present work. Before starting the deposition, the targets were pre-sputtered for 15 minutes with a shutter located in between the targets and the substrate. This shutter is also used to control the deposition time. All the deposition was performed at a fixed substrate to target distance of 50 mm. The sputtering parameters for Ti-Si-N films with varying Si content are included in **Table 5.1**.

Table 5.1: Sputtering parameters for Ti-Si-N films with varying Si content

Target	Titanium and Silicon
Base pressure	2×10^{-6} Torr
Gas Used	Ar + N ₂ (80:20)
Sputtering pressure	5 mTorr
Deposition time	90 minute
Sputtering power for Ti target	150 W
Sputtering power for Si target	25-125 W (3.0-21.4 at. %)
Substrate used	Si (100) and Stainless Steel (type 304)
Substrate Temperature	300° C

5.1.2.2 Characterization details

XRD (Bruker AXS, D8 Advance) measurements with using CuK α ($\lambda=1.54$ Å) radiation to characterize the Ti-Si-N thin films. The excitation voltage and current were set to a 40 kV and 30 mA respectively, in the diffractometer. The grain size of the Ti-Si-N films was estimated from the Scherrer's formula, as given in **Section 3.1.2.2 (Equation 3.1)**.

Cross sectional FE-SEM images were used to measure the thickness of Ti-Si-N films deposited on Si(100) substrate. FE-SEM (FEI, Quanta 200F) and HRTEM (FEI, Tecnai 20) were used to characterize the microstructures of the Ti-Si-N thin films at an acceleration voltage of 20 kV and 200 kV, respectively. The surface morphology (3D) of the Ti-Si-N films was characterized by AFM (NT-MDT, Ntegra) operated in semicontact (tapping) mode and the root-mean-square (RMS) roughness of the surface of the sample was calculated from AFM scan at five different spots for each sample.

The hardness and Young's modulus of the Ti-Si-N films were measured by nanoindentation technique (Hysitron). The diamond Berkovich indenter is forced into the thin films being tested under constant load conditions. The loading profile during indentation testing followed linearly increasing with a hold time of 5 sec at the peak load. The loads used were 10, 15, 20, 25 and 30 mN at loading rate of 20.0 mN/min in the present work. A total of four indentations for each load were made on each sample and the average hardness and Young's modulus of Ti-Si-N films were calculated from the load-displacement curve obtained from the nanoindentation testing.

5.1.3 Results and Discussion

The XRD peaks for the nanocomposite Ti-Si-N films deposited at varying Si contents on Si and Stainless Steel substrates are shown in **Figure 5.1(a) and (b)**, respectively. It is observed from these figures that with increasing Si content upto 12.8 at.%, the films exhibit (111) preferred orientation but with increase in Si contents above 12.8 at.%, intensity of (200) and (220) peaks grows up. However, no signals corresponding to crystalline Si_3N_4 and various phases of titanium silicide could be observed. It shows that Si was present in an amorphous phase of either Si_3N_4 or Si,

which are in agreement with previous reports on Ti-Si-N nanocomposite films prepared by CVD and PVD (Kim *et al.* 2002a, Xu *et al.* 2007). With increase in Si contents of above 15.6 at.%, no peak could be observed in the XRD spectra, indicating that the TiN crystals become too tiny to detect or the whole coating becomes amorphous.

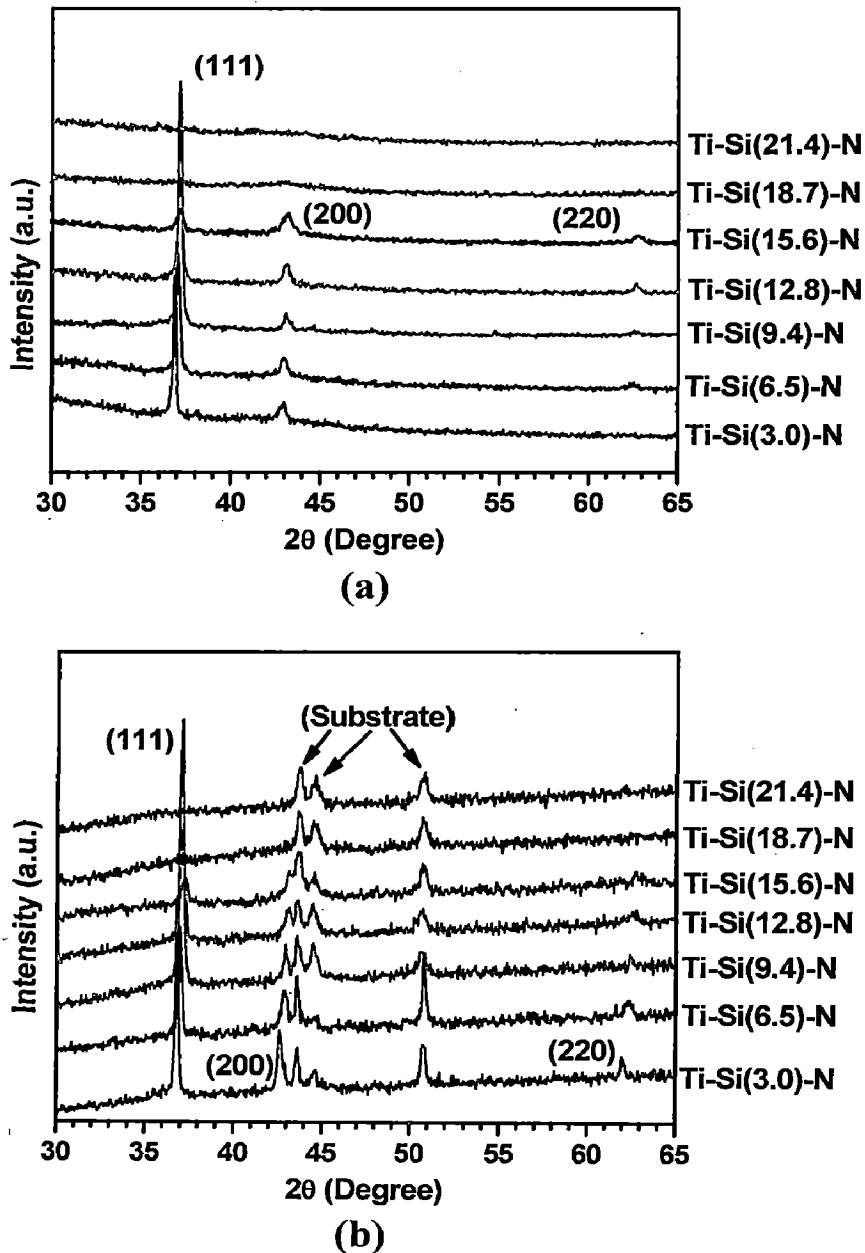


Figure 5.1: XRD peaks of Ti-Si-N films deposited with variation of Si content on (a) Si substrate and (b) Stainless Steel

The grain growth of TiN crystals is inhibited due to the presence of second phase particles causing Zener drag effect, which result in reduction of size of TiN crystals. The crystallite size of the thin film with 3.0 at.% Si, calculated from the X-ray peak broadening is 47.9 nm and crystallite size decreases with increase in Si content and the size reduces to 17.8 nm for 15.6 at.% Silicon. This indicates that TiN crystals become finer with the incorporation of the amorphous Si_3N_4 phase. It was also observed that with increase in Si contents, inter planar spacing, d decreases from 2.439 Å for 3.0 at% Si to 2.411 Å for 15.6 at % Si and thereafter, the films become amorphous with further increase in Si contents.

Figure 5.2 shows the texture coefficients of the nanocomposite Ti-Si-N films deposited at varying Si content calculated from their respective XRD peaks by using the formula, as given in **Section 4.1.3 (Equation 4.1)**. From **Figure 5.2**, it is observed that the texture coefficient of (111) peak dominates till the Si content reaches 12.8 at.% and afterwards, other orientations such as (220) and (200) peaks develops.

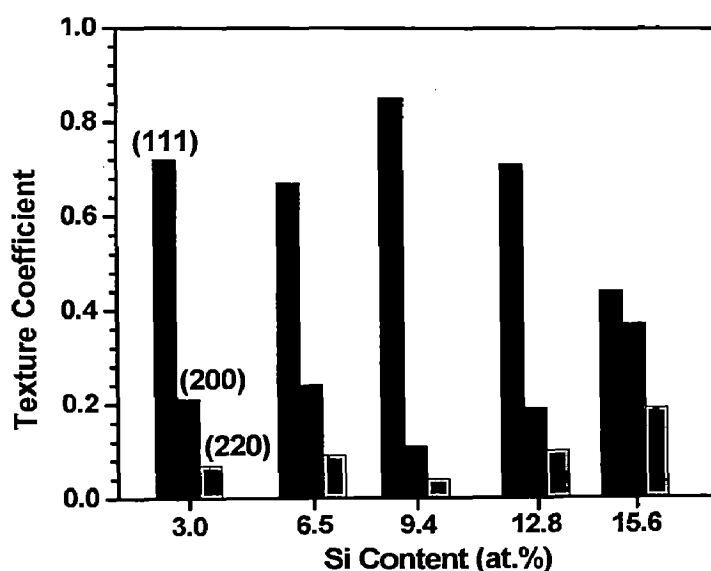


Figure 5.2: Texture coefficients of Ti-Si-N films with variation of Si content

The microstrain from (111) peak of Ti-Si-N films on Si and Stainless Steel substrates were calculated by the following equation (Ong *et al.* 2002, Singh *et al.* 2008):

$$\varepsilon = (a - a_0)/a_0 \times 100 \quad (5.1)$$

where, a and a_0 are the lattice parameters of the strained and unstrained Ti-Si-N films, respectively, which are calculated from XRD data (Vaz *et al.* 1999). The lattice parameter, a of Ti-Si-N films were calculated using the equation of cubic structure (Cullity *et al.* 2001):

$$\frac{1}{d^2} = \frac{(h^2 + k^2 + l^2)}{a^2} \quad (5.2)$$

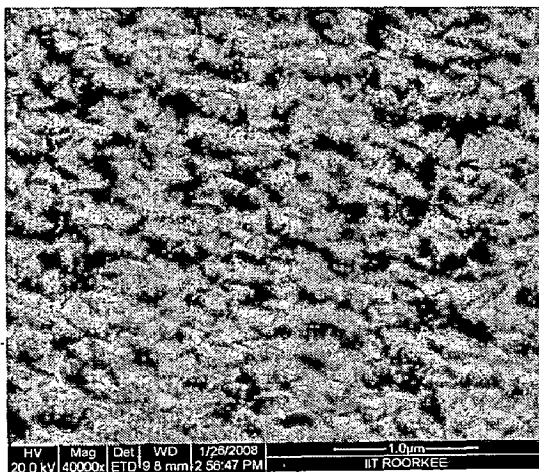
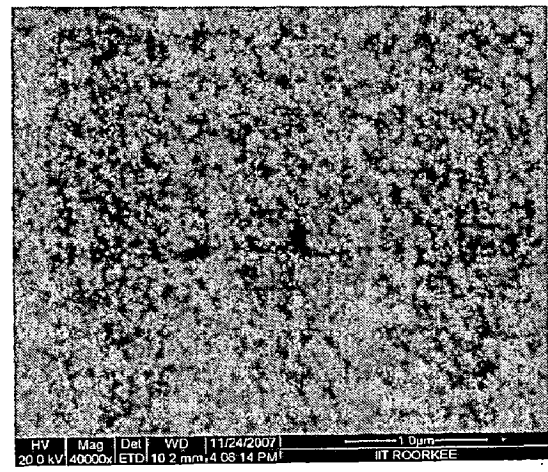
where, d is the interplanar distance obtained from the position of the (111) peak using the Bragg condition, a is the lattice parameter and h , k and l are planes.

The lattice parameters of the films on Si and Stainless Steel substrates for varying Si content are included in **Table 5.2** and it is observed that with increase in Si contents, lattice parameter, d decreases. It is also evident that with increase in Si contents, microrstrain, ε , decreases and the data of all Ti-Si-N films are included in **Table 5.2**.

Table 5.2: Properties of Ti-Si-N films with variation of Si content

Coating	Thickness (μm)	Interplanar spacing, d (111) peak	Crystallite size (nm) (111) peak XRD	Lattice parameter, a (\AA) (111) peak	Micro strain (111) peak	Average Roughness (nm) AFM	
						Si	SS
Ti-Si(3.0)-N	1.82	2.439	47.9	4.224	0.823	21.2	67.7
Ti-Si(6.5)-N	1.72	2.431	41.7	4.211	0.492	10.2	48.2
Ti-Si(9.4)-N	1.51	2.425	34.1	4.200	0.239	7.2	39.7
Ti-Si(12.8)-N	1.75	2.422	30.2	4.195	0.119	5.3	36.3
Ti-Si(15.6)-N	2.05	2.411	17.8	4.176	-0.096	4.1	33.8
Ti-Si(18.7)-N	1.72	--	--	--	--	4.0	29.4
Ti-Si(21.4)-N	2.35	--	--	--	--	3.9	22.8

The FE-SEM images of the Ti-Si-N films with increasing Si contents are shown in **Figure 5.3(a-d)**.

**(a)****(b)**

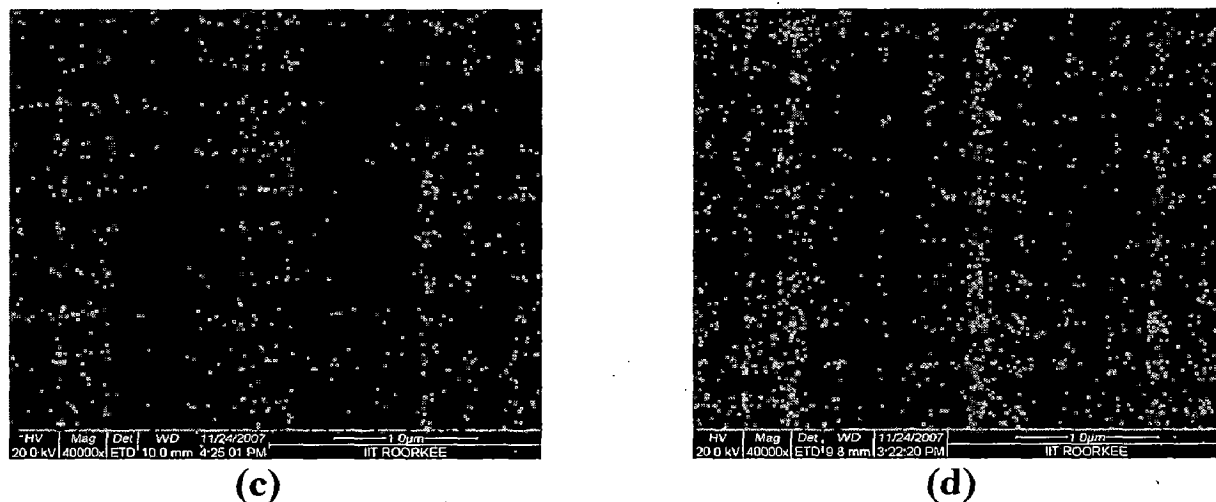


Figure 5.3: FE-SEM images of Ti-Si-N films deposited with variation of Si content
(a) 3.0 at.%, **(b)** 9.4 at.%, **(c)** 15.6 at.% and **(d)** 21.4 at.%

It is observed that with increase in Si contents, grain size decreases and the initial pyramidal shape grains transform into columnar and finally to amorphous structure. The atomic percentage of Si in the Ti-Si-N films is calculated from the EDS results.

Figure 5.4(a-d) shows the 3D AFM images of the Ti-Si-N films with increasing Si contents. It is evident from this figure that with increasing Si contents, grain size and surface roughness decreases, which could be explained from the XRD results. With increase in Si contents, X-ray peak broadening is observed indicating the size reduction of TiN. The root mean square values of surface roughness with different Si contents on Si (100) and Stainless Steel (Type 304) substrates calculated from the AFM images of the films are shown in **Table 5.2**.

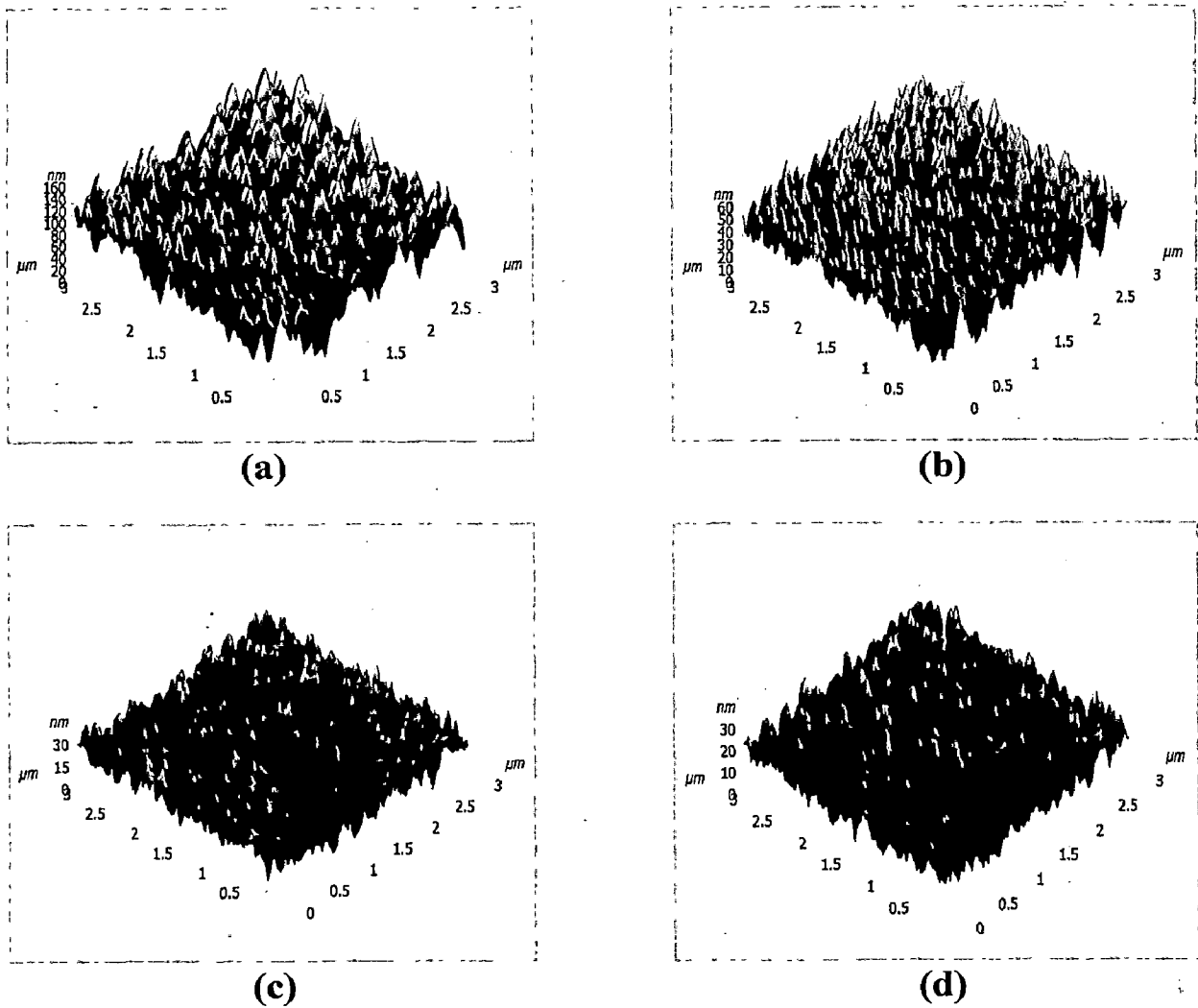


Figure 5.4: 3D AFM images of Ti-Si-N films deposited with variation of Si content
 (a) 3.0 at.%, (b) 9.4 at.%, (c) 15.6 at.% and (d) 21.4 at.%

Cross sectional FE-SEM images of varying Si content are shown in **Figure 5.5**. It shows a columnar morphology and it becomes denser with increasing Si content (21.4 at.%). The thickness of Ti-Si-N measured from cross sectional FE-SEM images is included in **Table 5.2**.

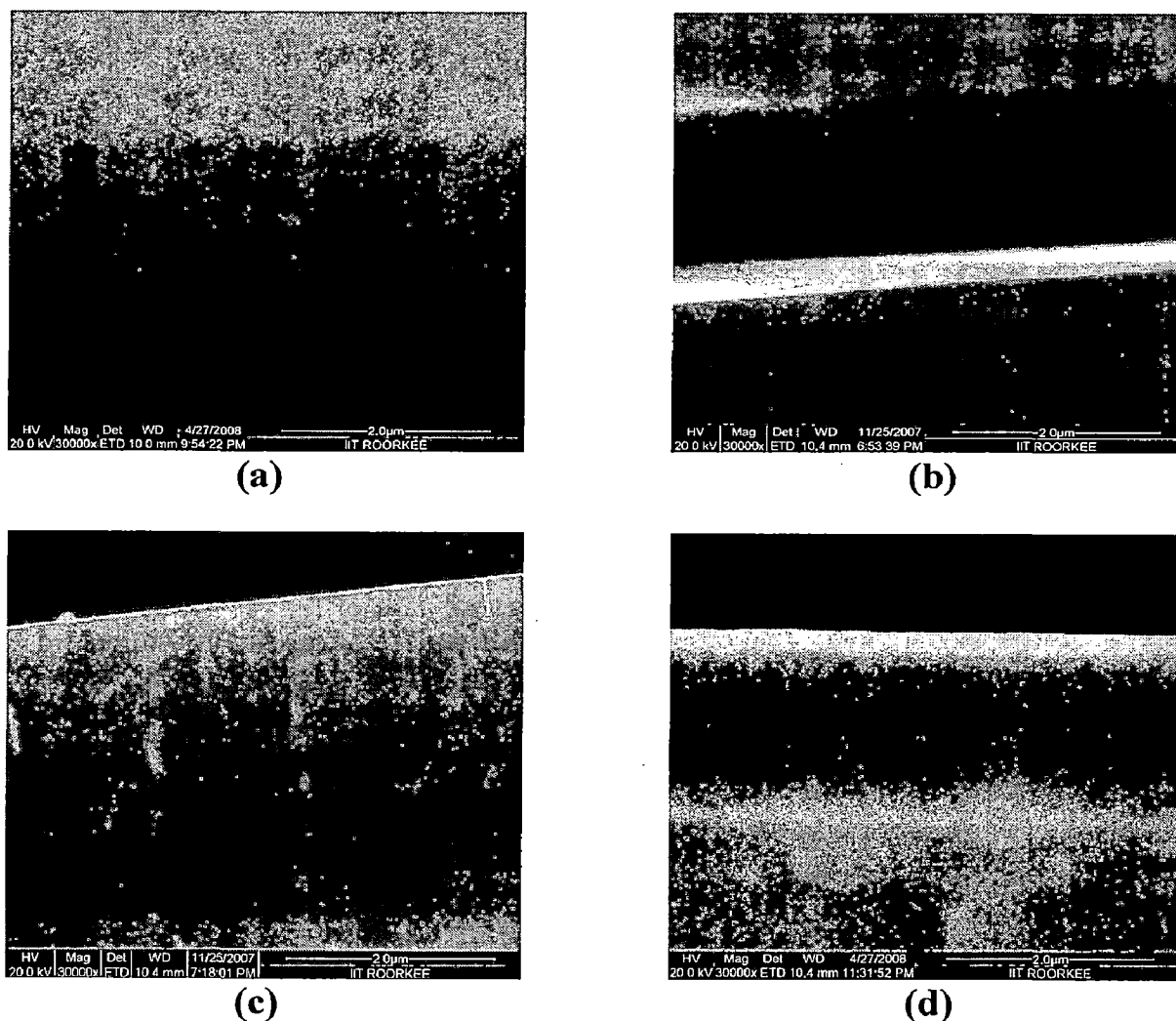


Figure 5.5: Cross section FE-SEM images of Ti-Si-N films deposited on Si substrate at varying Si content (a) 3.0 at.%, (b) 9.4 at.%, (c) 15.6 at.% and (d) 21.4 at.%

TEM images in Bright field mode and selected area diffraction modes of Ti-Si-N films with varying Si contents are shown in **Figure 5.6(a-d)**. From **Figure 5.6(a-b)**, it is observed that the Ti-Si-N film with Si contents 6.5 at.% shows crystalline structure in Bright field mode with corresponding rings in selected area diffraction mode. On the other hand, in **Figure 5.6 (c-d)**, with Si contents of 21.4 at.%, the diffraction patterns are diffused and bright field image revealed that the film consisted mainly of an amorphous phase. These results are in tandem with that of the XRD analysis.

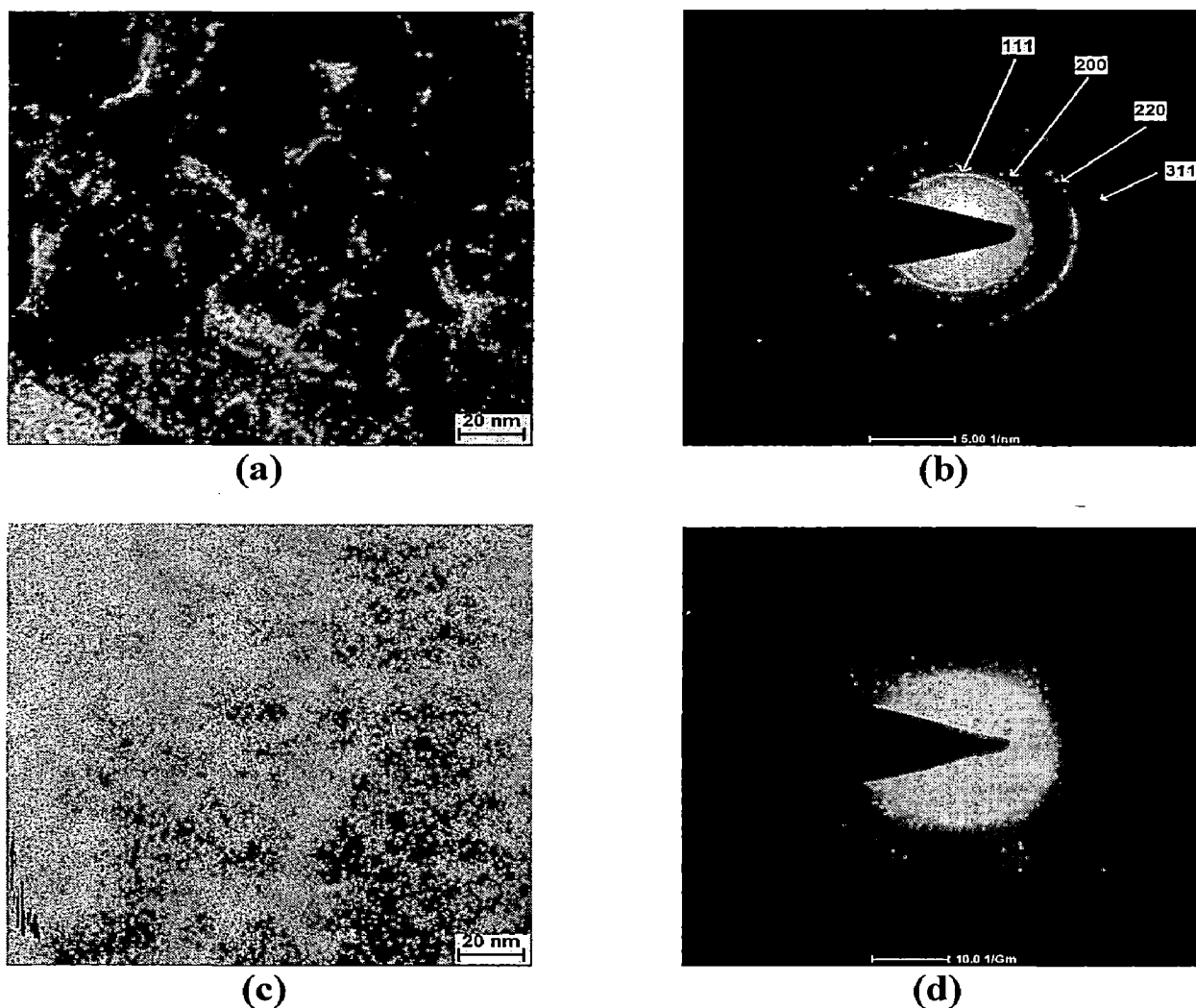


Figure 5.6: Bright field image and SAD patterns by TEM of Ti-Si-N films deposited on Si substrate at varying Si content (**a-b**) at 6.5 at % and (**c-d**) at 21.4 at %

Figure 5.7(a) and **(b)** shows the AFM *in-situ* image of the indent on the sample which is obtained after the indentation and the influence of Si content on hardness and Young's modulus (E) of Ti-Si-N thin films, respectively. From **Figure 5.7(b)**, it is observed that the hardness and E values increases with increasing Si content and the films with 15.6 at.% Si contents show a maximum hardness and E values of 34 GPa and 275 GPa, respectively. However, these values drop when the Si content is increased

beyond 15.6 at.%. An enhancement of mechanical properties of Ti-Si-N films is considered to be due to its improved microstructure.

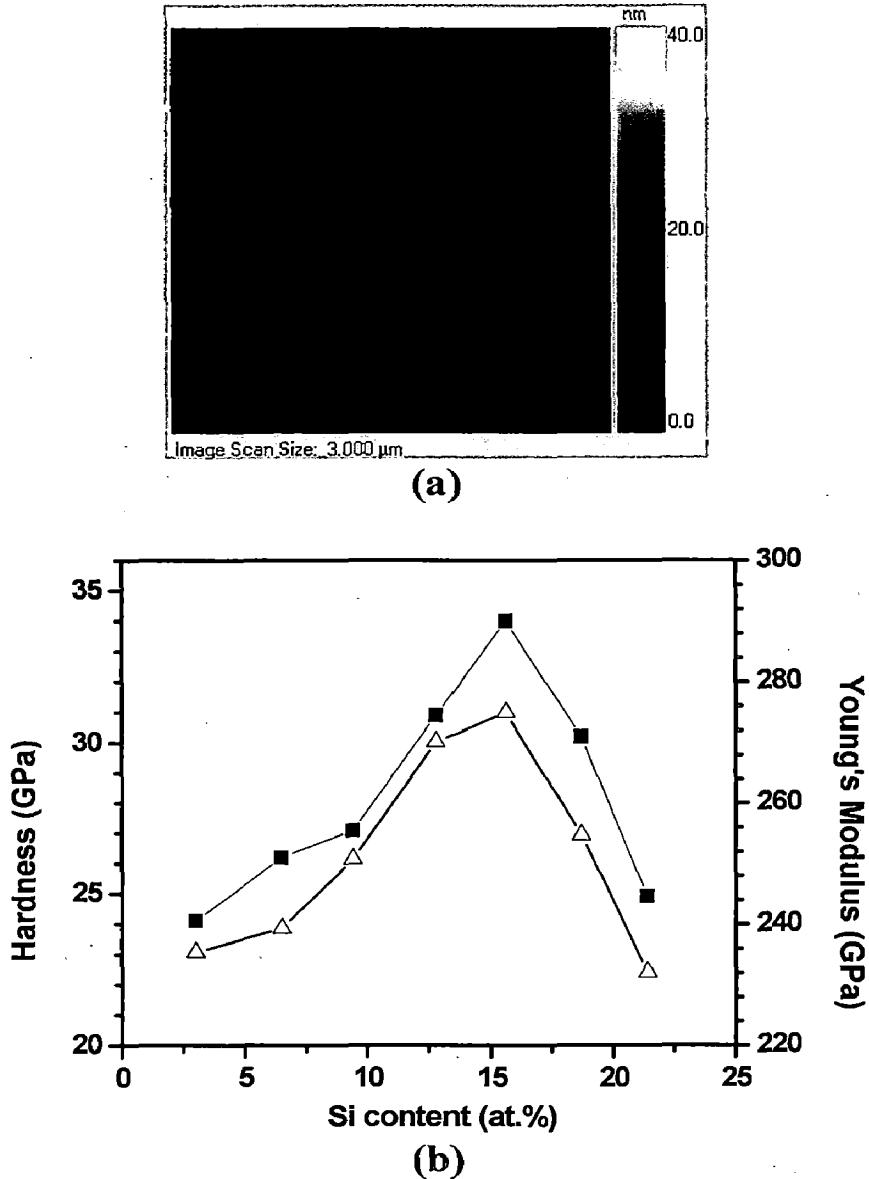


Figure 5.7: (a) AFM *in-situ* image of the indent on the sample
 (b) Hardness and Young's Modulus of Ti-Si-N films deposited with variation of Si content

A possible phenomenological explanation to the observed hardness can be deduced from results of structural analyses and their comparison with existing concepts on

nanocomposite mechanisms (Veprek *et al.* 1995b). The formation of superhard nanocomposites requires 3-4 nm crystallite sizes with less than 1 nm thick separation in an amorphous matrix (Veprek 1999). At these conditions, both dislocation formation and incoherence stress relaxation are suppressed, providing superhardness. The Ti-Si-N films prepared in the present work exhibit large crystallite size, ~ 17-48 nm, which was sufficient for the formation of nanosized dislocations. This has limited the increase in hardness of the films in the present study. Nevertheless, it is observed that the improved hardness coincides with a reduction in grain size, which implies the presence of high volume fraction of grain boundaries. Thus, the relationship between high hardness and film microstructure of Ti-Si-N films is governed by trends, firstly, a two-phase structure consisting of nanocrystalline TiN and amorphous Si₃N₄ coexists. Thus, nanocrystalline TiN surrounded by a matrix of amorphous Si₃N₄ will assist the relaxation of stresses and reduces grain boundary sliding under stress, and thus hardness increases. Secondly, the existence of free Si within the amorphous phase with large amounts of Si addition leading to incomplete nitridation of Si is due to limited nitrogen partial pressure. It results in reduction of hardness of the films because of the poor properties of amorphous phase.

5.1.4 Conclusion

Nanocomposite Ti-Si-N thin films were deposited on Si (100) and Stainless Steel (type 304) substrate by DC/RF magnetron sputtering. The effect of varying deposition parameters on the structure and mechanical properties of Ti-Si-N films was investigated by characterization techniques such as XRD, FE-SEM, AFM, TEM and Nanoindentation, respectively. XRD analysis of the thin films, with varying Si contents,

revealed the (111) orientation up to 15.6 at.% Si content, beyond which the films become amorphous. The crystallite size and lattice parameter calculated from XRD peaks show that it decreases with Si contents. The microstrain for Ti-Si-N was calculated by using lattice parameters and it decreases with varying Si content. Microstructural analysis revealed that with varying Si contents, grain size decreases and pyramidal shape grains transform into columnar and finally to amorphous structure. The surface roughness of the TiN films decreases slightly with varying Si contents. The hardness and Young's modulus values of Ti-Si-N films have increased upto 34 GPa and 275 GPa, respectively, with 15.6 at.% Si contents but it decreases afterwards with further increase in Si contents. The high hardness of Ti-Si-N films is governed by a two-phase structure consisting of nanocrystalline TiN and amorphous Si_3N_4 . These TiN nanocrystals surrounded by a matrix of amorphous Si_3N_4 could assist the relaxation of stresses and reduces grain boundary sliding under stress, causing the improvement in hardness values of Ti-Si-N films.

5.2 Influence of Deposition Parameters on the Structural and Mechanical Properties of nanocomposite Ti-Si-N thin films

5.2.1 Introduction

As discussed in **Section 5.1**, the effect of Si content on the morphological characteristics of nanocomposite Ti-Si-N films on its mechanical properties, it is also very essential to study the systematic investigation and quantification of the influence of other process parameters such as sputtering pressure on the microstructural and mechanical characteristics of nanocomposite Ti-Si-N films. Hence, the present work has been focused to deposit Ti-Si-N films in varying sputtering pressure by DC/RF Magnetron Sputtering and characterize their microstructural features by XRD, FE-SEM and AFM and their hardness and Young's modulus were measured by nanoindentation technique.

5.2.1 Experimental Details

5.2.1.1 Synthesis of Ti-Si-N films

The experiment procedures employed for the deposition of Ti-Si-N films are similar to that of it discussed in **Section 5.1.2.1**. The sputtering parameters used for the deposition of the films with varying sputtering pressure are included in **Table 5.3**.

Table 5.3: Sputtering parameters for Ti-Si-N films with variation of sputtering pressure

Target	Ti and Si
Base pressure	2×10^{-6} Torr
Gas Used	Ar+N ₂ (80:20)
Sputtering power for Ti target	150 W
Sputtering power for Si target	95 W
Deposition time	90 min
Sputtering pressure	5-50 mTorr
Substrate Used	Si (100)
Substrate Temperature	300° C

5.2.2.2 Characterization details

The characterization details are similar to that of it discussed in **Section 5.1.2.2**. The hardness and Young's modulus of the Ti-Si-N films were measured by nanoindentation technique (CSM+). The diamond Berkovich indenter is forced into the thin films being tested under constant load conditions. The loading profile during indentation testing followed linearly increasing with a hold time of 10 sec at the peak load. The load used was 20 mN at loading rate of 20.0 mN/min in the present work. A total of ten indentations were made on each sample and the average hardness and Young's modulus of Ti-Si-N films were calculated from the load-displacement curve obtained from the nanoindentation testing.

5.2.3 Results and Discussion

The XRD peaks and texture coefficients for the Ti-Si-N films deposited at varying sputtering pressure are shown in **Figure 5.8(a) and (b)**, respectively.

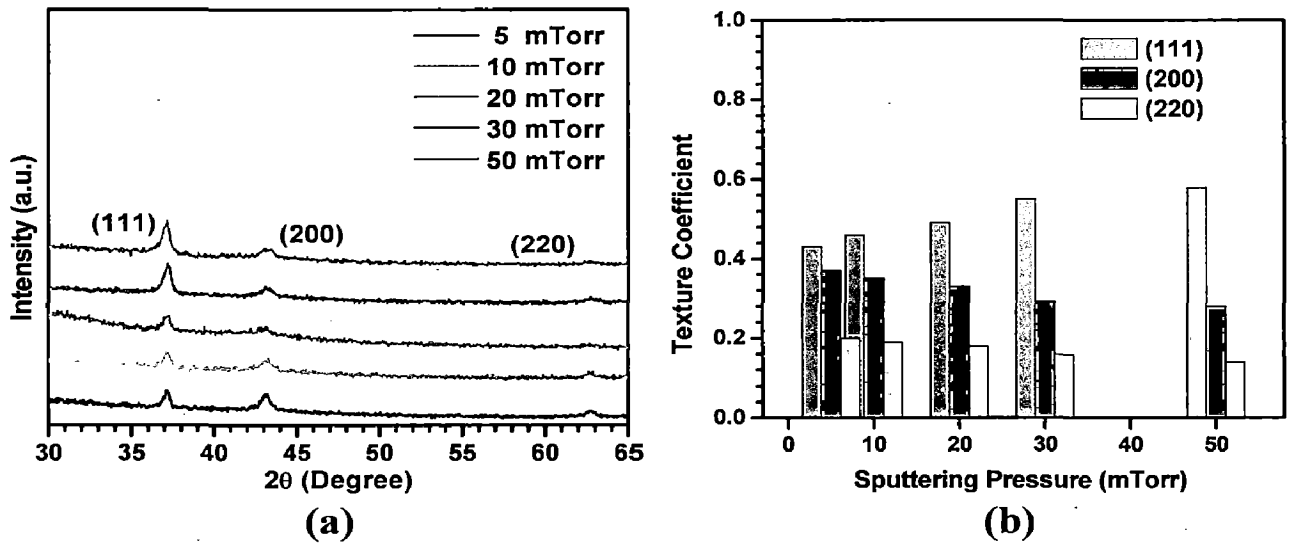


Figure 5.8: (a) XRD peaks of Ti-Si-N films deposited on Si substrate with variation of sputtering pressure
(b) Texture coefficients of the same films

Figure 5.8(a) shows that with increasing sputtering pressure, Ti-Si-N films initially exhibit all (111), (200) & (220) peaks but with increase in sputtering pressure, most of the grains are oriented towards (111) might be due to the increase in grain size which leads to crystallinity of the film and the increase in crystallite size can be explained by the relationship of the mean free path, λ (cm), with the sputtering pressure as given by

$$\lambda = 2.330 \times 10^{-20} \frac{T}{(P\delta_m^2)} \quad (5.3)$$

where, T (K) is the temperature, P (Torr) is the pressure and δ_m (cm) is the molecular diameter (Maissel *et al.* 1970, Chandra *et al.* 2005).

From **Equation 5.3**, sputtering pressure is inversely proportional to mean free path so the sputtered atoms undergo a large number of collisions when the sputtering pressure is high and have a higher probability of agglomeration i.e. increase in crystallite size before arriving at the substrate surface. Also in our case, the crystallite

size increases with increase in sputtering pressure due to reduction in mean free path. The crystallite size of the thin film with 5 mTorr sputtering pressure, calculated from the X-ray peak broadening, is 17.8 nm and it increases with increase in sputtering pressure to 23.4 nm for 50 mTorr sputtering pressure. However, no signals corresponding to crystalline Si_3N_4 and various phases of titanium silicide could be observed. It shows that Si was present in an amorphous phase of either Si_3N_4 or Si, which are in agreement with previous reports on Ti-Si-N nanocomposite films prepared by CVD and PVD (Kim *et al.* 2002a, Xu *et al.* 2007).

From **Figure 5.8(b)**, it is observed that initially texture coefficients of all (111), (200) & (220) peaks were observed which calculated from their respective XRD peaks by using the formula, as given in **Section 4.1.3 (Equation 4.1)** but with increase in sputtering pressure, more grains are oriented towards (111) peak.

The FE-SEM topographical and cross sectional view of the Ti-Si-N films with increasing sputtering pressure are shown in **Figure 5.9(a-f)**. It is observed from FE-SEM images (**Figure 5.9**) that initially dense blurred grains are observed, which subsequently transformed into uniform grains with increasing sputtering pressure and the microstructure become porous. From cross sectional view, with increasing sputtering pressure, non-uniform columnar structure transforms into uniform columnar structure as shown in **Figure 5.9(f)**.

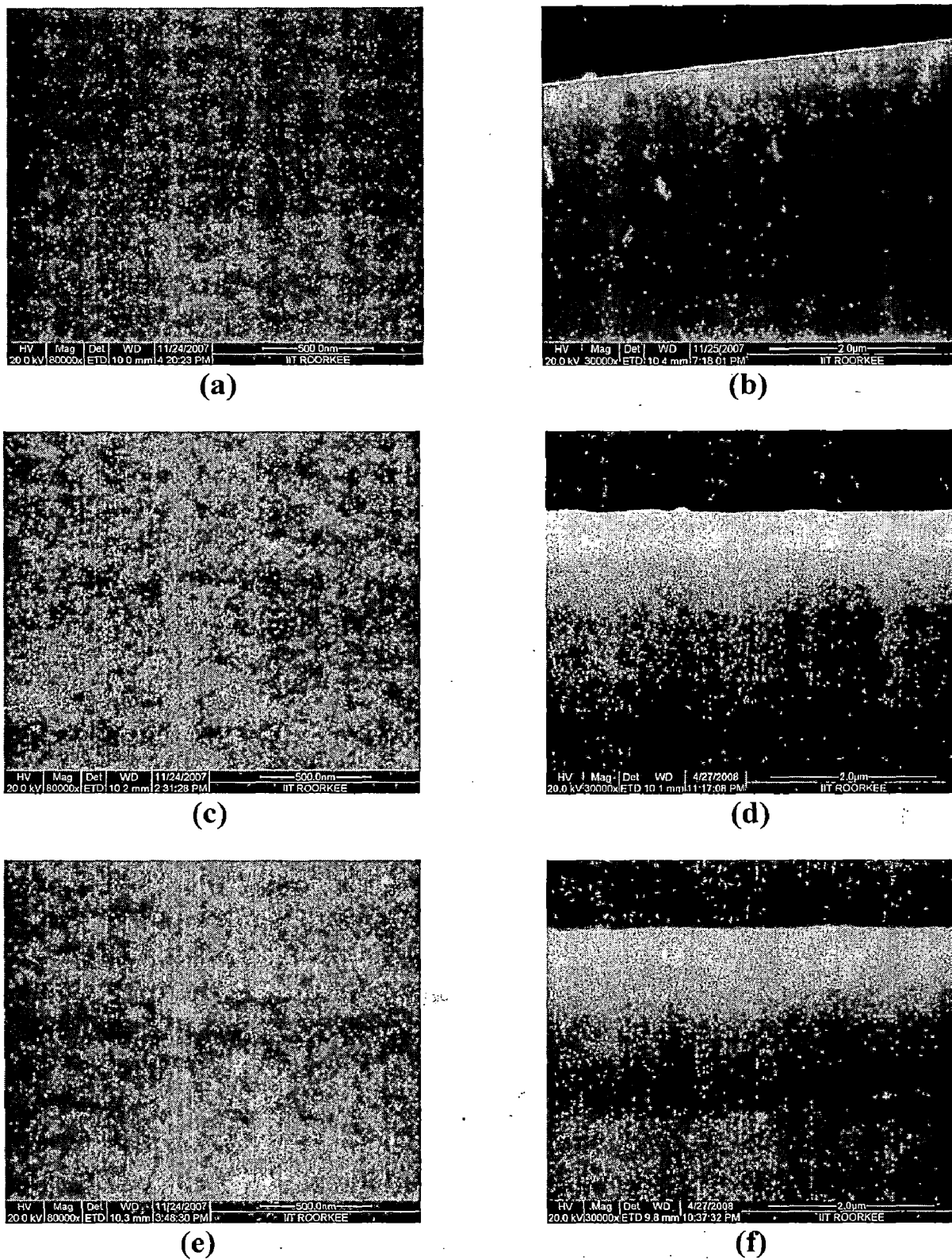


Figure 5.9: FE-SEM topographical and cross sectional view of Ti-Si-N films deposited on Si substrate at varying sputtering pressure (a-b) at 5 mTorr, (c-d) at 20 mTorr and (e-f) at 50 mTorr

The thickness of the Ti-Si-N films was measured from its cross sectional images and the thickness data of all Ti-Si-N film samples are given in **Table 5.4**.

Table 5.4: Properties of Ti-Si-N films with variation of sputtering pressure

S.N.	Coating Ti-Si (15.6 at%)-N	Thickness (μm)	Crystallite size (nm) XRD	Average Roughness (nm) AFM
1)	5 mTorr	2.05	17.8	4.1
2)	10 mTorr	2.07	18.6	5.8
3)	20 mTorr	2.07	19.7	7.6
4)	30 mTorr	2.08	21.1	9.4
5)	50 mTorr	2.10	23.4	11.8

Figure 5.10(a-f) shows the 2D and 3D AFM images of the Ti-Si-N films with increasing sputtering pressure and it is observed that grains become uniform with increase in porosity and the surface roughness increases with increasing sputtering pressure. The root mean square values of surface roughness with different sputtering pressure calculated from the AFM images of the films are shown in **Table 5.4**.

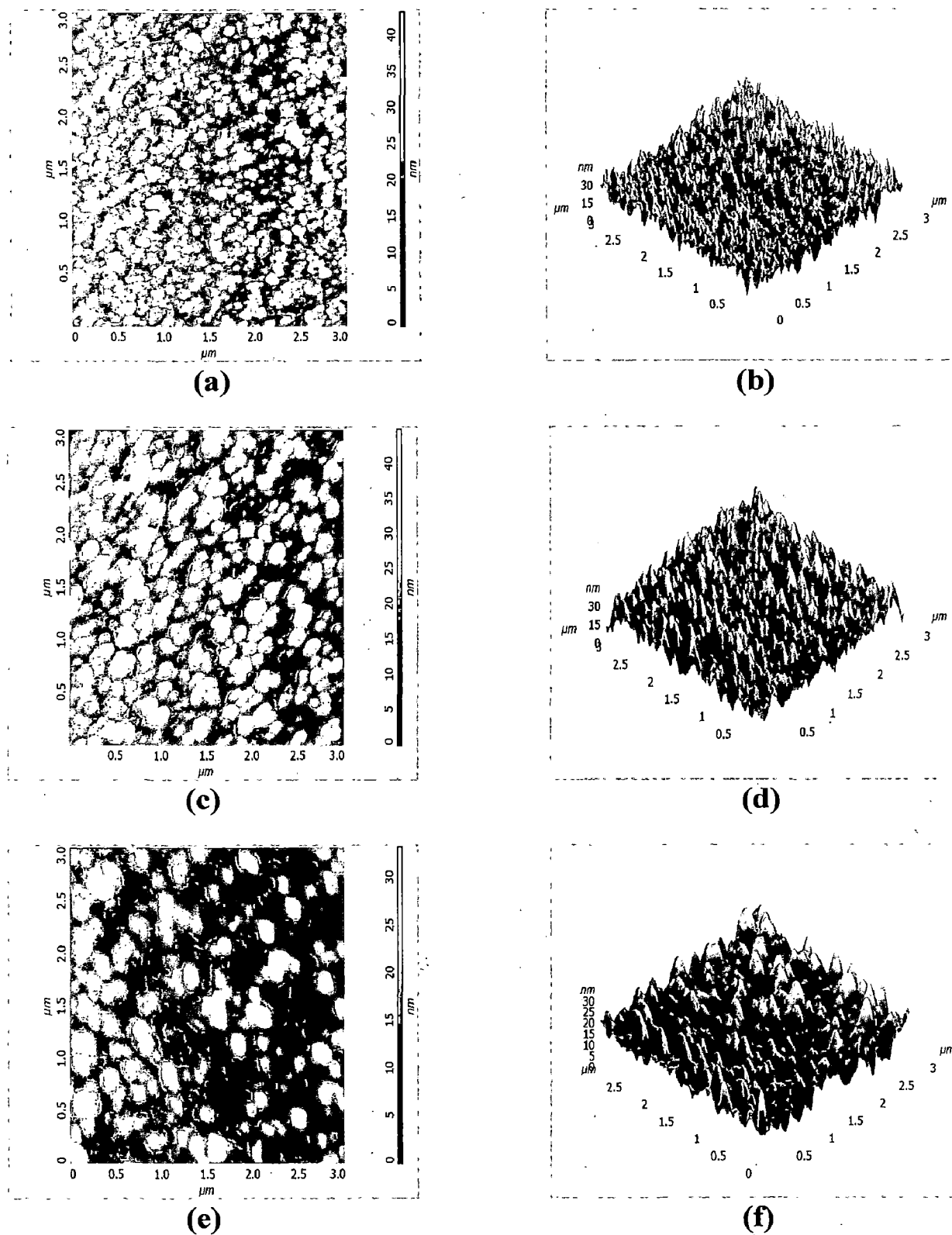


Figure 5.10: 2D and 3D AFM images of Ti-Si-N films deposited on Si substrate at varying sputtering pressure (a-b) at 5 mTorr, (c-d) at 20 mTorr and (e-f) at 50 mTorr

Figure 5.11 shows the influence of sputtering pressure on hardness and Young's modulus (E) of Ti-Si-N thin films. It is observed that the H and E values decrease with increasing sputtering pressure and the films with 5 mTorr sputtering pressure show a maximum H and E values of 33.7 GPa and 278.6 GPa, respectively.

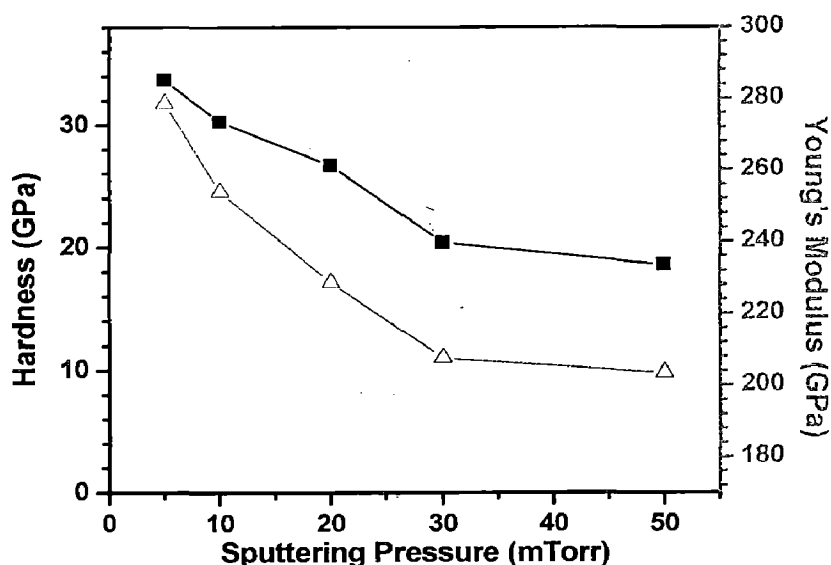


Figure 5.11: Hardness and Young's Modulus of Ti-Si-N films deposited on Si substrate with variation of sputtering pressure

However, these values drop when the sputtering pressure is increased, during deposition, as it decreases mean free path for elastic collisions between coating species and the sputtered gas atoms. This leads to low kinetic energy of coating species impinging on the substrate surface, thereby producing relatively porous microstructures (Tjong *et al.* 2004). It is observed that the drop in H and E is linear only up to sputtering pressure of 30mTorr and it deviates beyond this value to 18.6 GPa and 203.4 GPa, respectively due to the porous microstructure.

2.4 Conclusion

Nanocomposite Ti-Si-N thin films were deposited on Si (100) substrate by DC/RF magnetron sputtering. The effect of varying deposition parameters on the structure and mechanical properties of Ti-Si-N films was investigated by characterization techniques such as XRD, FE-SEM, AFM and nanoindentation, respectively. XRD analysis of the films exhibit all (111), (200) & (220) peaks initially with varying sputtering pressure but (111) peak dominates at higher sputtering pressure. The crystallite size calculated from XRD peaks shows that it increases with increasing sputtering pressure. Microstructural analysis revealed that the dense blurred grains transform into uniform grains in the films and showed porosity with increasing sputtering pressure. The surface roughness of the Ti-Si-N films increases with varying sputtering pressure. The hardness and Young's modulus values of Ti-Si-N films are 33.7 GPa and 278.6 GPa, respectively, with 5 mTorr sputtering pressure but it decreases with further increase in sputtering pressure due to increase in porosity of the films.

Chapter 6

Synthesis and Characterization of Titanium Nitride/Silicon Nitride Multilayer Films

6.1 Microstructural and Mechanical Properties of Sputter Deposited TiN/SiN_x Multilayer thin films

6.1.1 Introduction

TiN coatings are widely used as wear resistant coatings to protect cutting tools, dies, tools, sliding surfaces of bearings and gears from aggressive environments due to its good wear resistance and inertness to steels. TiN coatings predominantly grow with a columnar grain structure and its columnar grain boundaries are source of crack initiation, resulting in premature failure of the coatings (Polonsky *et al.* 1997, 1998). Therefore, SiN_x layer has been introduced between the TiN growth to periodically interrupt its columnar structure and force TiN to renucleate and form very fine, equiaxed grain microstructure as reported in the literature (Lacerda *et al.* 1999). The interlayers have reduced the porosity, cutting off the paths for the corrosive solution to the substrate and enhanced its tribological performance.

Soderberg *et al.* (2005) deposited TiN/SiN_x multilayer films on Si (100) wafer with a top layer of 100 nm SiO₂ by dual, unbalanced reactive dc magnetron-sputtering system and observed (002) preferred orientation for TiN layers in TiN/SiN_x multilayer with a thickness of 4.5 nm and below but (111) orientation has appeared with further increase in its thickness. All the multilayer films showed higher hardness than that of monolithic films grown under the same conditions. The higher hardness obtained for the multilayer films are due to its smaller grains and also due to the fact that dislocations cannot propagate unaffected throughout the film due to interlayers. The HRTEM of the hardest TiN/SiN_x multilayer (32 GPa), with a SiN_x thickness of 0.3 nm, has shown no amorphous interlayers; instead, lattice fringes continued throughout. Chen *et al.* (2001)

have deposited TiN/SiN_x multilayer films on Si (100) wafers and M2 steel substrates by a dual-cathode unbalanced reactive sputtering and characterized the films with XRD and TEM. With a substrate bias of -80 to -90 V, TiN/SiN_x multilayer coatings with distinct layers consisting of optimum SiN_x layer thickness of 0.5 nm was produced with no columnar structure in their work. Also, these multilayer coatings attained hardness values approximately twice of pure TiN coatings, are significantly smoother and showed lower internal compressive stresses than columnar TiN coatings. An *et al.* (2008) prepared TiN/SiN_x multilayer films, using a magnetron sputtering system, on Si (111) substrate and concluded that N₂/Ar gas flow ratio has a significant influence on the structures of TiN/SiN_x multilayer film. The texture for TiN layer in multilayer films has evolved from (200) to (111) with an increase of N₂/Ar gas flow ratio, and the multilayer film with TiN (111) texture was harder than that of it with (200) texture as reported in their work. Chen *et al.* (2002) deposited TiN/SiN_x multilayer coatings, by unbalanced reactive-magnetron sputtering, on Si (100) substrates and reported its hardness value of 37 GPa, almost twice the rule-of-mixtures value (22 GPa), as compared to pure TiN (24 GPa) and pure SiN_x (19 GPa). Perez-Mariano *et al.* (2006) deposited TiN/SiN_x multilayer coatings on stainless steel and Si wafer substrates by chemical vapor deposition in a fluidized bed reactor at atmospheric pressure by reaction of TiCl₄ and SiCl₄ with NH₃ at 850°C. It was observed that TiN layers are nanocrystalline, with lower crystallite sizes and less preferred orientation than single TiN films deposited under the same conditions. They have reported that the multilayer coatings consist of 6 or more sublayers with thickness around 250 nm showed higher hardness (26-27 GPa) than single TiN (21 GPa) or single SiN_x (21 GPa) coatings.

A detailed investigation on microstructural characteristics of TiN/SiN_x multilayer films deposited on Si(100) substrate as a function of varying process parameters, in magnetron sputtering, is essential to substantiate their influence on its mechanical properties. The knowledge of microstructural characteristics and mechanical properties of multilayer thin films would provide an insight into the compatibility and reliability issues when they are used in diffusion barriers and tribological applications. Therefore, in the present work, TiN/SiN_x multilayer films on Si (100) substrate were produced by the DC/RF magnetron sputtering. These multilayer films were characterized by XRD, FE-SEM, AFM to reveal the influence of processing parameters on microstructural characteristics and TEM analysis was made to characterize the TiN/SiN_x multilayer films. The hardness and Young's modulus of the TiN/SiN_x multilayer films were measured by nanoindentation technique.

6.1.2 Experimental Details

6.1.2.1 Synthesis of TiN/SiN_x multilayer films

The TiN/SiN_x multilayer films were deposited on Si (100) substrates by DC/RF magnetron sputtering. The substrates were cleaned by Hydro Fluoric acid to remove SiO₂ layer from the top of the substrate and then rinsing in ultrasonic baths of acetone and methanol and dried under nitrogen gas. The sputtering targets were 99.99% pure Ti & Si disc (2" diameter & 5 mm thick) fixed at an angle of 90° to each other and with the use of rotator, the substrate was rotated between Ti & Si targets after defined time to perform a reactive sputtering in an Ar + N₂ atmosphere (80:20) to deposit TiN/SiN_x multilayer films. DC sputtering and RF sputtering for Ti and Si targets were used, respectively, during deposition. The base pressure was better than 2×10^{-6} Torr in the

present work. Before starting the deposition, the targets were pre-sputtered for 15 minutes with a shutter located in between the targets and the substrate. This shutter is also used to control the deposition time. All the deposition was performed at a fixed substrate to target distance of 50 mm. Two sets of TiN/SiN_x multilayer films were prepared. The first set was made with a constant TiN layer deposition time and with a varying SiN_x layer deposition time. In the second set, the SiN_x layer deposition time was held constant, whereas the TiN layer deposition time was varied. The sputtering parameters for both set of samples are included in **Table 6.1**.

Table 6.1: Sputtering parameters for TiN/SiN_x multilayer films

Sputtering Parameters	(SET I)	(SET II)
Target	Ti and Si	Ti and Si
Base pressure	2×10^{-6} Torr	2×10^{-6} Torr
Gas Used	Ar+N ₂ (80:20)	Ar+N ₂ (80:20)
Sputtering pressure	10 mTorr	10 mTorr
Total Deposition time	90 min	90 min
TiN layer deposition time	15 sec	5-30 sec
SiN_x layer deposition time	5-30 sec	15 sec
Sputtering power for Ti target	150 W	150 W
Sputtering power for Si target	100 W	100 W
Substrate	Silicon(100)	Silicon(100)
Substrate Temperature	300°C	300°C

6.1.2.2 Characterization details

XRD (Bruker AXS, D8 Advance) measurements using $\text{CuK}\alpha$ ($\lambda=1.54 \text{ \AA}$) radiation was used to characterize the TiN/SiN_x multilayer films. The excitation voltage and current were set to a 40 kV and 30 mA respectively, in the diffractometer. The grain size t of the TiN/SiN_x multilayer films was estimated from the Scherrer's formula, as given in **Section 3.1.2.2 (Equation 3.1)**.

FE-SEM (FEI, Quanta 200F) was used to characterize the microstructures of the TiN/SiN_x multilayer films at an acceleration voltage of 20 kV. The surface morphology of the TiN/SiN_x multilayer films was characterized by AFM (NT-MDT, Ntegra) operated in a semicontact (tapping) mode in order to calculate its surface roughness and the root-mean-square (RMS) roughness of the surface of the sample was calculated from AFM scan at five different spots for each sample. TEM (FEI, Tecnai 20) analysis was carried out to characterize the TiN/SiN_x multilayer films.

The hardness and Young's modulus of the TiN/SiN_x multilayer films were measured by nanoindentation technique (CSM+). The diamond Berkovich indenter was forced into the thin films under constant load conditions and the loading profile was linear, during indentation testing, which is increased with a hold time of 10 sec at the peak load. The load and loading rate used were 20 mN and 20.0 mN/min, respectively. A total of ten indentations were made on each sample and the average hardness and Young's modulus of TiN/SiN_x multilayer films were calculated from the load-displacement curve obtained from the nanoindentation testing.

6.1.3 Results and Discussion

The XRD peaks for the first set of samples in which TiN/SiN_x multilayer films deposited at a constant TiN layer deposition time and with a varying SiN_x layer deposition time are shown in **Figure 6.1(a)**.

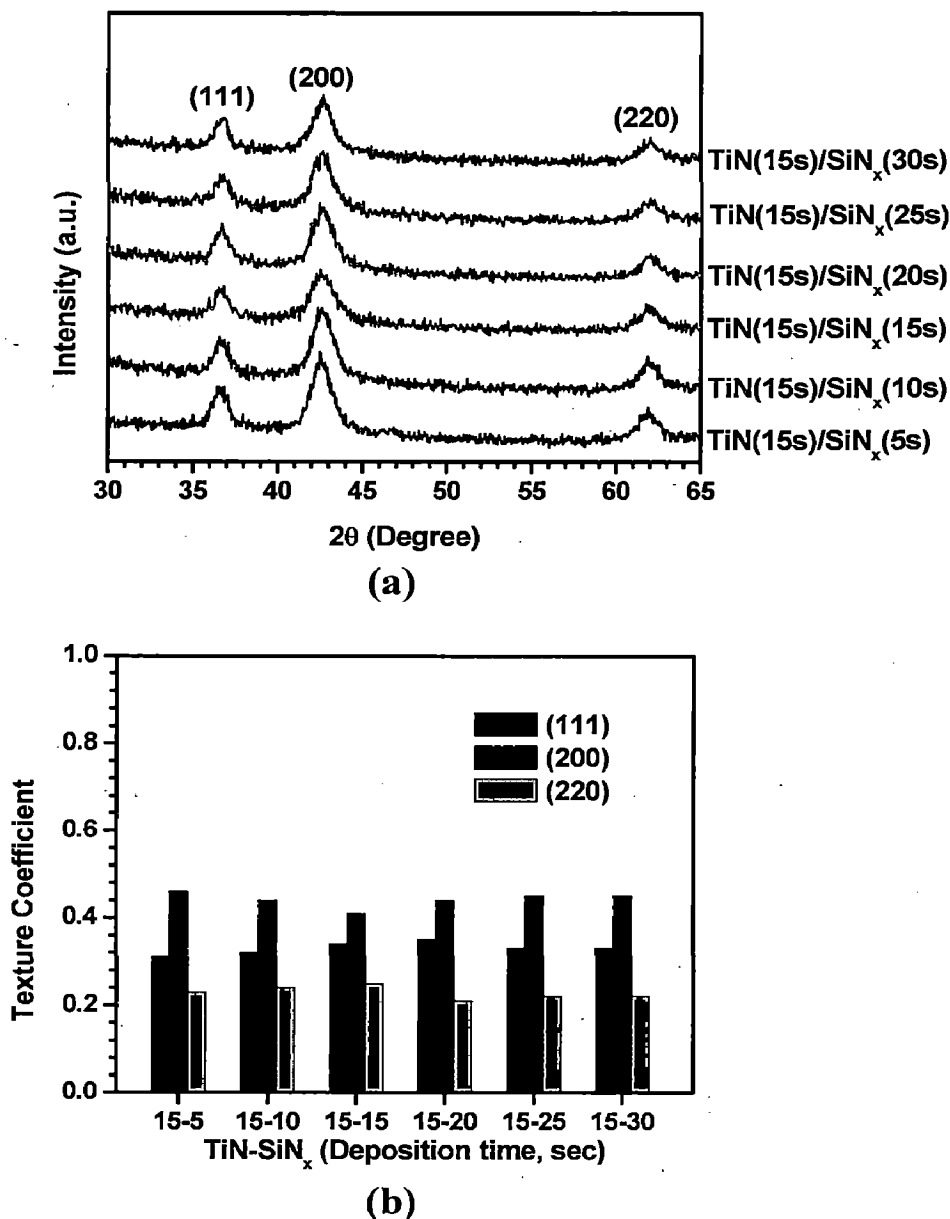


Figure 6.1: (a) XRD peaks of TiN/SiN_x multilayer films deposited on Si(100) substrate with variation of SiN_x layer deposition time
(b) Texture coefficients of same films

It is observed that the films exhibit (111), (200) and (220) orientations and with increase in SiN_x layer deposition time, the intensity of all peaks remains same. However, no signals corresponding to crystalline Si_3N_4 and various phases of titanium silicide could be observed. It shows that Si is present in an amorphous phase of either Si_3N_4 or Si, which is in agreement with previous reports (Kim *et al.* 2002a, Xu *et al.* 2007).

Therefore, in the present work, when the deposition time for TiN layer was kept constant, SiN_x layer deposition time was varied to interrupt the growth of TiN layer and facilitate its renucleation each time. Here, no peak of SiN_x was observed and with increase in SiN_x layer deposition time, no remarkable effect was observed in TiN/ SiN_x multilayer film. The crystallite size of the TiN/ SiN_x multilayer films calculated from the X-ray peak broadening is around 7.0 nm initially and with varying SiN_x layer deposition time, it remains constant as SiN_x layer is present in an amorphous form. The crystallite size of TiN layer, whose deposition time is kept constant, as function of varying deposition time for SiN_x layer is shown in **Table 6.2**.

Figure 6.1(b) shows the texture coefficients for the first set of samples in which TiN/ SiN_x multilayer films deposited with a varying SiN_x deposition time, keeping TiN layer deposition time constant calculated from their respective XRD peaks by using the formula, as given in **Section 4.1.3 (Equation 4.1)**. From **Figure 6.1(b)**, it is observed that the texture coefficient of all the three (111), (200) and (220) peaks remains constant with a varying SiN_x layer deposition time.

XRD peaks for the second set of samples in which TiN/ SiN_x multilayer films deposited with a varying TiN deposition time, keeping SiN_x layer deposition time constant, are shown in **Figure 6.2(a)**.

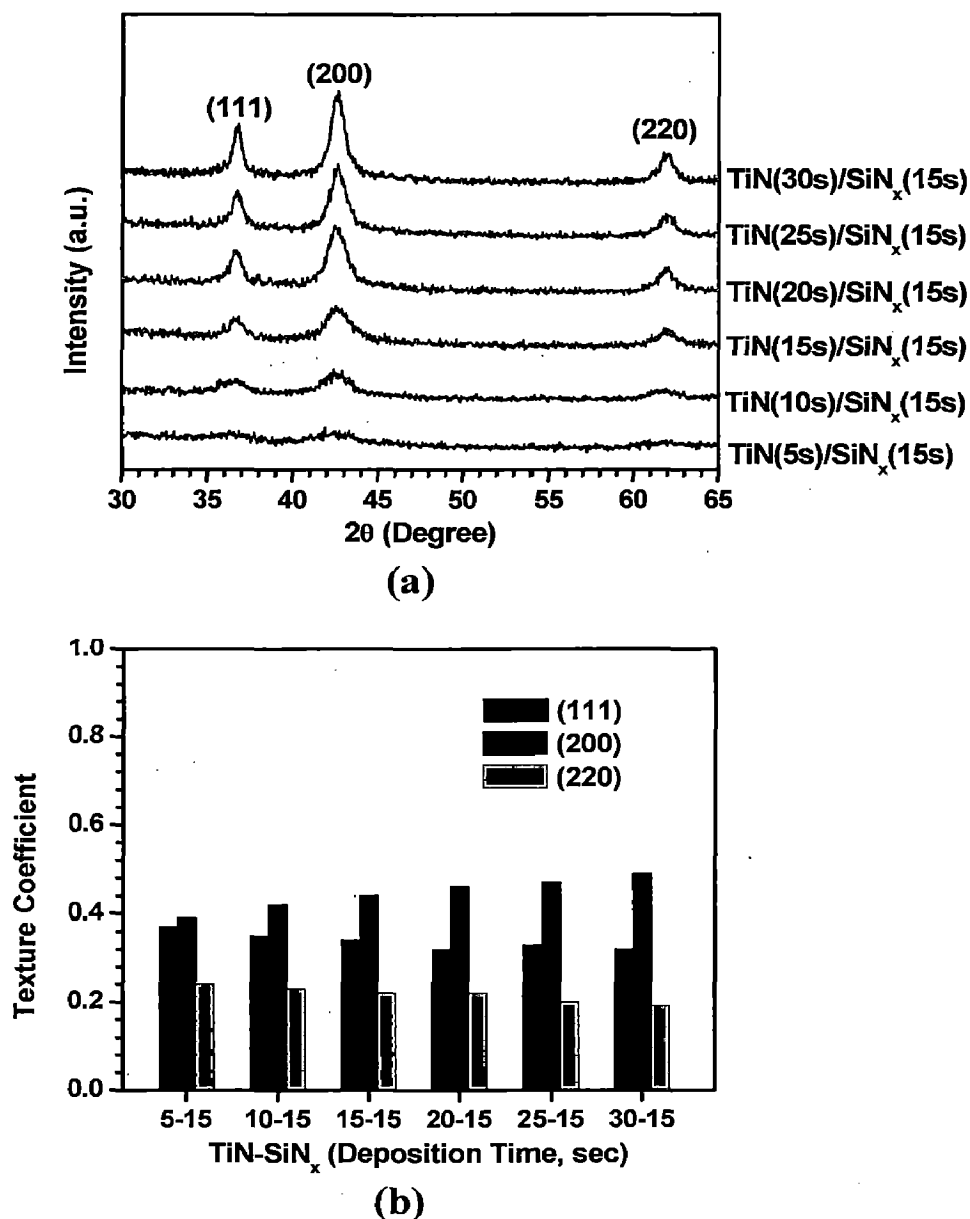


Figure 6.2: (a) XRD peaks of TiN/SiN_x multilayer films deposited on Si(100) substrate with variation of TiN layer deposition time
(b) Texture coefficients of same films

It is observed that the films exhibit (111), (200) and (220) orientations and with increase in TiN layer deposition time, the intensity of (200) peak increases and (111) and (220) peak intensity goes down. The results are in agreement with the Pelleg *et al.* (1991), who have reported that the preferred orientation of TiN film is controlled by the surface

free energy and the strain energy. Assuming that the strain energy in the film increases linearly with thickness, they postulated that when the film was sufficiently thin, the film orientation with minimum surface energy, i.e., (200) is favored (Pelleg *et al.* 1991).

According to Pelleg *et al.*, the preferred orientation of TiN in the multilayers should evolve from the (111) orientation to (200) orientation. Therefore, in the present case, initially there might be a competition between surface energy and strain energy during film growth and therefore no preferred orientation was observed but with increase in TiN layer deposition time, the adatom mobility is very high due to which the TiN layer grow along the (200) orientation with the lowest surface free energy (Greene 1993). Also with increase in deposition time of TiN layer, its layer thickness might be few nanometers and therefore grows preferentially along the (200) orientation as compared to (111) and (220) orientation. The crystallite size of the TiN/SiN_x multilayer films calculated from the X-ray peak broadening is 2.7 nm initially and with varying TiN layer deposition time, it increases to 11.3 nm. It is due to the reason that with varying TiN layer deposition time but keeping constant deposition time for SiN_x layer, the TiN layer has more time to nucleate and therefore crystallite size increases. The crystallite size of TiN/SiN_x multilayer films is shown in **Table 6.3**.

By using **Equation 4.1** in **Section 4.1.3**, the texture coefficients for the second set of samples in which TiN/SiN_x multilayer films deposited with a varying TiN deposition time, keeping SiN_x layer deposition time constant calculated from their respective XRD peaks are shown in **Figure 6.2(b)**. It is evident that the texture coefficient of all the three (111), (200) and (220) peaks are observed initially and there is no dominating peak. It shows that all grains are oriented in different planes but with increase in TiN layer deposition time, (200) orientation dominates but the other peaks decrease.

The FE-SEM topographical and cross sectional view of the TiN/SiN_x multilayer films deposited with a varying SiN_x layer deposition time but keeping TiN layer deposition time constant are shown in **Figure 6.3(a-d)**. It is observed that the grain size of multilayer films remains constant and there is no change in morphology of the films with increase in SiN_x layer deposition time.

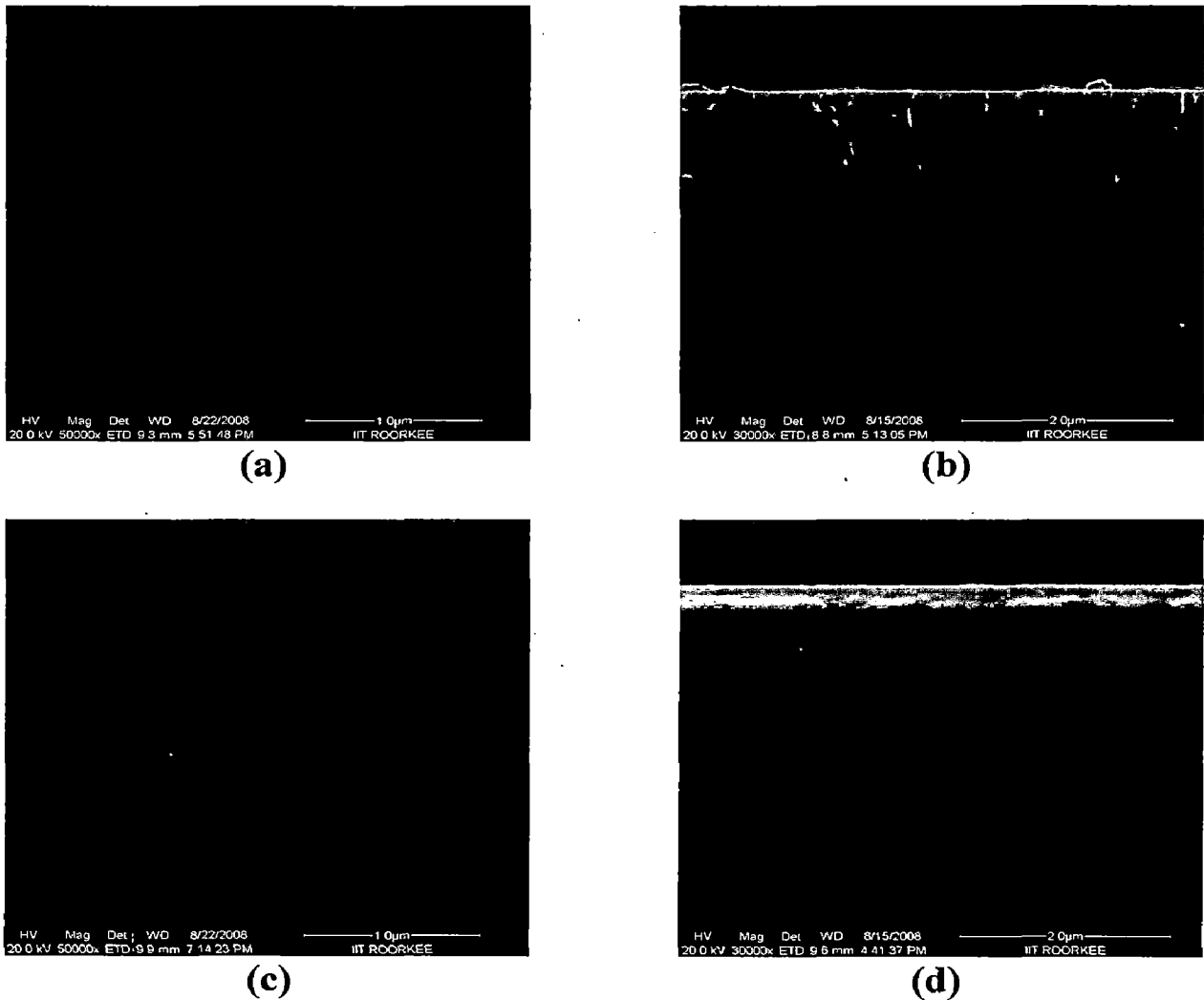


Figure 6.3: FE-SEM topographical and cross sectional view of TiN/SiN_x multilayer films deposited on Si(100) substrate with variation of SiN_x layer deposition time (a-b) 5 sec and (c-d) 30 sec

However, the cross sectional view of the same films shows that it becomes amorphous with increase in SiN_x layer deposition time.

Figure 6.4(a-d) shows the FE-SEM topographical and cross sectional view of the TiN/SiN_x multilayer films deposited with a varying TiN layer deposition time and keeping SiN_x layer deposition time constant. It is observed that with increase in TiN layer deposition time, its grain size increases and attains the columnar structure.

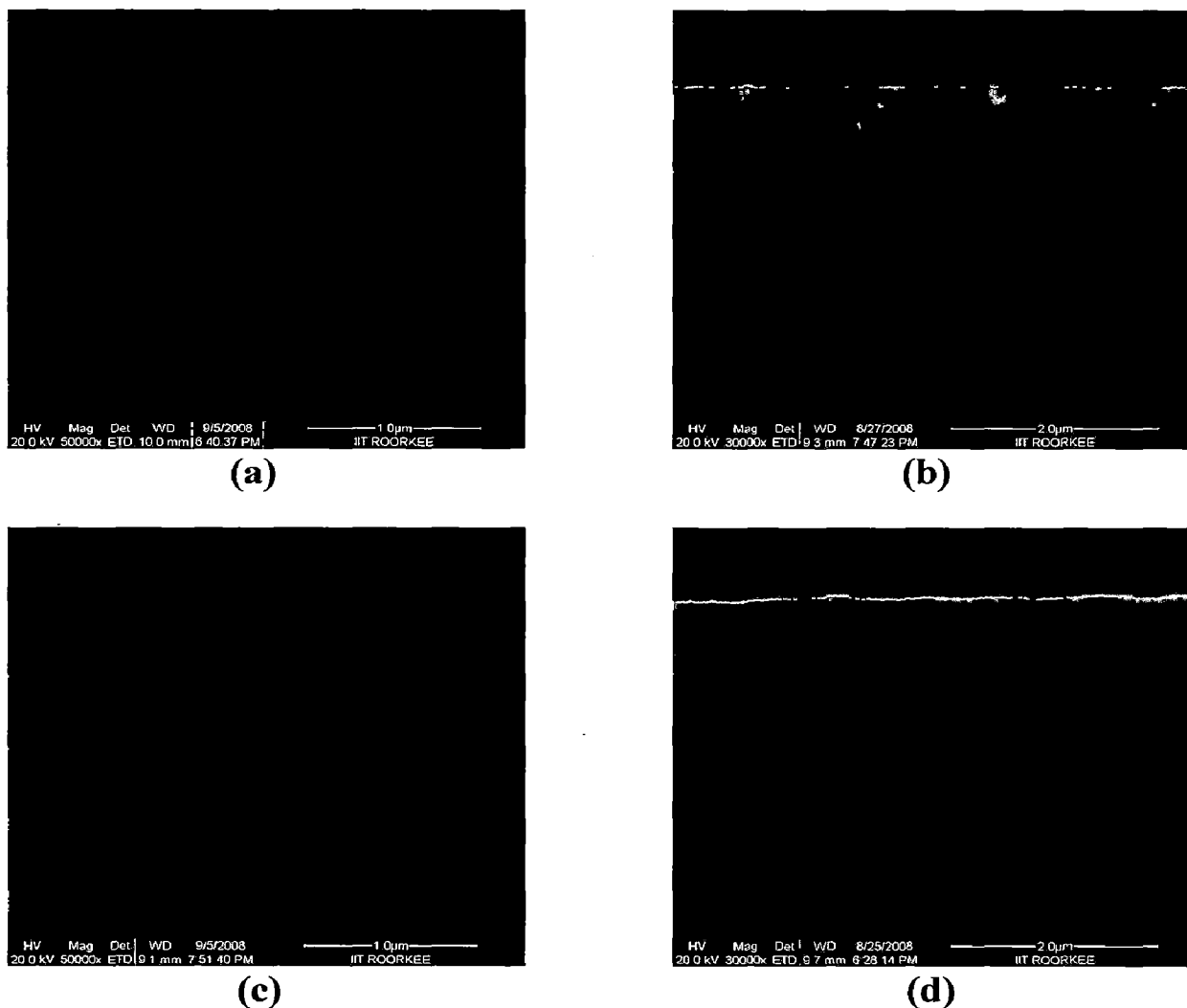


Figure 6.4: FE-SEM topographical and cross sectional view of TiN/SiN_x multilayer films deposited on $\text{Si}(100)$ substrate with variation of TiN layer deposition time (a-b) 5 sec and (c-d) 30 sec

The FE-SEM cross sectional view of same films shows the columnar structure with increase in TiN layer deposition time.

Figure 6.5(a-d) shows the 2D and 3D AFM images of the TiN/SiN_x multilayer films deposited with a varying SiN_x layer deposition time. It is evident from **Figure 6.5(a-d)** that with increasing SiN_x layer deposition time, grain size and surface roughness of the films remains constant.

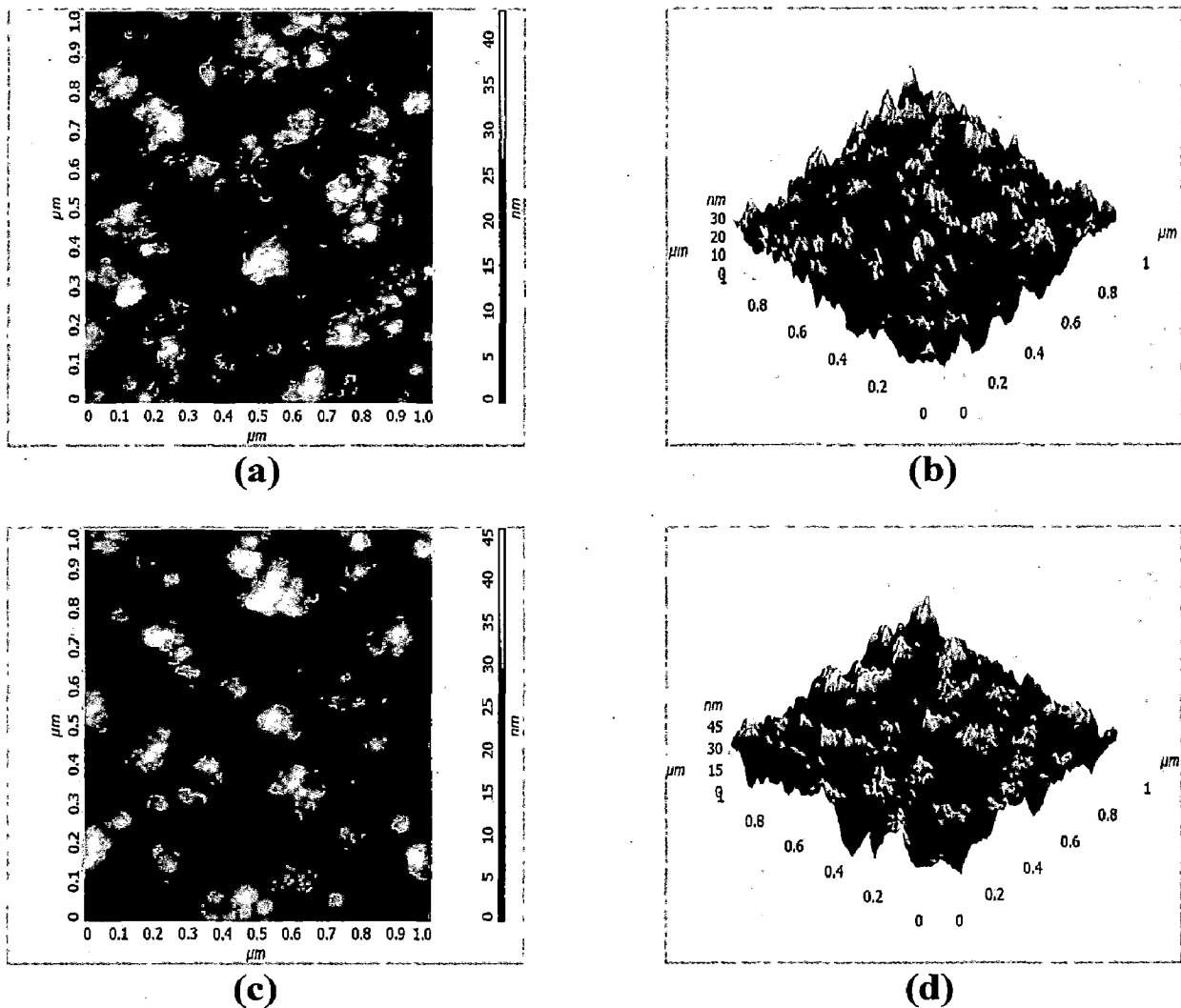


Figure 6.5: 2D & 3D AFM images of TiN/SiN_x multilayer films deposited on Si(100) substrate with variation of SiN_x layer deposition time (a-b) 5 sec and (c-d) 30 sec

The root mean square values of surface roughness of the films with different SiN_x layer deposition time calculated from its AFM images are shown in **Table 6.2**.

Table 6.2: Properties of TiN/SiN_x multilayer films with variation of SiN_x layer deposition time and keeping TiN layer deposition time constant

S.N.	TiN/SiN _x multilayer film	Thickness (μm)	Crystallite size (nm) XRD	Average Roughness (nm) AFM
1)	TiN(15s)/SiN _x (5s)	2.64	7.1	5.5
2)	TiN(15s)/SiN _x (10s)	3.01	7.0	5.3
3)	TiN(15s)/SiN _x (15s)	2.66	6.7	5.8
4)	TiN(15s)/SiN _x (20s)	2.46	7.0	4.7
5)	TiN(15s)/SiN _x (25s)	2.58	7.7	5.4
6)	TiN(15s)/SiN _x (30s)	2.56	7.6	6.3

Figure 6.6(a-d) shows the 2D and 3D AFM images of the TiN/SiN_x multilayer films deposited with a varying TiN layer deposition time. The grain size and surface roughness of the films have increased as observed from this figure. The root mean square values of surface roughness, with different TiN layer deposition time, calculated from its AFM images are shown in **Table 6.3**.

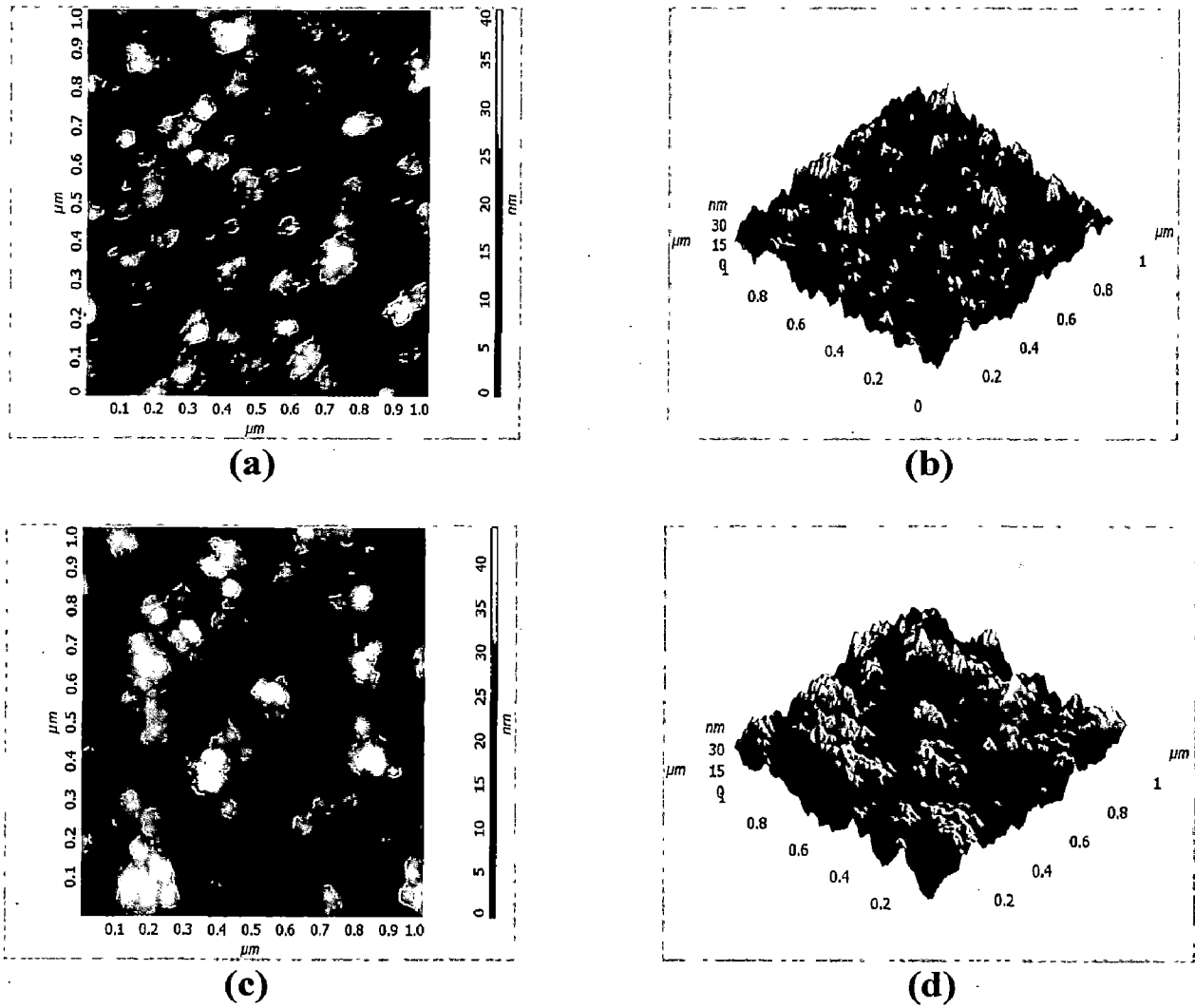
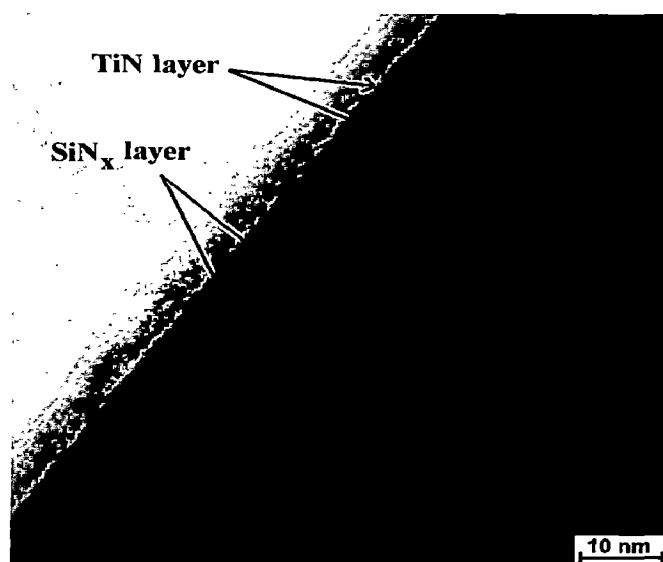


Figure 6.6: 2D & 3D AFM images of TiN/SiN_x multilayer films deposited on Si(100) substrate with variation of TiN layer deposition time (a-b) 5 sec and (c-d) 30 sec

Table 6.3: Properties of TiN/SiN_x multilayer films with variation of TiN layer deposition time and keeping SiN_x layer deposition time constant

S.N.	TiN/SiN _x multilayer film	Thickness (μm)	Crystallite size (nm) XRD	Average Roughness (nm) AFM
1)	TiN(5s)/SiN _x (15s)	2.12	2.7	5.7
2)	TiN(10s)/SiN _x (15s)	2.38	3.3	5.7
3)	TiN(15s)/SiN _x (15s)	2.66	6.7	5.8
4)	TiN(20s)/SiN _x (15s)	2.73	8.4	6.5
5)	TiN(25s)/SiN _x (15s)	2.84	9.4	6.8
6)	TiN(30s)/SiN _x (15s)	3.07	11.3	7.3

TEM cross sectional view of TiN/SiN_x multilayer film is shown in **Figure 6.7(a)**, in which it is observed that TiN and SiN_x layers are visible in a nanometer scale with a uniform deposition.



(a)

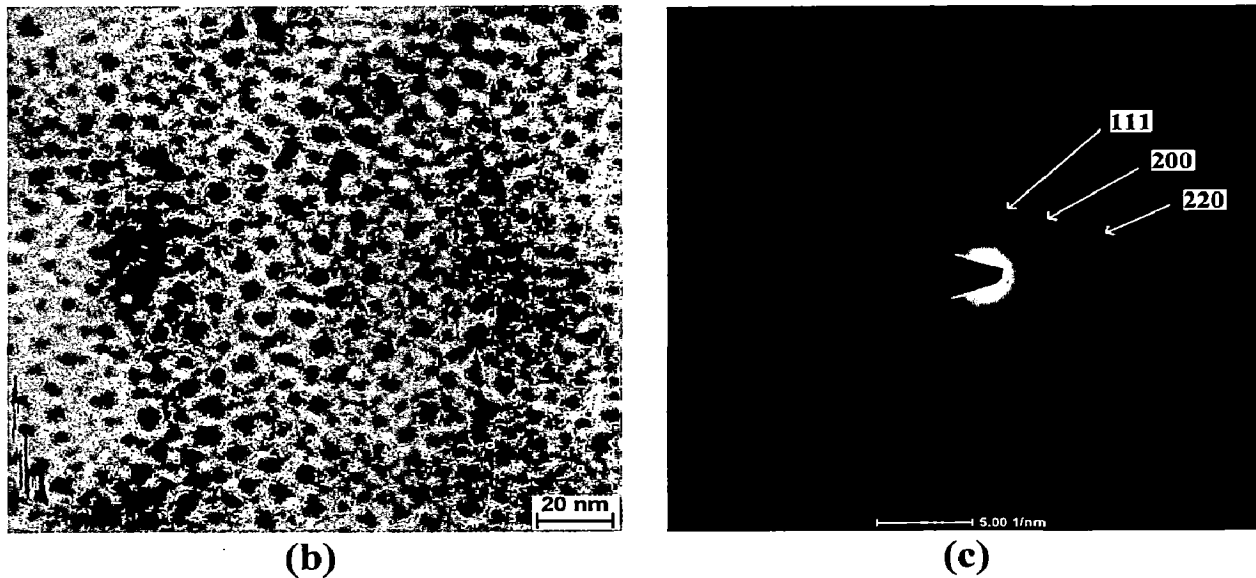
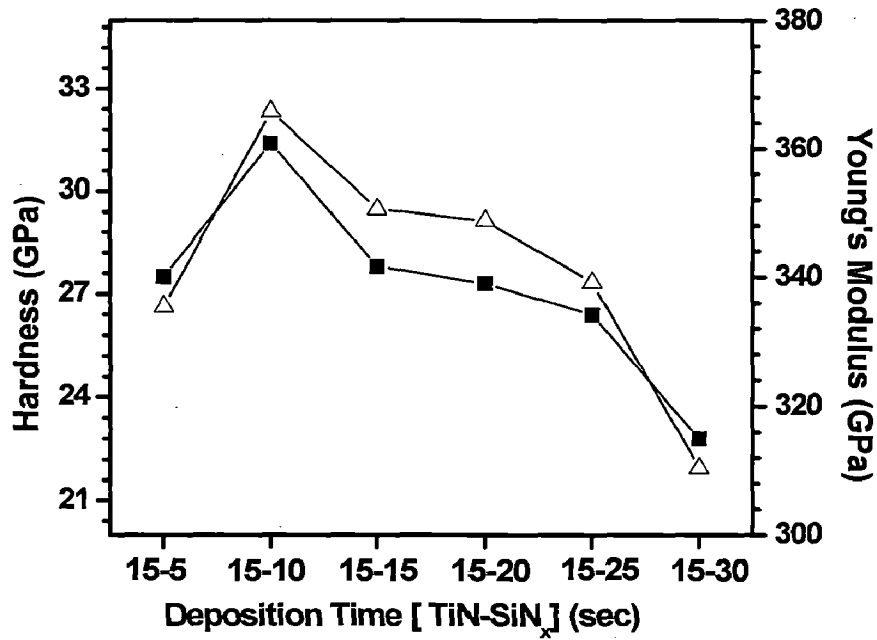


Figure 6.7: (a) TEM cross sectional view of TiN/SiN_x multilayer films showing TiN layer and SiN_x layer
 (b) TEM topographical view of TiN/SiN_x multilayer film and
 (c) SAD pattern

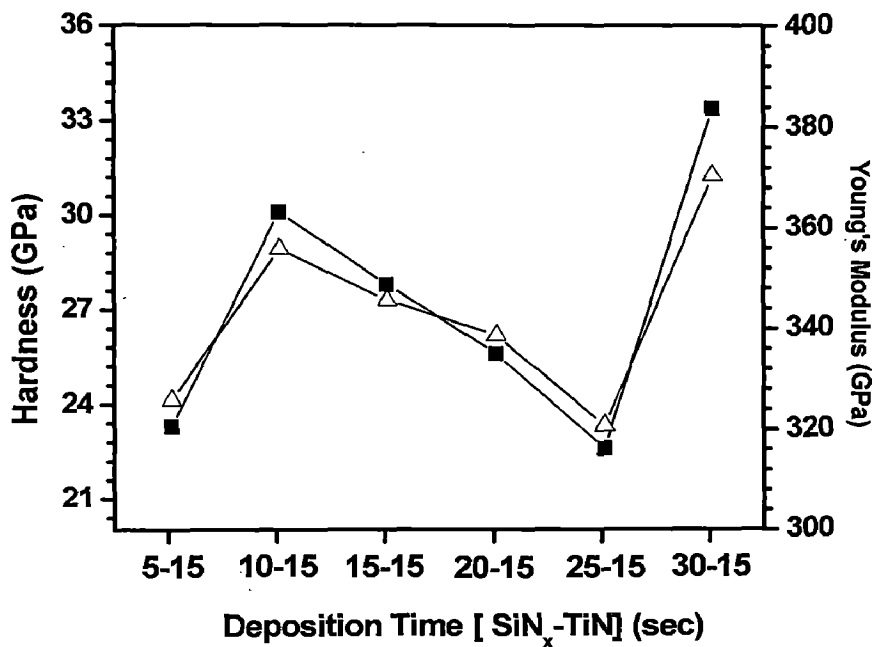
Figure 6.7(b) shows TEM topological view of the TiN/SiN_x multilayer film in which TiN crystals are embedded in SiN_x amorphous matrix since the top layer was TiN. The **Figure 6.7(c)** shows its patterns in selected area diffraction mode.

The influence of varying SiN_x layer deposition time on hardness and Young's modulus (E) of TiN/SiN_x multilayer films is shown in **Figure 6.8(a)**. It is observed that the hardness and E values of the films increase initially with increasing SiN_x layer deposition time and the films upon 10 sec deposition time, exhibit the maximum hardness and E values of 31.4 GPa and 365.8 GPa, respectively. The smaller grain size of TiN nanocrystals and very thin layer of SiN_x contribute for the higher hardness values of multilayer. The increased in hardness of TiN/SiN_x multilayer may be due to the one or the combination of the factors such as coherency stress hardening, epitaxial stabilization of meta stable structure of crystalline SiN_x layer, Orowan-like

strengthening and Hall-Petch strengthening as reported in the literature (Soderberg *et al.* 2005).



(a)



(b)

Figure 6.8: Hardness and Young's Modulus of TiN/SiN_x multilayer films deposited on Si(100) substrate with variation of (a) SiN_x layer deposition time and (b) TiN layer deposition time

However, these values drop when the SiN_x layer deposition time is increased beyond 10 sec, which is due to higher thickness of SiN_x does not facilitate renucleation kinetics of TiN to form equiaxed structures in the multilayers.

The influence of varying TiN layer deposition time on hardness and Young's modulus (E) of TiN/SiN_x multilayer films is shown in **Figure 6.8(b)**. It is observed that the H and E values increases initially with increasing TiN layer deposition time and the films after 10 sec deposition time showed the hardness and E values of 30.1 GPa and 355.8 GPa, respectively. However, these values drop when the TiN layer deposition time is increased beyond 10 sec but when the deposition time of TiN layer reached 30 sec, the maximum H and E values are 33.4 GPa and 370.5 GPa, respectively. The higher hardness of multilayers deposited at 30 seconds is due to the grain size effect. However, the decrease in hardness of multilayers may be due to intermixing leading to the formation of imperfect multilayer.

6.1.4 Conclusion

TiN/SiN_x multilayer films were deposited on Si (100) substrate by DC/RF magnetron sputtering in the present work. The effect of varying deposition parameters on the structural and mechanical properties of TiN/SiN_x multilayer films was investigated by several characterization techniques such as XRD, FE-SEM, AFM, TEM and nanoindentation technique. XRD analysis of the films, with varying SiN_x layer deposition time revealed the (111), (200) and (220) orientation and with variation of TiN layer deposition time, the same orientations were observed initially but (200) orientation grows up with increasing TiN layer deposition time. The grain size of the films was around 7.0 nm in varying SiN_x layer deposition time and it has increased from

from 2.7 to 11.3 nm when the deposition time for the TiN layer was increased. The surface roughness of the TiN/SiN_x multilayer films was calculated from its AFM images and it remains constant with varying SiN_x layer deposition time but increases in the other case, with varying TiN layer deposition time. The hardness and Young's modulus values of TiN/SiN_x multilayer films have increased upto 31.4 GPa and 365.8 GPa, respectively, with varying SiN_x layer deposition time (10 seconds) but it decreased with further increase in SiN_x layer deposition time. The decrease in hardness beyond the deposition time of (10 seconds) SiN_x layer is due to its higher thickness, which does not facilitate the formation of equiaxed structure of TiN crystals. In the other case, with increase in deposition time for TiN layer, hardness and Young's modulus values of TiN/SiN_x multilayer films increases initially but decreases uniformly and lastly increases sharply upto 33.4 GPa and 370.5 GPa, respectively.

Chapter 7

Conclusion

The main objectives of the present work was to synthesize high quality Titanium (Ti) based hard coatings especially Titanium Nitride (TiN), Titanium Silicon Nitride (Ti-Si-N), and multilayer of Titanium Nitride/Silicon Nitride (TiN/SiN_x) on various substrates by DC/RF magnetron sputtering technique and investigate the effect of sputtering parameters on structural and mechanical properties of these materials for its potential applications in tribological and functional applications. In addition, the effect of sputtering parameters on structural properties of Ti films has been studied. The following is a brief summary and conclusions made based on the results obtained on the aforementioned coatings. The suggestions for the future work are proposed at the end.

7.1 Magnetron Sputtered Ti films on Silicon substrate

The morphological characteristics of Ti films deposited on Si (100) substrates at different substrate temperatures by DC magnetron sputtering were investigated in the present work. The Ti film showed a (002) preferred orientation and its intensity increases with increase in the substrate temperature around 200°C. At above 300°C, the (101) preferred orientation has increased while (002) orientation decreased. The FE-SEM analysis of the Ti films, deposited in Ar atmosphere revealed two and three-dimensional hexagonal structure of grains depending upon the substrate temperature due to enhanced mobility of adatoms in the film surface. The increase in grain size of Ti thin films with increasing substrate temperature was confirmed by XRD, FE-SEM/EBSD and AFM. The grain size distribution is uniform for the films deposited at 200°C and 400°C but it transforms into non-uniform distribution for the films deposited

at 600°C. The anisotropic grain growth observed at higher substrate temperature is due to the texture of the grains.

7.2 Magnetron Sputtered Ti films on Glass substrate

The effects of sputtering parameters such as sputtering power, substrate temperature and sputtering pressure on the microstructural morphologies of the Ti films deposited on glass substrate by DC magnetron sputtering were investigated in the present work. XRD analysis of the textures of the Ti films, deposited under different conditions, revealed the initial (100) preferred orientation but the (002) and (101) orientations were observed with the increasing sputtering power and substrate temperature, respectively. The development of (100) orientation was due to the compressive stress induced in the films but it transformed into (002) preferred orientation at higher thickness. The (002) and (101) preferred orientations were observed for the films deposited with the sputtering pressure of 5 mTorr and 20 mTorr, respectively. The textures of the films were affected due to the competition between strain energy and surface free energy during deposition of thin films under various process conditions such as substrate temperature, power and sputtering pressure. The thermal stress induced in the thin films at higher substrate temperature has also contributed to the formation of preferred (101) orientation. The microstrain of Ti films was initially negative and then changed to positive value with increasing sputtering power, substrate temperature, and sputtering pressure. The crystallite size has increased with increase in microstrain in the films. The average surface roughness calculated from the AFM images of the films has shown an increasing trend with varying deposition parameters. The increase in surface roughness of Ti thin films with increase in substrate temperature was due to growth of grains with

preferred orientations dictated by surface and grain boundary diffusivity, adatom mobility, film thickness and induced thermal stress. The calculated grain size of Ti thin films using XRD results revealed an increasing trend with varying deposition parameters. The uniform and dense morphology of the Ti films were observed with the higher substrate temperature and sputtering pressure as observed from the FE-SEM characterization. The denser morphology of grains observed at higher substrate temperature is due to the higher surface and bulk diffusivity of sputtered atoms.

7.3 FEM Analysis of Thermal Stress in Magnetron Sputtered Ti thin films

The thermal stress of Ti-coating sputter deposited on glass and silicon substrate has been simulated by finite element simulation package ANSYS and compared with that of analytical model. The thermal stress of coatings exhibits a linear relationship with substrate temperature and Young's modulus of the coating, but it exhibit an inverse relationship with the coating thickness due to the stress relaxation. The radial stress of the coating-substrate exhibits a maximum value at the interface near the edge and it determines the failure of the coatings. The radial stress in the Ti coating is of compressive in nature on the glass substrate but tensile on the Si substrate. The higher shear stress of the Ti coating is observed along the interface at the edge due to the higher stress concentration. The tensile and compressive shear stresses are observed for Ti coating on glass and Si substrates, respectively. The spallation of the coatings from the edge is heavily dependent on these shear stresses. The adhesive strength of the Ti coating on Si substrate is higher when compared to glass substrate due to the high compressive stress in the former.

7.4 Structural and Mechanical Characterizations of Magnetron

Sputtered nanocrystalline TiN thin films

Nanocrystalline TiN thin films were deposited on Si(111) substrates by DC magnetron sputtering. The microstructural morphologies and mechanical properties of TiN films were studied in the present work. The XRD results indicate that the TiN films prepared under an Ar+N₂ atmosphere exhibit an initial (200) preferred orientation which gradually changes into a mixed (111) - (200) orientation with longer deposition time. However, the initial preferred orientation for the TiN films prepared under a pure N₂ atmosphere is (111); this also evolves with longer deposition time to a mixed (111) - (200) orientation. These changes in texture in the TiN thin films are due to one or combination of such factors as strain energy, surface free energy, surface diffusivity and adatom mobility; the influence of each factor depends on the processing conditions. The FE-SEM analysis of the nanocrystalline TiN thin films shows that the morphology of the films deposited in the Ar+N₂ atmosphere have a characteristic pyramidal grain shape, whereas the films deposited in a pure N₂ atmosphere exhibit a more columnar-type morphology. The AFM study revealed that the overall roughness of the films prepared in the N₂ atmosphere is less than that for the films prepared in the Ar+N₂ atmosphere. From the nanoindentation study, it is observed that the hardness and Young's modulus values of TiN films decreases with increase in deposition time in both Ar+N₂ and N₂ atmosphere. It is also observed that H and E values are higher in N₂ atmosphere as compared to Ar+ N₂ atmosphere.

7.5 Microstructural Characteristics and Mechanical Properties of Magnetron Sputtered nanocrystalline TiN films on Glass substrate

Structural and mechanical properties of nanocrystalline TiN thin films deposited on glass substrate by DC magnetron sputtering were investigated in the present work. The effect of film thickness on H and E was investigated by nanoindentation technique. The formation of nanosized crystallites in the thin films has been confirmed from the XRD, AFM and FE-SEM characterizations. The preferred orientation of TiN film is (200) up to thickness 1.26 μm and (220) & (200) peaks dominate, respectively, with increase in thickness up to 2.83 μm . It is because of the competition between surface energy and strain energy during film growth. The hardness of TiN thin film, increases with increase in thickness up to 1.89 μm (maximum hardness of 24 GPa) but it drops for $> 2.5 \mu\text{m}$ thick films. There was no drop in modulus of elasticity and it increases with increase in film thickness. The TiN films with highest hardness exhibits a less positive micro strain as observed in the present work.

7.6 Analysis of Thermal Stress in Magnetron Sputtered TiN coating by Finite Element Method

The thermal stress of TiN coating sputter deposited on glass and silicon substrate has been simulated by finite element analysis (ANSYS) and compared with that of analytical model. The influence of plane and rough substrate on the thermal stress in the coating has been studied. The thermal stress of coatings exhibits a linear relationship with substrate temperature, substrate thickness and Young's modulus of the coating. However, it exhibits an inverse relationship with the coating thickness due to the stress relaxation. The thermal stress induced in the coatings for the rough substrate is higher

as compared to that of the planar substrate. The radial stress of the TiN coating is tensile in nature on both substrates but it is high on the silicon substrate. The higher shear stress of the TiN coating is observed along the interface at the edge due to the higher stress concentration. The compressive shear stresses are observed for TiN coating on glass and silicon substrates. The spallation of the coatings from the edge is heavily dependent on these shear stresses. The adhesive strength of the TiN coating on silicon substrate is higher when compared to glass substrate due to the high compressive stress in the former.

7.7 Study of Structural and Mechanical Properties of Sputter

Deposited nanocomposite Ti-Si-N thin films

Nanocomposite Ti-Si-N thin films were deposited on Si (100) and Stainless Steel (type 304) substrate by DC/RF magnetron sputtering. The effect of varying deposition parameters on the structure and mechanical properties of Ti-Si-N films was investigated by characterization techniques such as XRD, FE-SEM, AFM, TEM and Nanoindentation, respectively. XRD analysis of the thin films, with varying Si contents, revealed the (111) orientation up to 15.6 at.% Si content, beyond which the films become amorphous. The crystallite size and lattice parameter calculated from XRD peaks show that it decreases with Si contents. The microstrain for Ti-Si-N was calculated by using lattice parameters and it decreases with varying Si content. Microstructural analysis revealed that with varying Si contents, grain size decreases and pyramidal shape grains transform into columnar and finally to amorphous structure. The surface roughness of the TiN films decreases slightly with varying Si contents. The hardness and Young's modulus values of Ti-Si-N films have increased upto 34 GPa and

275 GPa, respectively, with 15.6 at.% Si contents but it decreases afterwards with further increase in Si contents. The high hardness of Ti-Si-N films is governed by a two-phase structure consisting of nanocrystalline TiN and amorphous Si₃N₄. These TiN nanocrystals surrounded by a matrix of amorphous Si₃N₄ could assist the relaxation of stresses and reduces grain boundary sliding under stress, causing the improvement in hardness values of Ti-Si-N films.

7.8 Influence of Deposition Parameters on the Structural and Mechanical Properties of nanocomposite Ti-Si-N thin films

The effect of varying deposition parameters on the structure and mechanical properties of nanocomposite Ti-Si-N films, deposited on Si (100) substrates by DC/RF magnetron sputtering, were investigated by characterization techniques such as XRD, FE-SEM, AFM and nanoindentation, respectively in the present work. XRD analysis of the thin films exhibit all (111), (200) & (220) peaks initially with varying sputtering pressure but (111) peak dominates at higher sputtering pressure due to increase in grain size which leads to crystallinity of the films. The crystallite size calculated from XRD peaks shows that it increases with increasing sputtering pressure. Microstructural analysis revealed that the dense blurred grains transform into uniform grains in the films and porous microstructure with increasing sputtering pressure. The surface roughness of the Ti-Si-N films increases with varying sputtering pressure. The hardness and Young's modulus values of Ti-Si-N films are 33.7 GPa and 278.6 GPa, respectively, with 5 mTorr sputtering pressure but it decreases with further increase in sputtering pressure due to the increase in porosity.

7.9 Microstructural and Mechanical Properties of Sputter Deposited TiN/SiN_x Multilayer thin films

TiN/SiN_x multilayer films were deposited on Si (100) substrate by DC/RF magnetron sputtering in the present work. The effect of varying deposition parameters on the structural and mechanical properties of TiN/SiN_x multilayer films was investigated by several characterization techniques such as XRD, FE-SEM, AFM, TEM and nanoindentation technique. XRD analysis of the films, with varying SiN_x layer deposition time revealed the (111), (200) and (220) orientation and with variation of TiN layer deposition time, the same orientations were observed initially but (200) orientation grows up with increasing TiN layer deposition time. The grain size of the films was around 7.0 nm in varying SiN_x layer deposition time and it has increased from 2.7 to 11.3 nm when the deposition time for the TiN layer was increased. The surface roughness of the TiN/SiN_x multilayer films was calculated from its AFM images and it remains constant with varying SiN_x layer deposition time but increases in the other case, with varying TiN layer deposition time. The hardness and Young's modulus values of TiN/SiN_x multilayer films have increased upto 31.4 GPa and 365.8 GPa, respectively, with varying SiN_x layer deposition time (10 seconds) but it decreased with further increase in SiN_x layer deposition time. The decrease in hardness beyond the deposition time of (10 seconds) SiN_x is due to its higher thickness, which does not facilitate the formation of equiaxed structure of TiN crystals. In the other case, with increase in deposition time for TiN layer, hardness and Young's modulus values of TiN/SiN_x multilayer films increases initially but decreases uniformly and lastly increases sharply up to 33.4 GPa and 370.5 GPa, respectively.

SUGGESTIONS FOR FUTURE WORK

Based on the present work pursued on the Ti based nitrides thin films such as TiN, Ti-Si-N and TiN/SiN_x multilayers, the following recommendations for the future work are proposed:

- 1) The effect of sputtering process parameters such as substrate temperature, pressure, and power on the microstructural characteristics of TiN, Ti-Si-N, TiN/SiN_x multilayers has been studied thoroughly. However, it is very essential to study the influence of substrate bias, various gas compositions of Ar and N₂ on the growth of the aforementioned thin films for obtaining the desirable microstructural characteristics such as fine grain size, favorable textures, and high density in the films.
- 2) The influence of individual and the combined effect of sputtering process parameters such as substrate temperature, sputtering pressure, power, biasing, deposition time, and various gas compositions of Ar and N₂ on the morphology of the nitride films should be substantiated to produce the reproducible films, exhibiting excellent mechanical properties, with standard process parameters.
- 3) The fundamental understanding of the nucleation and growth kinetics of the nitride films contributing to the formation of nanograins is vital to realize the superior mechanical and functional properties of hardcoatings.
- 4) The mechanical properties of the TiN, Ti-Si-N, and TiN/SiN_x multilayers hardcoatings such as bond strength, scratch and wear resistance need to be studied extensively using nanoindentation technique to understand the failure

mechanisms, which would enable us to develop ultrahard coatings hitherto unachieved in the literature.

- 5) The thermal stress in Ti and TiN coatings has been simulated by using finite element analysis and compared with that of it calculated using analytical technique in the present work. However, it is important to measure thermal stress as well as the intrinsic residual stress of TiN, Ti-Si-N, and TiN/SiN_x multilayers experimentally. The nature of residual stress, tensile or compressive should be quantified as it renders an insight into the delamination of the coatings.
- 6) In the Ti-Si-N nanocomposite thin films and TiN/SiN_x multilayers, it is very essential to study the effect of various gas composition of Ar and N₂ on the formation of nanocrystals of TiN and amorphous/crystalline SiN_x layer. The thickness of SiN_x in multilayers ought to be controlled carefully through the apt Ar/N₂ ratio, during sputtering, so to realize the hardening mechanism manifested via tiny nanocrystals of TiN and very thin amorphous layer of SiN_x.

REFERENCES

- 1) **AFM lab manual**, "Atomic Force Microscopy: A guide to understanding and using the AFM", Galloway Group, Spring (2004)
- 2) **Ajikumar P.K.**, Kamruddin M., Nithya R., Shankar P., Dash S., Tyagi A.K. and Raj B., "Surface nitridation of Ti and Cr in ammonia atmosphere", *Scripta Materialia*, **51**, 361–366 (2004)
- 3) **Amin M.** and Antony S. J., "Compressive strength of Si-based Particulate Assemblies: A comparative study using DEM and atomistic simulations", *Computational Materials Science*, **36(4)**, 381-385 (2006)
- 4) **An T.**, Tian H.W., Wen M. and Zheng W.T., "Structures and mechanical properties of TiN/SiN_x multilayer films deposited by magnetron sputtering at different N₂/Ar gas flow ratios", *Vacuum*, **82**, 1187–1190 (2008)
- 5) **ANSYS: The General Purpose Finite Element Software, Version 8.0**, Swanson Analysis Systems, Inc, International, USA, Houston, TX, USA (2003)
- 6) **Averin D.** and Likharev K., "Mesoscopic phenomena in solids", Elsevier, Amsterdam, 173-271 (1991)
- 7) **Barnett S. A.** and Madan A., "Hardness and stability of metal–nitride nanoscale multilayers", *Scripta Materialia*, **50**, 739-744 (2004)
- 8) **Barsoum M. W.**, "Fundamentals of ceramics", *Materials science series*, McGRAW-Hill International Editions, Singapore (1997)
- 9) **Basame S.B.** and White H.S., "Pitting corrosion of titanium the relationship between pitting potential and competitive anion adsorption at the oxide

- film/electrolyte interface”, *Journal of Electrochemical Society*, **147**, 1376-1381 (2000)
- 10) **Batista J.C.A.**, Wilson A.D., Davison A., Matthews A. and Fancey K.S., “X-ray diffraction analyses of titanium coatings produced by electron beam evaporation in neon and argon inert gases”, *Journal of Vacuum Science and Technology A*, **21**, 1702-1707 (2003)
 - 11) **Batista J.C.A.**, Wilson A.D., Davison A., Matthews A. and Fancey K.S., “Gas scattering effects and microstructural evaluation of electron beam evaporated titanium coatings in neon and argon at different gas pressures”, *Vacuum*, **72**, 225-232 (2004a)
 - 12) **Batista J.C.A.**, Wilson A.D., Davison A., Matthews A. and Fancey K.S., “Gas scattering effects and microstructural evaluation of electron beam evaporated titanium coatings in neon and argon at different gas pressures” *Vacuum*, **72**, 225-232 (2004b)
 - 13) **Benegra M.**, Lamas D. G., Rapp M. E. F. D., Mingolo N., Kunrath A. O. and Souza R. M., “Residual stresses in titanium nitride thin films deposited by direct current and pulsed direct current unbalanced magnetron sputtering”, *Thin Solid Films*, **494**, 146-150 (2006)
 - 14) **Bielawski M.** and Seo D., “Residual stress development in UMS TiN coatings”, *Surface and Coatings Technology*, **200**, 1476-1482 (2005)
 - 15) **Boley B.** and Weiner J.H., “Theory of thermal stresses”, Kreiger Publishing, Florida (1985)
 - 16) **Boxley C.J.**, White H.S., Gardner C.E. and Macpherson J.V., “Nanoscale imaging of the electronic conductivity of the native oxide film on titanium using

- conducting atomic force microscopy”, *Journal of Physical Chemistry B*, **107**, 9677-9680 (2003)
- 17) **Boyer R. R.**, “An overview on the use of titanium in the aerospace industry”, *Material Science and Engineering A*, **213**, 103-114 (1996)
 - 18) **Brizoual L. L.**, Granier A., Clenet F., Briaud P., Lemperiere G. and Turban G., “Experimental study of Ti–Si–N films obtained by radio frequency magnetron sputtering”, *Surface and Coatings Technology*, **116-119**, 922-926 (1999)
 - 19) **Bull S.J.**, “Modelling the hardness response of bulk materials, single and multilayer coatings”, *Thin Solid Films*, **398–399**, 291-298 (2001)
 - 20) **Bunshah R. F.** and Juntz R. S., “Influence of condensation temperature on microstructure and tensile properties of titanium sheet produced by high-rate physical vapor deposition process”, *Metallurgical Transactions*, **4**, 21-26 (1973)
 - 21) **Cai K.**, Muller M., Bossert J., Rechtenbach A. and Jandt K.D., “Surface structure and composition of flat titanium thin films as a function of film thickness and evaporation rate”, *Applied Surface Science*, **250**, 252-267 (2005)
 - 22) **Cairney J. M.**, Hoffman M. J., Munroe P. R., Martin P. J. and Bendavi A., “Deformation and fracture of Ti–Si–N nanocomposite films”, *Thin Solid Films*, **479**, 193-200 (2005)
 - 23) **Chandra R.**, Chawla A. K., Kaur D. and Ayyub P., “Structural, optical and electronic properties of nanocrystalline TiN films”, *Nanotechnology*, **16**, 3053-3056 (2005)
 - 24) **Chandra R.**, Kaur D., Chawla A. K., Phinichka N. and Barber Z. H., “Texture development in Ti–Si–N nanocomposite thin films”, *Materials Science and Engineering A*, **423**, 111-115 (2006a)

- 25) **Chandra R.**, Chawla A. K., and Ayyub P., "Optical and structural properties of sputter- deposited nanocrystalline Cu₂O films: Effect of sputtering gas", *Journal of Nanoscience and Nanotechnology*, **6**, 1119-1123 (2006b)
- 26) **Chawla V.**, Jayaganthan R. and Chandra R., "Finite element analysis of thermal stress in magnetron sputtered Ti coating", *Journal of Materials Processing Technology*, **200**, 205-211 (2008a)
- 27) **Chawla V.**, Jayaganthan R. and Chandra R., "Structural characterizations of magnetron sputtered nanocrystalline TiN thin films", *Materials Characterization*, **59**, 1015-1020 (2008b)
- 28) **Checchetto R.**, "Titanium thin film deposition in a deuterium atmosphere", *Thin Solid Films*, **302**, 77-83 (1997)
- 29) **Chen Y.H.**, Lee K.W., Chiou W.A., Chung Y.W. and Keer L.M., "Synthesis and structure of smooth, superhard TiN/SiN_x multilayer coatings with an equiaxed microstructure", *Surface and Coatings Technology*, **146-147**, 209-214 (2001)
- 30) **Chen Y. H.**, Guruz M., Chung Y. W. and Keer L. M., "Thermal stability of hard TiN/SiN_x multilayer coatings with an equiaxed microstructure", *Surface and Coatings Technology*, **154**, 162-166 (2002)
- 31) **Chinmulgund M.**, Inturi R.B. and Barnard J.A., "Effect of Ar gas pressure on growth, structure, and mechanical properties of sputtered Ti, Al, TiAl, and Ti₃Al films", *Thin Solid Films*, **270**, 260-263 (1995)
- 32) **Chopra K.L.**, *Thin Film Phenomena*, New York: McGraw-Hill (1969)
- 33) **Chou W.J.**, Yu G. P. and Huang J. H., "Deposition of TiN thin films on Si(100) by HCD ion plating", *Surface and Coatings Technology*, **140**, 206-214 (2001)

- 34) **Choubey A.**, Basu B. and Balasubramaniam R., "Tribological behaviour of Ti- based alloys in simulated body fluid solution at fretting contacts", *Materials Science and Engineering A*, **379**, 234–239. (2004)
- 35) **Chung K.H.**, Liu G.T., Duh J.G. and Wang J.H., "Biocompatibility of a titanium- aluminum nitride film coating on a dental alloy", *Surface and Coatings Technology*, **188–189**, 745-749 (2004)
- 36) **Cullity B. D.** and Stock S. R., "Elements of X-ray diffraction", Third edition, Prentice Hall, New York (2001)
- 37) **Desirens M.**, Patscheider J., and Levy F., "Improving the properties of titanium nitride by incorporation of silicon", *Surface and Coatings Technology*, **108-109**, 241-246 (1998)
- 38) **Desirens M.**, Patscheider J., and Levy F., "Mechanical properties and oxidation resistance of nanocomposite TiN–SiN_x physical-vapor-deposited thin films", *Surface and Coatings Technology*, **120-121**, 158-165 (1999)
- 39) **Doyle B.L.**, Peercy P.S., Wiley J.D., Perepesko J.H. and Nordman J.E., "Au diffusion in amorphous and polycrystalline Ni_{0.55}Nb_{0.45}", *Journal of Applied Physics*, **53**, 6186-6190 (1982)
- 40) **Drexler K.E.**, "Molecular engineering: an approach to the development of general capabilities for molecular Manipulation", *Proceedings of the National Academy of Sciences*, **78**, 5275-5278 (1981)
- 41) **Drory M. D.**, Thouless M. D. and Evans A.G., "On the decohesion of residually stressed thin films", *Acta Metallurgica*, **36**, 2019-2028 (1988)
- 42) **Du H.**, Xiao J. Q., Zeu Y. S., Wang T. G., Gong J., Sun C. and Wen L. S., "Optical properties of ultrathin aluminum films deposited by magnetron sputtering in visible

- band”, *Optical Materials*, **28**, 994-949 (2006)
- 43) **Efeoglu I.**, Arnell R.D., and Teer D.G., “The mechanical and tribological properties of titanium aluminium nitride coatings formed in a four magnetron closed-field sputtering system”, *Surface and Coatings Technology*, **57**, 117-121 (1993)
 - 44) **Evans A. G.** and Hutchinson J. W., “On the mechanics of delamination and spalling in compressed films”, *International Journal of Solids and Structures*, **20**, 455-466 (1984)
 - 45) **Fischer- Cripps A. C.**, “Nanoindentation, mechanical engineering series”, Springer - Verlag, New York (2001)
 - 46) **Fleger S. L.**, Heckman J. W., Karen Jr. and Klomprens L., “Scanning and transmission electron microscopy: An introduction”, Oxford University Press, New York (1993)
 - 47) **Franks W.**, Schenker I., Schmutz P., and Hierlemann A., “Impedance characterization and modeling of electrodes for biomedical applications”, *IEEE Transactions on Biomedical Engineering*, **52**, 1295-1302 (2005)
 - 48) **Fujitsuka N.**, Sakata J., Miyachi Y., Mizuno K., Ohtsuka K, Taga Y., and Tabata O., “Monolithic pyroelectric infrared image sensor using PVDF thin film”, *Sensors and Actuators A: Physical*, **66**, 237-243 (1998)
 - 49) **Gandini C.**, Lacquaniti V., Monticone E., Portesi C., Pasca E. and Ventura G., “Correlation of critical temperatures and electrical properties in Titanium films”, *International Journal of Modern Physics B*, **17**, 948-952 (2003)
 - 50) **Gleiter H.**, “Mechanical properties and deformation behaviour of materials having ultra-fine microstructures”, *NATO ASI Series, E: Applied Sciences*, **233**, 3 (1993)
 - 51) **Glew M. R. L.**, Vollmer A., Schroeder S.L. M. and Barber Z. H., “The

- characterization of TiN thin films using optical reflectivity measurements”, *Journal of Physics D: Applied Physics*, **35**, 2643–2647 (2002)
- 52) **Godfroid T.**, Gouttebaron R., Dauchot J. P., Leclere P., Lazzaroni R. and Hecq M., “Growth of ultra thin Ti films deposited on SnO₂ by magnetron sputtering”, *Thin Solid Films*, **437**, 57–62 (2003)
- 53) **Gohil S.**, Banerjee R., Bose S. and Ayyub P., “Influence of synthesis conditions on the nanostructure of immiscible copper–silver alloy thin films”, *Scripta Materialia*, **58**, 842– 845 (2008)
- 54) **Greene J. E.**, “Handbook of Crystal Growth” in: D. T. J. Hurle (Ed.), Vol. 1 Elsevier, Amsterdam (1993)
- 55) **Grovenor C. R. M.**, Hentzell H. T. G., and Smith D. A., “The development of grain structure during growth of metallic films”, *Acta Metallurgica*, **32**, 773–781 (1984)
- 56) **Grundy P. J.** and Jones G. A., “Electron microscopy in the study of materials”, Edward Arnold Limited, London (1976)
- 57) **Gunnars J.** and Wiklund U., “Determination of growth-induced strain and thermo-elastic properties of coatings by curvature measurements”, *Materials Science and Engineering A*, **336**, 7–21 (2002)
- 58) **Habig K.-H.**, “Wear behaviour of surface coatings on steels”, *Tribology International*, **22**, 65–73 (1989)
- 59) **Habig K.-H.** and Zu Kocker G. M., “Simulation of the tribological behaviour of tools for cutting ductile materials”, *Journal of Physics D: Applied Physics*, **25**, A307–A312 (1992)
- 60) **Haider J.**, Rahman M., Corcoran B. and Hashmi M. S. J., “Simulation of thermal

- stress in magnetron sputtered thin coating by finite element analysis”, *Journal of Materials Processing and Technology*, **168**, 36-41 (2005)
- 61) **Hainsworth S. V.** and **Soh W. C.**, “The effect of the substrate on the mechanical properties of TiN coatings”, *Surface and Coatings Technology*, **163-164**, 515-520 (2003)
- 62) **Han S. M.**, **Shah R.**, **Banerjee R.**, **Viswanathan G.B.**, **Clemens B.M.** and **Nix W.D.**, “Combinatorial studies of mechanical properties of Ti–Al thin films using Nanoindentation”, *Acta Materialia*, **53**, 2059–2067 (2005)
- 63) **Hay J. L.** and **Pharr G. M.**, “Instrumented Indentation testing”, *ASM Handbook, Materials Testing and Evaluation*, **8**, 232-243 (2000)
- 64) **Helmersson U.**, **Sundgren J. E.** and **Greene J. E.**, “Microstructure evolution in TiN films reactively sputter deposited on multiphase substrates”, *Journal of Vacuum Science and Technology A*, **4**, 500-503 (1986)
- 65) **Helmersson U.**, **Todorova S.**, **Barnett S. A.**, **Sundgren J. E.**, **Markert L. C.** and **Greene J. E.**, “Growth of single-crystal TiN/VN strained-layer superlattices with extremely high mechanical hardness”, *Journal of Applied Physics*, **62**, 481-484 (1987)
- 66) **Henderson P. S.**, **Kelly P. J.**, **Amell R. D.**, **Backer H.** and **Bradley J. W.**, “Investigation into the properties of titanium based films deposited using pulsed magnetron sputtering”, *Surface and Coating Technology*, **174-175**, 779-783 (2003)
- 67) **Hirai T.** and **Hayashi S.**, “Density and deposition rate of chemically vapour-deposited Si₃N₄-TiN composites”, *Journal of Materials Science*, **18**, 2401-2406 (1983)
- 68) **Hitchman M.L.** and **Jensen K.F.**, “Chemical vapor deposition principles and

- applications", Academics Press, London (1993)
- 69) **Hofmann** K., Spangenberg B., Luysberg M. and Kurz H., "Properties of evaporated titanium thin films and their possible application in single electron devices", *Thin Solid Films*, **436**, 168-174 (2003)
 - 70) **Hoang** N. H., McKenzie D. R., McFall W. D. and Yin Y., "Properties of TiN films deposited at low temperature in a new plasma-based deposition system", *Journal of Applied Physics*, **80**, 6279-6285 (1996)
 - 71) **Huang** C. T. and Duh J. G., "Deposition of (Ti,Al)N films on A2 tool steel by reactive r.f. magnetron sputtering", *Surface and Coatings Technology*, **71**, 259-266 (2005a)
 - 72) **Huang** J. H., Lau K. W. and Yu G. P., "Effect of nitrogen flow rate on structure and properties of nanocrystalline TiN thin films produced by unbalanced magnetron sputtering", *Surface and Coatings Technology*, **191**, 17-24 (2005b)
 - 73) **Hultman** L., Sundgren J.E., Markert L.C. and Greene J.E., "Ar and excess N₂ incorporation in epitaxial TiN films grown by reactive bias sputtering in mixed Ar/N₂ and pure N₂ discharges", *Journal of Vacuum Science and Technology A*, **7**, 1187-1193 (1989)
 - 74) **Huth** M. and Flynn C.P., "Titanium thin film growth on small and large misfit substrates", *Applied Physics Letters*, **71**, 2466-2468 (1997)
 - 75) **Iida** S., "Observation of the surface and structure of very thin Ti film", *Japanese Journal of Applied Physics*, **29**, L361-L363 (1990)
 - 76) **Islamoglu** Y., Celik E., Parmaksizoglu C. and Hascicek Y.S., "Effects on residual stresses of annealing parameters in high-temperature ZrO₂ insulation coatings on Ag/Bi-2212 superconducting tapes using finite element method", *Materials &...*

Design, **23**, 531-536 (2002)

- 77) **Jeyachandran** Y.L., Karunagaran B., Narayandass S. K., Mangalaraj D., Jenkins T.E. and Martin P.J., "Properties of titanium thin films deposited by dc magnetron sputtering", *Materials Science and Engineering A*, **431**, 277-284 (2006)
- 78) **Jeyachandran** Y.L., Narayandass S. K., Mangalaraj D., Areva S. and Mielczarski J.A., "Properties of titanium nitride films prepared by direct current magnetron sputtering", *Materials Science and Engineering A*, **445-446**, 223-236 (2007)
- 79) **Jiang** N., Shen Y.G., Mai Y.-W., Chan Tai and Tung S. C., "Nanocomposite Ti-Si-N films deposited by reactive unbalanced magnetron sputtering at room temperature", *Materials Science and Engineering B*, **106**, 163-171 (2004)
- 80) **Jiang** N., Shen Y.G., Zhang H.J., Bao S.N. and Hou X.Y., "Superhard nanocomposite Ti-Al-Si-N films deposited by reactive unbalanced magnetron sputtering", *Materials Science and Engineering B*, **135**, 1-9 (2006)
- 81) **Jin** P., Nako S., Tanemura S. and Maruno S., "Evaluation of porosity and composition in reactively r.f.-sputtered $Ti_{1-x}Zr_xN$ films", *Thin Solid Films*, **271**, 19-25 (1995)
- 82) **Johansson** B. O., Sundgren J. E., Greene J. E., Rockett A. and Barnett S. A., "Growth and properties of single crystal TiN films deposited by reactive magnetron sputtering", *Journal of Vacuum Science and Technology A*, **3**, 303-307 (1985)
- 83) **Jung** M. J., Nam K. H., Shaginyan L. R. and Han J. G., "Deposition of Ti thin film using the magnetron sputtering method", *Thin Solid Films*, **435**, 145-149 (2003)
- 84) **Juo** K.J., Wiley J.D., Perepesko J.H., Nordman J.E., Aaron D.B., Dobisz E.A., Madisen D.E. and Thomas R.E., "Proc. high temperature electronics and instrumentation", (Sandia National Laboratories, SAND82-0425) 137 (1981)

- 85) **Kacsich T.** and Nicolet M.A., "Moving species in $Ti_{34}Si_{23}N_{43}$ oxidation?", *Thin Solid Films*, **349**, 1-3 (1999a)
- 86) **Kacsich T.**, Gasser S., Tsuji Y., Dommann A. and Nicolet M.A., "Wet oxidation of $Ti_{34}Si_{23}N_{43}$ ", *Journal of Applied Physics*, **85**, 1871-1875 (1999b)
- 87) **Kacsich T.**, Gasser S.M., Garland C. and Nicolet M.A., "Wet oxidation of $Ti_{34}Si_{23}N_{43}$ thin films with and without pre-annealing", *Surface and Coatings Technology*, **124**, 162-168 (2000)
- 88) **Kato K.**, "Microwear mechanisms of coatings", *Surface and Coatings Technology*, **76-77**, 469-474 (1995)
- 89) **Katz R.N.**, "High-temperature structural ceramics", *Science*, **208**, 841-847 (1980)
- 90) **Khor I.A.** and Gu Y.W., "Effects of residual stress on the performance of plasma sprayed functionally graded $ZrO_2/NiCoCrAlY$ coatings", *Material Science and Engineering A*, **277**, 64-76 (2000)
- 91) **Kim S. H.**, Kim J. K. and Kim K. H., "Influence of deposition conditions on the microstructure and mechanical properties of Ti-Si-N films by DC reactive magnetron sputtering", *Thin Solid Films*, **420-421**, 360-365 (2002a)
- 92) **Kim K. H.**, Choi S. R. and S. Y. Yoon, "Superhard Ti-Si-N coatings by a hybrid system of arc ion plating and sputtering techniques", *Surface and Coatings Technology*, **161**, 243-248 (2002b)
- 93) **Kim T. S.**, Park S. S. and Lee B.T., "Characterization of nano-structured TiN thin films prepared by R.F. magnetron sputtering", *Materials Letters*, **59**, 3929-3932 (2005)
- 94) **Knotek O.** and Leyendecker T., "On the structure of (Ti, Al)N-PVD coatings", *Journal of Solid State Chemistry*, **70**, 318-322 (1987)

- 95) **Ko D. H.**, Kim E. H., Choi S., Yoo B.Y. and Lee H. D., "Microstructure analyses of the titanium films formed by the ionized sputtering process", *Thin Solid Films*, **340**, 13-17 (1999)
- 96) **Lacerda M.M.**, Chen Y.H., Zhou B., Guruz M.U. and Chung Y.W., "Synthesis of hard TiN coatings with suppressed columnar growth and reduced stress", *Journal of Vacuum Science and Technology A*, **17**, 2915-2919 (1999)
- 97) **Lee A.T.**, Cabrera B., and Young B.A., "Phonon-mediated particle detection utilizing titanium superconducting transition edge sensors on silicon crystal surfaces", *IEEE Transactions of Magnetics*, **27**, 2753-2756 (1991)
- 98) **Li T. Q.**, Noda S., Komiyama H., Yanamoto T. and Ikuhara Y., "Initial growth stage of nanoscaled TiN films: Formation of continuous amorphous layers and thickness- dependent crystal nucleation", *Journal of Vacuum Science and Technology A*, **21**, 1717-1723 (2003)
- 99) **Li Z.G.**, Mori M., Miyake S., Kumagai M., Saito, H. and Muramatsu Y., "Structure and properties of Ti-Si-N films prepared by ICP assisted magnetron sputtering", *Surface and Coatings Technology*, **193**, 345-349 (2005)
- 100) **Liu A. Y.**, and Cohen M. L., "Structural properties and electronic structure of low-compressibility materials: β -Si₃N₄ and hypothetical β -C₃N₄", *Physical Review B*, **41**, 10727-10734 (1990)
- 101) **Liu Z.-J.**, Zhang C. H., Shen Y. G. and Mai Y.-W., "Monte Carlo simulation of nanocrystalline TiN/amorphous SiN_x composite films", *Journal of Applied Physics*, **95**, 758-760 (2004)
- 102) **Ma C. H.**, Huang J. H. and Chen H., "Texture evolution of transition-metal nitride thin films by ion beam assisted deposition", *Thin Solid Films*, **446**, 184-193 (2004)

- 103) **Ma L. W.**, Cairney J. M., Hoffman M. and Munroe P. R., "Deformation mechanisms operating during nanoindentation of TiN coatings on steel substrates", *Surface and Coatings Technology*, **192**, 11-18 (2005)
- 104) **Ma C. H.**, Huang J. H. and Chen H., "Nanohardness of nanocrystalline TiN thin films", *Surface and Coatings Technology*, **200**, 3868-3875 (2006)
- 105) **Ma L. W.**, Cairney J. M., Hoffman M. and Munroe P. R., "Three dimensional imaging of deformation modes in TiN-based thin film coatings", *Thin Solid Films*, **515**, 3190-3195 (2007)
- 106) **Mahony C.O.**, Hill M., Hughes P.J. and Lane W.A., "Titanium as a micromechanical material", *Journal of Micromechanics and Microengineering*, **12**, 438-443 (2002)
- 107) **Maissel L. I.** and Glang R., "Handbook of thin film technology", New York McGraw- Hill, 1-22 (1970)
- 108) **Mariano J. P.**, Caro J., and Colominas C., "TiN/SiN_x submicronic multilayer coatings obtained by chemical vapor deposition in a fluidized bed reactor at atmospheric pressure (AP/FBR-CVD)", *Surface & Coatings Technology*, **201**, 4021-4025 (2006)
- 109) **Martin N.**, Barette D., Rousselot C. and Rauch J. Y., "The effect of bias power on some properties of titanium and titanium oxide films prepared by r.f. magnetron sputtering", *Surface and Coatings Technology*, **107**, 172-182 (1998)
- 110) **Martin P.J.**, and Bendavid A., "Properties of Ti_{1-x}Si_xN_y films deposited by concurrent cathodic arc evaporation and magnetron sputtering", *Surface and Coatings Technology*, **163-164**, 245-250 (2003)
- 111) **Massiani Y.**, Medjahed A., Gravier P., Argeme L. and Fedrizzi L., "Electrochemical

- study of titanium nitride films obtained by reactive sputtering”, *Thin Solid Films*, **191**, 305-316 (1990)
- 112) **Mayrhofer P. H.**, Mitterer C., Hultman L., and Clemens H., “Microstructural design of hard coatings”, *Progress in Materials Science*, **51**, 1032-1114 (2006)
- 113) **Mei F.**, Shao N., Hu X., Li G. and Gu M., “Microstructure and mechanical properties of reactively sputtered Ti-Si-N nanocomposite films”, *Materials Letters*, **59**, 2442-2445 (2005)
- 114) **Mencik J.**, “Mechanics of components with treated or coated surfaces”, Kluwer Academic Publishers, Dordrech (1995)
- 115) **Movchan B. A.** and Demschishin A. V., “Study of the structure and properties of thick vacuum condensates of nickel, titanium, tungsten, aluminium oxide and zirconium dioxide”, *Physics of Metals and Metallography*, **28**, 83-90 (1969)
- 116) **Muraishi S.**, Aizawa T. and Kuwahara H., “Fabrication of nanostructured titanium thin films via N ion implantation and post annealing treatment”, *Surface and Coatings Technology*, **188-189**, 260-264 (2004)
- 117) **Musil J.**, Hard and superhard nanocomposite coatings, *Surface and Coatings Technology*, **125**, 322-330 (2000)
- 118) **Naeem M. D.**, Orr-Arienzo W. A. and Rapp J. G., “Effect of Ti deposition temperature on $TiSi_x$ resistivity”, *Applied Physics Letters*, **66**, 877-878 (1995)
- 119) **Naoe M.**, Ono S. and Hirata T., “Crystal orientation in titanium thin films deposited by the sputtering method without plasma damage”, *Materials Science and Engineering A*, **134**, 1292-1295 (1991)
- 120) **Nicolet M-A.**, Suni I. and Finetti M., “Amorphous metallic alloys in semiconductor contact metallizations”, *Solid State Technology*, **26**, 129-133 (1983)

- 121) **Nicolet M. A.**, "Ternary amorphous metallic thin films as diffusion barriers for Cu metallization", *Applied Surface Science*, **91**, 269-276 (1995)
- 122) **Ogawa S.**, Kousaki T., Yoshida T., and Sinclair R., "Interface microstructure of titanium thin-film/silicon single-crystal substrate correlated with electrical barrier heights", *Journal of Applied Physics*, **70**, 827-832 (1991)
- 123) **Ogawa H.**, Suzuki K., Kaneko S., Nakano Y., Ishikawa Y. and Kitahara T., "Tensile testing of microfabricated thin films", *Microsystem Technologies*, **3**, 117-121 (1997)
- 124) **Ohring M.**, "Materials science of thin films", Academic Press, San Diego, California (2002)
- 125) **Oliver W. C.** and Pharr G. M., "An improved technique for determining hardness and elastic modulus using load and displacement sensing indentation experiments", *Journal of Materials Research*, **7**, 1564-1583 (1992)
- 126) **Oliver W. C.** and Pharr G. M., "Measurement of hardness and elastic modulus by instrumented indentation: advances in understanding and refinements to methodology", *Journal of Materials Research*, **19**, 3-20 (2004)
- 127) **Okyar A.F.** and Gosz M., "Finite element modeling of a microelectronic structure under uniform thermal loading", *Finite Elements in Analysis and Design*, **37**, 961-977 (2001)
- 128) **Ong H. C.**, Zhu A. X. E., and Du G. T., "Dependence of the excitonic transition energies and mosaicity on residual strain in ZnO thin films", *Applied Physics Letters*, **80**, 941-943 (2002)
- 129) **Park J. S.**, Kang S. W. and Kim H., "Growth mechanism and diffusion barrier property of plasma-enhanced atomic layer deposition Ti-Si-N thin films", *Journal*

- of Vacuum Science and Technology B, **24**, 1327-1332 (2006)
- 130) **Passeggi M.C.G.**, Vergara L.I., Mendoza S.M. and Ferron J., "Passivation and temperature effects on the oxidation process of titanium thin films", *Surface Science*, **507-510**, 825-832 (2002)
- 131) **Patscheider J.**, Zehnder T., and Diserens M., "Structure-performance relations in nanocomposite coatings", *Surface and Coatings Technology*, **146-147**, 201-208 (2001)
- 132) **Patscheider J.**, "Nanocomposite hard coatings for wear protection", *Materials Research Society Bulletin*, **28**, 180 (2003)
- 133) **Patsalas P.**, Charitidis C. and Logothetidis S., "The effect of substrate temperature and biasing on the mechanical properties and structure of sputtered titanium nitride thin films", *Surface and Coatings Technology*, **125**, 335-340 (2000)
- 134) **Pelleg J.**, Zevin L.Z., Lungo S., "Reactive-sputter-deposited TiN films on glass substrates", *Thin Solid Films*, **197**, 117-128 (1991)
- 135) **Petrov I.**, Barna P. B., Hultman L. and Greene J. E., "Microstructural evolution during film growth", *Journal of Vacuum Science and Technology A*, **21**, S117-S128 (2003)
- 136) **Polonsky I.A.**, Chang T.P., Keer L.M. and Sproul W.D., "An analysis of the effect of hard coatings on near-surface rolling contact fatigue initiation induced by surface roughness", *Wear*, **208**, 204-219 (1997)
- 137) **Polonsky I.A.**, Chang T.P., Keer L.M., and Sproul W.D., "A study of rolling-contact fatigue of bearing steel coated with physical vapor deposition TiN films: Coating response to cyclic contact stress and physical mechanisms underlying coating effect on the fatigue life", *Wear*, **215**, 191-204 (1998)

- 138) **Poppeller M.** and Abermann R., "Influence of substrate properties on the growth of titanium films. Part I", *Thin Solid Films*, **295**, 60-66 (1997a)
- 139) **Poppeller M.** and Abermann R., "Influence of substrate properties on the growth of titanium films: Part II", *Thin Solid Films*, **311**, 310-316 (1997b)
- 140) **Powell M.J.**, Easton B.C. and Hill O.F., "Amorphous silicon-silicon nitride thin-film Transistors", *Applied Physics Letters*, **38**, 794-796 (1981)
- 141) **Prochazka J.**, Karvankova P., Heijman M. G. J. V., and S. Veprek, "Conditions required for achieving superhardness of ≥ 45 GPa in nc-TiN/a-Si₃N₄ nanocomposites", *Materials Science and Engineering A*, **384**, 102-116 (2004)
- 142) **Puchi E. S. C.**, Staia M.H., Lesage J., Gil L., Gutierrez C.V., Sosa J.L.B., Perez E.A.O. and Bourhis E.L., "Fatigue behavior of AA7075- T6 aluminum alloy coated with ZrN by PVD", *International Journal of Fatigue*, **30**, 1220-1230 (2008)
- 143) **Ramakrishna M.V.S.**, Karunasiri G., Neuzil P., Sridhar U. and Zeng W.J., "Highly sensitive infrared temperature sensor using self-heating compensated microbolometers", *Sensors and Actuators A: Physical*, **79**, 122-127 (2000)
- 144) **Rao S.S.**, "Finite element method in engineering", Butterworth-Heinemann, Fourth Edition (2004)
- 145) **Rebouta L.**, Tavares C. J., Aimo R., Wang Z., Pischow K., Alves E., Rojas T.C. and Odriozola J.A., "Hard nanocomposite Ti-Si-N coatings prepared by DC reactive magnetron sputtering", *Surface and Coatings Technology*, **133-134**, 234-239 (2000)
- 146) **Rother B.** and Mucha A., "Effects of plasma ion implantation from cathodic arc plasmas", *Surface and Coatings Technology*, **142-144**, 402-405 (2001)
- 147) **Rouzaud A.**, Barbier E., Ernould J. and Quesnel E., "A method for elastic modulus

- measurements of magnetron sputtered thin films dedicated to mechanical applications”, *Thin Solid Films*, **270**, 270-274 (1995)
- 148) **Sambasivan S.** and Petuskey W.T., “Phase chemistry in the Ti-Si-N system: Thermo- chemical review with phase stability diagrams”, *Journal of Materials Research*, **9**, 2362-2369 (1994)
- 149) **Sarathi R.**, Sindhu T.K. and Chakravarthy S.R., Generation of nano aluminium powder through wire explosion process and its characterization, *Materials Characterization*, **58**, 148-155 (2007)
- 150) **Sarikaya O.** and Celik E., “Effects of residual stress on thickness and interlayer of thermal barrier ceramic MgO–ZrO₂ coatings on Ni and AlSi substrates using finite element method”, *Materials & Design*, **23**, 645-650 (2002)
- 151) **Sarwar M.**, Zhang X.-Y. and Gillibrand D., “Performance of titanium nitride-coated carbide-tipped circular saws when cutting stainless steel and mild steel”, *Surface and Coatings Technology*, **94–95**, 617-621 (1997)
- 152) **Savaloni H.**, Taherizadeh A. and Zendehtnam A., “Residual stress and structural characteristics in Ti and Cu sputtered films on glass substrates at different substrate temperatures and film thickness”, *Physica B: Condensed Matter*, **349**, 44-55 (2004)
- 153) **Shen Y. G.**, Lu Y. H. and Liu Z. J., “Microstructure evolution and grain growth of nanocomposite TiN–TiB₂ films: experiment and simulation”, *Surface and Coatings Technology*, **200**, 6474-6478 (2006)
- 154) **Shimazaki Y.** and Winer W.O., “Frictional behavior of sputtered TiN”, *Wear*, **117**, 161-177 (1987)
- 155) **Shizhi L.**, Yulong S., Hongrui P., “Ti-Si-N films prepared by plasma-enhanced

- chemical vapor deposition”, *Plasma Chemistry and Plasma Processing*, **12**, 287-297 (1992)
- 156) **Shoesmith** D. W., Hardie D., Ikeda B. M. and Noel J. J., “Hydrogen absorption and lifetime performance of titanium waste containers”, Atomic Energy of Canada Limited Report, AECL-11770, COG-97-035-I (1997a)
- 157) **Shoesmith** D.W., Ikeda B.M. and LeNeveu D.M., “Modeling the failure of nuclear waste containers”, *Corrosion (Houston)*, **53**, 820-829 (1997b)
- 158) **Shojaei** O. R. and Karimi A., “Comparison of mechanical properties of TiN thin films using nanoindentation and bulge test” *Thin Solid Films*, **332**, 202-208 (1998)
- 159) **Shtansky** D.V., Lobova T.A., Fominski V.Y., Kulinich S.A., Lyasotsky I.V., Petrzhhik M.I., Levashov E.A. and Moore J.J., “Structure and tribological properties of WSe_x , WSe_x/TiN , $WSe_x/TiCN$ and $WSe_x/TiSiN$ coatings”, *Surface and Coatings Technology*, **183**, 328–336 (2004)
- 160) **Shum** P.W., Li K.Y., Zhou Z.F. and Shen Y.G., “Structural and mechanical properties of titanium–aluminium–nitride films deposited by reactive close-field unbalanced magnetron sputtering”, *Surface and Coatings Technology*, **185**, 245–253 (2004)
- 161) **Singh** P. and Kaur D., “Influence of film thickness on texture and electrical and optical properties of room temperature deposited nanocrystalline V_2O_5 thin films”, *Journal of Applied Physics*, **103**, (043507)1-9 (2008)
- 162) **Smith** G.B., David A. B. and Swift P.D., “A new type of TiN coating combining broad band visible transparency and solar control”, *Renewable Energy*, **22**, 79-84 (2001)
- 163) **Sneddon**, I.N., “The relation between load and penetration in the axisymmetric

- boussinesq problem for a punch of arbitrary profile”, *International Journal of Engineering Science*, **3**, 47-57 (1965)
- 164) **Soderberg H.**, Oden M., Aldareguia J. M. M. and Hultman L., “Nanostructure formation during deposition of TiN/SiN_x nanomultilayer films by reactive dual magnetron sputtering”, *Journal of Applied Physics*, **97**, 114327 (1-8) (2005)
- 165) **Soderberg H.**, Oden M., Larsson T., Hultman L. and Aldareguia J. M. M., “Epitaxial stabilization of cubic-SiN_x in TiN/SiN_x multilayers”, *Applied Physics Letters*, **88**, 91902-91904 (2006)
- 166) **Sonoda T.**, Watazu A., Zhu J., Shi W., Kato K. and Asahina T., “Structure and mechanical properties of pure titanium film deposited onto TiNi shape memory alloy substrate by magnetron DC sputtering”, *Thin Solid Films*, **459**, 212-215 (2004)
- 167) **Soriaga M. P.**, Stickney J., Bottomley E. A. and Kim Y.-G., “Thin films: preparation, characterization, applications”, Kluwer/Plenum, New York (2002)
- 168) **Srivastav S.**, Jain A. and Kanjilal D., “Improvement of adhesion of TiN coatings on stainless steel substrates by high energy heavy ion irradiation”, *Nuclear Instruments and Methods in Physics Research B*, **101**, 400-405 (1995)
- 169) **Stoney G.G.**, “The tension of metallic films deposited by electrolysis”, *Proceedings of the Royal Society of London. Series A*, **82**, 172-175 (1909)
- 170) **Straumal B.**, Gust W., Vershinin N., Dimitriou R., and Rabkin E., “Vacuum arc deposition of Ti coatings”, *Surface and Coatings Technology*, **125**, 157–160 (2000)
- 171) **Sun X.**, Reid J.S., Kolawa E. and Nicolet M.A., “Reactively sputtered Ti-Si-N films I: Physical properties”, *Journal of Applied Physics*, **81**, 656-663 (1997a)
- 172) **Sun X.**, Reid J.S., Kolawa E., Nicolet M.A. and Ruiz R., “Reactively sputtered

- Ti-Si-N films II: Diffusion barriers for Al and Cu metallizations on Si"; *Journal of Applied Physics*, **81**, 664-671 (1997b)
- 173) **Sun X.**, Kolawa E., Im S., Garland C. and Nicolet M.A., "Effect of Si in reactively sputtered Ti-Si-N films on structure and diffusion barrier performance"; *Applied Physics A*, **65**, 43-45 (1997c)
- 174) **Taneja P.**, Chandra R., Banerjee R., and Ayuub P., "Structure and properties of nanocrystalline Ag and Cu₂O synthesized by high pressure sputtering"; *Scripta Materialia*, **44**, 1915-1918 (2001)
- 175) **Tao M.**, Udeshi D., Agarwal S., Maldonado E. and Kirk W.P., "Negative schottky barrier between titanium and n-type Si (001) for low-resistance ohmic contacts"; *Solid State Electronics*, **48**, 335-338 (2004)
- 176) **Tarniowy A.**, Mania R. and Rekas M., "The effect of thermal treatment on the structure, optical and electrical properties of amorphous titanium nitride thin films"; *Thin Solid Films*, **311**, 93-100 (1997)
- 177) **Teixeira V.**, Andritschiky M., Fischer W., Buchkremer H.P. and Stoever D., "Analysis of residual stresses in thermal barrier coatings"; *Journal of Materials Processing and Technology*, **92-93**, 209-216 (1999)
- 178) **Teixeira V.**, "Mechanical integrity in PVD coatings due to the presence of residual stresses"; *Thin Solid Films*, **392**, 276-281 (2001)
- 179) **Textor M.**, Sittig C., Frauchiger V., Tosatti S. and Brunette D.M., "Titanium in medicine"; Springer-Verlag, Heidelberg, 172-230 (2001)
- 180) **Thompson C.V.**, "Structure evolution during processing of polycrystalline films"; *Annual Review of Materials Science*, **30**, 159-190 (2000)
- 181) **Thornton J. A.**, "High rate thick film growth"; *Annual Review of Materials*

- Science, **7**, 239-260 (1977)
- 182) **Thornton J.A.**, "Substrate heating in cylindrical magnetron sputtering sources",
Thin Solid Films, **54**, 23- 31 (1978)
- 183) **Thouless M. D.**, "Cracking and delamination of coatings", Journal of Vacuum
Science and Technology A, **9**, 2510-2517 (1991)
- 184) **Tjong S.C.**, Chen H., "Nanocrystalline materials and coatings", Materials Science
and Engineering: R: Reports, **45**, 1-88 (2004)
- 185) **Torok E.**, Perry A. J., Chollet L. and Sproul W. D., "Young's modulus of TiN,
TiC; ZrN and HfN", Thin Solid Films, **153**, 37-43 (1987)
- 186) **Troll L. E.**, "Transition metal carbides and nitrides", Academic, New York (1971)
- 187) **Tsuchiya T.**, Hirata M. and Chiba N., "Young's modulus, fracture strain, and
tensile strength of sputtered titanium thin films", Thin Solid Films, **484**, 245-250
(2005)
- 188) **Tsui Y.C.** and Clyne T.W., "An analytical model for predicting residual stresses in
progressively deposited coatings Part 1: Planar geometry", Thin solid films, **306**,
23-33(1997).
- 189) **Ucar V.**, Ozel A., Mimaroglu A., Taymaz I., Call I. and Gur M., "Use of the finite
element technique to analyze the influence of coating materials, material phase
state and the purity on the level of the developed thermal stresses in plasma coating
systems under thermal loading conditions", Surface Coatings and Technology,
142-144, 950-953 (2001)
- 190) **Uhm J.** and Jeon H., "TiN diffusion barrier grown by atomic layer deposition
method for Cu metallization", Japanese Journal of Applied Physics, **40**, 4657-4660
(2001)

- 191) **Varesi E.**, Pavia G., Zenkevich A., Lebedinskii Yu., Besana P., Giussani A. And Modelli A., "Structural and physical analysis on MOCVD Ti-Si-N films" *Journal of Physics and Chemistry of Solids*, **68**, 1046-1051 (2007)
- 192) **Vaz F.**, Rebouta L., Silva R. M. C., Silva M. F. and Soares J. C., "Characterization of titanium silicon nitride films deposited by PVD", *Vacuum*, **52**, 209-214 (1999)
- 193) **Vaz F.**, Rebouta L., Goudeau P., Pacaud J., Garem H., Riviere J.P., Cavaleiro A. and Alves E., "Characterisation of $Ti_{1-x}Si_xN_y$ nanocomposite films", *Surface and Coatings Technology*, **133-134**, 307-313 (2000)
- 194) **Vaz F.**, Rebouta L., Goudeau P., Girardeau T., Pacaud J., Riviere J.P. and Traverse A., "Structural transitions in hard Si-based TiN coatings: the effect of bias voltage and temperature", *Surface and Coatings Technology*, **146-147**, 274-279 (2001)
- 195) **Vaz F.**, Carvalho S., Rebouta L., Silva M. Z., Paul A., and Schneider D., "Young's modulus of (Ti,Si)N films by surface acoustic waves and indentation techniques", *Thin Solid Films*, **408**, 160-168 (2002).
- 196) **Vaz F.**, Cerqueira P., Rebouta L., Nascimento S.M.C., Alves E., Goudeau P., Riviere J.P., Pischow K. and Rijk J.D., "Structural, optical and mechanical properties of coloured TiN_xO_y thin films", *Thin Solid Films*, **447-448**, 449-454 (2004)
- 197) **Veprek S.**, Sarott F.A. and Iqbal Z., "Effect of grain boundaries on the Raman spectra, optical absorption, and elastic light scattering in nanometer-sized crystalline silicon", *Physical Review B*, **36**, 3344-3350 (1987).
- 198) **Veprek S.** and Reiprich S., "A concept for the design of novel superhard coatings" *Thin Solid Films*, **268**, 64-71 (1995a)
- 199) **Veprek S.**, Reiprich S. and Shizhi L., "Superhard nanocrystalline composite

- materials: The TiN/Si₃N₄ system”, Applied Physics Letters, **66**, 2640-2642 (1995b)
- 200) **Veprek S.**, Nesladek P., Niederhofer A., Glatz F., Jilek M., and Sima M., “Recent progress in the superhard nanocrystalline composites: towards their industrialization and understanding of the origin of the superhardness”, Surface and Coatings Technology, **108-109**, 138-147 (1998)
- 201) **Veprek S.**, “The search for novel, superhard materials”, Journal of Vacuum Science and Technology A, **17**, 2401-2420 (1999)
- 202) **Veprek S.**, Niederhofer A., Moto K., Bolom T., Mannling H.D., Nesladek P.M., Dollinger G., and Bergmaier A., “Composition, nanostructure and origin of the ultrahardness in nc-TiN/a-Si₃N₄/a- and nc-TiSi₂ nanocomposites with H_v = 80 to ≥105 GPa”, Surface and Coatings Technology, **133-134**, 152-159 (2000)
- 203) **Veprek S.**, Mannling H.-D, Niederhofer A., Ma D. and Mukherjee S., “Degradation of superhard nanocomposites by built-in impurities”, Journal of Vacuum Science and Technology B, **22**, L5-L9 (2004)
- 204) **Veprek S.**, Veprek-Heijman M. G.J., Karvankova P. and Procházka J., “Different approaches to superhard coatings and nanocomposites”, Thin Solid Films, **476**, 1-29 (2005)
- 205) **Vijaya H. S.**, Rao G. M., Mohan S., Muralidhar G. K. and Subbanna G. N., “Characterization of titanium thin films prepared by bias assisted magnetron sputtering”, Metallurgical and Materials Transactions B, **27**, 1057-1060 (1996)
- 206) **Wallen P.** and Hogmark S., Influence of TiN coating on wear of high speed steel at elevated temperature, Wear, **130**, 123-135 (1989)
- 207) **Wang S.N.**, Mizuno K., Fujiyoshi M., Funabashi H., and Sakata J., “Thermal micropressure sensor for pressure monitoring in a minute package”, Journal of

- Vacuum Science and Technology A, **19**, 353-357 (2001)
- 208) **Ward D.J.** and **Williams A.F.**, "Finite element simulation of the development of residual stress in IAPVD films", *Thin Solid Films*, **355-356**, 311-315 (1999)
- 209) **Web link 1** (<http://www.chem.sunysb.edu/msl/fullerene.html>)
- 210) **Web link 2** (<http://www.hardcoatings.ac.at/>)
- 211) **Web link 3** (<http://www.chem.lsu.edu/htdocs/people/sfwatkins/ch4570/lattices/lattice.html>)
- 212) **Web link 4** (http://www.en.wikipedia.org/wiki/Titanium_nitride.html)
- 213) **Web link 5** (http://www.serc.carleton.edu/research_education/geochemsheets/techniques/SEM.html)
- 214) **Web link 6** (<http://www.emal.engin.umich.edu/courses/TEMChem2000/sld006.html>)
- 215) **Weppelmann E. R.** and **Swain M. V.**, "Investigation of the stresses and stress intensity factors responsible for fracture of thin protective films during ultra-micro indentation tests with spherical indenters", *Thin Solid Films*, **286**, 111-121 (1996)
- 216) **Widjaja S.**, **Limarga A.M.** and **Yip T.H.**, "Modeling of residual stresses in a plasma-sprayed zirconia/alumina functionally graded-thermal barrier coating", *Thin Solid Films*, **434**, 216-227 (2003)
- 217) **Wiklund U.**, **Gunnars J.** and **Hogmark S.**, "Influence of residual stresses on fracture and delamination of thin hard coatings", *Wear*, **232**, 262-269 (1999)
- 218) **Wolf H.**, **Streiter R.**, **Tirschler W.**, **Giegengack H.**, **Urbansky N.** and **Gessner T.**, "Investigation of long throw PVD of titanium films from polycrystalline targets with texture", *Microelectronic Engineering*, **63**, 329-345 (2002)
- 219) **Wright J. K.**, **Williamson R. L.**, **Renusch D.**, **Veal B.**, **Grimsditch M.**, **Hou P. Y.**

- and Cannon R. M., "Residual stresses in convoluted oxide scales", *Material Science and Engineering A*, **262**, 246-255 (1999)
- 220) **Xu Y**, Li L., Cai X. and Chu P. K., "Hard nanocomposite Ti-Si-N films prepared by DC reactive magnetron sputtering using Ti-Si mosaic target", *Surface and Coatings Technology*, **201**, 6824-6827 (2007)
- 221) **Xue J.M.**, Ezhilvalavan S., Gao X.S. and Wang J., "Strontium titanate doped lead metaniobate ferroelectric thin films", *Applied Physics Letters*, **81**, 877-879 (2002)
- 222) **Yoshinari M.**, Oda Y., Inoue T., and Shimono M., "Dry-process surface modification for titanium dental implants", *Metallurgical and Materials Transactions A*, **33**, 511-519 (2002)
- 223) **Yu R. C.** and Wang W. K., "Formation of Ti amorphous films deposited on liquid nitrogen-cooled substrates by ion-beam sputtering", *Thin Solid Films*, **302**, 108-110 (1997)
- 224) **Yu B.**, Miyamoto Y., Sugino O., Sasaki T., and Ohno T., "Favorable formation of the C49-TiSi₂ phase on Si (001) determined by first-principles calculations", *Applied Physics Letters*, **72**, 1176-1178 (1998)
- 225) **Zerkout S.**, Achour S., Mosser A. and Tabet N., "On the existence of superstructure in TiN_x thin films", *Thin Solid Films*, **441**, 135-139 (2003)
- 226) **Zhang T. H.** and Huan Y., "Substrate effects on the micro/nanomechanical properties of TiN coatings", *Tribology Letters*, **17**, 911-916 (2004)